DYNAMICALLY TUNABLE NANOPOROUS GOLD FOR IONIC AND MOLECULAR SEPARATIONS

BY

DANIEL ARTHUR MCCURRY

DISSERTATION

Submitted in partial fulfillment of the requirements
for the degree of Doctor of Philosophy in Chemistry
in the Graduate College of the
University of Illinois at Urbana-Champaign, 2016

Urbana, Illinois

Doctoral Committee:

Professor Ryan C. Bailey, Chair
Professor Joaquín Rodríguez-López
Professor Catherine J. Murphy
Professor Kenneth S. Suslick

Abstract

The analysis of biomolecules, including proteins and DNA, is rapidly moving towards lab-on-a-chip devices in an effort to minimize sample volume and sample loss. Pores with diameters in the tens of nanometers range have gained significant attention recently through their use as single-molecule detectors and current rectifiers. Such devices must be designed for specific targets and the use of single pores limits high throughput applications. A membrane with adjustable properties in situ would provide a simple means of performing biomolecular separations and sample pre-concentration in microfluidic devices. The goal of this work is to fabricate a dynamic membrane that can be externally modulated and therefore tuned for specific analytes by uniting traditional separation methods based on size-exclusion principles with charge-based separations techniques. Gold serves as an attractive membrane material due to its high corrosion resistance, facile surface modification, and inherent conductivity. In our approach, a simple 2-day free-corrosion de-alloying procedure in concentrated nitric acid removes less noble metals (e.g. Cu, Ni, Zn, Ag) from Au-containing alloys to form a three-dimensional nanoporous network with a very large ($4.2 \pm 0.8\,m^2\,g^{-1}$) surface area density. The random orientation and small channel size of the network nearly guarantees analyte interaction with the walls. Pore sizes of 50 ± 20 nm, as measured by scanning electron microscopy, have been attained, but adjusting de-alloying time, temperature, and pH are shown to extend this range. As a model system of dynamic control, UV-visible detection of anionic and cationic tracers transport across the nanoporous gold membrane has been monitored as a function of applied potential.

Herein, surface area characterization of the bicontinuous porous structure with feature sizes on the nanometer scale was performed using the well-known Brunauer-Emmett-Teller gas adsorption isotherm, Pb underpotential deposition, and oxide stripping voltammetry. Gateable molecular and ionic transport through NPG was obtained by dynamic electrochemical modulation of the electrical double layer (EDL) within the pores. Application of a salt gradient across bare NPG was also used to impose an asymmetrical EDL thickness, whereas NPG coated with self-assembled monolayers altered the surface charge through the oxidation or reduction of surface moieties.

Initial studies regarding protein and DNA transport through NPG have been performed. Lysozyme (Lys), bovine serum albumin (BSA), and bovine hemoglobin (BHb) served as model proteins due to differences in their isoelectric points (Lys: 11.4, BHb: 6.8, BSA: 4.7). Lys was shown to have a much stronger correlation to an applied transverse migration potential through the NPG, most likely due to its small size (~14.3 kDa) compared to that of BSA (~66.4 kDa) and BHb (~64.5 kDa). DNA flux through NPG was found to be entropically unfavored and therefore demonstrated much lower rates of transport. Finally, a microfabrication route is proposed in order to scale the NPG membrane to a microfluidic device.

To my (very large) family

Acknowledgments

I would like to thank my committee and their respective group members for their advice and help during my time as a graduate student, the University of Illinois and the National Science Foundation for funding, and the Frederick Seitz Materials Research Laboratory on campus for providing the tools and instruction needed for SEM analysis, EDX analysis, electron beam evaporation, sputter coating, and ion beam milling.

I would especially like to acknowledge Prof. Ryan Bailey for his mentorship in this challenging project. Despite the numerous complications throughout the years, he (for some reason) never gave up on the project, allowing me to grow as an independent researcher. Bailey group members, past and present, were incredibly supportive throughout my time here and I am extremely grateful for all of the help and community they have provided. The undergraduates I have mentored, Nguyen Phuong Thuy, Mallika Modak, Meifeng Lin, and John Orlet, were also all imperative to my project and I greatly appreciate their efforts. Additionally, I would like to thank others outside of the Bailey group, specifically Dr. Edward Chainani and Prof. Joaquín Rodríguez-López, for improving my knowledge of electrochemistry and circuits far beyond what is ever taught in the classroom.

One of the reasons I came to Illinois was because of the strong sense of community I felt on my visit weekend. UIUC certainly did not disappoint in that respect, as I have made some of the greatest friends during my graduate career. I had the joy of sharing the "Analytical House" with Ivan Lenov and David Wetzel for 4 years, during which we experienced such defining moments as beer bread making, thrift shop prom, rodent removal, and not having 305 S. Prairie collapse while we lived there. Along with them, Katie Baker, Grant Hisao, and Kevin Schmitt made the greatest incoming analytical class I could have asked for and I am happy to have experienced the formative years of graduate school with them. I would also like to thank Ellen Muehl, Rory Alsop, and John Alsop for their incredible friendship and support as they helped see me through some of the most stressful times of graduate school.

Of course, I could not have gotten this far without the support of my family. I am eternally grateful for all of the encouragement I received, not just during graduate school, but through everything leading up to this point.

Table of Contents

List of Abbreviations

α-HL	α-hemolysin
BET	Brunaur-Emmett-Teller isotherm
BSA	bovine serum albumin
BHg	bovine hemoglobin
BS^-	benzene sulfonate
CE	counter electrode
ChIP	chromatin immunoprecipitation
EDL	electrical double layer
EDX	energy dispersive x-ray spectroscopy
Fc	ferrocene
ICR	ion current rectification
ISODATA	Iterative Self-Organizing Data Analyzing Technique
Lys	lysozyme
MSE	mercury-mercurous sulfate (Hg/Hg_2SO_4) electrode
MV^{2+}	methyl viologen
NDS^{2+}	naphthalene disulfonate
NPG	nanoporous gold
PCR	polymerase chain reaction
PCTFE	polychlorotrifluoroethylene (Kel-F)
PEG	polyethylene glycol
PTFE	polytetrafluoroethylene (Teflon)
REF	reference electrode
RTA	rapid thermal anneal
SAM	self-assembled monolayer
SBS	sodium benzenesulfonate
SEM	scanning electron microscopy
SLRR	surface limited redox replacement
TEM	transmission electron microscopy
UHP	ultra high purity
UPD	underpotential deposition
WE	working electrode

List of Symbols

A	area	K	equilibrium constant
c	concentration	L	length (thickness)
D_i	Diffusion coefficient	Λ	molar conductivity
d	diameter	λ	wavelength
ΔE	potential difference	μ	ion mobility
e	elementary charge	n	ion pair density
ϵ	relative permittivity	N_A	Avogadro's number
ϵ_0	permittivity of free space	ϕ	potential
ϵ_p	porosity	r	radius
F	Faraday's constant	σ	surface charge
G	conductivity	T	temperature
i	current	τ	tortuosity
j	flux	z	ion charge
k	Boltzmann constant	κ^{-1}	Debye length

Chapter 1

Introduction

The rate at which molecules diffuse through nanometer-sized pores is dictated by surface interactions. As the ratio of pore to analyte diameter decreases, the effects of sterics and surface charge increase.[1,2] This effect has been exploited for nanoparticle characterization and DNA sequencing in biological pores and synthetic mimics, such as SiO_2, SiN, and graphene.[3–6] The ability to adjust nanopore surface functionality for specific analytes suggests that such pores can also be used for molecular separations.[7–9] The diameter of the pore imparts size exclusion properties to the membrane, while the surface charge of the pore can make the membrane anion- or cation-selective.[10,11] Furthermore, dynamic modulation of the surface functionality, through changes in solution pH or application of an external potential, allows for tunable transport by reversing or even eliminating the charge-selective properties of the nanopore.[12–15]

Herein, a nanoporous gold (NPG) membrane is presented as a means to unite the size- and charge-selective properties of nanopores for high-throughput separations. NPG is an attractive membrane material due to its high pore density, biocompatibility, durability, inherent conductivity, and ease of modification with surface functional groups.[16–19] The goal of this project is to develop NPG membranes for ionic and molecular separations and to leverage these membranes for biological applications.

This thesis is organized in such a way as to highlight the progression from the basics of nanopores to the future of tunable, small-volume separations. *Chapter 1* introduces a brief history of nanopores and work thus far performed in the literature. *Chapter 2* discusses the advantanges of nanoporous gold as a membrane material, namely its ease of fabrication and modification. *Chapter 3* explores the mathematical concepts behind nanopores and how they translate to NPG. *Chapter 4* demonstrates the dynamic tuning of molecular transport through NPG using external stimuli. *Chapter 5* applies the concepts of NPG surface charge towards ionic control of molecule translocation. Finally, *Chapter 6* brings a practical application of biomolecular separations to NPG membranes with the intent of eventual incorporation in microfluidic devices.

1.1 Biological Nanopores

The earliest nanopore studies were focused primarily on transmembrane proteins. Such proteins carefully maintain the intercellular environment at specific pH and ionic strength, even against large concentration gradients. The most commonly studied transmembrane protein is α-hemolysin (α-HL), the structure of which is provided in Figure 1.1.[20] This protein, secreted from *Staphylococcus aureus* before binding to human and other mammalian cell membranes, permits the translocation of ions and small molecules, including DNA and RNA oligomers.[20–22] Due to its ability to self-assemble within lipid bilayers, it served as an ideal model protein channel as it was trivial to prepare.[23] Furthermore, it was noted that by polarizing the different sides of an α-HL pore with an applied potential, molecular transport could be induced, permitting the fine tuning of transmembrane transport.[21]

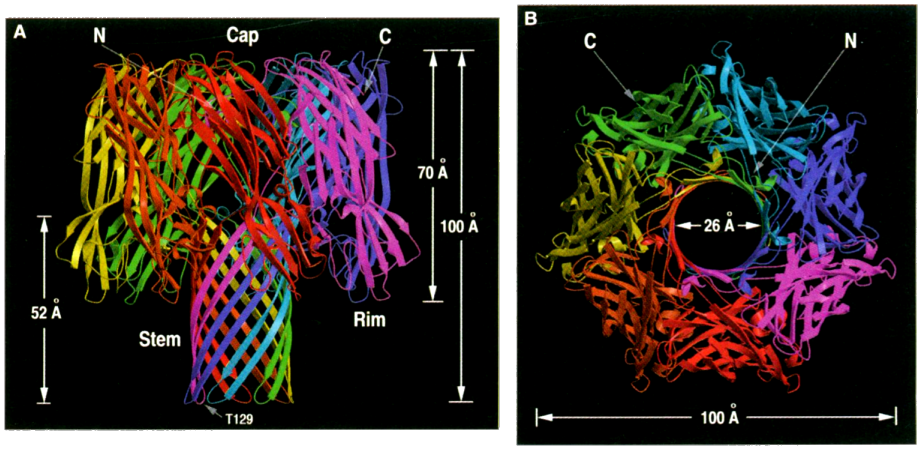

Figure 1.1: The asymmetric structure of α-HL. (a) Note the wider cap region and narrower stem. This protein sits within a lipid bilayer to modulate transport through the cell membrane. (b) A top-down view of α-HL. The interior pore has a diameter of 2.6 nm. From Song, L. et al. Structure of Staphylococcal α-Hemolysin, a Heptameric Transmembrane Pore. *Science* **1996**, *274*, 1859–1865, DOI: 10.1126/science.274.5294.1859. Reprinted with permission from AAAS.

The first report detailing characterization of oligomers as they passed through the α-HL pore was published in 1996.[24] It was noted that the current magnitude changed significantly, due to either occlusion of the cross-sectional area by the molecule through which current passed or inclusion of counterions surrounding the molecule, increasing the conductivity in the pore.[25,26] Similar to the operating principles of a Coulter counter, α-HL nanopores were used to quantify concentrations based purely on the frequency of translocation events through the pore in a process known as resistive pulse sensing, shown schematically in Figure 1.2. Additionally, the length or magnitude of the conductivity difference of the translocation event, or "pulse", could be quantified to calculate parameters including analyte size or structure.[24,27]

Since its introduction, α-HL has been transformative in the field of DNA sequencing. Due to its small

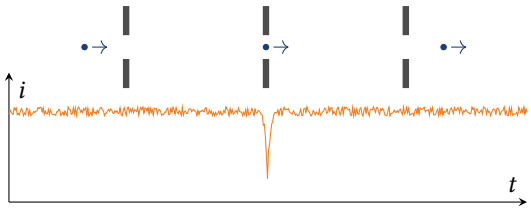

Figure 1.2: Schematic representation of a spherical particle translocating through a nanopore with a simulated current over time curve illustrating the resistive pulse sensing technique.

diameter and biocompatibility, resistive pulse sensing through α-HL of DNA has not only provided simple detection capabilities, but has introduced a rapid, inexpensive form of DNA sequencing. Miniscule differences between the individual bases of DNA strands are much more discernible in the nanoscale size regime, eliminating the previously used labor-intensive amplification steps prone to human error.[26,28,29] With recent commercialization by Oxford Nanopore Technologies, numerous advancements in nanopore sequencing, including the use of different membrane proteins to improve DNA translocation, have demonstrated accurate sequencing reads of tens of thousands of bases.[30]

In order to use the α-HL pore, it must be suspended in a lipid bilayer membrane, as shown in Figure 1.3. Often, this involves affixing a lipid bilayer to a silicon substrate with a larger pore for sandwiching between two reservoirs or across a glass capillary tube that is then filled with one solution and immersed in another.[23,24,31] This provides a fairly native environment for the membrane protein at the expense of possible stability issues of the bilayer.[23]

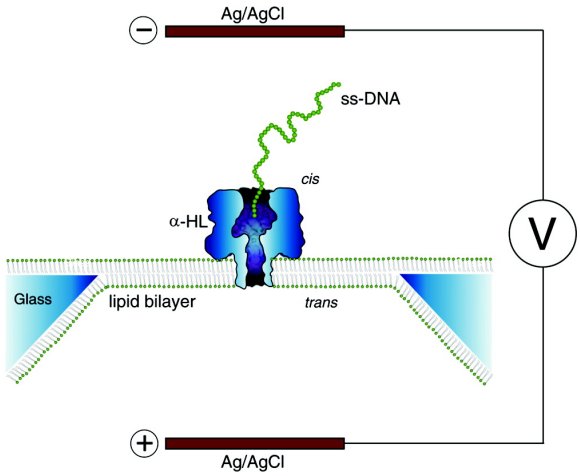

Figure 1.3: Illustration of single-stranded DNA, α-HL channel, and lipid bilayer supported on a glass nanopore membrane. Reprinted with permission from Kawano, R. et al. Controlling the Translocation of Single-Stranded DNA through α-Hemolysin Ion Channels Using Viscosity. *Langmuir* **2008**, *25*, 1233–1237, DOI: 10.1021/la803556p. Copyright © 2009 American Chemical Society.

1.2 Synthetic Nanopores

Synthetic nanopores, prepared from materials including SiO_2,[32] SiN,[33] polyethylene terephthalate (PET),[34] and graphene,[35] have been explored as an alternative to the lipid bilayer-supported α-HL. One of the most common and simplest approaches for fabricating nanopores involves milling the pore through the substrate material using a transmission electron microscope (TEM).[36] Increasing the milling time or electron beam profile creates larger pores, but pore size can also be altered by submerging the pore in a basic solution, such as NaOH, in order to etch the edges of the material over time.[37] By exposing only one side of the membrane to the basic solution, NaOH etching provided a simple method of producing geometrically asymmetrical pores.

Provided the success of biological nanopores, various groups began to investigate the importance of the geometrical asymmetry present across the α-HL pore. "Conical" nanopores present a narrow pore tip and a wide base, as shown by the representative scanning electron micrograph in Figure 1.4. In addition to the NaOH etching process, procedures including glass capillary pulling and focused ion beam milling have been used to produce conical nanopores.[2,32,38] A peculiar effect often observed when measuring current through such geometrically asymmetrical pores is ion current rectification (ICR). Briefly, differences in the electrostatic fields surrounding the pore base and mouth lead to a different measured current dependent upon the applied potential polarity.[15,37,39,40] The specifics of ICR will be discussed in further detail in Section 3.3. Conical, synthetic nanopores have been shown to be more than capable of mimicking their α-HL counterparts in biosensing studies, permitting increased durability and stability of the nanopores with the additional benefit of facile tunability.[3,41]

1.3 Gold-Coated Nanopores

The importance of the surface charge present in synthetic nanopores has been studied in detail.[40,42] Because the majority of synthetic nanopores are prepared with SiO_2 or polymers, surface charge tuning efforts largely depend upon alteration of the solution pH.[13,43–45] Unfortunately, this limits the applications of tunable nanopores to specific pH ranges, which can be especially troubling when attempting biomolecular separations, due to stability of the analyte. Attempts to combat this issue generally include electrolessly depositing Au on the pore surfaces. The first and most transformative study was performed by Martin and coworkers, where they noted that ion selectivity could be induced by applying potentials directly to the nanopore.[11] Briefly, a polycarbonate membrane was electrolessly deposited with a thin layer of Au. Altering the potential applied to the Au nanopore allowed for tuning of the ionic currents through the

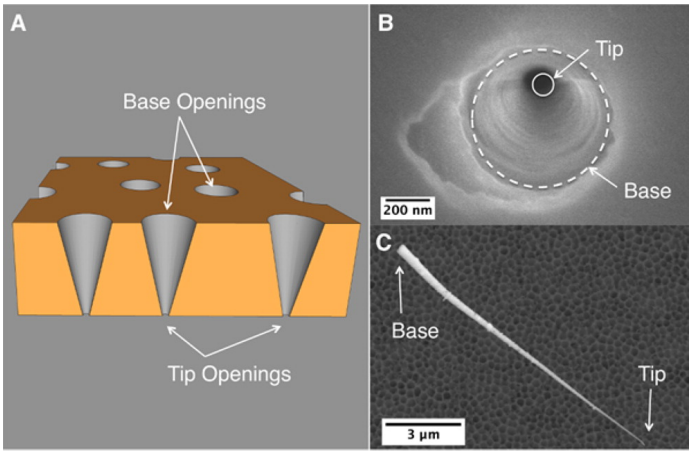

Figure 1.4: (A) Schematic illustration of a PET membrane with conically shaped pores. Dimensions are not to scale. Scanning electron micrographs of (B) the base opening of a pore in a PET membrane and (C) a gold replica of a conical PET pore. Reprinted with permission from Wu, X. et al. An Alternating Current Electroosmotic Pump Based on Conical Nanopore Membranes. *ACS Nano* **Apr. 2016**, DOI: 10.1021/acsnano.6b00939. Copyright © 2016 American Chemical Society.

pores. Since this 1995 study, numerous other laboratories have examined direct electrochemical control of pore surface charge.[46–49] By introducing an electric potential across the narrow pore diameter, selective external gating of chemicals of interest is possible.[42,50,51]

Electrochemical gating of nanopores was considered in the context of biomolecular separations by Stroeve and coworkers.[9,48,52] By using two similarly-sized, yet oppositely charged proteins, bovine serum albumin (BSA) and bovine hemoglobin (BHg), they were able to show a preferred transport of BSA vs the BHg due to the screening of the protein with a potential applied directly to the membrane. Such studies form the underlying basis for the work presented in this thesis. Although electrochemical gating in single nanopores or small arrays demonstrates selective transport, the practicality of such devices is limited due to the low molecular throughput. Furthermore, the pore size strongly contributes to not only the electrostatic effects of the pore interior, but also the size-exclusion properties of the membrane. A membrane combining a large porosity, electrochemical selectivity, and a wide distribution of pore sizes is therefore required in order to unite the desired size- and charge-selective properties into a single device.

1.4 Nanoporous Gold

As mentioned previously, NPG exhibits very attractive properties towards its use as a membrane material. It combines the ease of surface charge tuning in gold-coated pores with a very high porosity and variable pore size. NPG has historically been used as a decorative material as it dispays a rich, red color. In fact, it was many years until the underlying structure that gave NPG its interesting aesthetics was discovered.[53,54]

The quickest method of preparing NPG involves rolling a gold and silver alloy to a few nanometers thickness and then placing the resulting film on top of a concentrated nitric acid bath. Selective dissolution of the less noble Ag has been shown to produce a bicontinuous, porous Au structure.[55] This "free corrosion" method works quite well to produce consistent geometries within a matter of minutes as this procedure leaves NPG with a characteristic pore size that is intrinsic to the alloy composition, as explained in further detail in Section 2.1.

The Stine group has extensively explored NPG as a capture substrate for various biomolecules.[18,56] By coating the high surface area NPG with antibodies, a large amount of protein could be extracted from a solution flowing through the NPG. The tortuous geometry ensures that any material flowing through the pores interacts iwth the surface. A subsequent rinse or application of a potential could then release the captured material, suggesting its use as a drug delivery agent.[57]

In contrast, other groups had prevented biomolecules from flowing through NPG. Proteins that are larger than the pore sizes are inhibited from translocation, thereby permitting purification of a mixture of large proteins and small DNA strands during electrochemical analysis.[58,59] Additionally, NPG has found applications as a high surface area electrode for catalysis and fuel cells.[60,61] Such methods highlight the electrochemically accessible pore volume inside NPG, which is imperative for the proposed dynamically tunable separations.

1.5 References

1. Buchsbaum, S. F.; Mitchell, N.; Martin, H.; Wiggin, M.; Marziali, A.; Coveney, P. V.; Siwy, Z.; Howorka, S. Disentangling Steric and Electrostatic Factors in Nanoscale Transport Through Confined Space. *Nano Letters* **2013**, *13*, 3890–3896, DOI: 10.1021/nl401968r.

2. Kovarik, M. L.; Zhou, K.; Jacobson, S. C. Effect of Conical Nanopore Diameter on Ion Current Rectification. *J. Phys. Chem. B* **2009**, *113*, 15960–15966, DOI: 10.1021/jp9076189.

3. Choi, Y.; Baker, L. A.; Hillebrenner, H.; Martin, C. R. Biosensing with conically shaped nanopores and nanotubes. *Physical Chemistry Chemical Physics* **2006**, *8*, 4976–4988, DOI: 10.1039/b607360c.

4. Freedman, K. J.; Ahn, C. W.; Kim, M. J. Detection of Long and Short DNA Using Nanopores with Graphitic Polyhedral Edges. *ACS Nano* **2013**, *7*, 5008–5016, DOI: 10.1021/nn4003665.

5. Oja, S. M.; Wood, M.; Zhang, B. Nanoscale Electrochemistry. *Analytical Chemistry* **2013**, *85*, 473–486, DOI: 10.1021/ac3031702.

6. Guan, W.; Reed, M. A. Electric Field Modulation of the Membrane Potential in Solid-State Ion Channels. *Nano Letters* **2012**, *12*, 6441–6447, DOI: 10.1021/nl303820a.

7. Lee, S. B.; Martin, C. R. Electromodulated Molecular Transport in Gold-Nanotube Membranes. *Journal of the American Chemical Society* **2002**, *124*, 11850–11851, DOI: 10.1021/ja027494f.

8. Hulteen, J. C.; Jirage, K. B.; Martin, C. R. Introducing Chemical Transport Selectivity into Gold Nanotubule Membranes. *J. Am. Chem. Soc.* **1998**, *120*, 6603–6604, DOI: 10.1021/ja980045o.

9. Chun, K.-Y.; Mafé, S.; Ramírez, P.; Stroeve, P. Protein transport through gold-coated, charged nanopores: Effects of applied voltage. *Chemical Physics Letters* **2006**, *418*, 561–564, DOI: 10.1016/j.cplett.2005.11.029.

10. Martin, C. R.; Nishizawa, M.; Jirage, K.; Kang, M. Investigations of the Transport Properties of Gold Nanotubule Membranes. *J. Phys. Chem. B* **2001**, *105*, 1925–1934, DOI: 10.1021/jp003486e.

11. Nishizawa, M.; Menon, V. P.; Martin, C. R. Metal Nanotubule Membranes with Electrochemically Switchable Ion-Transport Selectivity. *Science* **1995**, *268*, 700–702, DOI: 10.1126/science.268.5211.700.

12. Yeh, L.-H.; Zhang, M.; Qian, S. Ion Transport in a pH-Regulated Nanopore. *Analytical Chemistry* **2013**, *85*, 7527–7534, DOI: 10.1021/ac401536g.

13. Ramírez, P.; Mafé, S.; Alcaraz, A.; Cervera, J. Modeling of pH-Switchable Ion Transport and Selectivity in Nanopore Membranes with Fixed Charges. *The Journal of Physical Chemistry B* **2003**, *107*, 13178–13187, DOI: 10.1021/jp035778w.

14. Anderson, B. N.; Muthukumar, M.; Meller, A. pH Tuning of DNA Translocation Time through Organically Functionalized Nanopores. *ACS Nano* **2013**, *7*, 1408–1414, DOI: 10.1021/nn3051677.

15. Guo, W.; Tian, Y.; Jiang, L. Asymmetric Ion Transport through Ion-Channel-Mimetic Solid-State Nanopores. *Accounts of Chemical Research* **2013**, *46*, 2834–2846, DOI: 10.1021/ar400024p.

16. Shulga, O. V.; Jefferson, K.; Khan, A. R.; D'Souza, V. T.; Liu, J.; Demchenko, A. V.; Stine, K. J. Preparation and Characterization of Porous Gold and Its Application as a Platform for Immobilization of Acetylcholine Esterase. *Chem. Mater.* **2007**, *19*, 3902–3911, DOI: 10.1021/cm070238n.

17. Seker, E.; Reed, M. L.; Begley, M. R. Nanoporous Gold: Fabrication, Characterization, and Applications. *Materials* **2009**, *2*, 2188–2215, DOI: 10.3390/ma2042188.

18. Stine, K. J.; Jefferson, K.; Shulga, O. V., Nanoporous Gold for Enzyme Immobilization. In *Enzyme Stabilization and Immobilization: Methods and Protocols*, Minteer, S. D., Ed.; Methods in Molecular Biology; Humana Press: Totowa, NJ, 2011; Chapter Nanoporous Gold for Enzyme Immobilization, pp 67–83, DOI: 10.1007/978-1-60761-895-9_7.

19. Tan, Y. H.; Davis, J. A.; Fujikawa, K.; Ganesh, N. V.; Demchenko, A. V.; Stine, K. J. Surface area and pore size characteristics of nanoporous gold subjected to thermal, mechanical, or surface modification studied using gas adsorption isotherms, cyclic voltammetry, thermogravimetric analysis, and scanning electron microscopy. *Journal of Materials Chemistry* **2012**, *22*, 6733–6745, DOI: 10.1039/c2jm16633j.

20. Song, L.; Hobaugh, M. R.; Shustak, C.; Cheley, S.; Bayley, H.; Gouaux, J. E. Structure of Staphylococcal α-Hemolysin, a Heptameric Transmembrane Pore. *Science* **1996**, *274*, 1859–1865, DOI: 10.1126/science.274.5294.1859.

21. Meller, A.; Nivon, L.; Branton, D. Voltage-Driven DNA Translocations through a Nanopore. *Phys. Rev. Lett.* **2001**, *86*, 3435–3438, DOI: 10.1103/PhysRevLett.86.3435.

22. Movileanu, L.; Howorka, S.; Braha, O.; Bayley, H. Detecting protein analytes that modulate transmembrane movement of a polymer chain within a single protein pore. *Nat. Biotechnol.* **2000**, *18*, 1091–1095, DOI: 10.1038/80295.

23. Jetha, N. N.; Wiggin, M.; Marziali, A., Forming an α-Hemolysin Nanopore for Single-Molecule Analysis. In *Micro and Nano Technologies in Bioanalysis: Methods and Protocols*, Foote, S. R., Lee, W. J., Eds.; Humana Press: Totowa, NJ, 2009, pp 113–127, DOI: 10.1007/978-1-59745-483-4_9.

24. Kasianowicz, J. J.; Brandin, E.; Branton, D.; Deamer, D. W. Characterization of individual polynucleotide molecules using a membrane channel. *Proceedings of the National Academy of Sciences* **1996**, *93*, 13770–13773, DOI: 10.1073/pnas.93.24.13770.

25. Smeets, R. M. M.; Keyser, U. F.; Krapf, D.; Wu, M.-Y.; Dekker, N. H.; Dekker, C. Salt Dependence of Ion Transport and DNA Translocation through Solid-State Nanopores. *Nano Letters* **2006**, *6*, 89–95, DOI: 10.1021/nl052107w.

26. Wanunu, M. Nanopores: A journey towards DNA sequencing. *Physics of Life Reviews* **2012**, *9*, 125–158, DOI: 10.1016/j.plrev.2012.05.010.

27. Wu, H.; Chen, Y.; Zhou, Q.; Wang, R.; Xia, B.; Ma, D.; Luo, K.; Liu, Q. Translocation of Rigid Rod-Shaped Virus through Various Solid-State Nanopores. *Analytical Chemistry* **2016**, *88*, 2502–2510, DOI: 10.1021/acs.analchem.5b04905.

28. Ip, C. L. et al. MinION Analysis and Reference Consortium: Phase 1 data release and analysis. *F1000Research* **2015**, DOI: 10.12688/f1000research.7201.1.

29. Shendure, J.; Ji, H. Next-generation DNA sequencing. *Nat Biotechnol* **2008**, *26*, 1135–1145, DOI: 10.1038/nbt1486.

30. Loose, M.; Malla, S.; Stout, M. Real-time selective sequencing using nanopore technology. *Nature Methods* **2016**, DOI: 10.1038/nmeth.3930.

31. Kawano, R.; Schibel, A. E. P.; Cauley, C.; White, H. S. Controlling the Translocation of Single-Stranded DNA through α-Hemolysin Ion Channels Using Viscosity. *Langmuir* **2008**, *25*, 1233–1237, DOI: 10.1021/la803556p.

32. Li, W.; Bell, N. A. W.; Hernández-Ainsa, S.; Thacker, V. V.; Thackray, A. M.; Bujdoso, R.; Keyser, U. F. Single Protein Molecule Detection by Glass Nanopores. *ACS Nano* **2013**, *7*, 4129–4134, DOI: 10.1021/nn4004567.

33. Heng, J. B.; Aksimentiev, A.; Ho, C.; Marks, P.; Grinkova, Y. V.; Sligar, S.; Schulten, K.; Timp, G. The Electromechanics of DNA in a Synthetic Nanopore. *Biophysical Journal* **2006**, *90*, 1098–1106, DOI: 10.1529/biophysj.105.070672.

34. Wu, X.; Rajasekaran, P. R.; Martin, C. R. An Alternating Current Electroosmotic Pump Based on Conical Nanopore Membranes. *ACS Nano* **Apr. 2016**, DOI: 10.1021/acsnano.6b00939.

35. He, Z.; Zhou, J.; Lu, X.; Corry, B. Bioinspired Graphene Nanopores with Voltage-Tunable Ion Selectivity for Na+ and K+. *ACS Nano* **2013**, DOI: 10.1021/nn4043628.

36. Van den Hout, M.; Hall, A. R.; Wu, M. Y.; Zandbergen, H. W.; Dekker, C.; Dekker, N. H. Controlling nanopore size, shape and stability. *Nanotechnology* **2010**, *21*, 115304, DOI: 10.1088/0957-4484/21/11/115304.

37. Apel, P. Y.; Blonskaya, I. V.; Orelovitch, O. L.; Ramirez, P.; Sartowska, B. A. Effect of nanopore geometry on ion current rectification. *Nanotechnology* **2011**, *22*, 175302, DOI: 10.1088/0957-4484/22/17/175302.

38. Haywood, D. G.; Saha-Shah, A.; Baker, L. A.; Jacobson, S. C. Fundamental Studies of Nanofluidics: Nanopores, Nanochannels, and Nanopipets. *Analytical Chemistry* **2015**, *87*, 172–187, DOI: 10.1021/ac504180h.

39. Kosińska, I. D. How the asymmetry of internal potential influences the shape of I-V characteristic of nanochannels. *The Journal of Chemical Physics* **2006**, *124* 244707, 244707, DOI: 10.1063/1.2212394.

40. Siwy, Z.; Heins, E.; Harrell, C. C.; Kohli, P.; Martin, C. R. Conical-Nanotube Ion-Current Rectifiers: The Role of Surface Charge. *J. Am. Chem. Soc.* **2004**, *126*, 10850–10851, DOI: 10.1021/ja047675c.

41. Siwy, Z.; Trofin, L.; Kohli, P.; Baker, L. A.; Trautmann, C.; Martin, C. R. Protein Biosensors Based on Biofunctionalized Conical Gold Nanotubes. *J. Am. Chem. Soc.* **2005**, *127*, 5000–5001, DOI: 10.1021/ja043910f.

42. White, H. S.; Bund, A. Mechanism of Electrostatic Gating at Conical Glass Nanopore Electrodes. *Langmuir* **2008**, *24*, 12062–12067, DOI: 10.1021/la801776w.

43. Zhang, H.; Ito, Y. pH Control of Transport through a Porous Membrane Self-Assembled with a Poly(acrylic acid) Loop Brush. *Langmuir* **2001**, *17*, 8336–8340, DOI: 10.1021/la0106079.

44. Wanunu, M.; Meller, A. Chemically Modified Solid-State Nanopores. *Nano Letters* **2007**, *7*, 1580–1585, DOI: 10.1021/nl070462b.

45. Hou, Z.; Abbott, N. L.; Stroeve, P. Self-Assembled Monolayers on Electroless Gold Impart pH-Responsive Transport of Ions in Porous Membranes. *Langmuir* **2000**, *16*, 2401–2404, DOI: 10.1021/la991045k.

46. Agonafer, D. D.; Oruc, M. E.; Chainani, E.; Lee, K. S.; Hu, H.; Shannon, M. A. Study of ionic transport through metalized nanoporous membranes functionalized with self-assembled monolayers. *Journal of Membrane Science* **2014**, *461*, 106–113, DOI: 10.1016/j.memsci.2014.03.009.

47. Makra, I.; Jágerszki, G.; Bitter, I.; Gyurcsányi, R. E. Nernst–Planck/Poisson model for the potential response of permselective gold nanopores. *Electrochimica Acta* **2012**, *73*, 70–77, DOI: 10.1016/j.electacta.2012.02.074.

48. Chun, K.-Y.; Stroeve, P. External Control of Ion Transport in Nanoporous Membranes with Surfaces Modified with Self-Assembled Monolayers. *Langmuir* **2001**, *17*, 5271–5275, DOI: 10.1021/la010066n.

49. Kalman, E. B.; Sudre, O.; Vlassiouk, I.; Siwy, Z. S. Control of ionic transport through gated single conical nanopores. *Analytical and Bioanalytical Chemistry* **2008**, *394*, 413–419, DOI: 10.1007/s00216-008-2545-3.

50. White, H. S.; Bund, A. Ion Current Rectification at Nanopores in Glass Membranes. *Langmuir* **2008**, *24*, 2212–2218, DOI: 10.1021/la702955k.

51. Karnik, R.; Fan, R.; Yue, M.; Li, D.; Yang, P.; Majumdar, A. Electrostatic Control of Ions and Molecules in Nanofluidic Transistors. *Nano Letters* **2005**, *5*, 943–948, DOI: 10.1021/nl050493b.

52. Ku, J.-R.; Stroeve, P. Protein Diffusion in Charged Nanotubes: "On–Off" Behavior of Molecular Transport. *Langmuir* **2004**, *20*, 2030–2032, DOI: 10.1021/la0357662.

53. Uwe Renner, F. et al., *Nanoporous Gold*; RSC Nanoscience & Nanotechnology; The Royal Society of Chemistry: 2012, DOI: 10.1039/9781849735285.

54. Ding, Y.; Kim, Y.-J.; Erlebacher, J. Nanoporous Gold Leaf: "Ancient Technology"/Advanced Material. *Advanced Materials* **2004**, *16*, 1897–1900, DOI: 10.1002/adma.200400792.

55. Erlebacher, J.; Aziz, M. J.; Karma, A.; Dimitrov, N.; Sieradzki, K. Evolution of nanoporosity in dealloying. *Nature* **2001**, *410*, 450–453, DOI: 10.1038/35068529.

56. Tan, Y. H.; Schallom, J. R.; Ganesh, N. V.; Fujikawa, K.; Demchenko, A. V.; Stine, K. J. Characterization of protein immobilization on nanoporous gold using atomic force microscopy and scanning electron microscopy. *Nanoscale* **2011**, *3*, 3395–3407, DOI: 10.1039/C1NR10427F.

57. Gittard, S. D.; Pierson, B. E.; Ha, C. M.; Wu, C.-A. M.; Narayan, R. J.; Robinson, D. B. Supercapacitive transport of pharmacologic agents using nanoporous gold electrodes. *Biotechnology Journal* **2010**, *5*, 192–200, DOI: 10.1002/biot.200900250.

58. Patel, J.; Radhakrishnan, L.; Zhao, B.; Uppalapati, B.; Daniels, R. C.; Ward, K. R.; Collinson, M. M. Electrochemical Properties of Nanostructured Porous Gold Electrodes in Biofouling Solutions. *Analytical Chemistry* **2013**, DOI: 10.1021/ac403013r.

59. Daggumati, P.; Matharu, Z.; Wang, L.; Seker, E. Biofouling-Resilient Nanoporous Gold Electrodes for DNA Sensing. *Anal Chem* **2015**, *87*, 8618–22, DOI: 10.1021/acs.analchem.5b02969.

60. Wittstock, A.; Neumann, B.; Schaefer, A.; Dumbuya, K.; Kübel, C.; Biener, M. M.; Zielasek, V.; Steinrück, H.-P.; Gottfried, J. M.; Biener, J.; Hamza, A.; Bäumer, M. Nanoporous Au: An Unsupported Pure Gold Catalyst? *The Journal of Physical Chemistry C* **2009**, *113*, 5593–5600, DOI: 10.1021/jp808185v.

61. McCurry, D. A.; Kamundi, M.; Fayette, M.; Wafula, F.; Dimitrov, N. All Electrochemical Fabrication of a Platinized Nanoporous Au Thin-Film Catalyst. *ACS Appl. Mater. Interfaces* **2011**, *3*, 4459–4468, DOI: 10.1021/am2011433.

Chapter 2

Fabrication, Functionalization, and Characterization of Nanoporous Gold

Nanoporous gold (NPG), as prepared from an Au-containing alloy, follows a "spinodal decomposition" mechanism whereby the less noble, sacrificial material is dissolved and the remaining Au reorganizes on the surface to form stable Au islands.[2] As the less noble metal is removed, the coordination sites surrounding the exposed Au adatoms are left empty. This energetically unfavorable condition is only remedied through the surface diffusion of the Au adatoms towards each other. As the de-alloying continues, the rate at which the Au adatoms can cluster leads to a characteristic distance, λ, between the islands. Ultimately, these islands will be undercut as new islands begin to form in the plane of the de-alloying front and a bicontinuous structure with a fairly homogeneous ligament size distribution will remain.[3] This process is key to the versatility of NPG. The Au adatom diffusion can be controlled to tune the resulting characteristic pore size distribution. In particular, altering the temperature or electrochemically altering the rate of de-alloying are simple methods of controlling pore size.[3–7]

2.1 Free Corrosion De-alloying

One of the simplest protocols for producing NPG involves immersing an Au-containing alloy in a solution that specifically attacks the less noble metals, solvating the undesired material and leaving behind a bicontinuous Au nanostructure. Adding to its simplicity, precursor alloys are often readily available from jewelry companies and craft stores. Although a majority of the literature surrounding NPG considers two-component AuAg alloys due to the similar lattice parameters of Ag and Au,[8–12] Stine and coworkers explored the use of 10 karat white (10KW) alloys from Hoover and Strong (North Chesterfield, VA) as NPG precursors.[8,13] The thinnest available alloys were 250 µm (30 GA) and contained a mixture of Au, Cu, Ni, and Zn. The Stine group was primarily focused on protein capture and enzyme immobilization, which

This chapter contains previously published material, adapted with permission from McCurry, D. A.; Bailey, R. C. Nanoporous Gold Membranes as Robust Constructs for Selectively Tunable Chemical Transport. *Journal of Physical Chemistry* **2016**, DOI: 10.1021/acs.jpcc.6b02759.
Yurun Miao, from the Suslick laboratory, is acknowledged for performing the Brunauer-Emmett-Teller isotherm measurements and analysis.

required a very high surface area and the ability to access much of the interior of the NPG monolith.[8,14] Such monoliths were therefore ideal for our own studies in tunable molecular transport through NPG.

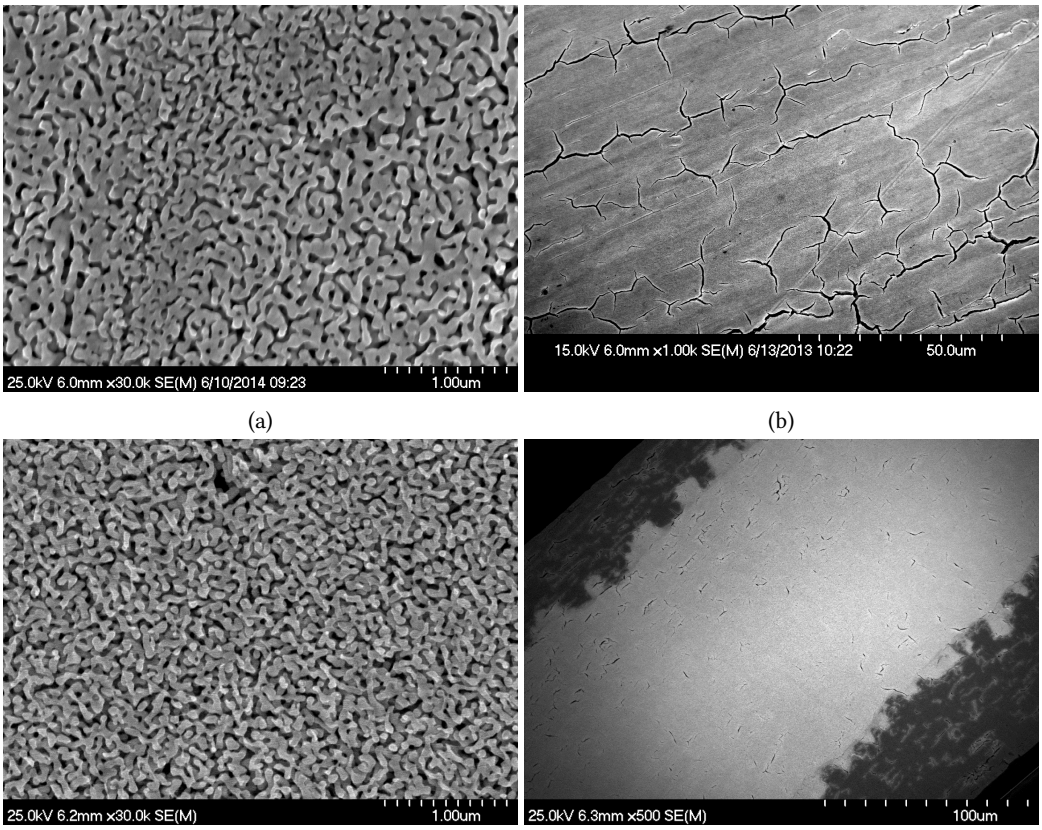

Figure 2.1: Scanning electron micrograph of (a) the NPG surface, (b) stress corrosion cracking at the NPG surface, (c) a high magnification BIB cross-section of the NPG, and (d) a BIB cross section of the entire NPG thickness. The dark gray areas at the edges of (d) are lacquer that was used affix the NPG to a gold contact in some early experiments.

Herein, the 10KW monoliths were cut into 0.2 in. by 0.2 in. squares using a wire saw. The diced alloy pieces were immersed for up to 48 hours in concentrated HNO_3 with replacement of the HNO_3 bath at 24 hours to produce NPG. Such a long time period was required for the 250 µm monoliths, as the HNO_3 must travel an increasingly longer distance as the porosity develops to continue the de-alloying front. The NPG monoliths were rinsed well with ultrapure (18.2 MΩ cm) water prior to use. Representative scanning electron micrographs of the resulting NPG are provided in Figure 2.1. A Hitachi S-4700 field emission gun scanning electron microscope (SEM) was used to image the NPG in ultra-high resolution mode at a working distance of 6 mm both before and after transport experiments, using accelerating voltages between 15 kV to 25 kV and an extracting current of 10 µA. Figure 2.1a shows the surface of a typical NPG sample with the developed nanoporosity. A lower magnification image of the surface is provided in Figure 2.1b, where

large microscale cracks can be observed. Stress corrosion cracking is a common effect in free corrosion de-alloying that results from the buildup of excess stress on the surface of the material.[15] These cracks did not appear to span the entire thickness of the NPG monolith, as evidenced by Figure 2.1d and the pore conductivity experiments performed in Section 3.1.

Cross-sectional images (Figure 2.1c-d) were taken using the SEM by embedding the NPG in an epoxy resin, followed by mechanical polishing at 2000 grit, and ultimately flat-milling with a Hitachi Ion Milling System IM4000 set to an 80° milling angle with 3 mm eccentricity. The sample was milled at 25 RPM for 45 min with accelerating and discharge voltages set to 5 kV and 1.5 kV, respectively. The nanoporosity was shown to extend throughout the entire monolith.

ImageJ image processing software was used to analyze the pore size distribution in the NPG membranes.[16] To maintain consistency between all samples, the micrographs were taken at 30 kV in ultra high resolution mode on a Hitachi S-4700 SEM with a working distance of 6 mm and magnification of 30,000X. The micrograph (Figure 2.2a) was converted to a binary, black and white image using the ISODATA (Iterative Self-Organizing Data Analysis Technique) thresholding algorithm (Figure 2.2b). The particle size analysis tool was then used where the black areas (pores) were considered particles. The ImageJ software automatically calculated the areas of the pores (Figure 2.2c), ignoring those pores on the edges of the micrograph. Each pore size could then be mapped on a histogram to determine the pore size distribution, as shown in Figure 2.2d. For free corrosion de-alloying of the NPG monoliths, median pore sizes of 50 ± 20 nm were obtained.

It is important to note, however, that the automatic pore size determination often overestimated pore sizes, since it assumed that the pore area related to perfectly circular pores. The aspect ratio of the pores varied and was more often than not, far from 1:1, meaning that the dimension in the x direction was much larger than that in the y. Manually measuring the distances between the ligaments provided constrictions as low as 10 nm and as high as 60 nm. While the values obtained using the automated method overestimated pore diameter, they served as an important metric for comparison between NPG samples.

2.1.1 Material Composition

To confirm the complete de-alloying of the 10KW Au, the elemental composition of the NPG was determined through electron dispersive X-ray spectroscopy (EDX). A LinkISIS EDX spectrometer was coupled to the Hitachi S-4700 SEM used in the present study and allowed for simultaneous imaging and composition analysis. Figure 2.3 shows the EDX spectrum for both the precursor alloy and the NPG post immersion in concentrated HNO_3 taken at a working distance of 12 mm in analysis mode. After 48 hours of de-alloying,

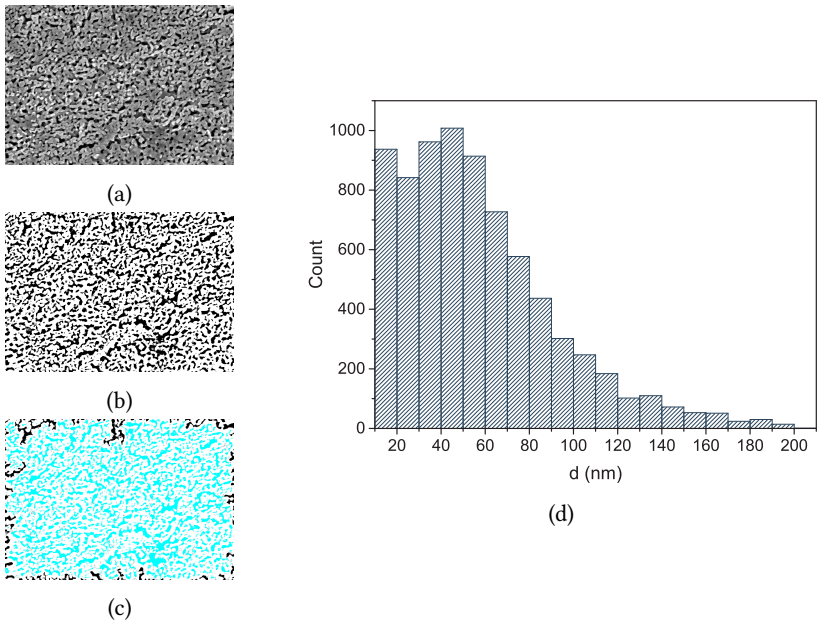

Figure 2.2: NPG pore size was determined using ImageJ. (a) Original SEM image of NPG. (b) ISODATA thresholding of NPG image. The black areas are pores and the white areas are ligaments. (c) Automated particle size analysis. The blue regions are assumed to be pores. Pore radii were then calculated from the individual blue areas, assuming circular pores. (d) Pore size distribution of NPG as determined by ImageJ analysis. The pore sizes were roughly 50 ± 20 nm.

the only detectable element was Au.

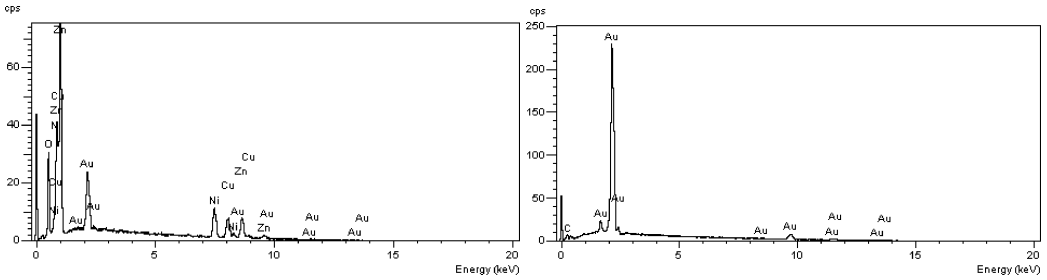

Figure 2.3: EDX spectrum for (a) a precursor 10KW alloy from Hoover and Strong and (b) a de-alloyed NPG sample.

The 2-day de-alloying time was specified in the literature to ensure complete de-alloying.[8] A more thorough, time-dependent compositional analysis was performed by immersing the alloy in concentrated HNO_3 for only a few hours at a time and subsequently dissolving the entire sample in aqua regia. The resulting solution was then analyzed using inductively coupled plasma optical emission spectroscopy (ICP-OES). As shown in Figure 2.4, the sample was nearly fully de-alloyed after 24 hours. This did not take into consideration the time required for full Au adatom diffusion, however, so a 2-day de-alloying protocol was still followed for consistent NPG structure.

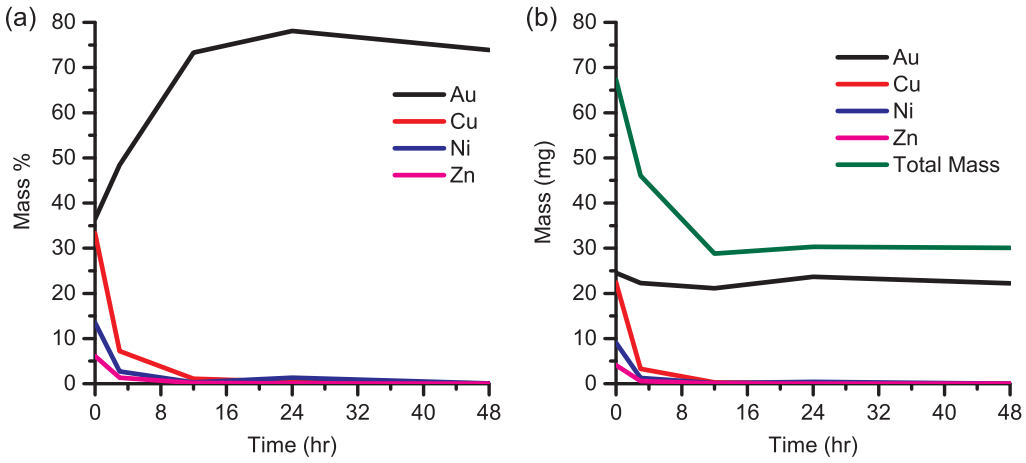

Figure 2.4: Elemental composition of the 10KW alloy sample over time by (a) mass and (b) mass percentage. The sample had no measurable amount of other elements after 24 hours.

2.2 Modification of NPG Pore Size

2.2.1 De-Alloying Bath Parameter Tuning

Pore sizes ranging between 30 nm to 70 nm have been obtained in our lab by altering the rate of the coarsening step through adjustments to the time, temperature, and pH of the de-alloying bath. As the coarsening step proceeds even after de-alloying is complete, thermally annealing NPG can also be used to tune pore sizes.[5,17] An exhaustive comparison was performed in Figure 2.5 where de-alloying bath temperature and de-alloying time of AgAu leaf was compared. The pore size overall increased as bath temperature increased due to the increased energy available for Au adatom diffusion. For the time-dependent de-alloying, shorter times were associated with a decreased average pore diameter, but a pore diameter maximum of ~60 nm was obtained, consistent with the characteristic length scale, λ, discussed *vide supra*. While no compositional analysis of the Au leaf was performed, it was expected that the smaller pore sizes in Figure 2.5b were not completely de-alloyed.

2.2.2 Post De-Alloy Thermal Annealing

For separation of larger biomolecules and nanoparticles, larger pore sizes than the as-prepared 50 nm were desired. Numerous reports have detailed the effects of thermal annealing on NPG.[5,17,18] Heat treatment induces a coarsening effect of the NPG whereby surface Au diffuses into the ligaments and causes an increase in pore size. Figure 2.6 shows pore sizes between 50 nm to 100 nm after annealing the NPG at various temperatures under N_2 gas. N_2 process gas was used in order to prevent oxide formation on the Au surface.

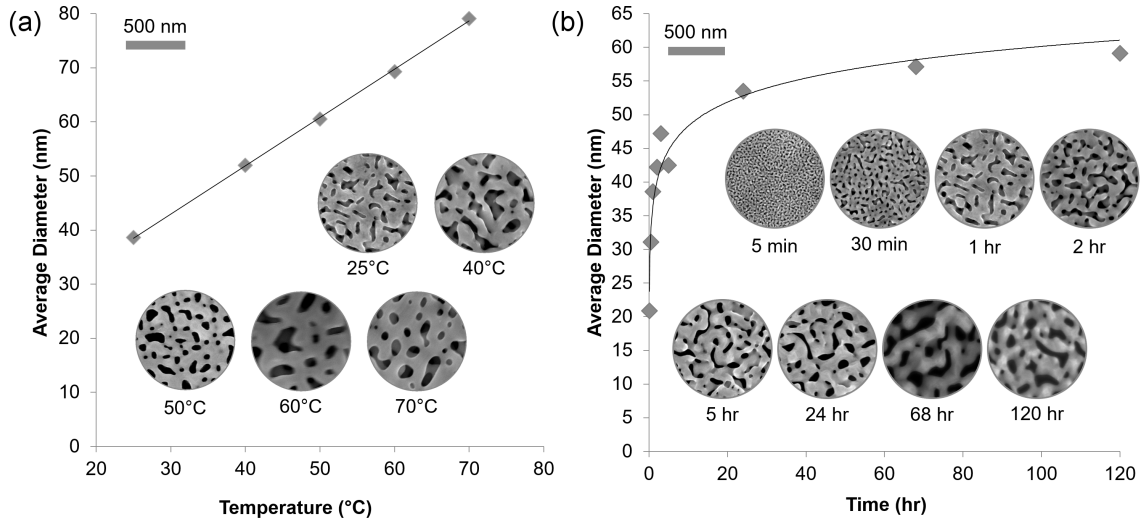

Figure 2.5: (a) 100 nm thick NPG leaf floated on HNO_3 baths (a) of different temperatures for 1 hour and (b) for different amounts of time at 25 °C. Higher temperature de-alloying baths and de-alloying for at most 5 hours created larger pores. 60 nm appeared to be the maximum pore size for time-dependent de-alloying. Insets show the SEM images of the samples used for analysis.

Figure 2.6d shows cyclic voltammograms in 0.5 M H_2SO_4 at a scan rate of 100 mV s^{-1} of both an as-prepared (non-annealed) and annealed NPG sample. Integration of the reduction peak between +1 V and +0.2 V provided the surface area of the NPG samples.[19]. The surface area of the sample annealed at 400 °C was determined to be one third the surface area of the as-prepared sample, consistent with a pore size increase.

2.2.3 Surface Limited Redox Replacement

Efforts in our group also focused on decreasing the average pore diameter. As many of the synthetic nanopores and even the α-HL nanopore were between the 1 nm to 10 nm diameter regime,[20–22] we were curious as to whether smaller NPG pores would demonstrate more pronounced effects. A smaller pore diameter would indicate that electrical double layer overlap could occur at higher concentrations. Because NPG is conductive, electrochemically depositing more Au on the surface was assumed to be the simplest approach in decreasing pore size. Previous efforts on developing smaller Au nanopores either used longer electroless deposition times.[23] Other groups had even examined the creation of bimodal distributions of pores in NPG through further gas phase deposition of an alloy within the NPG.[24]

Poising the potential of the NPG at a sufficiently reductive potential to plate Au, however, would not drive deposition uniformly across the entire NPG surface. Diffusion through the tortuous network would cause limited deposition within the pore interior and instead, significant bulk deposition on the exterior, possibly occluding the pores completely. Surface limited redox replacement (SLRR) provides an alterna-

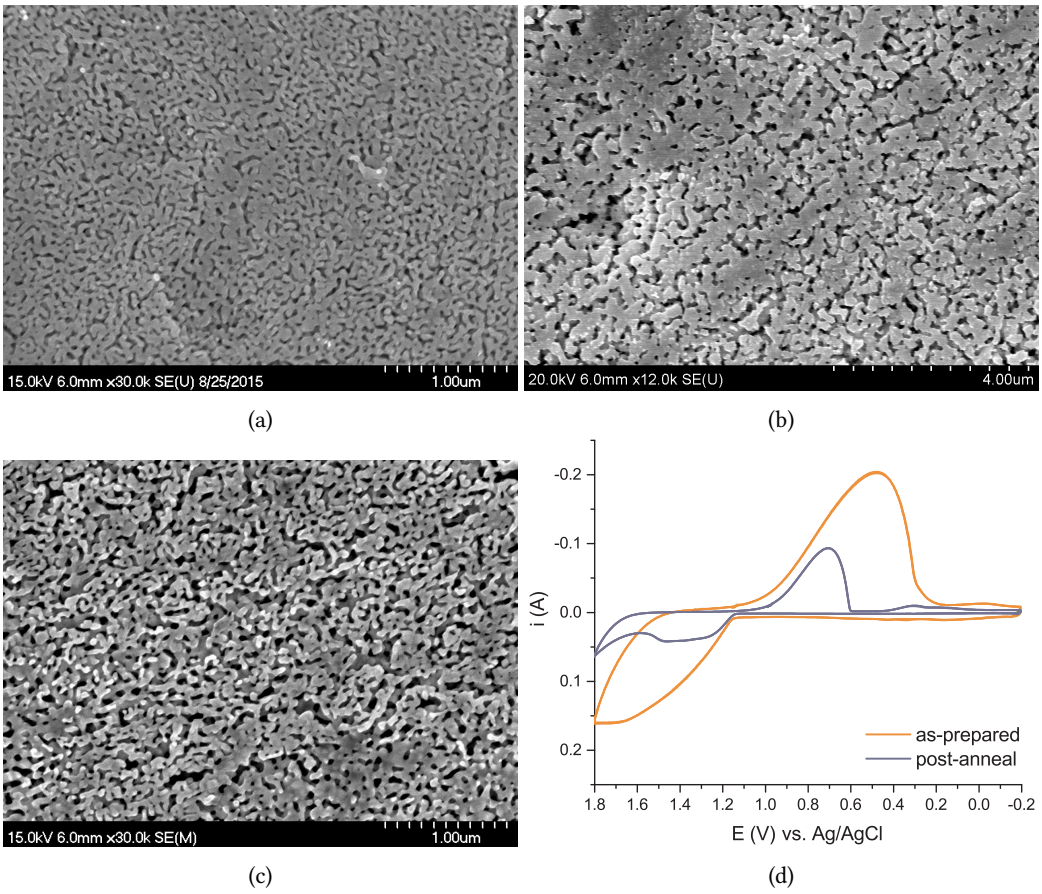

Figure 2.6: NPG annealed at (a) 200 °C, (b) 300 °C, and (c) 400 °C. (d) Cyclic voltammetry at 100 mV s^{-1} in H_2SO_4 of NPG before (as-prepared) and after de-alloying for 1 hr at 400 °C. The surface area density was 3-fold lower after de-alloying.

tive electrodeposition method by following a layer-by-layer approach.[25–27] SLRR borrows concepts from underpotential deposition, but adds another step after the sacrificial monolayer has formed; the applied potential is released after monolayer formation and the sacrificial layer is galvanically displaced by the desired metal.

A 3 mM lead (II) perchlorate, 0.1 M sodium perchlorate, 0.01 M perchloric acid, and 0.520 mM sodium tetrachloroaurate solution was purged with ultra high purity (UHP) N_2 gas for at least 1 hr. A Pt wire counter electrode was cleaned in a 1:1 (%) HNO_3:H_2O solution at 50 °C followed by flame annealing to red hot. A Hg/Hg_2SO_4 reference electrode (MSE) was held in a glass salt bridge containing 0.1 M sodium perchlorate to prevent contamination of the electrode. During the deposition process, a UHP N_2 gas blanket protected the solution from O_2 dissolution. When -0.75 V vs. MSE was applied to the NPG using the Pine AFCBP1 with custom LabVIEW software (Figure B.5), a monolayer of Pb formed on the NPG surface. In this case, the potential was only applied for 10 s prior to switching the potentiostat to open circuit mode. This had the effect of disconnecting the counter electrode and allowing measurement of the open circuit

potential (OCP). As shown in Figure 2.7a, the OCP decayed towards -0.37 V, indicating replacment of the Pb monolayer with Au (OCP measured prior to the experiment was at -0.35 V). This process was repeated, assuming that each cycle, or replacement, corresponded to the growth of an additional Au monolayer.

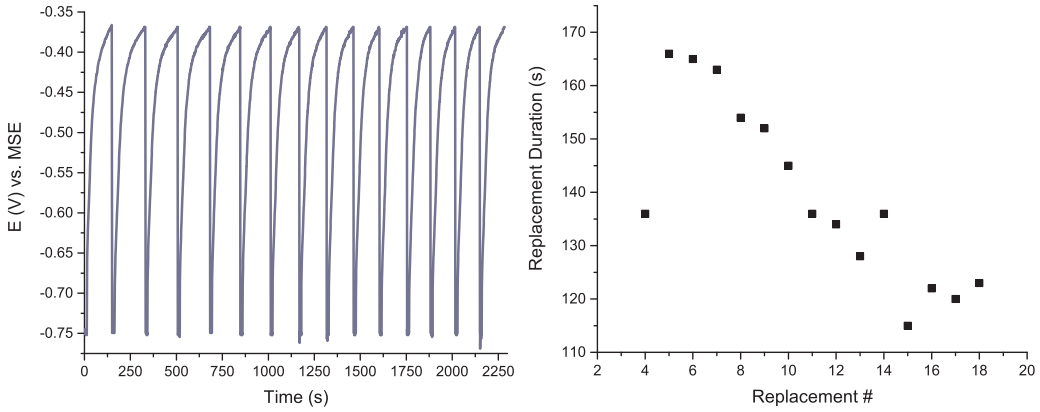

(a) (b)

Figure 2.7: (a) Measured potential at NPG. The flat region at -0.75 V is the applied potential. When the circuit was switched to OCP, the measured potential decayed towards -0.37 V. (b) Length of time required to meet the desired OCP before another replacement was performed. As the replacement number grew, it required less time to form a monolayer.

Figure 2.7b shows the time required before the appropriate OCP was obtained before switching back to the applied potential. As the number of replacements increased, it appeared that the time required for each replacement decreased. This could be an indication of a decreased surface area as the pores decreased in size. After a total of 18 replacements, the NPG sample appeared black. The NPG with Au growth was subjected to SEM analysis, as shown in Figure 2.8, in order to determine the extent of the Au growth. Clearly, Au has been deposited on the surface, although it most likely did not occur with exact monolayer replacement. Figure 2.8b shows a region where there appeared to be significant 3-dimensional growth. Figure 2.8c shows the sharp edges of Au compared to the smooth ligaments observed in Figure 2.1. Au-by-Pb SLRR may have preferential growth on certain crystal faces of the Au, leading to such a geometry. Future analysis using X-ray diffraction may provide further insight as to whether one face is preferred over others.

As will be discussed in Section 2.3.2, the time allowed for each Pb monolayer to grow may not have been sufficient for complete formation.[28] This not only prevented the interior pores from being coated by more Au, but most likely also contributed to the increased 3D growth (Figure 2.8b) from sites of increased Pb nucleation. Furthermore, due to the preferential adsorption of Pb to certain crystal facets of Au, incomplete formation of a monolayer may also be a contributing factor to the sharp geometry shown in Figure 2.8c.[25,29]

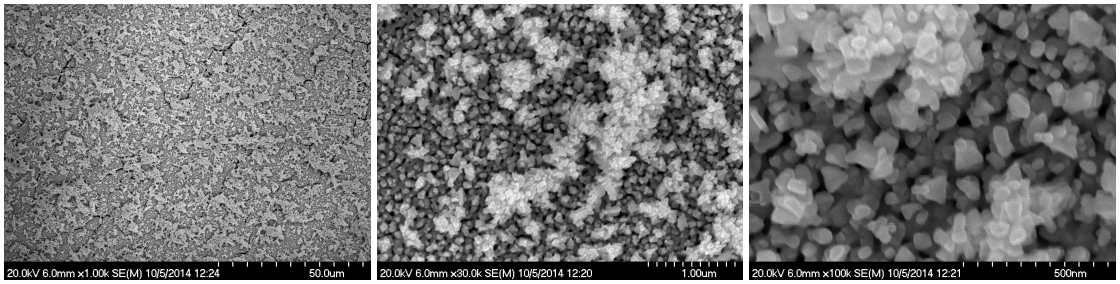

(a) (b) (c)

Figure 2.8: (a) Low magnification SEM image of NPG after surface limited redox replacement. The deposit, overall, appeared very nonuniform. (b) A magnified image showing a region of increased bulk deposition. (c) An even higher magnified image, showing the resulting geometry of the ligaments. There appeared to be much sharper edges present compared to the smooth ligaments of as-prepared NPG.

2.2.4 Bipolar Growth of NPG

Bipolar electrodes are unique in that they do not require direct attachment to a potentiostat; rather, bipolar electrodes are free-standing metallic interfaces across which a transverse electric field applied tangential to the surface induces a different metal/electrolyte interface potential at either end of the electrode.[30] Due to the high conductivity of metal compared to the surrounding solution, the potential of the metal interface is maintained at a constant value everywhere on its surface. When a transverse electric field is applied, the solution potential at one end of the bipolar electrode is significantly different than the potential at the other end.

Bipolar electrodes have found practical use in applications including multiplexible bioarrays,[31] rapid electrocatalyst prototyping,[32] and even fabrication of Janus particles.[33] Of particular interest to the present study is the introduction of dendritic growth at bipolar electrodes.[34] When a sufficiently large potential is applied across the driving electrodes, the bipolar electrode can simultaneously dissolve while plating the dissolved material on its opposite pole. In Figure 2.9, the NPG was sandwiched between two reservoirs as 200 V was applied to two external Pt electrodes. Very rough spherical growth occurred only on one side of the NPG membrane, suggesting that Au was redeposited in the presence of the electric field.

An interesting and unintentional side effect of the high 200 V transverse potential is shown in Figure 2.10. While the potential was applied, the solution volume in each reservoir changed significantly. At the positive electrode, the volume (V) decreased and at the negative electrode, the volume increased. As will be discussed in Chapter 3, the NPG is negatively charged in a Cl^- containing solution. In the narrow pores, the EDL prohibits significant anion migration and therefore there is an increased flux of cations towards the negative electrode. This increase in overall ionic strength of the reservoir presents a very large osmotic pressure difference and subsequently pulls a large volume of solvent across the pores to

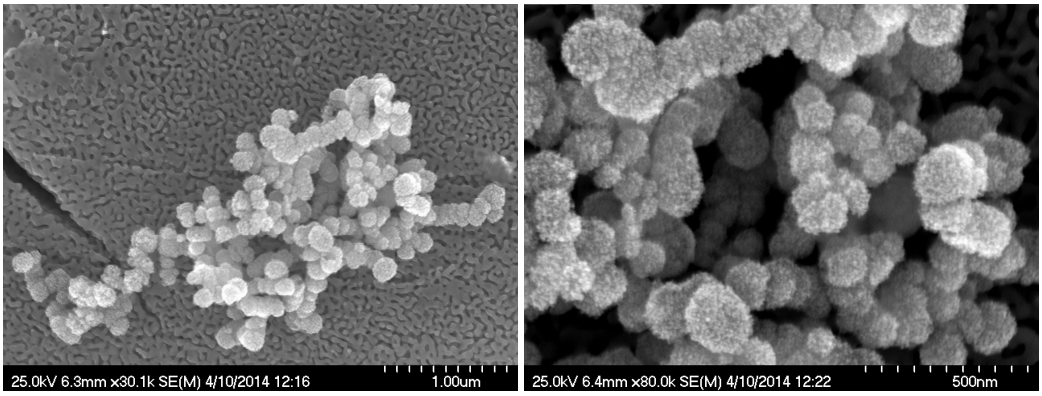

(a) (b)

Figure 2.9: Bipolar growth of NPG at (a) low and (b) high magnification. Rough spheres seemed to grow only on one side of the NPG, corresponding to deposition on the more reductive face.

maintain equilibrium.

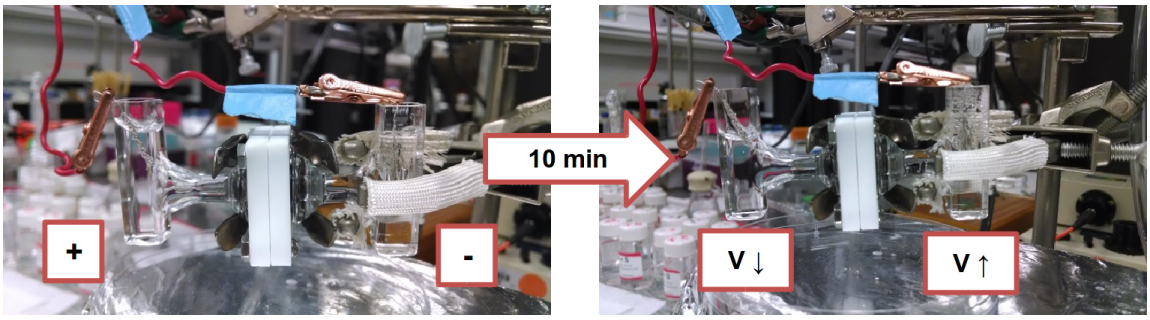

Figure 2.10: Application of 200 V across Pt driving electrodes surrounding a NPG membrane (sealed inside PTFE assembly).

2.3 Surface Area Characterization of NPG

2.3.1 Brunauer-Emmett-Teller Isotherm

The Brunauer-Emmett-Teller isotherm (BET) is the "gold standard" method of determining surface area of materials.[5,19,28] Briefly, surface area is determined by quantifying the gas adsorption to the surface. The study is initiated by thoroughly drying the material in vacuum to ensure that there is no water or prior gas adsorption to the sample. After full evacuation, an analysis gas, often N_2 is bled into the chamber. The pressure of the chamber is recorded along with the amount of gas allowed in to the chamber and any discrepancies can be attributed to N_2 adsorption to the sample surface. NPG was outgassed for 10 hr at 130 °C prior to BET analysis. N_2 analysis gas was used during the 205 min run, presented in Figure 2.11.

The steady rise and slight hysteresis of the isotherm presented in Figure 2.11 is due to the porosity of

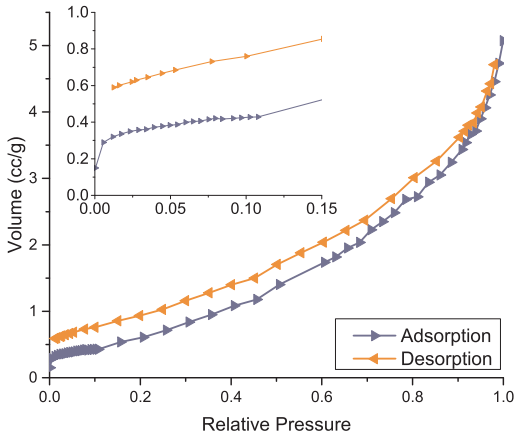

Figure 2.11: A BET gas adsorption isotherm of NPG. The process gas was N_2.

NPG. The shape of the curve is similar to other NPG studies, demonstrating characteristics of macroporous solids.[5] BET analysis provided a surface area of $2.74\,m^2\,g^{-1}$. After the process was complete, the NPG samples were much more yellow in color compared to their original deep red. Provided the raised temperature during the outgassing procedure, it was reasonable to suspect that the NPG may have been annealed slightly.[19,28] SEM images of the NPG after BET analysis is provided in Figure 2.12, where it appears that the pores are slightly larger than observed in Figure 2.1a.

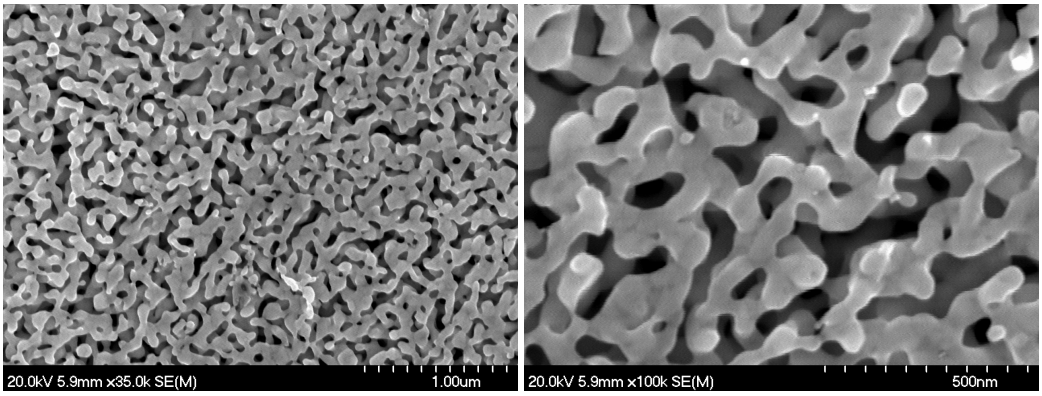

(a) (b)

Figure 2.12: (a) Low and (b) high magnification SEM images of NPG after being subjected to BET analysis. Pore size analysis provided average pore sizes of 64 ± 5 nm.

Although BET is generally considered a non-destructive technique, the NPG nanoporosity seemed to be too sensitive to the heating step of the outgassing procedure.[28] Additionally, a minimum surface area is required for accurate BET analysis, so multiple NPG monoliths were required for a single experiment. Alternative means of determining surface area were therefore imperative to the present study. A popular approach, underpotential deposition (UPD), is the electrochemical formation of a sacrificial monolayer on

the surface of the material. Integration of the current provides the charge passed during the deposition and stripping of the layer, allowing a relation to the material surface area in a non-destructive and sample size independent manner.[19,28]

2.3.2 Pb Underpotential Deposition

At potentials more negative than 0 V vs a Pb wire (Pb/Pb^{2+}) pseudoreference electrode, bulk electrodeposition of Pb will occur. By poising the potential slightly more positive to this value, however, a single monolayer can be grown on the surface of Au due to the free energy available at the surface contributing to the Pb deposition overpotential.[25,28,29] Using a solution of 18.2 mM lead (II) perchlorate, 0.1 M sodium perchlorate, and 0.01 M perchloric acid, a monolayer of Pb was reversibly deposited on an Au substrate, as shown in Figure 2.13. A Pb wire (Pb/Pb^{2+}) was used as the reference electrode and a Pt wire was used as the counter electrode. Multiple peaks are visible due to the preferential adsorption of Pb^{2+} at Au(111), Au(110), or Au(100) depending on the applied potential.[28]

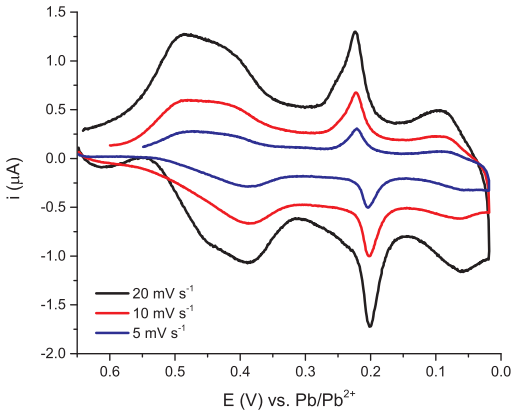

Figure 2.13: Pb UPD on a 2 mm (Area = 0.0314 cm^2) Au disk electrode at various scan rates. Note the multiple reversible peaks corresponding to Pb deposition on the different crystal faces of Au.

For the porous NPG sample, diffusion to the interior pores requires a significant amount of time.[27,28] In fact, 18.2 mM $PbClO_4$ was used instead of the usual 3 mM $PbClO_4$ in order to decrease the amount of time required for complete monolayer fomration. Despite this concentration increase, cyclic voltammetry in the Pb UPD solution of NPG never seemed to provide sufficient time for full monolayer coverage as evidenced by very broad peaks. Chronoamperometric UPD was therefore performed where the potential was held at the oxidative (+0.650 V) and reductive (+0.120 V) limits in order to ensure full monolayer formation.[27,28] Traces of the current and charge obtained over time are provided in Figure 2.14.

Noting that the charge relation to surface area for Pb UPD, as determined via comparison to the geometrical area of flat Au, is 260 $\mu C\,cm^{-2}$,[29] surface areas of $5.4 \pm 0.4\,m^2\,g^{-1}$ were obtained. Although this

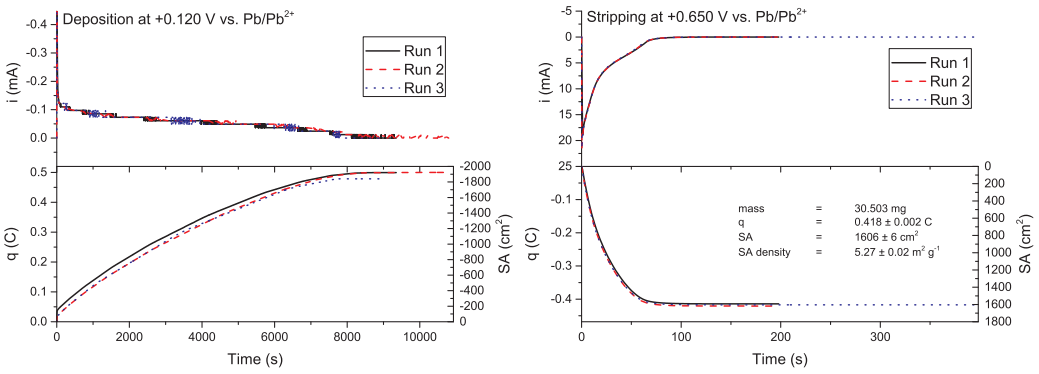

(a) (b)

Figure 2.14: (a) Chronoamperometric deposition of a Pb monolayer at +0.120 V vs Pb/Pb^{2+}. (b) Stripping of the resulting Pb monolayer at +0.650 V vs Pb/Pb^{2+}. A factor of 260 $\mu C\,cm^{-2}$ was used to relate the charge to surface area.

is much larger than the surface area calculated via BET, it is well in agreement with previous reports of $4\,m^2\,g^{-1}$ to $10\,m^2\,g^{-1}$ for NPG surface area density.[8] Surface area analysis of NPG using Pb UPD was very time intensive, however, as shown in Figure 2.14a. Over 2 hours were required to ensure complete formation of a Pb monolayer. Rouya and coworkers compared Cu UPD with H_2SO_4 cycling, and found no significant difference between the two methods for Au surface area measurement, suggesting that this new method may be a viable alternative.[19]

2.3.3 Oxide Stripping Voltammetry

Rather than the formation of a sacrificial monolayer on the Au surface, the Au can be oxidized followed by stripping of the formed oxide layer. Integration of the cathodic stripping peak of the formed oxide layer provides an estimate of the surface area.[19] The NPG was immersed in 0.5 M H_2SO_4 for electrochemical surface area characterization in a 3-electrode configuration. A Pt gauze counter electrode (CE) was cleaned in 1:1 HNO_3:H_2O (v/v) at 50 °C followed by a flame anneal with a propane torch to "red hot." A mercury-mercurous sulfate electrode (MSE, CH Instruments) served as the reference (REF). The NPG was electrochemically polished by cycling between -0.6 V and +1.1 V vs MSE at $1\,V\,s^{-1}$ for 500 cycles using a Pine AFCBP1 potentiostat.[35,36] Any bubbles on the surface were removed by withdrawing and re-submerging the NPG. Surface characterization was then performed by running 1 cycle at $5\,mV\,s^{-1}$ between +0.2 V and +1 V followed by 3 chronoamperometric cycles performed by fixing the potential at the upper and lower limits until the change in current was equal to $0\,A\,s^{-1}$. Similar to the Pb UPD chronoamperometric steps, this was required to ensure complete oxide layer formation. Typical results for this procedure are provided in Figure 2.15. Compared to the Pb UPD surface area determination, oxidation of NPG in H_2SO_4 required

under 30 s for full oxide layer formation. After electrochemical characterization, the samples were rinsed well with and stored in ultrapure (18.2 MΩ cm) water until use.

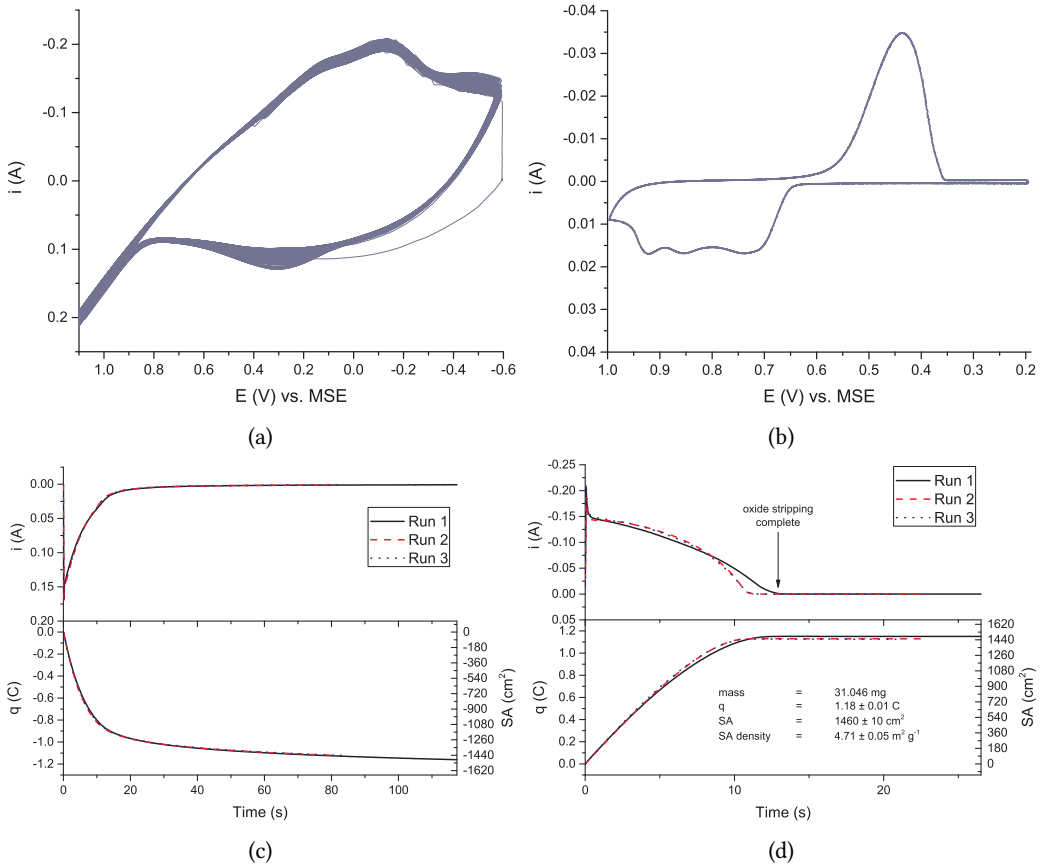

Figure 2.15: (a) Electropolishing of an NPG sample in 0.5 M H_2SO_4 at 1 V s^{-1}. (b) Cyclic voltammogram of an NPG sample in 0.5 M H_2SO_4 at 5 mV s^{-1}. (c) Chronoamperometry of an NPG sample in 0.5 M H_2SO_4. A potential of +1 V formed a surface oxide layer on the NPG. The current is displayed in the top panel and charge in the lower panel. (d) Subsequent chronoamperometric reduction at +0.2 V allowed for integration of current and conversion to surface area density. Current is displayed in the top panel and charge is displayed in the bottom panel.

For de-alloyed NPG without any further modifications, a surface area density of $4.2 \pm 0.8\,\mathrm{m^2\,g^{-1}}$ is obtained. The free corrosion mechanism involves two simultaneous processes: dissolution of the less noble metals at the de-alloying front and coarsening of the Au ligaments through Au adatom diffusion.[37] As the less noble elements are dissolved, the remaining Au adatoms are coordinated only in one dimension, leading to a very high energy state. The Au adatoms therefore travel along the surface of the Au to increase their coordination number and decrease energy. The rate of diffusion influences the characteristic distance, λ, which translates to the NPG ligament and pore size. The coarsening process does not end as soon as the sample is removed from the HNO_3, however. The SA of various NPG samples were tracked as a function of days since their original de-alloying date. As shown in Figure 2.16a, the surface area appears to decrease

to a final value of roughly 2.5 $m^2\ g^{-1}$. This is much more consistent with the SA value obtained via the BET isotherm, suggesting that the heating step of the isotherm accelerated the coarsening procedure. Figure 2.16b indicates that the NPG coarsening is strongly dependent on storage conditions. Coordination of the Au adatoms with solvent may aid in reducing the barrier energy required for surface diffusion.

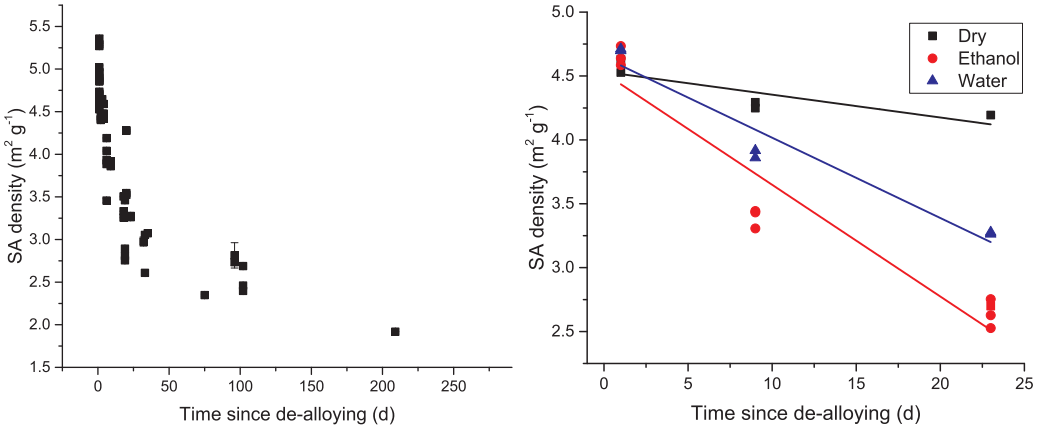

(a) (b)

Figure 2.16: (a) Surface area density measurements of NPG samples stored in 18.2 MΩ m water over time. (b) Comparison of NPG sample surface area density when stored in water, in ethanol, or dry.

2.4 Self-Assembled Monolayer Functionalization of NPG

In order to protect the NPG surface from biofouling as well as impart specific surface functionality to the NPG, modification of the Au surface is necessary. Self assembly of organic monolayers on Au substrates is a very well known phenomenon, and has been used in such applications as nanoparticle stabilization,[38,39] biomolecular capture,[40,41] hydrophobic tuning,[42,43] and nanopore gating.[44,45] A linear alkanethiol is commonly chosen as the affinity of the sulfur to the Au surface causes spontaneous adsorption. The Au-S bond is very stable, with desorption energies ranging from 15 $kcal\,mol^{-1}$ to 20 $kcal\,mol^{-1}$.[46] The self-assembled monolayers (SAMs) therefore do not readily leave the Au surface, often requiring mechanical removal, photooxidation, or electrochemical reduction in order to clean the Au.[46] SAMs provide very useful means of introducing chemical selectivity to our NPG membranes. Figure 2.17 shows a schematic of both the pH-sensitive SAMs and electroactive SAM used in Chapter 4. By simply adjusting the pH, the NPG surface charge could be tuned from positive for the amine (-NH_2 ⟶ -NH_3^+) to negative for the carboxylic acid (-COOH ⟶ -COO^-) in Figure 2.17a. Electrochemical modulation of surface charge was attained by oxidizing the ferrocene-terminated thiols of Figure 2.17b.

SAMs self-organize in order to stabilize via van der Waals forces and therefore pack very tightly on the

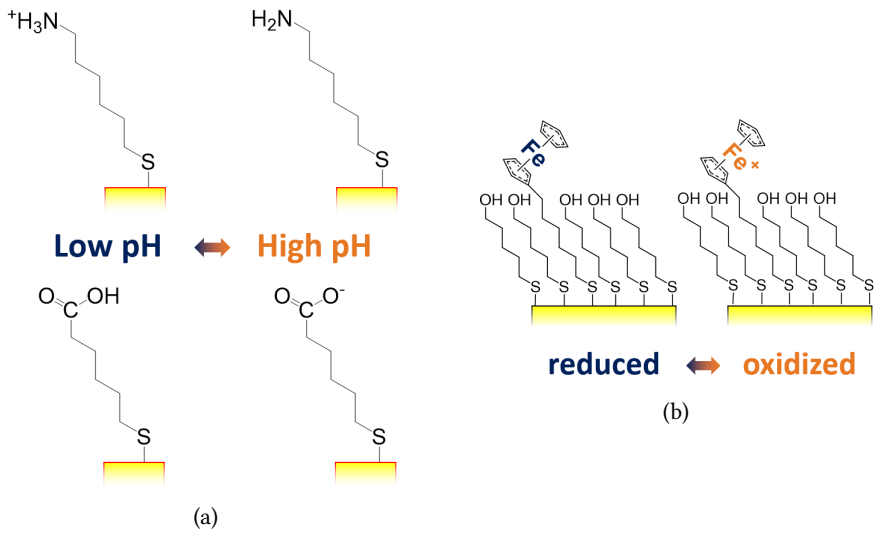

Figure 2.17: A schematic of charge control of the Au surface via (a) solution pH and (b) electrochemistry.

Au surface.[46] The time allowed for thiol functionalization therefore determines the quality of the SAM, with longer times permitting greater self-organization. For very rough surfaces, however, the irregular geometry may lead to significant defects in the SAM or even decreased stability of the monolayer.[47] Therefore, Cl^- contaminants or other non-specific adsorption to the NPG surface may lead to a diminished ability to tune transport. A recent report, however, discussed the quality of SAMs on NPG substrates.[48] It was noted that the 50 nm NPG ligaments were large enough on an atomic level to mimic a flat surface from a self-assembly standpoint. This provides further confidence that the facile surface modification of NPG can provide a means of tunable transport.

2.5 References

1. McCurry, D. A.; Bailey, R. C. Nanoporous Gold Membranes as Robust Constructs for Selectively Tunable Chemical Transport. *Journal of Physical Chemistry* **2016**, DOI: 10.1021/acs.jpcc.6b02759.

2. Erlebacher, J.; Aziz, M. J.; Karma, A.; Dimitrov, N.; Sieradzki, K. Evolution of nanoporosity in dealloying. *Nature* **2001**, *410*, 450–453, DOI: 10.1038/35068529.

3. Erlebacher, J. An Atomistic Description of Dealloying: Porosity Evolution, the Critical Potential, and Rate-Limiting Behavior. *Journal of The Electrochemical Society* **2004**, *151*, C614–C626, DOI: 10.1149/1.1784820.

4. Detsi, E.; van de Schootbrugge, M.; Punzhin, S.; Onck, P.; Hosson, J. D. On tuning the morphology of nanoporous gold. *Scripta Materialia* **2011**, *64*, 319–322, DOI: 10.1016/j.scriptamat.2010.10.023.

5. Tan, Y. H.; Davis, J. A.; Fujikawa, K.; Ganesh, N. V.; Demchenko, A. V.; Stine, K. J. Surface area and pore size characteristics of nanoporous gold subjected to thermal, mechanical, or surface modification studied using gas adsorption isotherms, cyclic voltammetry, thermogravimetric analysis, and scanning electron microscopy. *Journal of Materials Chemistry* **2012**, *22*, 6733–6745, DOI: 10.1039/c2jm16633j.

6. Damian, A.; Maroun, F.; Allongue, P. Electrochemical de-alloying in two dimensions: role of the local atomic environment. *Nanoscale* **2016**, *8*, 13985–13996, DOI: 10.1039/C6NR01390B.

7. Dorofeeva, T. S.; Seker, E. Electrically tunable pore morphology in nanoporous gold thin films. *Nano Research* **2015**, *8*, 2188–2198, DOI: 10.1007/s12274-015-0726-x.

8. Stine, K. J.; Jefferson, K.; Shulga, O. V., Nanoporous Gold for Enzyme Immobilization. In *Enzyme Stabilization and Immobilization: Methods and Protocols*, Minteer, S. D., Ed.; Methods in Molecular Biology; Humana Press: Totowa, NJ, 2011; Chapter Nanoporous Gold for Enzyme Immobilization, pp 67–83, DOI: 10.1007/978-1-60761-895-9_7.

9. Ding, Y.; Kim, Y.-J.; Erlebacher, J. Nanoporous Gold Leaf: "Ancient Technology"/Advanced Material. *Advanced Materials* **2004**, *16*, 1897–1900, DOI: 10.1002/adma.200400792.

10. Ge, X.; Wang, R.; Liu, P.; Ding, Y. Platinum-Decorated Nanoporous Gold Leaf for Methanol Electrooxidation. *Chemistry of Materials* **2007**, *19*, 5827–5829, DOI: 10.1021/cm702335f.

11. Hakamada, M.; Mabuchi, M. Microstructural evolution in nanoporous gold by thermal and acid treatments. *Materials Letters* **2008**, *62*, 483–486, DOI: 10.1016/j.matlet.2007.05.086.

12. Uwe Renner, F. et al., *Nanoporous Gold*; RSC Nanoscience & Nanotechnology; The Royal Society of Chemistry: 2012, DOI: 10.1039/9781849735285.

13. Shulga, O. V.; Jefferson, K.; Khan, A. R.; D'Souza, V. T.; Liu, J.; Demchenko, A. V.; Stine, K. J. Preparation and Characterization of Porous Gold and Its Application as a Platform for Immobilization of Acetylcholine Esterase. *Chem. Mater.* **2007**, *19*, 3902–3911, DOI: 10.1021/cm070238n.

14. Pandey, B.; Demchenko, A.; Stine, K. Nanoporous gold as a solid support for protein immobilization and development of an electrochemical immunoassay for prostate specific antigen and carcinoembryonic antigen. *Microchimica Acta* **2012**, *179*, 71–81, DOI: 10.1007/s00604-012-0870-x.

15. Ling, Y.; Elkenbracht, J. C.; Flanagan, W. F.; Lichter, B. D. The Electrochemical Oxidation of Gold in 0.6 M NaCl and 0.3 M Na2SO4 Solutions. *Journal of The Electrochemical Society* **1997**, *144*, 2689, DOI: 10.1149/1.1837883.

16. Seker, E.; Reed, M. L.; Begley, M. R. Nanoporous Gold: Fabrication, Characterization, and Applications. *Materials* **2009**, *2*, 2188–2215, DOI: 10.3390/ma2042188.

17. Seker, E.; Gaskins, J. T.; Bart-Smith, H.; Zhu, J.; Reed, M. L.; Zangari, G.; Kelly, R.; Begley, M. R. The effects of post-fabrication annealing on the mechanical properties of freestanding nanoporous gold structures. *Acta Materialia* **2007**, *55*, 4593–4602, DOI: 10.1016/j.actamat.2007.03.018.

18. Seker, E.; Reed, M. L.; Begley, M. R. A thermal treatment approach to reduce microscale void formation in blanket nanoporous gold films. *Scripta Materialia* **2009**, *60*, 435–438, DOI: 10.1016/j.scriptamat.2008.11.027.

19. Rouya, E.; Cattarin, S.; Reed, M. L.; Kelly, R. G.; Zangari, G. Electrochemical Characterization of the Surface Area of Nanoporous Gold Films. *Journal of the Electrochemical Society* **2012**, *159*, 97–102, DOI: 10.1149/2.097204jes.

20. Song, L.; Hobaugh, M. R.; Shustak, C.; Cheley, S.; Bayley, H.; Gouaux, J. E. Structure of Staphylococcal α-Hemolysin, a Heptameric Transmembrane Pore. *Science* **1996**, *274*, 1859–1865, DOI: 10.1126/science.274.5294.1859.

21. Van den Hout, M.; Hall, A. R.; Wu, M. Y.; Zandbergen, H. W.; Dekker, C.; Dekker, N. H. Controlling nanopore size, shape and stability. *Nanotechnology* **2010**, *21*, 115304, DOI: 10.1088/0957-4484/21/11/115304.

22. Wanunu, M. Nanopores: A journey towards DNA sequencing. *Physics of Life Reviews* **2012**, *9*, 125–158, DOI: 10.1016/j.plrev.2012.05.010.

23. Nishizawa, M.; Menon, V. P.; Martin, C. R. Metal Nanotubule Membranes with Electrochemically Switchable Ion-Transport Selectivity. *Science* **1995**, *268*, 700–702, DOI: 10.1126/science.268.5211.700.

24. Ding, Y.; Erlebacher, J. Nanoporous Metals with Controlled Multimodal Pore Size Distribution. *J. Am. Chem. Soc.* **2003**, *125*, 7772–7773, DOI: 10.1021/ja035318g.

25. Viyannalage, L. T.; Vasilic, R.; Dimitrov, N. Epitaxial Growth of Cu on Au(111) and Ag(111) by Surface Limited Redox Replacement - An Electrochemical and STM Study. *J. Phys. Chem. C* **2007**, *111*, 4036–4041, DOI: 10.1021/jp067168c.

26. Fayette, M.; Liu, Y.; Bertrand, D.; Nutariya, J.; Vasiljevic, N.; Dimitrov, N. From Au to Pt via Surface Limited Redox Replacement of Pb UPD in One-Cell Configuration. *Langmuir* **2011**, *27*, 5650–5658, DOI: 10.1021/la200348s.

27. McCurry, D. A.; Kamundi, M.; Fayette, M.; Wafula, F.; Dimitrov, N. All Electrochemical Fabrication of a Platinized Nanoporous Au Thin-Film Catalyst. *ACS Appl. Mater. Interfaces* **2011**, *3*, 4459–4468, DOI: 10.1021/am2011433.

28. Liu, Y.; Bliznakov, S.; Dimitrov, N. Comprehensive Study of the Application of a Pb Underpotential Deposition-Assisted Method for Surface Area Measurement of Metallic Nanoporous Materials. *J. Phys. Chem. C* **2009**, *113*, 12362–12372, DOI: 10.1021/jp901536f.

29. Kirowa-Eisner, E.; Bonfil, Y.; Tzur, D.; Gileadi, E. Thermodynamics and kinetics of upd of lead on polycrystalline silver and gold. *Journal of Electroanalytical Chemistry* **2003**, *552*, 171–183, DOI: 10.1016/s0022-0728(03)00181-5.

30. Fosdick, S. E.; Knust, K. N.; Scida, K.; Crooks, R. M. Bipolar Electrochemistry. *Angewandte Chemie International Edition* **2013**, *52*, 10438–10456, DOI: 10.1002/anie.201300947.

31. Wu, M.-S.; Liu, Z.; Shi, H.-W.; Chen, H.-Y.; Xu, J.-J. Visual Electrochemiluminescence Detection of Cancer Biomarkers on a Closed Bipolar Electrode Array Chip. *Anal. Chem.* **2015**, *87*, 530–537, DOI: 10.1021/ac502989f.

32. Fosdick, S. E.; Crooks, R. M. Bipolar Electrodes for Rapid Screening of Electrocatalysts. *J. Am. Chem. Soc.* **2011**, *134*, 863–866, DOI: 10.1021/ja210354m.

33. Hossan, M. R.; Gopmandal, P. P.; Dillon, R.; Dutta, P. Bipolar Janus particle assembly in microdevice. *ELECTROPHORESIS* **2015**, *36*, 722–730, DOI: 10.1002/elps.201400423.

34. Bradley, J.-C. Programmable Hard-Wiring of Circuitry Using Spatially Coupled Bipolar Electrochemistry. *Journal of The Electrochemical Society* **1999**, *146*, 194, DOI: 10.1149/1.1391586.

35. Fischer, L. M.; Tenje, M.; Heiskanen, A. R.; Masuda, N.; Castillo, J.; Bentien, A.; Émneus, J.; Jakobsen, M. H.; Boisen, A. Gold cleaning methods for electrochemical detection applications. *Microelectronic Engineering* **2009**, *86*, 1282–1285, DOI: 10.1016/j.mee.2008.11.045.

36. Köntje, C.; Kolb, D. M.; Jerkiewicz, G. Roughening and Long-Range Nanopatterning of Au(111) through Potential Cycling in Aqueous Acidic Media. *Langmuir* **2013**, *29*, 10272–10278, DOI: 10.1021/la4018757.

37. Dotzler, C. J.; Ingham, B.; Illy, B. N.; Wallwork, K.; Ryan, M. P.; Toney, M. F. In Situ Observation of Strain Development and Porosity Evolution in Nanoporous Gold Foils. *Advanced Functional Materials* **2011**, *21*, 3938–3946, DOI: 10.1002/adfm.201100735.

38. Dahl, J. A.; Maddux, B. L. S.; Hutchison, J. E. Toward Greener Nanosynthesis. *Chemical Reviews* **2007**, *107*, 2228–2269, DOI: 10.1021/cr050943k.

39. Lin, S.-Y.; Tsai, Y.-T.; Chen, C.-C.; Lin, C.-M.; Chen, C.-h. Two-Step Functionalization of Neutral and Positively Charged Thiols onto Citrate-Stabilized Au Nanoparticles. *The Journal of Physical Chemistry B* **2004**, *108*, 2134–2139, DOI: 10.1021/jp036310w.

40. Li, C.; Wu, D.; Hu, X.; Xiang, Y.; Shu, Y.; Li, G. One-Step Modification of Electrode Surface for Ultrasensitive and Highly Selective Detection of Nucleic Acids with Practical Applications. *Analytical Chemistry* **2016**, DOI: 10.1021/acs.analchem.6b01250.

41. Wu, Z.-S.; Guo, M.-M.; Zhang, S.-B.; Chen; Jiang, J.-H.; Shen, G.-L.; Yu, R.-Q. Reusable Electrochemical Sensing Platform for Highly Sensitive Detection of Small Molecules Based on Structure-Switching Signaling Aptamers. *Analytical Chemistry* **2007**, *79*, 2933–2939, DOI: 10.1021/ac0622936.

42. Biswas, G. C.; Watanabe, T.; Carlen, E. T.; Yokokawa, M.; Suzuki, H. Switchable Hydrophobic Valve for Controlled Microfluidic Processing. *ChemPhysChem* **2016**, *17*, 817–821, DOI: 10.1002/cphc.201501015.

43. Abbott, N. L.; Folkers, J. P.; Whitesides, G. M. Manipulation of the Wettability of Surfaces on the 0.1- to 1 -Micrometer Scale Through Micromachining and Molecular Self-Assembly. *Science* **1992**, *257*, 1380–1382, DOI: 10.1126/science.257.5075.1380.

44. Hou, Z.; Abbott, N. L.; Stroeve, P. Self-Assembled Monolayers on Electroless Gold Impart pH-Responsive Transport of Ions in Porous Membranes. *Langmuir* **2000**, *16*, 2401–2404, DOI: 10.1021/la991045k.

45. Chun, K.-Y.; Stroeve, P. Protein Transport in Nanoporous Membranes Modified with Self-Assembled Monolayers of Functionalized Thiols. *Langmuir* **2002**, *18*, 4653–4658, DOI: 10.1021/la011250b.

46. Love, J. C.; Estroff, L. A.; Kriebel, J. K.; Nuzzo, R. G.; Whitesides, G. M. Self-Assembled Monolayers of Thiolates on Metals as a Form of Nanotechnology. *Chemical Reviews* **2005**, *105*, 1103–1170, DOI: 10.1021/cr0300789.

47. Vericat, C.; Vela, M. E.; Benitez, G.; Carro, P.; Salvarezza, R. C. Self-assembled monolayers of thiols and dithiols on gold: new challenges for a well-known system. *Chemical Society Reviews* **2010**, *39*, 1805–1834, DOI: 10.1039/B907301A.

48. Patel, D. A.; Weller, A. M.; Chevalier, R. B.; Karos, C. A.; Landis, E. C. Ordering and defects in self-assembled monolayers on nanoporous gold. *Applied Surface Science* **2016**, *387*, 503–512, DOI: 10.1016/j.apsusc.2016.05.149.

Chapter 3

Theoretical Basis

There has been a significant amount of theoretical research performed in the field of nanopores. The nanoscale geometry, with sizes on the order of the electrical double layer (EDL), introduces numerous complications that are often not considered on the macroscale. Specifically, the charge present at the pore surfaces have the capability of altering the ionic environment in the entire pore volume.[1] Similarly, molecules translocating through the pores have the ability to shuttle counter-ions across the pore, leading to a large shift in local conductivity during translocation.[2] This provides the theoretical basis behind the most common application of nanopores currently, resistive pulse sensing.

Nanoporous gold (NPG) presents a complex scenario for nanofluidic transport. Whereas the length scale of the pore diameter is on the order of commonly studied nanopores, the intricate interior geometry provides a high tortuosity not often considered. In the current chapter, factors affecting transport and the results of molecular flux through NPG simulations will be discussed.

3.1 The Electrical Double Layer

Surfaces in contact with an aqueous solution often present a charge excess either due to a reaction at the surface, ionizable moieties, or specifically adsorbed ions. NPG is no exception to this rule, as it is well known that Cl^- ions will spontaneously adsorb to Au surfaces.[3] The charge difference between the surface and the solution generates a potential difference that decays outwardly from the surface as free counterions orient themselves in order to neutralize the surface charge. The rate of decay from the surface is summarized by the Poisson equation:[4]

$$-\epsilon\epsilon_0\nabla^2\phi = \sum_{i=1}^{n} Fz_i c_i \tag{3.1}$$

where $\epsilon\epsilon_0$ is the permittivity of the fluid, ϕ is the electric potential, F is the Faraday constant, z_i is the valence if species i, and c_i is the concentration of species i. The distribution of species i can then be

described by the Boltzmann equation:[4]

$$c_i = c_i^0 \exp\left(- z_i \frac{F\phi}{RT} \right) \tag{3.2}$$

where c_i^0 is the bulk concentration of species i and R is the universal gas constant. Equation 3.2 suggests that the cation (anion) concentration at positive (negative) ϕ is much smaller than the concentration in the bulk, c_i^0. Qualitatively, positive (negative) surface potentials repel cations (anions) leading to a decreased concentration of co-ions and increased concentration of counterions nearer to the surface.

The negative surface charge on Au arising from the spontaneous adsorption of Cl^- anions in solution causes local cation enrichment and anion exclusion in the solution volume immediately adjacent to the Au surface. This region, referred to as the electrical double layer (EDL), has a thickness inversely related to the ionic strength of the solution. For a binary z:z electrolyte, the thickness, or Debye length, κ^{-1}, is represented by the following equation:[5]

$$\kappa^{-1} = \sqrt{\frac{\epsilon\epsilon_0 kT}{2cN_A z^2 e^2}} \tag{3.3}$$

where c is concentration, N_A is Avogadro's number, z is the charge of the ions, e is the elementary charge, $\epsilon\epsilon_0$ is the permittivity of the medium, k is Boltzmann's constant, and T is temperature. The ionic strength dependence arises from an electroneutrality argument; greater ionic strengths will supply more counterions to the EDL, allowing the potential from the surface to decay more quickly. From Equation 3.3, the EDL thickness can be estimated to be on the order of a few tens of nanometers, which, in the confines of a nanopore with sizes on the order of the EDL, can have significant effects on the chemical environment within the pores.

This effect is schematically represented in Figure 3.1. The EDL is shown in blue (not to scale) within a representative cross-section of NPG. When the EDL is small compared to the pore radius ($r_{pore} \times \kappa \gg 1$), both cations and anions are free to exist within the pore volume. However, when the EDL thickness is on the order of the pore radius ($r_{pore} \times \kappa \approx 1$), anions are excluded from the pore volume. Figure 3.2 plots the relationship between thickness and concentration for KCl at 25 °C. The EDL is very thin at high salt concentrations and has a negligible impact on the potential profile across the nanopore; at low ionic strengths, however, the EDL can span across the entire pore diameter, as shown by the dashed line demarcating the NPG pore radii as determined via SEM in Section 2.1. At the point of intersection, the electrostatic environment within the pore is defined solely by the NPG surface charge.[6] As the salt concentration in the bulk solution is decreased, a minimum counterion concentration exists within the pores to neutralize

excess surface charge.[1] The conductance through the pore is therefore fixed at a minimum value where further decreasing the bulk KCl concentration will not affect conductivity. For a single cylindrical pore, the relation between conductivity at low electrolyte concentrations, where the EDL dominates, and high electrolyte concentrations, where the concentration of KCl in the pore is equal to that of the bulk solution is provided in the following equation:[1,7]

$$G_{\text{pore}} = \frac{\pi}{4}\frac{d_{\text{pore}}^2}{L_{\text{pore}}}\left(\underbrace{(\mu_+ + \mu_-)\, ne}_{\text{bulk}} + \underbrace{\mu_+ \frac{4\sigma}{d_{\text{pore}}}}_{\text{interior}}\right) \tag{3.4}$$

where G_{pore} is the conductivity, d_{pore} is the pore diameter, L_{pore} is the length of the pore, $\mu_\pm$ is the mobility of either the anion (-) or cation (+), n is the number density of ion pairs, e is the elementary charge, and σ is the surface charge density. The first term relates the bulk conductivity to the concentration of KCl and the access resistance of the pore. The second term is independent of concentration, but introduces the contribution of pore surface charge. Smeets et al. have shown experimentally that nanopores separating two reservoirs can alter the measured conductivity, due to access resistance of the pores and electrostatic contributions of the EDL within the pores.[1]

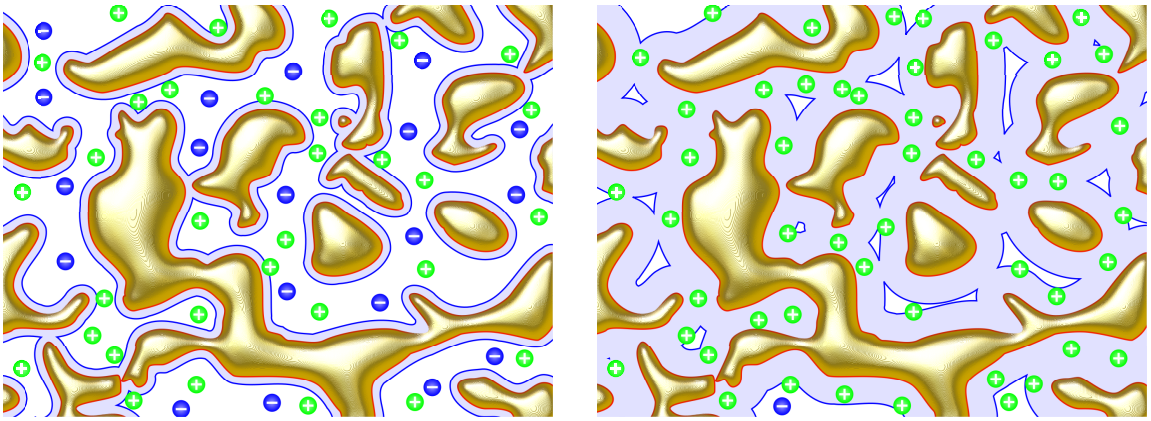

$\kappa^{-1} < 0.1$ nm
$r_{pore} \times \kappa \gg 1$

$\kappa^{-1} > 0.1$ nm
$r_{pore} \times \kappa \approx 1$

Figure 3.1: At high ionic strengths, the EDL (blue) is small and both anions (-) and cations (+) are free to exist within the NPG (left). At higher ionic strengths, the EDL grows to fill nearly the entire pore volume, excluding anions from the NPG (right).

The $\frac{\pi}{4} d_{\text{pore}}^2$ of Equation 3.4 arises from a geometrical correction to conductivity by assuming that the cross-sectional area of a single pore, $A = \pi \left(\frac{d}{2}\right)^2$, is the only conductive pathway. In the case of NPG, however, the pore area is equal to the sum of all pores on the exposed face. Since the pores are stacked in the L_{NPG} direction (i.e., the NPG thickness), the 3-dimensional network also contributes to the overall conductivity. The NPG can therefore be considered as a series of parallel circuits that sum to the overall

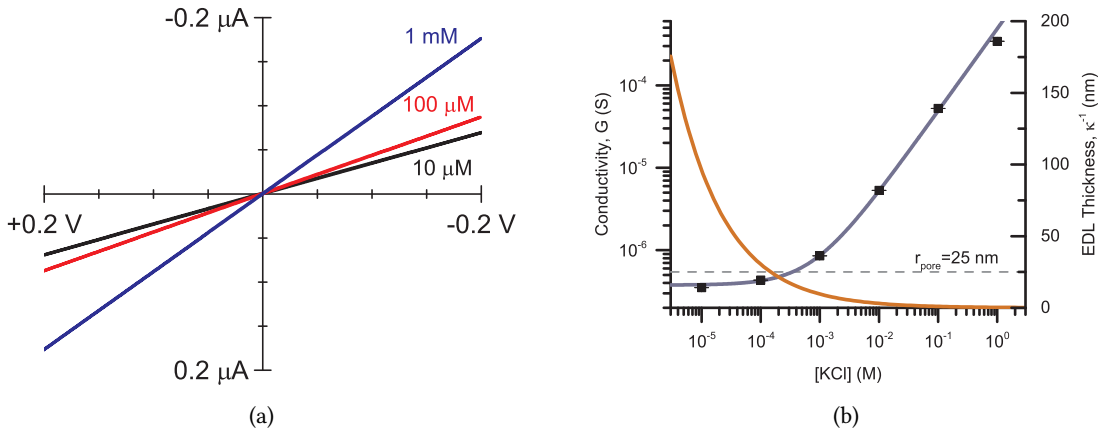

(a) (b)

Figure 3.2: (a) Current vs applied ΔE across the NPG membrane for various concentrations. A linear response was observed for all ionic strengths considered. (b) Through-pore conductivity, G, of NPG (■) Conductivity was calculated as the inverse of the slope of the i-V curve in (a) according to Ohm's law ($E = iR$ and $R = 1/G$). A fit to Equation 3.5 is provided in blue. The electrical double layer thickness, κ^{-1}, as calculated from Equation 3.3 is also shown in orange. Note that the conductivity trends towards a constant value where the EDL thickness approaches the estimated NPG pore radius (as determined in Section 2.1).

conductivity of the system, where the conductivity of pores in a single layer of NPG is represented by G_{parallel} and the conductivity of all layers is represented by G_{series}. Thus, the conductivity through NPG can be calculated as

$$G_{\text{parallel}} = \sum G_{\text{pore}} \tag{3.5a}$$

$$= \epsilon_p A_{\text{face}} G_{\text{pore}} \tag{3.5b}$$

where A_{face} is the exposed, geometrical surface area of the broad face of the NPG and ϵ_p is the porosity (i.e., ratio of void space to Au volume). Following Ohm's law for series conductance,

$$\frac{1}{G_{\text{series}}} = \sum \frac{1}{G_{\text{parallel}}} \tag{3.5c}$$

$$= \epsilon_p L_{\text{NPG}} \left(\frac{1}{\epsilon_p A_{\text{face}} G_{\text{pore}}} \right) \tag{3.5d}$$

the conductivity equation for the entire NPG monolith is then obtained as

$$G_{\text{NPG}} = G_{\text{series}} = \frac{A_{\text{face}}}{L_{\text{NPG}}} G_{\text{pore}} \tag{3.5e}$$

with L_{NPG} representing the NPG thickness and assuming $L_{\mathrm{pore}} = d_{\mathrm{pore}}$ due to the average uniform pore size in all directions,

$$\boxed{G_{\mathrm{NPG}} = \frac{A_{\mathrm{face}}}{L_{\mathrm{NPG}}} \frac{\pi}{4} d_{\mathrm{pore}} \left((\mu_+ + \mu_-)\, ne + \mu_+ \frac{4\sigma}{d_{\mathrm{pore}}} \right)} \tag{3.5f}$$

Using Equation 3.5 and the following assumptions:*

$$\begin{aligned} \mu_+ &= \mu_{\mathrm{K}^+} = 7.62 \times 10^{-8} \mathrm{m^2\,S\,C^{-1}} \\ \mu_- &= \mu_{\mathrm{Cl}^-} = 7.91 \times 10^{-8} \mathrm{m^2\,S\,C^{-1}} \\ L_{\mathrm{NPG}} &= 250 \times 10^{-6} \mathrm{m} \\ d_{\mathrm{pore}} &= 50 \times 10^{-9} \mathrm{m} \end{aligned}$$

the NPG surface charge density was calculated to be $-1.9 \pm 0.1\,\mathrm{mC\,m^{-2}}$, with an effective total pore area of $20.7 \pm 0.6\,\mu\mathrm{m}^2$. The surface charge is negative, as expected for Au in a chloride-containing solution, and is similar in magnitude to previous studies of Au with Cl^- adsorption.[3] This equation most likely greatly oversimplifies the complex transport mechanisms inside the NPG, but the results serve as a useful starting point for finite-element simulations.

Clearly, the EDL holds imporant implications for transport through nano-sized constrictions. Modulation of surface charge has been used in the prior studies in order to form nanoscale transistors and diodes.[6,9,10] In the present study, dynamic modulation of the nanopore wall surface charge was employed in order to control the electrostatic properties of the EDL. This in turn permitted complete control over the ionic environment within the pores and thus, direct tuning of transport through the NPG membrane.

3.2 Transport Equations for Molecular and Ionic Flux

The most common approach in analyzing transport through nanopores considers ionic flux of species i, j_i, to be governed by the Nernst-Planck equation:[11–14]

$$j_i = -D_i \Bigg[\underbrace{\nabla c_i}_{\text{diffusion}} + \underbrace{\frac{z_i e}{kT} c_i \nabla E}_{\text{migration}} \Bigg] + \underbrace{c_i u}_{\text{convection}} \tag{3.6}$$

*The molar conductivities of the electrolytes used ($\Lambda_{\mathrm{K}^+} = 73.48{\times}10^{-4}\mathrm{m^2\,S\,mol^{-1}}$ and $\Lambda_{\mathrm{Cl}^-} = 76.31{\times}10^{-4}\mathrm{m^2\,S\,mol^{-1}}$) are provided in the CRC Chemical Handbook.[8] In order to convert molar conductivity to ion mobilities, the following was used: $\Lambda_\pm = F\mu_\pm$, where F is Faraday's constant.

where u is the fluid velocity, c_i is the concentration of species i, D_i is the diffusion coefficient of species i, z_i is the charge of species i, k is the Boltzmann constant, T is temperature, and ∇E is the electric potential gradient. The first term corresponds to diffusion due to a concentration gradient, the second is migration in an electric field, and the third relates ionic flux due to convection. In the present study, the absence of an external pressure gradient suggests

$$c_i u = 0 \tag{3.7}$$

so that transport through the NPG membranes is guided purely by passive diffusion of the tracer molecule from the high concentration reservoir to the low concentration reservoir and migration from any externally applied electric field. Additionally, the molecular flux is sufficiently low enough to consider the concentrations in the reservoirs constant throughout the duration of the experiments.[15] This allows for a steady-state approximation whereby

$$\nabla j_i = 0 \tag{3.8}$$

greatly simplifying the analysis of flux through NPG.

Compared to flux in free solution, the diffusion coefficient for species i, D_i in a porous domain is decreased due to the limited free space for diffusion to occur and the high probability of collisions with the pore walls. The effective diffusion coefficient in porous media is thereofre related as[16]

$$D_i^{\text{eff}} = D_i \times \frac{\epsilon_p}{\tau} \tag{3.9a}$$

where τ is the tortuosity and ϵ_p is the porosity of the media. The tortuosity of NPG can be related to porosity following the Bruggeman relation as[17]

$$\tau = \epsilon_p^{-\frac{1}{2}} \tag{3.9b}$$

providing the simplified effective diffusion relation,

$$D_i^{\text{eff}} = \epsilon_p^{\frac{3}{2}} \times D_i \tag{3.9c}$$

As the diffusional flux in NPG is expected to be very small ($0.45 \times D_i$, assuming $\epsilon_p = 30\%$), a potential difference across the membrane is necessary to accelerate transport through NPG and obtain separations on a practical time scale. In the present study, two mechanisms of applying a potential difference were examined; Chapter 4 employs an externally applied potential across two electrodes in either reservoir whereas Chapter 5 exploits the induced potential generated when the electrolyte concentrations on either

side of the NPG membrane differ.

3.3 Effect of an Asymmetrical Nanopore Geometry

A peculiar effect observed in α-HL current measurements was that the current magnitude was dependent upon the orientation of the α-HL.[18–20] This suggested preferential transport in one direction. In order to accomplish this feat, α-HL has an asymmetrical profile across the lipid bilayer, with a wider pore base (the "cap") and a narrow pore tip (the "stem"), as shown in Figure 1.1. This geometrical asymmetry imparts a potential barrier towards entry of the pore from one side. As shown in Figure 3.3, this effect, known as ionic current rectification (ICR) can be considered a "rocking ratchet" since flow is preferentially driven in one direction.[21]

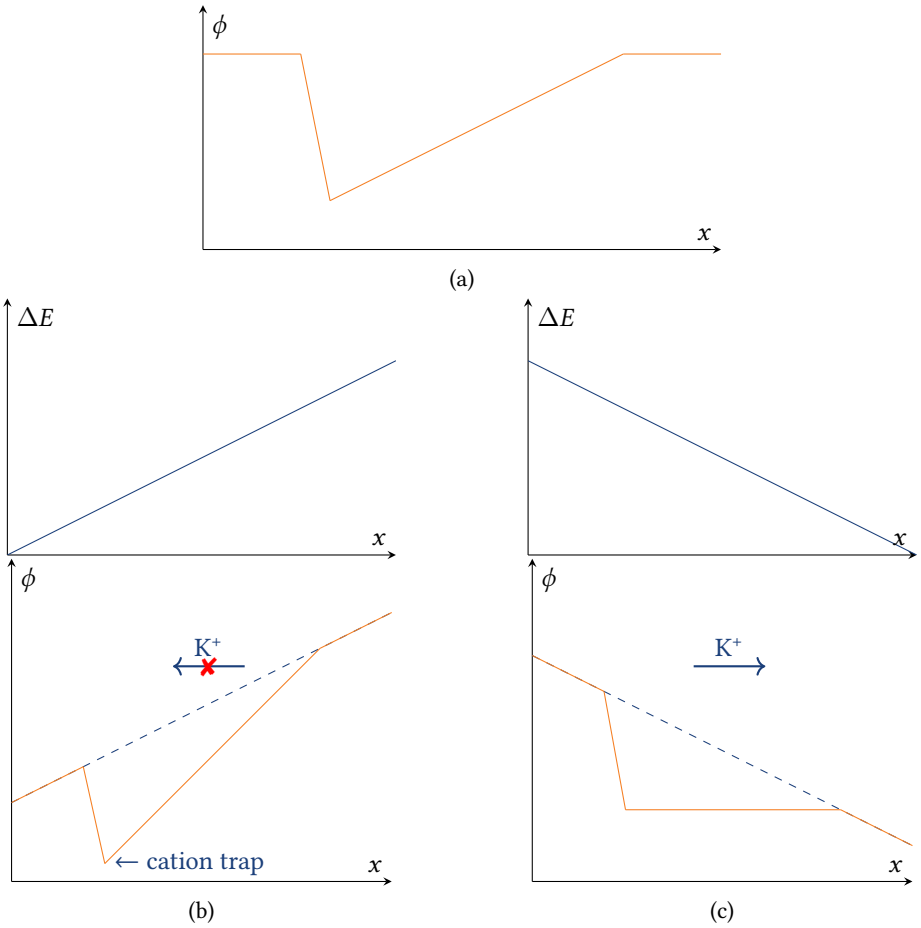

Figure 3.3: "Rocking ratchet" mechanism for ion current rectification. (a) Potential profile across an asymmetric pore. (b) Superposition of a positive potential ($+\Delta E$) in the x direction. A cation trap prohibits K^+ translocation. (c) Superposition of a negative potential ($-\Delta E$) in the x direction. The potential drop does not create a local potential minimum, permitting K^+ translocation. Adapted with permission from Siwy, Z. et al. Conical-Nanotube Ion-Current Rectifiers: The Role of Surface Charge. *J. Am. Chem. Soc.* **2004**, *126*, 10850–10851, DOI: 10.1021/ja047675c. Copyright © 2004 American Chemical Society.

The properties of ionic exclusion can be advantageous when combined with a geometrical asymmetry. A narrow opening will have a larger conductivity due to the ratio of EDL thickness to pore radius trending towards unity ($r \times \kappa \approx 1$), whereas the larger opening will not provide such a ratio. This asymmetrical conductivity introduces a difference in pore access resistance for the translocating ions or molecules. From one direction (the narrower to wider direction), the conductivity will be greater due to a decreased resistance, as shown schematically in Figure 3.4.[23] Biomimetic nanopores also include a geometrical asymmetry, often introduced as a byproduct of the fabrication process when an ion beam mills one side of the support for a longer time than the other, when an etchant is introduced only on one side of the membrane, or during glass capillary pulling.[21,22,24–27]

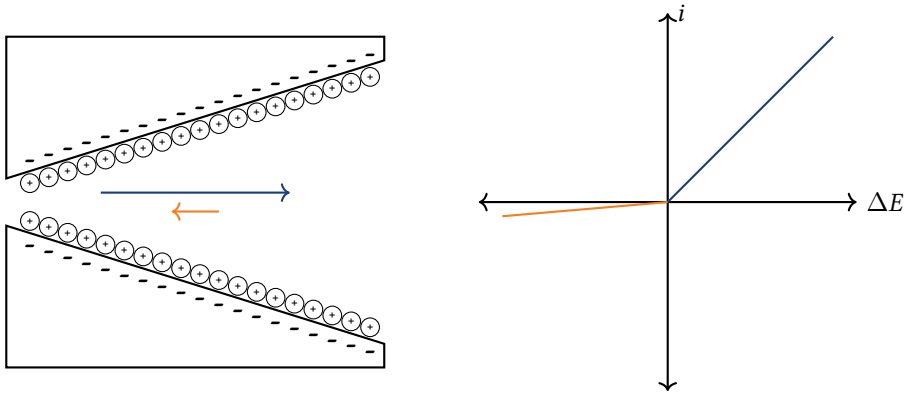

Figure 3.4: Schematic of a negatively charged conical nanopore (left) demonstrating ion current rectification. The *i*-*E* curve (right) shows decreased conductivity from the wide base to narrow tip (orange) and increased conductivity from the narrow tip to wide base (blue).

Surprisingly, the ionic current through NPG, as shown in Figure 3.2a, did not exhibit rectification as was expected for a material with such an intricate and seemingly random geometry. It was therefore assumed that the average geometry of each side of the NPG was similar enough as to present the NPG as a collection of symmetrical nanopores. An alternative means of introducing asymmetry to the NPG was therefore sought, as any asymmetry, geometrical or not, was expected to induce asymmetric behavior.[26,28]

3.4 Induced Potential Gradients with a Salt Gradient

The conductivity determined in Equation 3.5 is a result of co-ion exclusion inside the pores. In the case of NPG with a negative surface charge, Cl^- ions are excluded from the pores and the conductivity is maintained by the concentration of K^+ ions in the NPG. The difference in mobility across the NPG between the cations and anions permits the formation of a potential difference across the membrane, should the chemical potential between the reservoirs differ. This can be explained using classical equations of ther-

modynamics. To begin, the Gibbs free energy is described as[29,30]

$$\Delta G = \Delta H - T\Delta S + \sum_i \mu_i dn \tag{3.10}$$

Under the steady-state conditions of membrane transport, however, there are no changes in temperature and pressure. Thus, the only difference in free energy is the difference in chemical potential between the two sides of the membrane,[30]

$$\Delta G = \sum_i \mu_i dn \tag{3.11a}$$

$$= -RT \ln K = -nF\Delta E \tag{3.11b}$$

where K describes the equilibrium conditions between the reservoirs. For a membrane separating two equimolar solutions, $K = 1$ and therefore $\Delta E = 0$ V. Should equilibrium be perturbed, for example, by increasing the electrolyte concentration on one side of the membrane, the reservoirs will eventually become equal in concentration as the electrolyte passes through the NPG. In the case of a charged membrane, however, transport of counter-ions are favored over co-ions, as described in Section 3.1. In this scenario, the ability for the reservoirs to reach equilibrium is limited and $\Delta E \neq 0$ V. This condition, known as the Gibbs-Donnan effect,[11,31] introduces an electric field that has important implications for molecular flux through the membrane.[32–34]

Qian et al., for example, examined the presence of salt gradients in nanochannels.[35] In a pore with nonzero surface charge, ionic transport across the pore was not equal for both cations and anions as one was excluded from the pore volume near the pore surface. Preferential transport of ions lead to an accumulation of charge across the pore and the formation of an electric potential. In a phenomenon known as diffusioosmosis, two cooperative effects dictate transport through nanopores under a salt gradient: a chemiosmotic contribution due to induced pressure within the EDL from counterions in the high concentration reservoir and an electroosmotic contribution due to the electric field resulting from charge accumulation.[36,37] As noted prior, the NPG in this study exhibits a negative surface charge due to spontaneous adsorption of Cl^- to Au. It was therefore expected that the NPG exhibits cation permselectivity, especially at low ionic strength, due to exclusion of anions in the EDL. Nishizawa et al. examined the extent of ionic permselectivity through Au-coated nanopores by relating the measured potential difference across the pores with the following equation:[32]

$$\Delta E = \Delta t \left(\frac{RT}{nF}\right) \ln \frac{[\text{sink}]}{[\text{feed}]} \tag{3.12}$$

where ΔE is the potential between the reservoirs, R is the universal gas constant, F is the Faraday constant, Δt is the difference between cation (t_+) and anion (t_-) transference numbers, and [sink] ([feed]) is the ionic strength of the sink (feed) reservoir. Equation 3.12 is simply an extension of Equation 3.11 that introduces the effects of ion transport selectivity to the well-known Nernst equation. Considering Equation 3.12 in the context of Equation 3.6 reveals the importance of the migration terms in the Nernst-Planck equation. Similarly, the selective transport of cations across the NPG in the presence of a salt gradient produces diffusioosmosis, now creating a nonzero convective term. Concentration gradients such as these have had very important applications in recent nanopore studies. The induced electric field and ion advection have shown to be capable of slowing DNA translocation to improve sequencing sensitivity as well as improve biomolecule capture within nanopores.[12,38,39] The contributions of these effects are not negligible in nanoporous media, such as NPG, and are explored in further detail in Chapter 5.

3.5 Finite Element Simulations

Transport through NPG was modeled using COMSOL Multiphysics software following two different approaches: (1) modeling transport within a representative section of the porous network; and (2) assuming transport occurs through a single pore with diffusion coefficients adjusted for a tortuous network. In each attempt, the Transport of Diluted Species, Electrostatics, and Laminar Flow modules were employed. The full reports from the simulations are provided in Appendix A. Briefly, the Transport of Diluted Species module considered the Nernst-Planck equation (Equation 3.6) to calculate flux based on the electric field introduced by the Electrostatics module and fluid velocity introduced by the Laminar Flow module. Both simulations indicated that a large potential well exists within the NPG structure, which, in turn, suggested that NPG may have a strong tendency to either trap or completely exclude counterions or co-ions, respectively.

3.5.1 Modeling of a Porous Domain

After ISODATA thresholding in ImageJ, a representative SEM image was imported into Adobe Illustrator in order to trace the ligament structure. This sketch could then be exported as a Drawing Interchange Format (*.dxf) file and modified using AutoCAD for import into COMSOL. The sketch was then manually re-sized to an appropriate scale for accurate modeling.

The geometry used is presented in Figure 3.5. Boundary conditions were defined at the left and right sides of the sketch assuming that the feed and sink concentrations, respectively, would not change as a function of time. The top and bottom boundaries were left open to permit lateral diffusion.

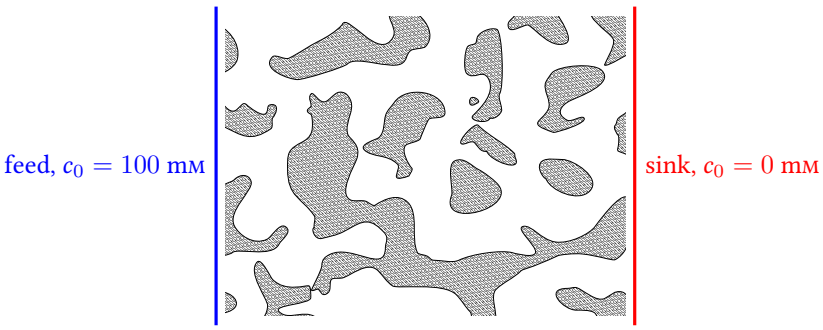

Figure 3.5: Model used for porous domain simulations. The hatched areas are the Au ligaments. A surface potential, σ, was imposed on the ligaments (black border). The annotated concentrations of an anionic tracer ($z = -1$) were maintained constant in the feed and sink reservoirs.

Two parameters, background electrolyte concentration (in this case, NaCl) and the NPG surface charge, σ, were adjusted through a parametric sweep. The results are summarized in Figure 3.6. At negative surface charge, it appeared that the anion was only excluded for lower background electrolyte concentrations. This was most likely a result of the induced laminar flow through the NPG structure, illustrated in Figure 3.6c. Laminar flow overall increased with higher surface charge. Note that there was no laminar flow calculated for $\sigma = 0$ mC m^{-1}. Importantly, it appeared that a potential well existed within the NPG structure, as shown in Figure 3.6b. At negative (positive) surface charges, the potential well polarity was negative (positive). This well appeared to trap the anionic tracer at positive surface charges as shown in Figure 3.6a at $\sigma = +2.5$ mC m^{-1}.

3.5.2 Modeling of a Single Pore with a Tortuosity Correction Factor

The nanoporous domain approach described above was performed using a 2-dimensional simulation. It therefore did not consider surface charge contributions above and below the 2D plane. Simulations concerning single nanopores often employ a 2D-axisymmetric model whereby the pore can be represented in a 2D image, but rotation around the axis of symmetry extends the model in 3 dimensions.[11,40–42] Compared to the previous nanoporous geometry approach, this simulation used a time-dependent solver rather than a stationary solver.

The geometry in Figure 3.7 was used to simulate transport through NPG, assuming the diffusion through the single pore would be altered according to Equation 3.9. *AB* and *GH* were set at constant concentrations of the tracer analyte for the feed and sink reservoirs, respectively. The surface charge, σ, was applied to *CDEF* to simulate the negatively charged Au surface. The axis of symmetry was centered around *AH* to create a 3-dimensional simulation through rotation about this axis. Diffusion coefficients for the electrolytes and tracer used were equal to their bulk constants in the *ABCD* feed and *EFGH* sink reservoirs,

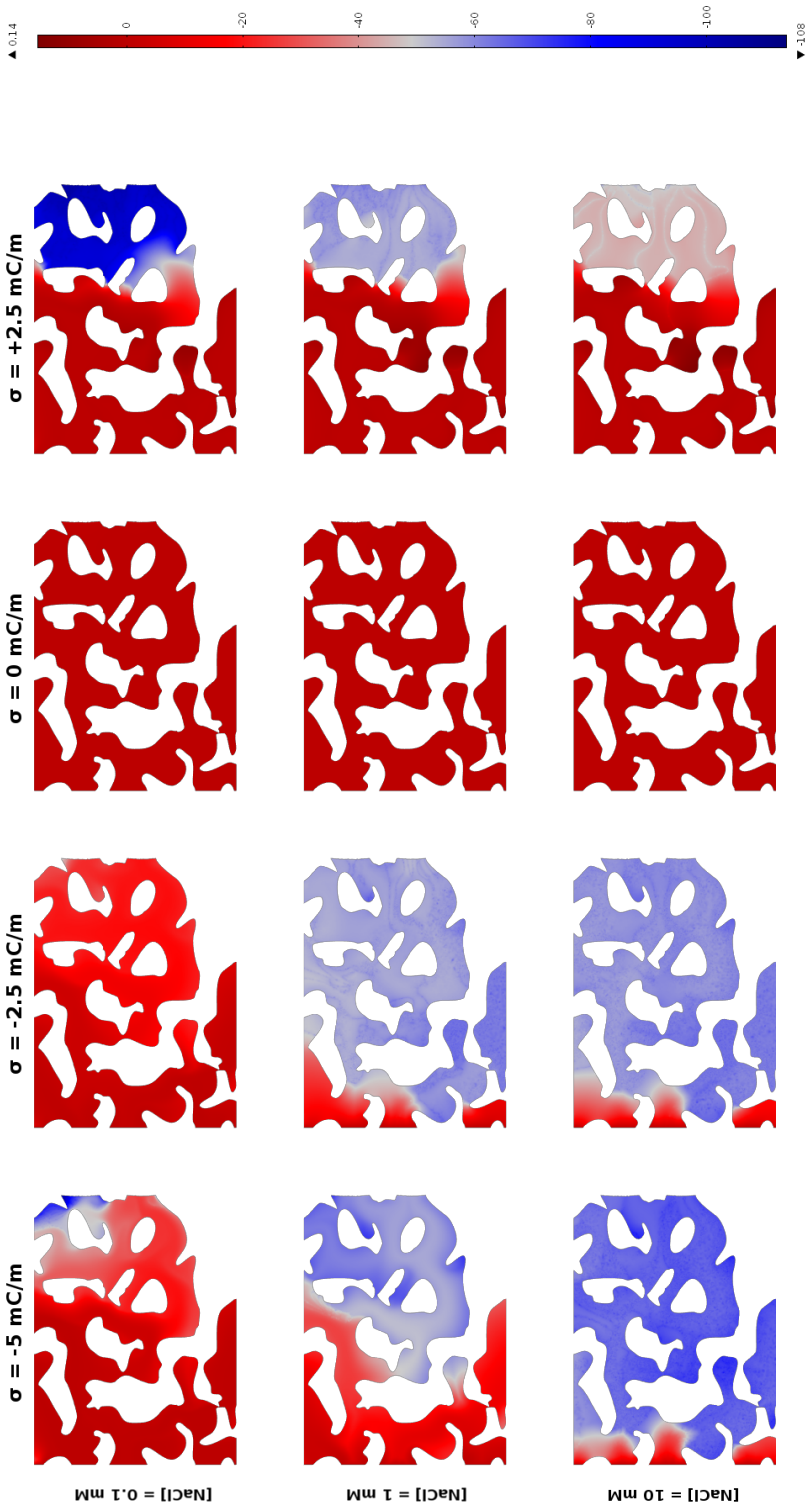

(a) Concentration of anionic tracer within pores (log scale).

Figure 3.6: Finite element simulation results of a monovalent anionic tracer through NPG. The geometry was imported from an SEM image and scaled to provide, on average, a 50 nm pore size.

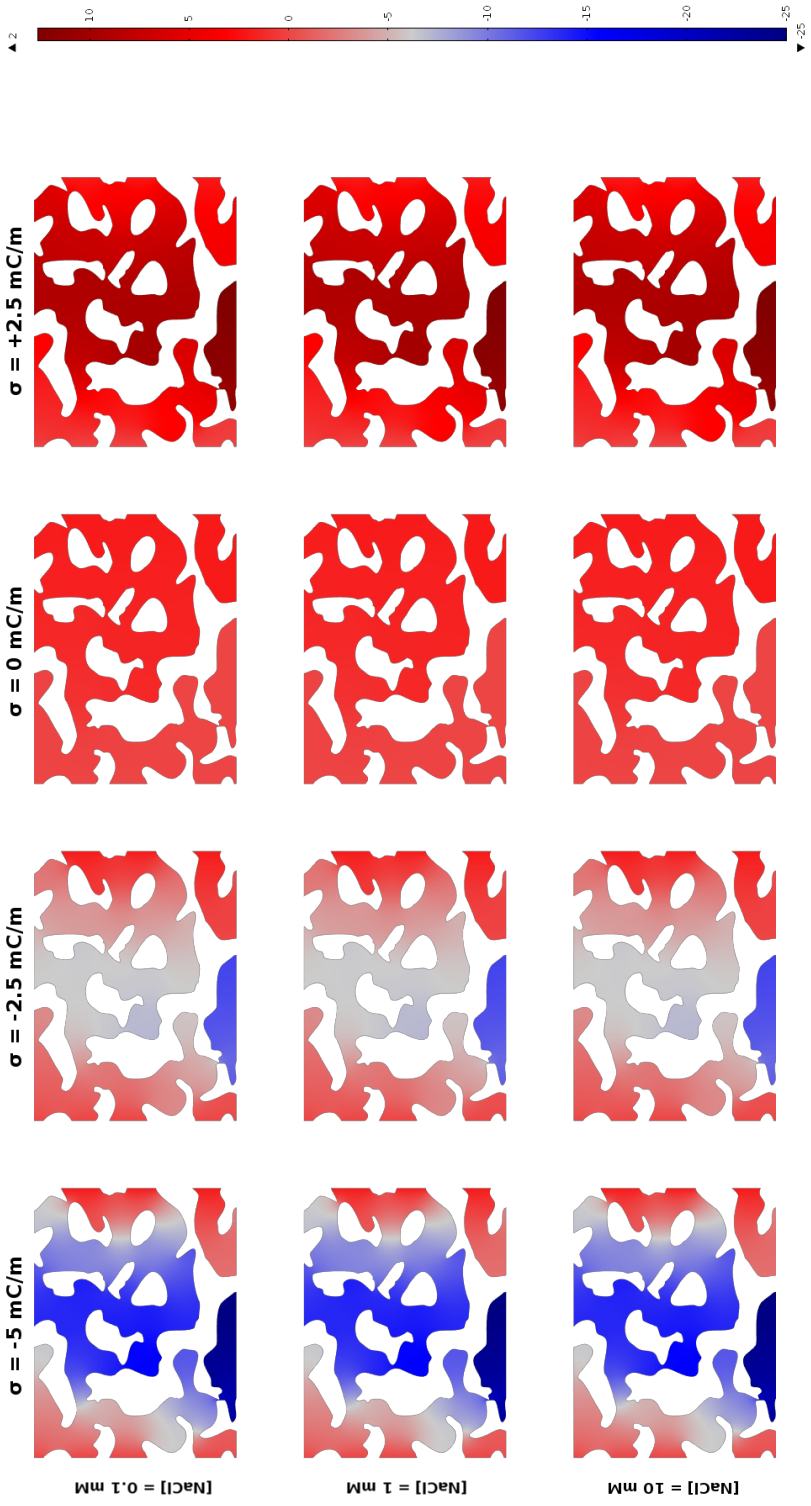

(b) Electric potential within pores.

Figure 3.6: *Continued from previous page.*

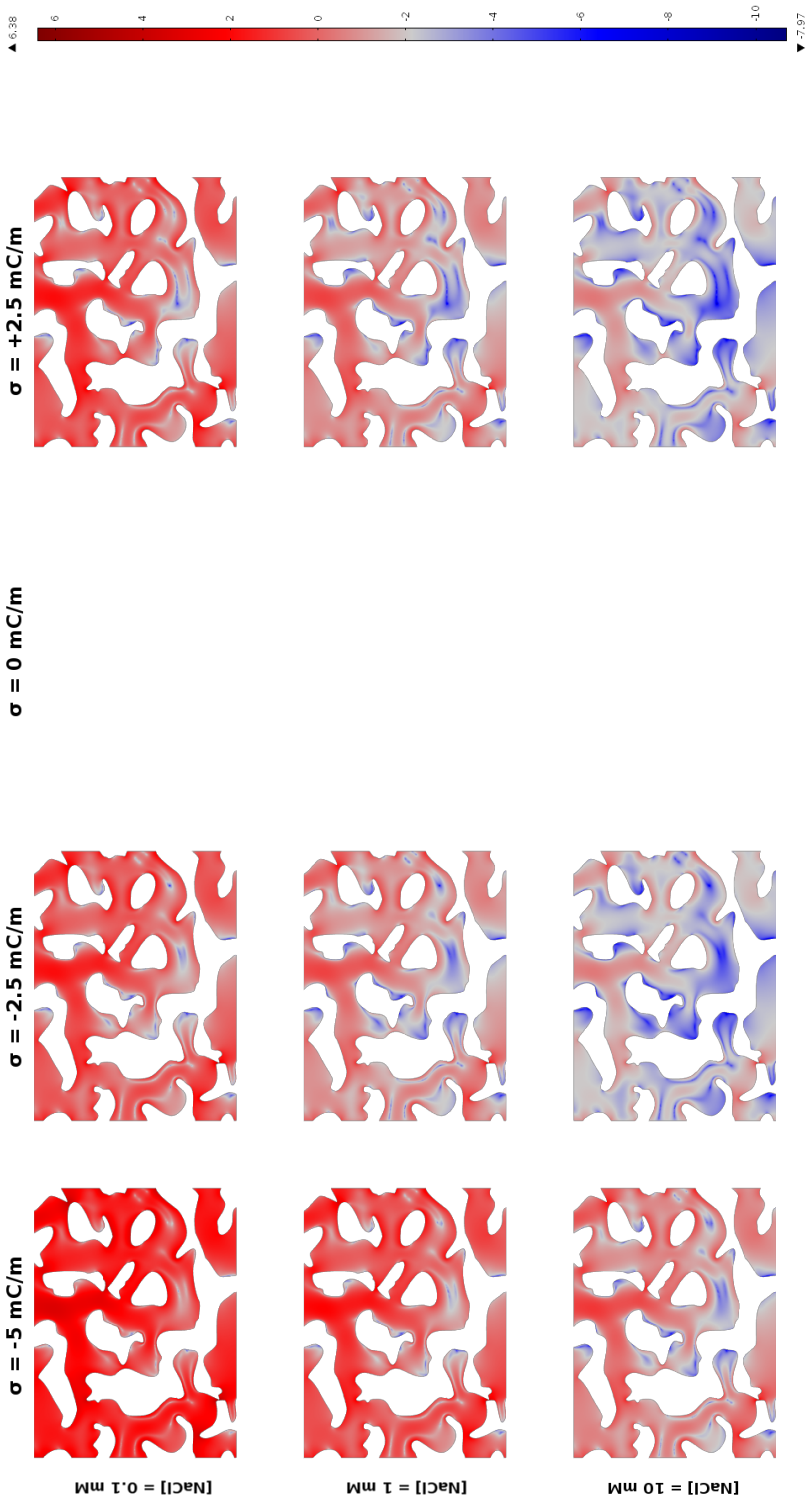

(c) Electroosmotic flow velocity within pores.

Figure 3.6: *Continued from previous page.*

but the effective diffusion coefficients calculated from Equation 3.9 were used within the nanopore region, *DE*.

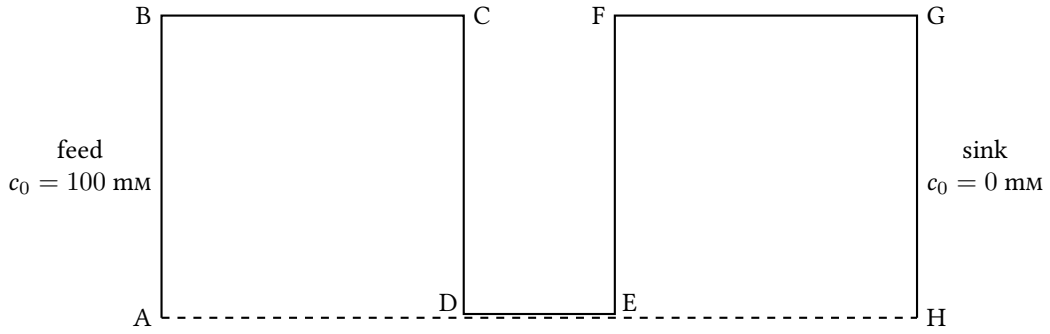

Figure 3.7: The geometry used in the single pore approach. The dashed line indicates the axis of symmetry. The geometry was rotated around this axis to create a 3-dimensional simulation.

Simulation of a divalent cationic tracer was performed and the concentration and potential profiles along *AH* were plotted in Figure 3.8. This simulation was used to study the presence of an asymmetric electrolyte concentration on either side of the pore. As shown in Figure 3.8b, there exists a large potential well, similar to that observed in Figure 3.6b. This had the effect of trapping much of the cationic tracer in the center of the pore, as shown in Figure 3.8a. Note that laminar flow was not taken into account in the present study, which explains the large growth of cation concentration over time.

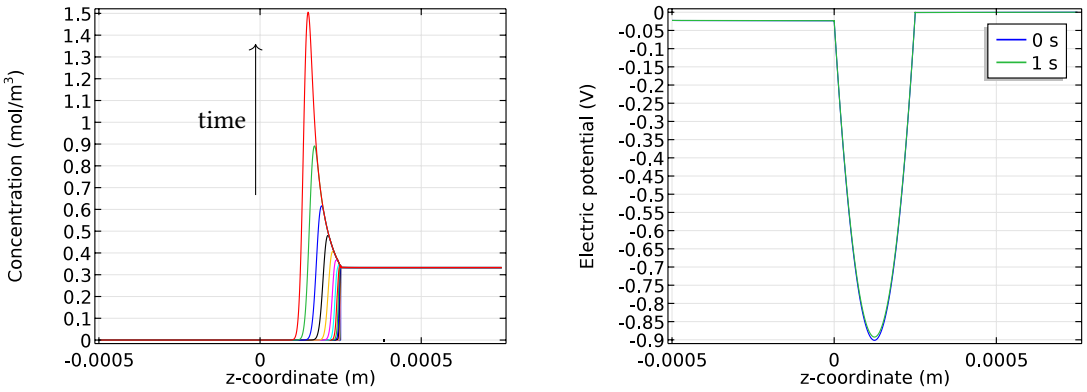

(a) (b)

Figure 3.8: Time-dependent simulation of a divalent cationic tracer through a nanopore with diffusion coefficients adjusted for tortuosity. For reverence, the feed is on the right side and sink is on the left. (a) Cation concentration profile along *AH*. Over time, a large peak appears to grow in the center of the nanopore. (B) Potential profile along *AH*. A well exists, causing the cations to become trapped.

3.6 References

1. Smeets, R. M. M.; Keyser, U. F.; Krapf, D.; Wu, M.-Y.; Dekker, N. H.; Dekker, C. Salt Dependence of Ion Transport and DNA Translocation through Solid-State Nanopores. *Nano Letters* **2006**, *6*, 89–95, DOI: 10.1021/nl052107w.

2. Wanunu, M. Nanopores: A journey towards DNA sequencing. *Physics of Life Reviews* **2012**, *9*, 125–158, DOI: 10.1016/j.plrev.2012.05.010.

3. Shi, Z.; Lipkowski, J. Chloride adsorption at the Au(111) electrode surface. *Journal of Electroanalytical Chemistry* **1996**, *403*, 225–239, DOI: 10.1016/0022-0728(95)04313-6.

4. Qian, S.; Ai, Y., Numerical Simulations of Electrical Double Layer and Electroosmotic Flow in a Nanopore. In *Electrokinetic Particle Transport in Micro-/Nanofluidics*; Surfactant Science; CRC Press: 2012, pp 23–51, DOI: 10.1201/b12128-3.

5. Bard, A. J.; Faulkner, L. R., *Electrochemical Methods: Fundamentals and Applications*; John Wiley & Sons, Inc.: New York, 2001; Vol. 2.

6. Daiguji, H.; Yang, P.; Majumdar, A. Ion Transport in Nanofluidic Channels. *Nano Letters* **2004**, *4*, 137–142, DOI: 10.1021/nl0348185.

7. Frament, C. M.; Bandara, N.; Dwyer, J. R. Nanopore Surface Coating Delivers Nanopore Size and Shape through Conductance-Based Sizing. *ACS Applied Materials & Interfaces* **2013**, DOI: 10.1021/am4026455.

8. Dissociation Constants of Organic Acids and Bases. In, Haynes, W., Ed., 96th ed.; CRC Handbook of Chemistry and Physics; CRC Press: 2016; Chapter 5, pp 94–103.

9. Daiguji, H.; Oka, Y.; Shirono, K. Nanofluidic Diode and Bipolar Transistor. *Nano Letters* **2005**, *5*, 2274–2280, DOI: 10.1021/nl051646y.

10. Karnik, R.; Fan, R.; Yue, M.; Li, D.; Yang, P.; Majumdar, A. Electrostatic Control of Ions and Molecules in Nanofluidic Transistors. *Nano Letters* **2005**, *5*, 943–948, DOI: 10.1021/nl050493b.

11. Makra, I.; Jágerszki, G.; Bitter, I.; Gyurcsányi, R. E. Nernst–Planck/Poisson model for the potential response of permselective gold nanopores. *Electrochimica Acta* **2012**, *73*, 70–77, DOI: 10.1016/j.electacta.2012.02.074.

12. Yeh, L.-H.; Hughes, C.; Zeng, Z.; Qian, S. Tuning Ion Transport and Selectivity by a Salt Gradient in a Charged Nanopore. *Analytical Chemistry* **2014**, DOI: 10.1021/ac4040136.

13. Mao, M.; Sherwood, J. D.; Ghosal, S. Electro-osmotic flow through a nanopore. *J. Fluid Mech.* **2014**, *749*, 167–183, DOI: 10.1017/jfm.2014.214.

14. Lan, W.-J.; Holden, D. A.; Zhang, B.; White, H. S. Nanoparticle Transport in Conical-Shaped Nanopores. *Analytical Chemistry* **2011**, *83*, 3840–3847, DOI: 10.1021/ac200312n.

15. Kontturi, K.; Murtomäki, L.; Manzanares, J. A., Transport in membranes. In *Ionic Transport Processes in Electrochemistry and Membrane Science*; Oxford University Press Inc.: New York, 2008; Chapter 4, pp 126–231.

16. Pisani, L. Simple Expression for the Tortuosity of Porous Media. *Transp Porous Med* **2011**, *88*, 193–203, DOI: 10.1007/s11242-011-9734-9.

17. Chung, D.-W.; Ebner, M.; Ely, D. R.; Wood, V.; García, R. E. Validity of the Bruggeman relation for porous electrodes. *Modelling and Simulation in Materials Science and Engineering* **2013**, *21*, 074009, DOI: 10.1088/0965-0393/21/7/074009.

18. Bhattacharya, S.; Muzard, J.; Payet, L.; Mathé, J.; Bockelmann, U.; Aksimentiev, A.; Viasnoff, V. Rectification of the Current in α-Hemolysin Pore Depends on the Cation Type: The Alkali Series Probed by Molecular Dynamics Simulations and Experiments. *J. Phys. Chem. C* **2011**, *115*, 4255–4264, DOI: 10.1021/jp111441p.

19. O'Keeffe, J.; Cozmuta, I.; Bose, D.; Stolc, V. A predictive MD-Nernst–Planck model for transport in alpha-hemolysin: Modeling anisotropic ion currents. *Chemical Physics* **2007**, *342*, 25–32, DOI: 10.1016/j.chemphys.2007.09.013.

20. Misakian, M.; Kasianowicz, J. J. Electrostatic Influence on Ion Transport through the aHL Channel. *Journal of Membrane Biology* **2003**, *195*, 137–146, DOI: 10.1007/s00232-003-0615-1.

21. Siwy, Z. S. Ion-Current Rectification in Nanopores and Nanotubes with Broken Symmetry. *Advanced Functional Materials* **2006**, *16*, 735–746, DOI: 10.1002/adfm.200500471.

22. Siwy, Z.; Heins, E.; Harrell, C. C.; Kohli, P.; Martin, C. R. Conical-Nanotube Ion-Current Rectifiers: The Role of Surface Charge. *J. Am. Chem. Soc.* **2004**, *126*, 10850–10851, DOI: 10.1021/ja047675c.

23. Kovarik, M. L.; Zhou, K.; Jacobson, S. C. Effect of Conical Nanopore Diameter on Ion Current Rectification. *J. Phys. Chem. B* **2009**, *113*, 15960–15966, DOI: 10.1021/jp9076189.

24. White, H. S.; Bund, A. Ion Current Rectification at Nanopores in Glass Membranes. *Langmuir* **2008**, *24*, 2212–2218, DOI: 10.1021/la702955k.

25. Apel, P. Y.; Blonskaya, I. V.; Orelovitch, O. L.; Ramirez, P.; Sartowska, B. A. Effect of nanopore geometry on ion current rectification. *Nanotechnology* **2011**, *22*, 175302, DOI: 10.1088/0957-4484/22/17/175302.

26. Guo, W.; Tian, Y.; Jiang, L. Asymmetric Ion Transport through Ion-Channel-Mimetic Solid-State Nanopores. *Accounts of Chemical Research* **2013**, *46*, 2834–2846, DOI: 10.1021/ar400024p.

27. Shi, W.; Sa, N.; Thakar, R.; Baker, L. A. Nanopipette delivery: influence of surface charge. *Analyst* **2015**, *140*, 4835–4842, DOI: 10.1039/C4AN01073F.

28. Velleman, L.; Losic, D.; Shapter, J. G. The effects of surface functionality positioning on the transport properties of membranes. *Journal of Membrane Science* **2012**, *411–412*, 211–218, DOI: 10.1016/j.memsci.2012.04.033.

29. Seddon, J. M.; Gale, J. D., *Thermodynamics And Statistical Mechanics*; Wiley-Interscience: New York, 2002.

30. Hamann, C. H.; Hamnett, A.; Vielstich, W., *Electrochemistry*; Wiley-VCH: Weinheim, 2007.

31. Galama, A. H.; Post, J. W.; Cohen Stuart, M. A.; Biesheuvel, P. M. Validity of the Boltzmann equation to describe Donnan equilibrium at the membrane–solution interface. *Journal of Membrane Science* **2013**, *442*, 131–139, DOI: 10.1016/j.memsci.2013.04.022.

32. Nishizawa, M.; Menon, V. P.; Martin, C. R. Metal Nanotubule Membranes with Electrochemically Switchable Ion-Transport Selectivity. *Science* **1995**, *268*, 700–702, DOI: 10.1126/science.268.5211.700.

33. Martin, C. R.; Nishizawa, M.; Jirage, K.; Kang, M. Investigations of the Transport Properties of Gold Nanotubule Membranes. *J. Phys. Chem. B* **2001**, *105*, 1925–1934, DOI: 10.1021/jp003486e.

34. Martin, C. R.; Nishizawa, M.; Jirage, K.; Kang, M.; Lee, S. B. Controlling Ion-Transport Selectivity in Gold Nanotubule Membranes. *Advanced Materials* **2001**, *13*, 1351–1362, DOI: 10.1002/1521-4095(200109)13:18<1351::aid-adma1351>3.0.co;2-w.

35. Qian, S.; Das, B.; Luo, X. Diffusioosmotic flows in slit nanochannels. *Journal of colloid and interface science* **2007**, *315*, 721–730, DOI: 10.1016/j.jcis.2007.06.075.

36. Liu, K.-L.; Hsu, J.-P.; Tseng, S. Capillary Osmosis in a Charged Nanopore Connecting Two Large Reservoirs. *Langmuir* **2013**, *29*, 9598–9603, DOI: 10.1021/la401925n.

37. Keh, H. J. Diffusiophoresis of charged particles and diffusioosmosis of electrolyte solutions. *Current Opinion in Colloid & Interface Science* **2016**, *24*, 13–22, DOI: 10.1016/j.cocis.2016.05.008.

38. Wanunu, M.; Morrison, W.; Rabin, Y.; Grosberg, A. Y.; Meller, A. Electrostatic focusing of unlabelled DNA into nanoscale pores using a salt gradient. *Nature Nanotechnology* **2010**, *5*, 160–165, DOI: 10.1038/nnano.2009.379.

39. Chou, T. Enhancement of charged macromolecule capture by nanopores in a salt gradient. *Journal of Chemical Physics* **2009**, *131*, 034703, DOI: 10.1063/1.3170952.

40. Kaya, D.; Dinler, A.; San, N.; Kececi, K. Effect of Pore Geometry on Resistive-Pulse Sensing of DNA Using Track-Etched PET Nanopore Membrane. *Electrochimica Acta* **2016**, *202*, 157–165, DOI: 10.1016/j.electacta.2016.04.014.

41. Liu, J.; Wang, D.; Kvetny, M.; Brown, W.; Li, Y.; Wang, G. Quantification of Steady-State Ion Transport through Single Conical Nanopores and a Nonuniform Distribution of Surface Charges. *Langmuir* **2013**, *29*, 8743–8752, DOI: 10.1021/la4009009.

42. White, H. S.; Bund, A. Mechanism of Electrostatic Gating at Conical Glass Nanopore Electrodes. *Langmuir* **2008**, *24*, 12062–12067, DOI: 10.1021/la801776w.

Chapter 4

Tunable Ionic and Molecular Transport through Nanoporous Gold Membranes

4.1 Introduction

Nanopores have gained significant interest due to the unique properties that are presented at length scales below 100 nm. For example, biomimetic pores fabricated from materials including silicon and graphene have emerged as promising architectures for nucleic acid sequencing, allowing for unprecedented resolution between base pairs and single molecule detection.[2,3] Nanopores have been able to resolve different DNA strands, proteins, nanoparticles, and a variety of other small chemical analytes, including dyes and amino acids.[4–9] Whereas the primary focus of such applications has been detection or single molecule characterization, nanopores have also been demonstrated as enabling membranes for highly selective (bio)chemical separations.[10–12]

Common approaches for fabrication of synthetic nanopores involve the top down milling of solid substrates with a focused ion beam or laser-assisted capillary pulling.[7,9,13] The resulting pore has a defined size that physically occludes larger particles from passing through. In addition, the most commonly used materials for preparing synthetic pores, such as SiO_2, often present a charged surface in solution.[7,14] Charge-based selection therefore occurs as pore diameters on the length scale of the Debye layer can lead to ionic exclusion. In both regimes, analyte discrimination is directly related to the physical dimensions of the pore and therefore not typically able to be adjusted for different analytical separations. Furthermore, many studies focus on transport through only a single nanopore, which, while essential for fundamental studies, would likely not provide sufficient flux for many applications. Motivated by these two potential limitations, we have investigated nanoporous gold (NPG) as a versatile membrane construct for chemical separations.

NPG, which is easily fabricated by chemical or electrochemical de-alloying, features properties that

This chapter contains previously published material, adapted with permission from McCurry, D. A.; Bailey, R. C. Nanoporous Gold Membranes as Robust Constructs for Selectively Tunable Chemical Transport. *Journal of Physical Chemistry* **2016**, DOI: 10.1021/acs.jpcc.6b02759.

are attractive for many applications in molecular separation, including a high pore density, inherent conductivity, corrosion resistance, biocompatibility, and facile surface modification.[15,16] NPG also has a large surface area, which in addition to utility in separations, has also been used to promote catalysis and current collection in batteries and fuel-cells.[17–19] Furthermore, the large ionic and chemical storage capacity of NPG have led to its use in supercapacitor and drug delivery applications.[20,21] Herein, the ability to tune the NPG surface charge is exploited to promote selective transport of charged analytes. The NPG was modified with either pH-sensitive or electroactive self-assembled monolayers. In either case, modulation of the charge at the NPG surface by either solution pH regulation or electric potential led to differences between anionic and cationic transport through the NPG monoliths.

4.2 Results and Discussion

For a typical sample, the median pore diameter was 50 ± 20 nm (see Figure 2.2d). The interior volume of NPG is highly accessible,[22,23] and solution wetting of the NPG can be controlled by an externally applied potential,[24] suggesting to us that dynamic molecular transport through NPG membranes might be achievable.

As the size of nanopores is reduced, the solution conductivity across the pore is controlled by the thickness of the electrical double layer (EDL), κ^{-1}.[25,26] The concentration dependence arises from the required minimum number of counterions within the EDL that establish electroneutrality at the surface of the pore. In this way, the charge carrier concentration is effectively constant within the nanopore volume at EDL thicknesses equivalent to the pore radii. Conductivity is generally related to bulk ionic strength and a lower conductivity limit exists across the pore as described in Equation 3.4.[27] Curious as to whether this description would hold for the interconnecting network of pores, we measured the conductivity across a NPG membrane as a function of solution ionic strength. As shown in Figure 3.2, the conductivity across the membrane is fit by Equation 3.4 and plateaus at an ionic strength at which the theoretical EDL thickness is equivalent to the radius of the pore, consistent with expectations for single synthetic nanopore systems and suggesting that the transport of chemical species might be controlled via modulation of surface charge within the NPG. This relationship is highly dependent on pore diameter, with larger pores demonstrating conductivity closer to that of the bulk solution at all ionic strengths due to the pore diameter becoming much greater than the EDL thickness.[28,29] Furthermore, smaller pores will demonstrate a higher minimum conductivity limit as the EDL encompasses a greater proportion of the pore. This effect has been examined in detail in prior studies[28–31] and has important implications for NPG as a separations device; specifically, adjusting pore size may not only affect size discrimination of the membrane, but may also alter the surface

charge contribution towards molecular flux within the NPG.

To assess the ability for selective molecular transport, a NPG membrane was sandwiched between two reservoirs and transport was monitored via UV-visible absorption spectroscopy as a function of an applied electrophoretic potential, as shown in Figure 4.1). The molecular flux was calculated as the slope of concentration over time. Note that the flux rapidly reaches steady state after each potential switch. The final magnitude of $[MV^{2+}]$ in the sink reservoir is orders of magnitude less than the initial $[MV^{2+}]$ in the feed reservoir, permitting the assumption of a constant tracer concentration difference across the NPG throughout the duration of each experiment. Previous studies of transport through nanopores have described molecular flux as following Nernst-Planck behavior, where the total flux is a sum of convection, diffusion, and migration fluxes.[32] The convection term is assumed to be negligible in the absence of an electroosmotic contribution, as no cross convection is introduced between reservoirs. Therefore, at very high ionic strengths, flux is governed only by diffusion from a concentration gradient and electrophoretic migration, whereas flux at low ionic strengths may also be affected by the electroosmotic flow arising from a thicker EDL.[33]

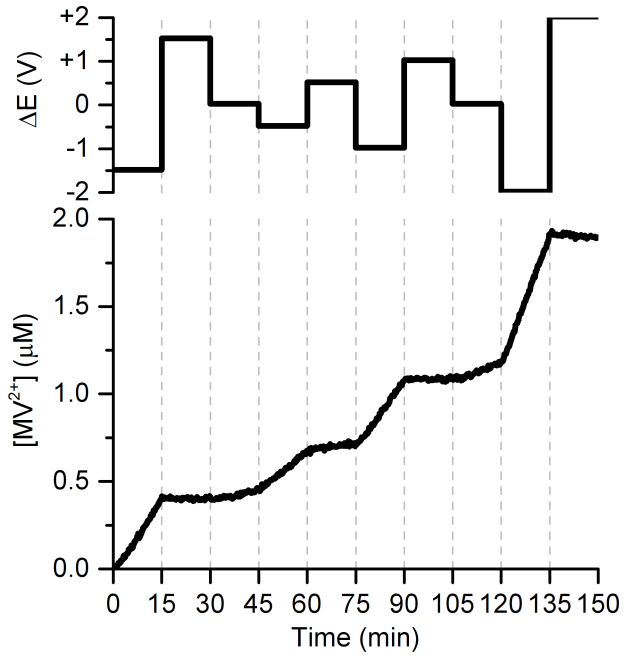

Figure 4.1: A typical flux measurement in the presence of an applied electric field. The potential applied is presented in the top graph and was run in a semi-random order to ensure that results were not dependent upon the time or order of potentials applied. The UV-visible response of the sink reservoir of MV^{2+} is presented in the bottom graph.

As model analytes, either cationic methyl viologen (MV^{2+}) or anionic benzene sulfonate (BS^-) were introduced to the feed reservoir along with the reference/counter electrode. Molecular transport was mea-

sured via fiber-optically coupled UV-visible spectroscopy in the adjacent sink reservoir, which also contained the working electrode (see Figure 4.2). In this way, applied potentials were referenced to the feed reservoir, regardless of polarity. Flux values from a typical MV^{2+} transport experiment in an electric field is shown in Figure 4.3a. Note that the molecular flux is presented in a relative form, defined as the flux at applied ΔE divided by the flux at ΔE=0 V (see Section 4.5 for normalization procedure). This ensures that any differences between specific NPG samples are removed as flux is only considered as an increase or decrease from the purely diffusive flux of a given membrane.[34]

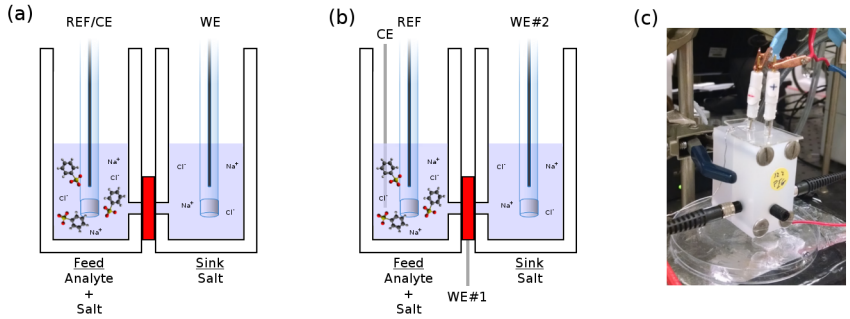

Figure 4.2: (a) Schematic of reservoir assembly used for pH sensitive thiol coated NPG. (b) Schematic of reservoir assembly for NPG with direct applied potential. Note the addition of a Pt CE to the feed reservoir. This was required to account for the additional current from the large surface area of the NPG. (c) Photograph of the custom reservoir assembly. The NPG is sandwiched between the two reservoirs. A fiber-optically coupled UV-visible spectrometer measured flux in real time as potentials were applied across and to the NPG. The CAD designs for the assembly are provided in Figure C.7

The relative flux of MV^{2+} increases with increasing applied negative potential, whereas positive potentials show no flux enhancement, and even an effective decrease in flux compared to purely diffusive transport. This potential-dependent transport is due to a combination of diffusive and electrophoretic flux; at negative applied potentials, the concentration gradient of MV^{2+} and electrophoretic transport of MV^{2+} work synergistically to deliver the analyte towards the sink reservoir. At positive potentials, the electrophoretic and diffusional terms are in opposition. The transport of anionic BS^- was similarly investigated, as shown in Figure 4.3b. In general, the negative surface charge of the NPG from adsorbed Cl^- hindered BS^- flux across the membrane, resulting in much lower rates of relative flux compared with MV^{2+}.

These trends are consistent across a wide range of salt concentrations, but the extent to which flux is affected by applied potential was also dependent on ionic strength. Enhanced transport was seen at lower ionic strengths due to the increased EDL thickness in the pores and therefore and increased electroosmotic contribution. In the case of MV^{2+}, electroosmotic flow through the negatively charged NPG is in the same direction as the migration, so at lower ionic strengths there is a greater enhancement of transport

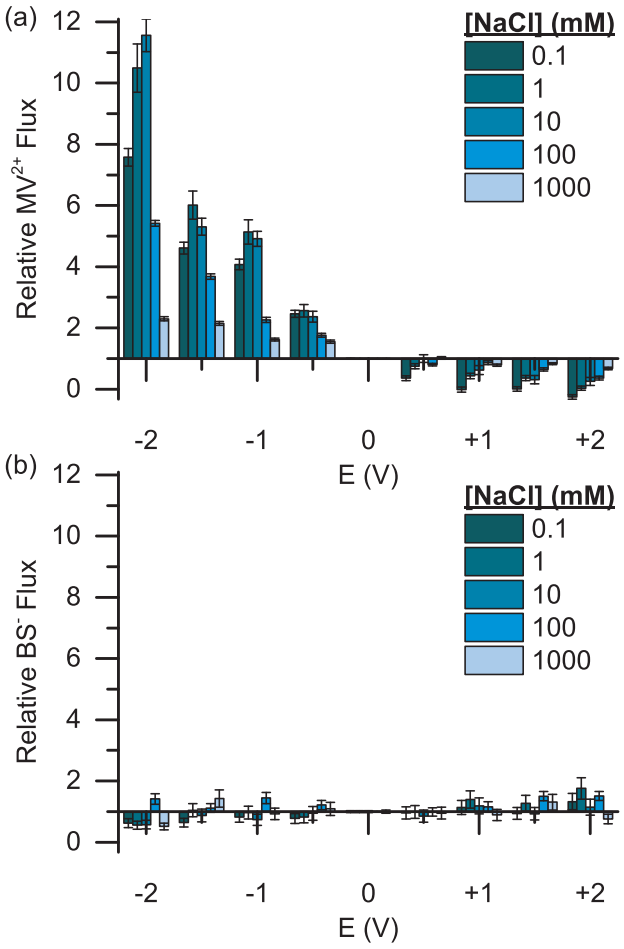

Figure 4.3: Molecular flux ratio as calculated from the change in absorbance in response to the applied electric fields over a range of concentrations are provided for (a) MV^{2+} and (b) BS^-.

at negative potentials and a greater inhibition at positive potentials. At very low (0.1 mM) ionic strength, extensive double layer overlap introduces a high resistance towards counter-ion flow and, in turn, leads to a decrease in flux through membranes and pores.[29] For BS^-, not only does the negative surface charge preclude BS^- flux to an extent, but the electroosmotic and migration terms are in opposite directions, further reducing flux.

Given the important role that charge within the NPG has on transport, we reasoned that the perms-electivity of the membrane could be modulated by rational tuning of the surface charge. To accomplish this, self-assembled monolayers (SAMs) from thiol-containing solutions were formed on the NPG surface. The first monolayers investigated featured amine ($-NH_2$) and carboxylic acid (-COOH) functional groups with charges that can be externally controlled via solution pH, and have previously been investigated in other nanopore geometries.[35,36]

Transport of MV^{2+} and BS^- through NPG functionalized with these SAMs is summarized in Figure

4.4. Importantly, for both SAMs, transport was measured under both acidic (pH≈3) and basic (pH≈11) conditions, rendering the amine-modified surface positively-charged or uncharged, respectively, and the carboxylic acid-terminated SAM neutral or negatively-charged. Similar to bare NPG, MV^{2+} transport is increased at negative applied trans-membrane potentials; however, transport was greatest at basic pH, where the amine was neutral and the carboxylic acid was negatively charged. The negatively charged carboxylic acid and positively charged amine were particularly effective at enhancing MV^{2+} and BS^- transport, respectively, as evident by the very large relative flux compared to their neutral states (Figures 4.4a(ii) and b(i)). Overall, relative flux for BS^- was much greater for the SAM-modified NPG compared to that of the bare membrane with adsorbed Cl^-, and flux was greatest at acidic pH, where the amine was positively charged and the carboxylic acid group was neutral. The protonated amine moiety demonstrated a much greater enhancement towards BS^- flux compared to the neutral carboxyl group at the surface, possibly due to partial neutralization of any residually adsorbed Cl^- at SAM defects. An additional factor that was not examined in the present study, but is of great interest to our laboratory in the future, are the hydrophobic interactions that may be occurring with the thiols at the surface.

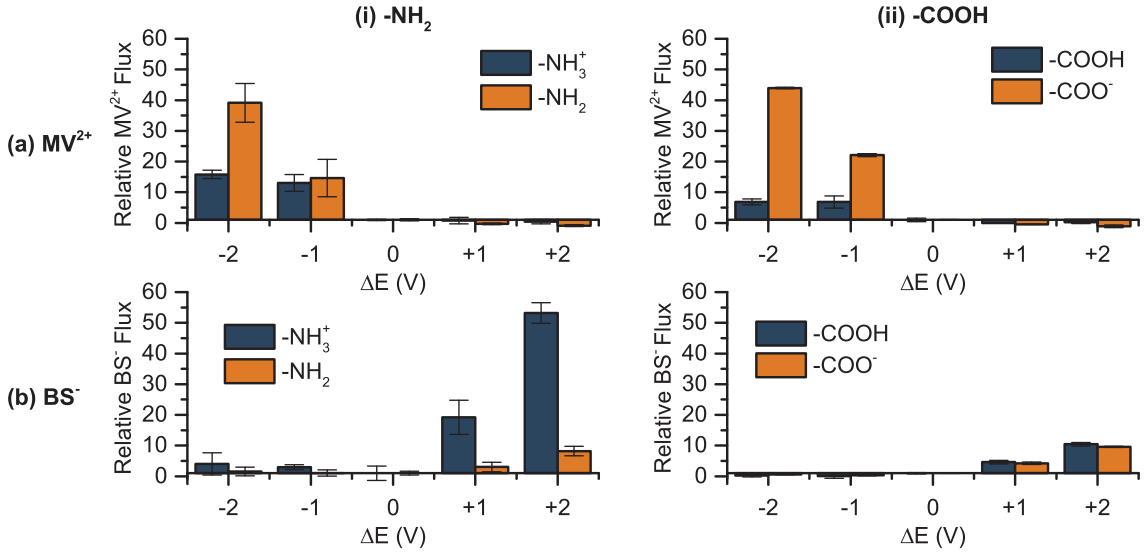

Figure 4.4: Electrokinetic flux relative to flux at $\Delta E = 0$ for (a) MV^{2+} (b) BS^- through NPG functionalized with (i) amine- and (ii) carboxylic acid-terminated thiols. The relative flux for the pH-responsive thiols was compared in acidic (dark bars) and basic (light bars) solutions.

To afford a further level of dynamic control over NPG surface charge, we next functionalized the membrane with a ferrocene-terminated thiol (-Fc) to enable redox-gateable transport. Ferrocene is a classic electroactive molecule featuring very high reversibility between a positively-charged oxidized state, and a neutral, reduced state.[37] Figure 4.5(i) shows the relative MV^{2+} and BS^- flux through a NPG membrane

functionalized with ferrocene in both the oxidized and reduced states. This experiment was performed similarly to above, but now using a bipotentiostat to control the redox potential applied to the membrane independently of the transmembrane electrophoretic potential.

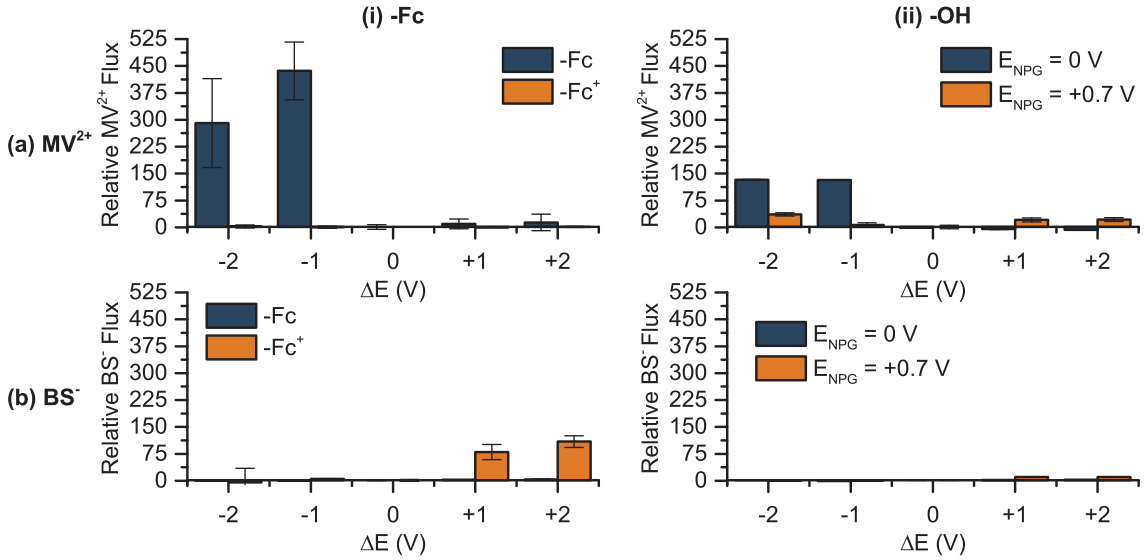

Figure 4.5: Electrokinetic flux relative flux at $\Delta E = 0$ for (a) MV^{2+} and (b) BS^- through NPG functionalized with (i) ferrocene- and (ii) hydroxyl-terminated thiols. The relative flux compared at either oxidative (+0.7 V, light bars) or reductive (0 V, dark bars) potentials applied directly to the NPG.

When uncharged, transport of MV^{2+} through the ferrocene-modified NPG was very high at negative transmembrane potentials. Electrochemical oxidation to Fc^+ effectively eliminated flux due to cation exclusion from the pores. For BS^-, electrochemical oxidation of ferrocene led to a marked increase in flux at positive applied transmembrane potentials.

Compared to pH-sensitive NPG samples, the use of electroactive moieties seemed to introduce a convective current through the NPG as a result of the applied potential. Ideally, the application of +0.7 V would instantaneously oxidize all ferrocene groups at the surface and the EDL at the Au surface would quickly become fully charged. In practice, though, the extremely large surface area of the NPG and close proximity of ferrocene groups within the pores appears to present a significant non-faradaic charging current at the NPG. Figure 4.6 shows the slight irreversibility present in cycling the potential on an Fc-thiol-modified NPG sample and its effects on the current transients measured during BS^- and MV^{2+} transport. Such residual charging currents may have had a significant effect on the measured flux, leading to a marked difference between the relative flux measured at neutral surface charge for the pH sensitive thiols vs the ferrocene thiol. While the commercial availability of ferrocene-terminated thiols make it an attractive monolayer material, potential complications in terms of stability in aqueous solutions and electrochemical

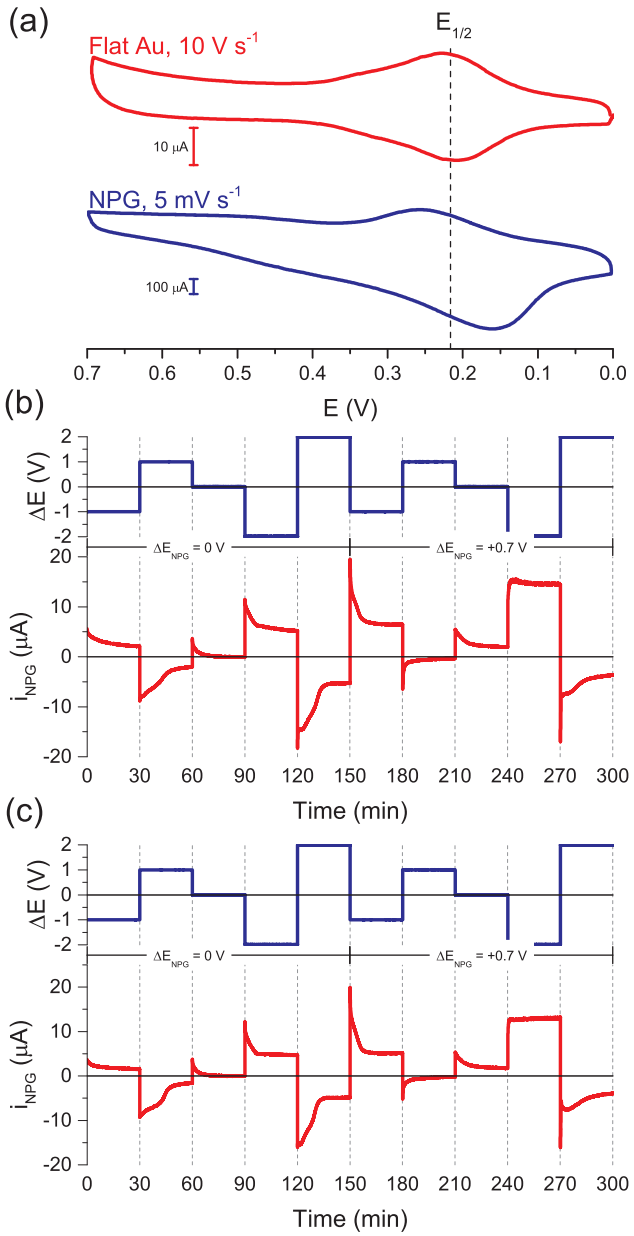

Figure 4.6: (a) Cyclic voltammogram of the Fc-terminated thiol on both flat Au and NPG in 0.1 M sodium perchlorate. The thiol was deposited in a 1:22 ratio of 6-mercapto-1-hexanol to 6-ferrocenyl-1-hexanethiol and the scan rates were adjusted to clearly resolve the peaks. The $E_{½}$ should ideally be equal to the E_{pa} and E_{pc} for a surface adsorbed electroactive species. The peak deviation and non-faradaic charging increases for the NPG due to the close proximity of the ferrocene groups and very large surface area, respectively. The current measured at the NPG (red) during application of a transverse potential (blue) for (b) methyl viologen and (c) benzene sulfonate demonstrates large currents at the NPG for a significant period of time. These currents may contribute to the measured flux.

irreversibility[38,39] suggest that alternative electroactive monolayers may have result in even finer regulation of electrochemical tuning of molecular transport.

Previous studies examining gated protein transport using an external potential applied to Au-coated

pores in the absence of electroactive moieties suggested that transport through NPG coated terminated with ferrocene might have contributions from both the fixed positive charges and the simple presence of the applied electric field.[34,36,40,41] To parse these effects, we deposited a non-electroactive hydroxyl-terminated thiol on the NPG. Figure 4.5(ii) shows the MV^{2+} and BS^- flux through OH-coated NPG at the same potentials used to oxidize and reduce the ferrocene groups in Figure 4.5(i). Both analytes demonstrated the expected migration towards the oppositely charged reservoirs. While the application of a gating potential did appear to have an effect on the MV^{2+} and BS^- flux, it was not nearly as substantial as on the ferrocene-coated NPG. It is therefore clear that the incorporation of an electroactive moiety provided a greater transport enhancement and further efforts will focus on using an alternative electroactive surface functionality, rather than depending on non-faradaic charging alone. Viologen derivatives, for example, could be used to gate transport as they have been tethered to Au surfaces in prior studies and exhibit reversible oxidation and reduction in aqueous solutions.[42]

4.3 Conclusions

We have firstly demonstrated NPG as a promising membrane material for dynamically tunable molecular separations. Analyte flux through NPG can be controlled not only via an applied transverse electric field, but also by changes to the NPG surface charge, which we tuned via three different mechanisms. Bare NPG membranes were cation permselective due to the spontaneous chloride adsorption to Au surfaces. Depending on the ionic strength of the solution, the electrical double layer can extend far into the pore volume and impart significant electroosmotic contributions to transport flux. Formation of a self-assembled monolayers on the NPG surface prevented significant chloride adsorption and allowed for finer adjustments to the NPG surface charge through either solution pH or applied electrochemical potentials, providing motivation for investigating additional redox active monolayer constructs. Future efforts will be directed towards continuing to develop NPG as a tunable membrane for chemical and biomolecular separations through the investigation of alternative gating strategies and modes of dynamic regulation of transport.

4.4 Experimental Details

Nitric acid, sulfuric acid, acetone, isopropyl alcohol, sodium benzenesulfonate, methyl viologen dichloride, sodium chloride, and sodium perchlorate were used without further purification. 200 proof ethanol was dried with 3 Å molecular sieves. Water was purified using an ELGA ultrapure water purification system to 18.2 MΩ cm and dispensed through a 0.22 μm filter cartridge. Preparation and surface area characterization

of the NPG monoliths was performed as described in sections 2.1 and 2.3, respectively.

4.4.1 Through-Pore Conductivity Determination

A NPG-on-Kapton sample was sandwiched between two custom polytetrafluoroethylene (PTFE, Teflon, Figure C.6) reservoirs with a 1 mm diameter access port to each face of the NPG. Ag wires were plated with AgCl followed a procedure described by Hassel and coworkers.[43] The Ag/AgCl wires were submerged in various concentrations of KCl ranging from 10 μM to 1 M KCl. Using a CH Instruments 760 Potentiostat in a two-electrode configuration (the CE was shorted to REF), the potential was cycled at 6 $mV\,s^{-1}$ between the two Ag/AgCl wires. The current was measured and the slope of current with respect to applied potential was calculated as the total of bulk and pore volume conductivities.

4.4.2 Self-Assembled Monolayer Formation

10 mM total thiol solutions were prepared in ethanol using 6-mercaptohexanoic acid (90%, Sigma-Aldrich, -COOH), 6-amino-1-hexanethiol hydrochloride (Sigma-Aldrich, $-NH_2$), 6-(ferrocenyl)hexanethiol (Sigma-Aldrich, -Fc), or 6-mercapto-1-hexanol (99%, Sigma-Aldrich, -OH). The NPG monoliths were rinsed three times with ultrapure water and three times with ethanol over the course of one day following electrochemical cleaning and surface area characterization to promote removal of water from the pores. The NPG samples were immersed in the thiol-containing solutions for at least 48 hours. They again were rinsed three times with ethanol to remove any excess thiols remaining inside the pores and then three times with water to wet the pores prior to transport experiments.

4.4.3 Molecular Transport Measurement

A custom polychlorotrifluoroethylene (PCTFE, Figure C.7) reservoir apparatus similar to the conductivity measurement setup was used for molecular transport, except that one reservoir (the sink) was fiber-optically coupled to a StellarNet SL3-LL deuterium lamp with collimating lens and StellarNet Black Comet UV-Visible spectrometer. Two spherical ball lenses (5.55 mm sapphire, Edmund Optics) were positioned directly across from each other on either side of the reservoir to collimate light between the two fiber optic cables (400 μm, 0.22 NA Thorlabs). Two Ag/AgCl electrodes (CH Instruments) were filled with 1 M NaCl and immersed in each reservoir. A Pine AFCBP1 potentiostat with custom LabVIEW software (See Appendix B) was used to apply a potential program to the electrodes ranging between ±2 V with potential steps every 30 minutes. The rates at which either 1 mM methyl viologen (MV^{2+}) or 10 mM benzenesulfonate (BS^-) transported through the bare NPG in 0.1 mM, 1 mM, 10 mM, 100 mM, and 1000 mM were measured

by monitoring the change in absorbance at 255 nm and 262 nm, respectively, as a result of the applied potential. Calibration curves were performed at the end of each NaCl concentration to calculate the flux in terms of concentration. For comparison, all flux is reported as relative to the passive diffusive flux, i.e. the flux at E_{NPG} = 0 V.

Flux through the pH-sensitive thiol coated pores was determined by first soaking the membrane in either the high pH (1 mM NaOH, pH = 10.8) or low pH (1 mM HCl, pH = 3.3) solution for at least 15 minutes. The reservoirs were then rinsed with ultrapure water and filled with 2 mM total ionic strength solutions of either 1 mM MV^{2+} or BS^- in the feed, 1 mM NaCl in the sink, and either NaOH or HCl in both the feed and sink.

Flux through 6-(ferrocenyl)hexanethiol- and 6-mercapto-1-hexanol-coated pores followed a similar setup as the pH-sensitive pores with the following exceptions: (1) $NaClO_4$ was used as the background electrolyte instead of NaCl, (2) no NaOH or HCl was added, so $NaClO_4$ was used to make up the difference of 2 mM ionic strength, and (3) the AFCBP1 was operated in bipotentiostatic mode with a Ag/AgCl REF and Pt wire CE in the feed, NPG as WE #1, and Ag/AgCl as WE #2 in sink. A potential of either 0 V or +0.7 V was applied to the NPG to maintain the ferrocene groups in either the reduced or oxidized state, respectively.

4.5 Data Normalization Procedure

Due to the intricate geometry of each NPG sample, flux through the pores is sample dependent. The nonlinear effect of altering pore size (electroosmotic contributions and the ratio of EDL to pore volume) complicates direct comparison. In order to accurately compare experimental results, the molecular flux measured for each run was averaged to obtain an average flux. The datasets were then normalized to one another (Figure 4.7a ⟶ b) according to:

$$j\prime = j\frac{j_{ref,mean}}{j_{mean}} \tag{4.1}$$

where $j\prime$ is the normalized flux at a value of ΔE, j is the non-normalized flux at a value of ΔE, $j_{ref,mean}$ is the flux of the reference averaged dataset, and j_{mean} is the flux of the individual averaged dataset. This allows for each dataset to be normalized to arbitrary molecular flux values and subsequently averaged (Figure 4.7b ⟶ c), correcting for NPG samples with different baseline translocation rates. Division of the average values at $\Delta E \neq 0$ V by $\Delta E = 0$ V (Figure 4.7c ⟶ d) permits comparison of flux relative to the flux at $\Delta E = 0$ V, or in other words, the transport enhancement factor with applied potential relative to

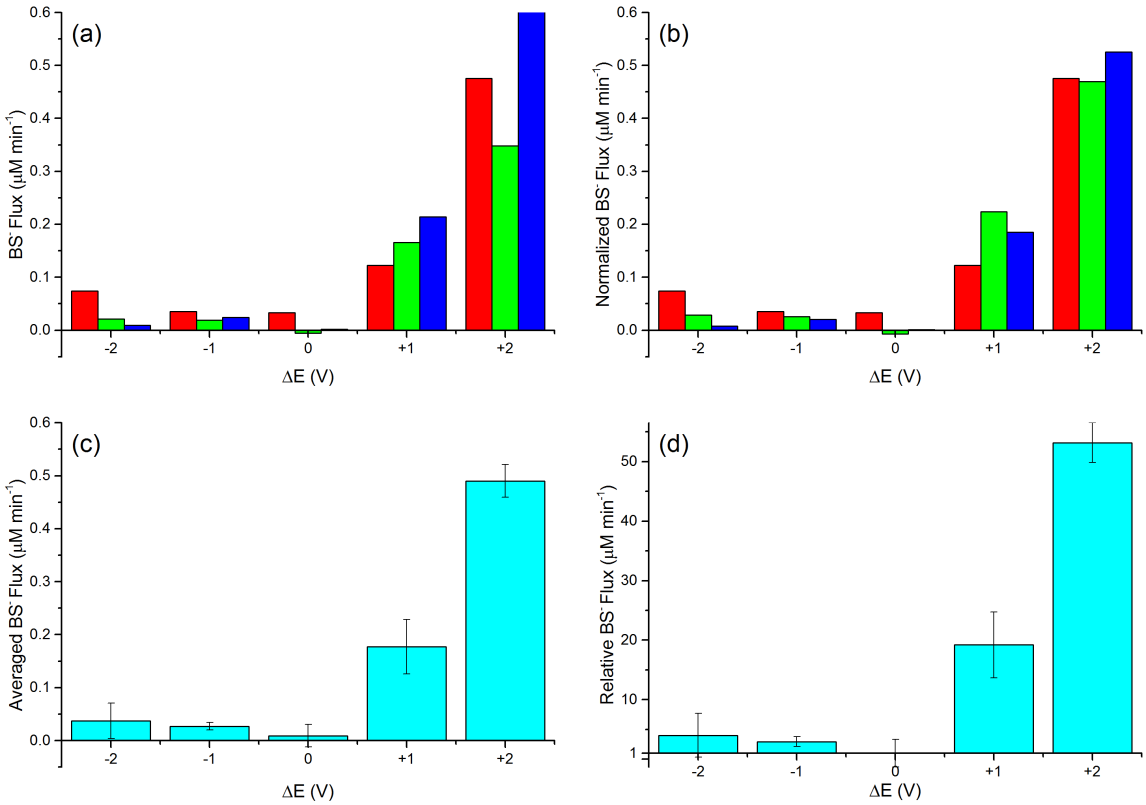

Figure 4.7: (a) BS^- flux through amine-thiol-functionalized NPG at acidic pH as measured from the real-time slope of absorbance vs. time from three runs. Qualitatively, all three runs demonstrate similar trends of increased translocation rate at more positive potentials. (b) Normalization of the molecular fluxes to the average flux of the first run (red). The second run (green) had a lower average flux than the first run and was therefore normalized to have the same average flux. Similarly, the average flux of the third run was normalized. (c) Average normalized flux from all three runs. (d) Flux relative to the flux at $\Delta E = 0$ V. Note that the x-intercept has changed from 0 to 1.

passive diffusion.

4.6 References

1. McCurry, D. A.; Bailey, R. C. Nanoporous Gold Membranes as Robust Constructs for Selectively Tunable Chemical Transport. *Journal of Physical Chemistry* **2016**, DOI: 10.1021/acs.jpcc.6b02759.

2. Hyun, C.; Kaur, H.; Rollings, R.; Xiao, M.; Li, J. Threading Immobilized DNA Molecules through a Solid-State Nanopore at >100 μs per Base Rate. *ACS Nano* **2013**, *7*, 5892–5900, DOI: 10.1021/nn4012434.

3. Koenig, S. P.; Wang, L.; Pellegrino, J.; Bunch, J. S. Selective molecular sieving through porous graphene. *Nature Nanotechnology* **2012**, *7*, 728–732, DOI: 10.1038/nnano.2012.162.

4. Wanunu, M. Nanopores: A journey towards DNA sequencing. *Physics of Life Reviews* **2012**, *9*, 125–158, DOI: 10.1016/j.plrev.2012.05.010.

5. Wanunu, M.; Morrison, W.; Rabin, Y.; Grosberg, A. Y.; Meller, A. Electrostatic focusing of unlabelled DNA into nanoscale pores using a salt gradient. *Nature Nanotechnology* **2010**, *5*, 160–165, DOI: 10.1038/nnano.2009.379.

6. Wanunu, M.; Bhattacharya, S.; Xie, Y.; Tor, Y.; Aksimentiev, A.; Drndic, M. Nanopore Analysis of Individual RNA/Antibiotic Complexes. *ACS Nano* **2011**, *5*, 9345–9353, DOI: 10.1021/nn203764j.

7. Li, W.; Bell, N. A. W.; Hernández-Ainsa, S.; Thacker, V. V.; Thackray, A. M.; Bujdoso, R.; Keyser, U. F. Single Protein Molecule Detection by Glass Nanopores. *ACS Nano* **2013**, *7*, 4129–4134, DOI: 10.1021/nn4004567.

8. Lan, W.-J.; Holden, D. A.; Zhang, B.; White, H. S. Nanoparticle Transport in Conical-Shaped Nanopores. *Analytical Chemistry* **2011**, *83*, 3840–3847, DOI: 10.1021/ac200312n.

9. Howorka, S.; Siwy, Z. Nanopore analytics: sensing of single molecules. *Chem. Soc. Rev.* **2009**, *38*, 2360–2384, DOI: 10.1039/B813796J.

10. Armstrong, J. A.; Bernal, E. E. L.; Yaroshchuk, A.; Bruening, M. L. Separation of Ions Using Polyelectrolyte-Modified Nanoporous Track-Etched Membranes. *Langmuir* **2013**, *29*, 10287–10296, DOI: 10.1021/la401934v.

11. Yu, S.; Lee, S. B.; Kang, M.; Martin, C. R. Size-Based Protein Separations in Poly(ethylene glycol)-Derivatized Gold Nanotubule Membranes. *Nano Lett.* **2001**, *1*, 495–498, DOI: 10.1021/nl0100441.

12. Striemer, C. C.; Gaborski, T. R.; McGrath, J. L.; Fauchet, P. M. Charge- and size-based separation of macromolecules using ultrathin silicon membranes. *Nature* **2007**, *445*, 749–753, DOI: 10.1038/nature05532.

13. Plett, T.; Shi, W.; Zeng, Y.; Mann, W.; Vlassiouk, I.; Baker, L. A.; Siwy, Z. S. Rectification of nanopores in aprotic solvents – transport properties of nanopores with surface dipoles. *Nanoscale* **2015**, *7*, 19080–19091, DOI: 10.1039/c5nr06340j.

14. Shi, W.; Sa, N.; Thakar, R.; Baker, L. A. Nanopipette delivery: influence of surface charge. *Analyst* **2015**, *140*, 4835–4842, DOI: 10.1039/C4AN01073F.

15. Fujita, T.; Qian, L.-H.; Inoke, K.; Erlebacher, J.; Chen, M.-W. Three-dimensional morphology of nanoporous gold. *Applied Physics Letters* **2008**, *92*, 251902, DOI: 10.1063/1.2948902.

16. Seker, E.; Reed, M. L.; Begley, M. R. Nanoporous Gold: Fabrication, Characterization, and Applications. *Materials* **2009**, *2*, 2188–2215, DOI: 10.3390/ma2042188.

17. McCurry, D. A.; Kamundi, M.; Fayette, M.; Wafula, F.; Dimitrov, N. All Electrochemical Fabrication of a Platinized Nanoporous Au Thin-Film Catalyst. *ACS Appl. Mater. Interfaces* **2011**, *3*, 4459–4468, DOI: 10.1021/am2011433.

18. Ding, Y.; Kim, Y.-J.; Erlebacher, J. Nanoporous Gold Leaf: "Ancient Technology"/Advanced Material. *Advanced Materials* **2004**, *16*, 1897–1900, DOI: 10.1002/adma.200400792.

19. Biener, J.; Biener, M. M.; Madix, R. J.; Friend, C. M. Nanoporous Gold: Understanding the Origin of the Reactivity of a 21st Century Catalyst Made by Pre-Columbian Technology. *ACS Catalysis* **2015**, *5*, 6263–6270, DOI: 10.1021/acscatal.5b01586.

20. Gittard, S. D.; Pierson, B. E.; Ha, C. M.; Wu, C.-A. M.; Narayan, R. J.; Robinson, D. B. Supercapacitive transport of pharmacologic agents using nanoporous gold electrodes. *Biotechnology Journal* **2010**, *5*, 192–200, DOI: 10.1002/biot.200900250.

21. Zhao, H.; Wang, C.; Vellacheri, R.; Zhou, M.; Xu, Y.; Fu, Q.; Wu, M.; Grote, F.; Lei, Y. Self-Supported Metallic Nanopore Arrays with Highly Oriented Nanoporous Structures as Ideally Nanostructured Electrodes for Supercapacitor Applications. *Adv. Mater.* **2014**, *26*, 7654–7659, DOI: 10.1002/adma.201402766.

22. Stine, K. J.; Jefferson, K.; Shulga, O. V., Nanoporous Gold for Enzyme Immobilization. In *Enzyme Stabilization and Immobilization: Methods and Protocols*, Minteer, S. D., Ed.; Methods in Molecular Biology; Humana Press: Totowa, NJ, 2011; Chapter Nanoporous Gold for Enzyme Immobilization, pp 67–83, DOI: 10.1007/978-1-60761-895-9_7.

23. Tan, Y. H.; Fujikawa, K.; Pornsuriyasak, P.; Alla, A. J.; Ganesh, N. V.; Demchenko, A. V.; Stine, K. J. Lectin–carbohydrate interactions on nanoporous gold monoliths. *New Journal of Chemistry* **2013**, *37*, 2150–2165, DOI: 10.1039/c3nj00253e.

24. Xue, Y.; Markmann, J.; Duan, H.; Weissmüller, J.; Huber, P. Switchable imbibition in nanoporous gold. *Nature Communications* **2014**, *5*, 4237, DOI: 10.1038/ncomms5237.

25. Bard, A. J.; Faulkner, L. R., *Electrochemical Methods: Fundamentals and Applications*; John Wiley & Sons, Inc.: New York, 2001; Vol. 2.

26. Trefalt, G.; Behrens, S. H.; Borkovec, M. Charge Regulation in the Electrical Double Layer: Ion Adsorption and Surface Interactions. *Langmuir* **2016**, *32*, 380–400, DOI: 10.1021/acs.langmuir.5b03611.

27. Smeets, R. M. M.; Keyser, U. F.; Krapf, D.; Wu, M.-Y.; Dekker, N. H.; Dekker, C. Salt Dependence of Ion Transport and DNA Translocation through Solid-State Nanopores. *Nano Letters* **2006**, *6*, 89–95, DOI: 10.1021/nl052107w.

28. Kovarik, M. L.; Zhou, K.; Jacobson, S. C. Effect of Conical Nanopore Diameter on Ion Current Rectification. *J. Phys. Chem. B* **2009**, *113*, 15960–15966, DOI: 10.1021/jp9076189.

29. Haywood, D. G.; Harms, Z. D.; Jacobson, S. C. Electroosmotic Flow in Nanofluidic Channels. *Analytical Chemistry* **2014**, *86*, 11174–11180, DOI: 10.1021/ac502596m.

30. Stein, D.; Kruithof, M.; Dekker, C. Surface-Charge-Governed Ion Transport in Nanofluidic Channels. *Phys. Rev. Lett.* **2004**, *93*, DOI: 10.1103/physrevlett.93.035901.

31. Baldessari, F. Electrokinetics in nanochannels. *Journal of Colloid and Interface Science* **2008**, *325*, 539–546, DOI: 10.1016/j.jcis.2008.06.008.

32. Makra, I.; Jágerszki, G.; Bitter, I.; Gyurcsányi, R. E. Nernst–Planck/Poisson model for the potential response of permselective gold nanopores. *Electrochimica Acta* **2012**, *73*, 70–77, DOI: 10.1016/j.electacta.2012.02.074.

33. Haywood, D. G.; Saha-Shah, A.; Baker, L. A.; Jacobson, S. C. Fundamental Studies of Nanofluidics: Nanopores, Nanochannels, and Nanopipets. *Analytical Chemistry* **2015**, *87*, 172–187, DOI: 10.1021/ac504180h.

34. Chun, K.-Y.; Mafé, S.; Ramírez, P.; Stroeve, P. Protein transport through gold-coated, charged nanopores: Effects of applied voltage. *Chemical Physics Letters* **2006**, *418*, 561–564, DOI: 10.1016/j.cplett.2005.11.029.

35. Hou, Z.; Abbott, N. L.; Stroeve, P. Self-Assembled Monolayers on Electroless Gold Impart pH-Responsive Transport of Ions in Porous Membranes. *Langmuir* **2000**, *16*, 2401–2404, DOI: 10.1021/la991045k.

36. Chun, K.-Y.; Stroeve, P. External Control of Ion Transport in Nanoporous Membranes with Surfaces Modified with Self-Assembled Monolayers. *Langmuir* **2001**, *17*, 5271–5275, DOI: 10.1021/la010066n.

37. Gagne, R. R.; Koval, C. A.; Lisensky, G. C. Ferrocene as an internal standard for electrochemical measurements. *Inorganic Chemistry* **1980**, *19*, 2854–2855, DOI: 10.1021/ic50211a080.

38. Breuer, R.; Schmittel, M. Redox-Stable SAMs in Water (pH 0–12) from 1,1′-Biferrocenylene-Terminated Thiols on Gold. *Organometallics* **2012**, *31*, 6642–6651, DOI: 10.1021/om300718k.

39. Buyukserin, F.; Kohli, P.; Wirtz, M. O.; Martin, C. R. Electroactive Nanotube Membranes and Redox-Gating. *Small* **2007**, *3*, 266–270, DOI: 10.1002/smll.200600477.

40. Nishizawa, M.; Menon, V. P.; Martin, C. R. Metal Nanotubule Membranes with Electrochemically Switchable Ion-Transport Selectivity. *Science* **1995**, *268*, 700–702, DOI: 10.1126/science.268.5211.700.

41. Kalman, E. B.; Sudre, O.; Vlassiouk, I.; Siwy, Z. S. Control of ionic transport through gated single conical nanopores. *Analytical and Bioanalytical Chemistry* **2008**, *394*, 413–419, DOI: 10.1007/s00216-008-2545-3.

42. Han, B.; Li, Z.; Wandlowski, T.; Błaszczyk, A.; Mayor, M. Potential-Induced Redox Switching in Viologen Self-Assembled Monolayers: An ATR-SEIRAS Approach. *J. Phys. Chem. C* **2007**, *111*, 13855–13863, DOI: 10.1021/jp073208g.

43. Hassel, A. W.; Fushimi, K.; Seo, M. An agar-based silver|silver chloride reference electrode for use in micro-electrochemistry. *Electrochemistry Communications* **1999**, *1*, 180–183, DOI: 10.1016/s1388-2481(99)00035-1.

Chapter 5

Electrolyte Gradient-Based Tuning of Molecular Transport

5.1 Introduction

Advanced fabrication methods (e.g. focused ion beam,[1] photolithography,[2] and clever template-based approaches[3]) have led to the facile fabrication of nanometer-scale structures, including synthetic nanopores. In general, nanopores having diameters from 1-100 nm show unique (bio)molecular transport properties on account of the similarities between pore diameter and molecular dimensions. As the ratio of pore diameter to analyte size decreases, steric and electrostatic surface interactions dominate molecular transport through the pore.[4,5] Pioneering early nanopore transport work focused on α-hemolysin, a biological nanopore which has been subsequently developed into an emerging sequencing technology based upon the analysis of DNA translocation and resistive pulse sensing.[6,7] Fueled by the advanced fabrication methods described above, synthetic membranes comprised of materials such as SiO_2,[8] SiN,[9] and graphene,[10] have also emerged as robust nanoporous constructs for (bio)molecular separations. In addition to increased structural integrity, these synthetic nanopores can be finely tuned to a specific pore size and chemically modified to impart selective gating of transport.[11–13] As a result, nanopores have expanded beyond applications in DNA sequencing to nanoparticle characterization,[14] desalination,[10] and molecular separations.[15,16]

Of particular relevance here are nanopores tailored towards molecular separations. Size-selective separations are made possible by controlling the diameter of the nanopores, whereas charge-selective separations can be performed after addition of charged moieties to the pore surface, such as pH-responsive self-assembled monolayers.[17] Ionic and molecular transport through discrete Au-coated nanopores on both the basis of size and charge has been studied extensively.[15,16,18–25] The electroless deposition of Au allows for easy tuning of the pore diameter and the well-studied chemisorption of thiols to Au make it an attractive membrane material. While the majority of recent separation nanopore studies have examined only single pores or arrays of pores, molecular throughput for practical separations may be limited as the effective pore area cross section is very small.

In the interest of further increasing membrane porosity and imparting external dynamic control to the

membrane, we investigated nanoporous gold (NPG) monoliths as molecular separation membranes. The intricate NPG geometry was examined in detail by Erlebacher and coworkers at the turn of the century and was found to be formed through a spinodal decomposition mechanism; the de-alloying process involves a continual dissolution of the less noble material with simultaneous re-arrangement of surface Au adatoms.[26] An important aspect of the de-alloying process is the introduction of a characteristic length scale, where the remaining Au ligaments are fairly homogeneous in size. The resulting geometry has had important applications in catalysis and fuel cells due to its extremely high surface area as well as its underlying crystal lattice properties.[27–30] Furthermore, this geometry lends itself to be a very capable enzyme- and protein-loading substrate, as studied extensively by Stine and coworkers.[31–33]

NPG shares the benefits of surface modification and inherent conductivity of the single Au-coated pores, but will increase throughput due to its higher porosity as well as enable higher-order molecular separations due to its extensive 3-dimensional pore network. NPG is also very simple to fabricate through either free corrosion or electrochemical de-alloying, greatly reducing the complexity required by electroless deposition. Recently, we have shown that gateable transport through NPG is possible when a transverse potential is applied on either side of the NPG membrane.[34]

Herein, NPG separated two reservoirs containing different ionic strength solutions. A UV-absorbing tracer, was added to only one reservoir and its translocation rate through the NPG was monitored using a fiber-optically coupled UV-Visible spectrometer. Similar to previous experiments containing Au-coated nanopores, we observed the formation of an electric potential difference between each reservoir.[22] This induced potential was dependent on the ionic strengths of each reservoir and was found to alter tracer translocation rate. Methyl viologen (MV^{2+}) and naphthalene disulfonic acid (NDS^{2-}) were used to study the effects of salt gradient magnitude on molecular transport through the negatively-charged NPG. Both tracers demonstrated diminished transport at very low ionic strengths due to a thick electrical double layer (EDL). The MV^{2+} and NDS^{2-} flux differed, however, in maximum flux as a result of the different transport mechanisms for cations vs. anions. To examine such differences in further detail, a monovalent anion, benzene sulfonate (BS^{-}) and an uncharged tracer, pyridine, were used to compare the effects of different background electrolytes. Notably, the differing electrolyte species had pronounced effects on overall flux through the NPG, indicating that transport is not solely due to diffusion along a concentration gradient, but also from an induced electric potential and ion advection.

5.2 Results and Discussion

5.2.1 Preparation and Characterization of NPG Monoliths

De-alloying via free corrosion was used to remove metals less noble than Au from the 10K alloy monoliths. Cu, Ni, and Zn are soluble in nitric acid and therefore spontaneously dissolve, leaving behind only Au.[32] The leaching process follows a spinodal decomposition mechanism whereby Au adatoms cluster into islands as the less noble metals dissolve. The result is a bicontinuous structure with ligaments and pores of equal size, dependent upon the initial Au concentration in the alloy.[26]

A reddish-brown color was imparted to the NPG upon immersion in concentrated nitric acid, which indicated the formation of nano-roughened surface features.[35] Inspection under an SEM allowed for visual confirmation of the expected bicontinuous, nanoporous geometry. There were no detectable traces of Cu, Ni, or Zn in the de-alloyed monolith as determined under EDX analysis (see Figure 2.3). Figure 2.1 shows the developed porosity of a typical NPG sample. Constrictions as low as 10 nm and upwards of 60 nm were present. The SEM images were imported to ImageJ for ISODATA (Iterative Self-Organizing Data Analysis Technique) thresholding prior to particle size analysis to obtain a distribution of 50 ± 20 nm.[34,36] The nanoporous geometry extends throughout the monolith, as evidenced by the cross section of the NPG provided in Figure 2.1c.

Large cracks several microns across are present on the NPG surface, as shown in Figure 2.1d. These appear to be uniformly distributed, travel in one dimension, and do not exhibit necking that could occur through flexing of the sample.[37] The cracks are therefore a result of stress corrosion cracking, a phenomenon commonly observed during the employed free corrosion de-alloying technique.[38–40] Cracks of this magnitude would be detrimental to the desired applications in separations, but cross section analysis using SEM provided no evidence of cracks extending throughout the entire NPG monolith and conductivity measurements vide infra support pore sizes well below the micrometer range.

Prior to use, all NPG samples were electrochemically cleaned in a 0.5 M H_2SO_4 solution.[41] The potential of the NPG was cycled to rapidly form and subsequently dissolve an oxide layer on the surface. After 250 cycles at $1\,V\,s^{-1}$, reproducible voltammograms were obtained, indicating a loss of atomic roughness and a more stable surface. Integration of the oxide stripping peak at +0.2 V vs. MSE provided the charge passed during reduction of the Au oxide layer and is related to surface area of the Au by a factor of $0.772\,mC\,cm^{-2}$.[42] Figure 2.15b shows a representative voltammogram for the surface area of bare NPG. The NPG voltammogram had very broad peaks due to the immense surface area. Surface areas in excess of $4.2 \pm 0.8\,m^2\,g^{-1}$ were obtained.

5.2.2 Verification of Conductive Pathway and EDL

While cyclic voltammetry allows for probing the electrochemically accessible surface area of the NPG and SEM analysis showed that the porosity extended across the entire monolith, it was necessary to ensure that there was a conductive pathway between both sides of the NPG for molecular transport. Since de-alloying occurred from all sides, it is possible that the pores did not join at the center of the monolith. To ensure that the pores extended across the entire NPG monolith and that solution could flow from one side to the other, conductivity measurements were performed with a KCl electrolyte. According to Ohm's law, ramping the potential between two non-polarizable electrodes in a conducting medium will produce a linear response with slope equal to the electrical conductance of the solution. As shown in Figure 3.2a, linear responses were obtained for a variety of KCl concentrations.

At sufficiently low ionic strength, Cl^- is excluded from the NPG pores and its mobility through the pores therefore becomes negligible. As a result, Equation 3.5 only considers μ_+ in the second term. The NPG monolith separating the two reservoirs was expected to exhibit the same effect as the single pores studied by Smeets et al, whereby a minimum in conductivity was obtained due to the exclusion of Cl^-.[43] As shown in Figure 3.2, the conductivity was linear with respect to KCl concentration above 1 mM. Below 1 mM KCl, however, the conductivity began to level off, eventually reaching a minimum below concentrations less than 100 µM. This is consistent with observations of the average pore diameter and the discussion of EDL thickness in Sections 2.1 and 3.1, respectively. At 100 µM KCl, the EDL was expected to extend 30 nm into the pore. For the NPG pores with average diameters < 60 nm, this translates to the entire pore volume being dominated by the surface charge of the Au. A minimum concentration of K^+ was required to neutralize the negative surface charge of the NPG. The calculated surface charge density ($-1.9 \pm 0.1\,\mathrm{mC\,m^{-2}}$, Equation 3.5) in addition to the immense surface area and tortuosity of NPG suggests that anion flux through NPG experiences significant inhibition.

An effect that was expected for NPG during the transverse potential cycling, but was not observed, was that of ion current rectification (ICR). Nanopores with asymmetrical geometry present high and low conductivity states dependent upon the polarity of the applied potential. For example, in a conical SiO_2 nanopore, a negative potential applied to the narrower side will produce a smaller current response compared to the same negative potential applied to the wide side.[5] This effect has been attributed to a potential barrier which favors the transport of cations over anions across the negatively charged pore. The lack of an ordered geometry on either side of the NPG suggested that ICR would be observed upon potential cycling. According to Figure 3.2a, a linear response was observed instead, which indicated that the nanoporous geometry was, on average, symmetrical across the length of the monolith. This presents a challenge in

using NPG for separations. Many nanopores, including the well-studied α-hemolysin pores, depend on a geometrical asymmetry to impart directional transport through the pore.[5,6,44] To work around this issue, modifications of the external environment of cylindrical pores have shown promise in introducing an asymmetrical aspect to an otherwise symmetrical system. For example, pH gradients across SiO_2 pores introduce nonlinear surface charge across the nanopore interior. While this did not impose a geometrical asymmetry, the electrostatic gradient was sufficient to introduce ICR.[45] Because the surface charge of NPG should not be affected by pH, an alternative method involved adding different concentrations of supporting electrolyte to impose a salt gradient across the NPG. Wanunu et al. have shown differences in the translocation rate of DNA through nanopores in the presence of a salt gradient.[46,47]

5.2.3 Charged Tracer Transport in the Presence of a Salt Gradient

Transport of anionic NDS^{2-} and cationic MV^{2+} was measured under varying salt gradient conditions in order to determine those that had the greatest contribution to molecular flux. Concentrations of the background electrolyte were independently altered through the orders of magnitude from 1 mM to 1000 mM. The tracer concentration was maintained at 1 mM in order to reduce effects of ionic strength contributions from the tracer. Figure 5.1 shows the flux magnitudes for MV^{2+} and NDS^{2-}. MV^{2+} demonstrated higher molecular flux when both reservoirs were held at a high ionic strength (1000 mM NaCl). Regardless of the salt gradient direction, higher ionic strength produced a higher flux magnitude. In the case of MV^{2+}, then, flux magnitude was dominated solely by the EDL thickness, with a thinner EDL permitting a greater flux area. Contrary to this result, NDS^{2-} demonstrated increased flux only when one reservoir was maintained at a higher ionic strength (Figure 5.1b). When both reservoirs were at a high ionic strength (1000 mM NaCl) the molecular flux was diminished, despite the expectation that flux would increase as was observed for MV^{2+}.

Provided the lack of an externally applied potential or pressure difference, an additional flux contribution must come from either the induced electric field, advection of the electrolyte, or a combination of both. As Figure 5.2a-b shows, the induced electric fields for both MV^{2+} and NDS^{2-} were very similar. As the concentration decreases, a minimum in potential difference is observed, most likely as a result of the conductivity dependence of the NPG as described by Equation 3.5. A fit of the measured potentials to Equation 3.12 is provided in Figure 5.2c-d for each of the tracers. As expected due to the similar measured potentials, an equivalent transference number of +0.18 was obtained; the NPG presents cation semipermselectivity from its negative surface charge.

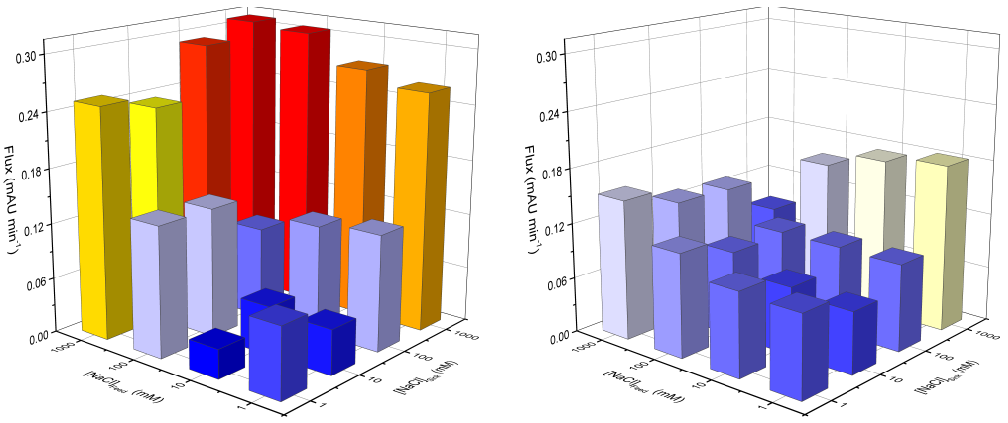

(a) (b)

Figure 5.1: (a) MV^{2+} and (b) NDS^{2-} transport through an NPG membrane under varying salt gradient conditions. The bottom left axis presents the ionic strength of the feed reservoir, whereas the bottom right axis presents that of the sink reservoir. Note that the oppositely charged ionic species responded differently to the salt gradients; MV^{2+} had the greatest flux magnitude when both reservoirs had a high concentration of NaCl, while NDS^{2-} had the greatest flux magnitude when only one reservoir was maintained at a higher concentration.

5.2.4 Charged Tracer Transport with Various Cation Species

As the salt gradient conditions for an anionic species provided the most pronounced differences where one reservoir was held at a higher concentration than the other, transport of BS^- through the NPG in the presence of a salt gradient, where one reservoir was maintained at 1 M background electrolyte, was monitored using UV-visible absorption spectroscopy. BS^- (pK_a=0.70)[48] has a negative charge at the neutral pH considered in this study and has a small hydrodynamic diameter which limits effects of steric hindrance during transport. Furthermore, the concentration of the tracer was increased from 1 mM to 100 mM in order to increase the concentration terms of Equation 3.6. In the absence of a salt gradient, BS^- was able to translocate across the NPG through passive diffusion. Although the negative surface charge on NPG from Cl^- adsorption should have inhibited BS^- transport, the EDL is too thin at the > 100 μM concentrations examined for the membrane to exhibit complete permselectivity (see Figure 3.2). In the presence of a salt gradient, the translocation rate was greater than that under no gradient conditions regardless of the direction of the salt gradient, although the [Feed] > [Sink] (1000 mM feed) was enhanced to an even greater extent, as shown in Figure 5.3. This was consistent with the results shown in Figure 5.1b.

The enhancement in tracer translocation for the [Feed] > [Sink] gradients in Figure 5.3 was intuitive as both tracer diffusion and electrolyte advection were in the same direction. A cooperative effect was therefore present whereby both tracer and salt were drawn into the nanopores. Likewise, when no salt gradient was present for [Feed] = [Sink] (no gradient), only the passive diffusional flux of the tracer was

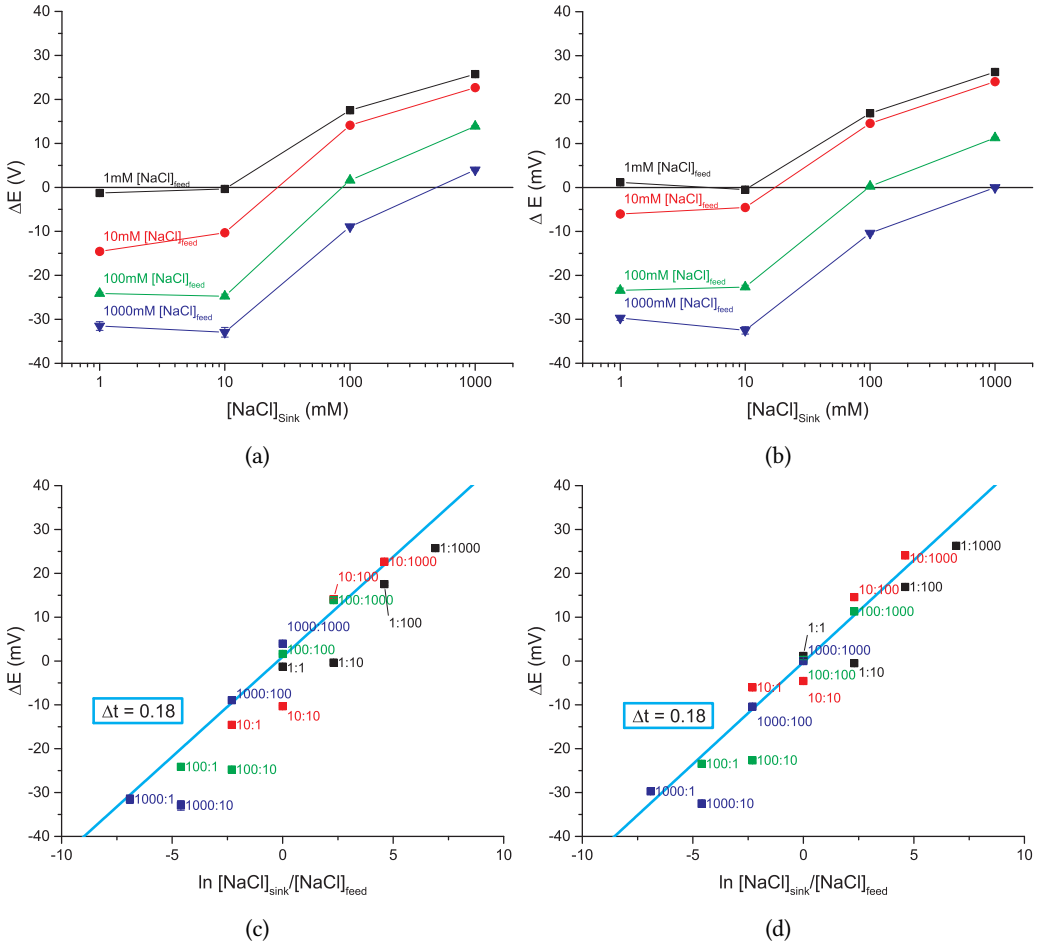

Figure 5.2: The measured potential difference between the two reservoirs under varying salt gradients for (a) MV^{2+} and (b) NDS^{2-}. The potential difference as it relates to the natural logarithm of the concentration ratio of sink to feed NaCl for (c) MV^{2+} and (d) NDS^{2-}.

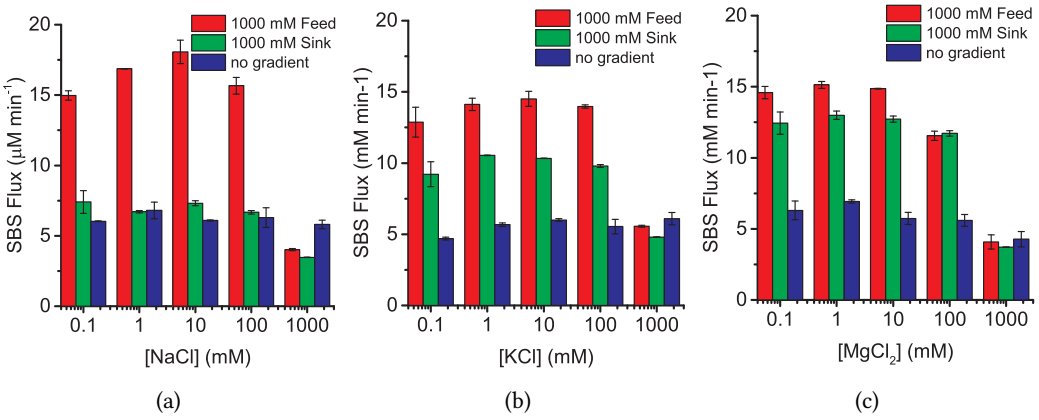

Figure 5.3: BS^- transport through NPG as measured by UV absorption in the sink reservoir over time in (a) NaCl, (b) KCl, and (c) $MgCl_2$.

present and no enhancement was observed. For [Feed] < [Sink] (1000 mM sink), however, BS^- translocation appeared to vary depending upon the cationic species present. No enhancement was observed compared to the purely diffusional no gradient condition with Na^+, whereas K^+ or Mg^{2+} seemed to respectively reduce or completely remove the effect of the opposing salt gradient for BS^- transport, as shown in Figures 5.3b-c. Explanations considering purely diffusional effects cannot account for the tunable behavior for the [Feed] < [Sink] gradients.

The potential difference across NPG was measured for each salt gradient, as shown in Figure 5.4. In order to fit the data to Equation 3.12, the data is plotted against $\ln {}^{[Sink]}/_{[Feed]}$. For [Feed] = [Sink], a very large potential difference was measured at the lower average ionic strengths as a result of the ionic contribution from BS^-. In order to correct for the error introduced from the BS^-, the total measured ΔE was assumed to be the sum of the BS^- and background electrolyte ΔE contributions. Without a background electrolyte gradient present, it was assumed that the measured ΔE was therefore solely due to the BS^-. A fit to ΔE_{BS^-} vs $\ln {}^{[Sink]}/_{[Feed]}$ (Figure 5.5) could then provide the relationship between ionic strength ratio and ΔE_{BS^-}, allowing for subsequent subtraction of the tracer contribution and a more accurate representation of the induced potential difference as a result of the salt gradient, $\Delta E_{gradient}$, as provided in Figure 5.6. The slope of Figure 5.6 was then used to obtain the Δt for each species, presented in Table 5.1. A positive value of Δt was obtained for all cation species, indicating preferential cation transport, as expected for a negatively charged membrane. The transference numbers appeared to be correlated to the diffusion coefficients of each cation, with a lower diffusion coefficient promoting a higher transference number, which suggests that cation advection has a strong influence on translocation through the NPG. Compared to the NaCl and KCl gradients, the $MgCl_2$ also differed in the divalent charge of Mg^{2+}. While there was an enhancement of transport in the presence of a salt gradient, it appeared to be directionally independent, as shown in Figure 5.3c. Multivalent, asymmetric salts require a much more rigorous analysis than the simple Poisson-Boltzmann approach that provided Equation 3.3.[49]

Table 5.1: Measured transport numbers, calculated from Figure 5.6, along with the diffusion coefficients for each cation. For reference, $D_{Cl^-} = 2.032 \times 10^{-5}$ cm^2 s^{-1}.

Cation	**D (10^{-5} cm^2 s^{-1})**	**Δt**
Na^+	1.344	0.263 ± 0.008
K^+	1.957	0.166 ± 0.005
½Mg^{2+}	0.706	0.33 ± 0.02

ΔE is negative (positive) when [Feed] > [Sink] ([Feed] < [Sink]), suggesting that the migration term in Equation 3.6 opposes (enhances) ionic flux towards the sink reservoir. As such, the migration term therefore does not dominate transport through NPG as the [Feed] > [Sink] demonstrates a much greater

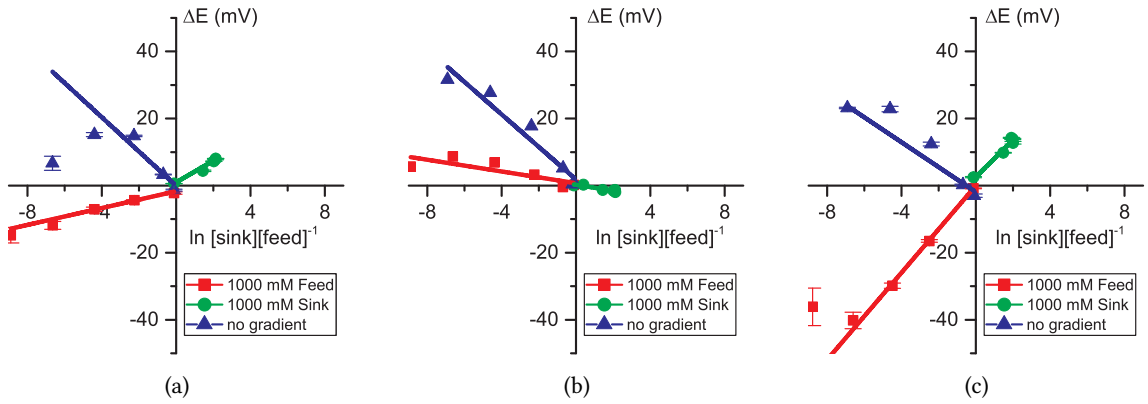

Figure 5.4: The raw potential difference across NPG as measured with [Feed] > [Sink] (red), [Feed] < [Sink] (green), and [Feed] = [Sink] (blue) gradient conditions for (a) NaCl, (b) KCl, and (c) $MgCl_2$.

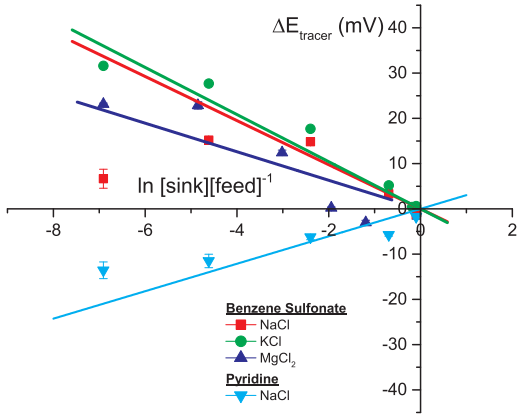

Figure 5.5: The benzene sulfonate contribution to the measured potential difference across NPG for NaCl (red), KCl (green), and $MgCl_2$ (blue). The pyridine contribution in NaCl is also provided (cyan).

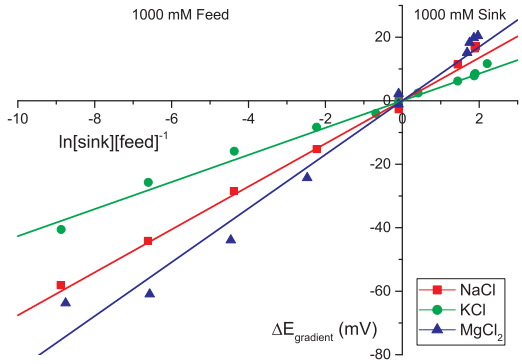

Figure 5.6: The corrected potential difference measured across NPG for BS^- in (a) NaCl, (b) KCl, and (c) $MgCl_2$.

BS^- flux through NPG compared to the [Feed] < [Sink]. Transport therefore most likely occurs as a result of diffusioosmosis, or the combined effect of the electroosmotic flow and subsequent advection from the chemiosmosis of background electrolyte.

Further evidence of the importance of the background electrolyte to flux through NPG was provided by Keh and Ma, who modeled transport across a charged surface and noted that the bulk fluid velocity was highly dependent not just on the induced transverse electric field parallel to the pore walls, but also the electric field normal to the surface.[50] The relation of surface potential ($\frac{Ze\zeta}{kT}$) to the ratio of anion/cation diffusivities, β, calculated as

$$\beta = \frac{D_+ - D_-}{D_+ + D_-} \tag{5.1}$$

where D_+ (D_-) is the diffusion coefficient of the cation (anion), can be used to determine the direction of diffusioosmotic velocity within the pores. In other words, the fluid did not always move in a single direction at every point within the pores and differences in surface charge or ionic diffusivities could be sufficient to reverse the bulk fluid flow. Table 5.2 lists the calculated β values for the salts considered in the present study. At higher magnitude β and low ζ potential, much like the case with NaCl or $MgCl_2$, fluid velocity is most likely in the direction of lower concentration (in this case, towards the sink reservoir) through the centers of the pores. KCl, on the other hand, has a much lower β and the bulk fluid flows towards the higher concentration (feed) reservoir. It is instances such as these that lead to slight differences in the flux magnitudes across the [Feed] < [Sink] BS^- translocation rates. While a full analytical solution to the flux rates is outside the scope of this paper, it is clear that the different cation species have a direct effect on translocation rate through the nanopores. An even greater effect may be realized if an external electric field was applied directly to the NPG or if the pores were smaller so that the EDL encompassed an even greater volume at the concentrations studied.

Table 5.2: β values as calculated from the diffusion coefficients. Note that $KClO_4$ and $Mg(ClO_4)_2$ were not used in the present study.

Ion ($\mathbf{D = 10^{-5}\ cm^2\ s^{-1}}$)	**Cl^-** **(2.032)**	**ClO_4^-** **(1.792)**
Na^+ **(1.344)**	-0.204	-0.143
K^+ **(1.957)**	-0.019	0.044
½Mg^{2+} **(0.706)**	-0.484	-0.435

5.2.5 Neutral Tracer Transport

Pyridine (pK_a=5.23)[48] is neutral at the neutral pH considered in this study and, similar to BS^-, has a small hydrodynamic diameter. In the absence of a salt gradient, pyridine was able to translocate across the NPG through passive diffusion similar to BS^-, but the overall rate appeared to be smaller, as shown in Figure

5.7a. As pyridine is slightly smaller than BS^- and did not experience the same magnitude of repulsion by the pore walls, it is possible that pyridine required a longer time to traverse the tortuous NPG geometry. In the presence of a salt gradient, pyridine transport was enhanced to the same extent regardless of the direction of the salt gradient. This further supports the additional convective term in Equation 3.6 to account for the enhancement as a result of diffusioosmosis. Both ionic flux and fluid velocity contribute to reach equilibrium in the salt concentrations across the NPG, but in doing so, there is a relaxation effect where flow in the opposite direction occurs.[50] Since the magnitude of flow from one reservoir to another must equal the reverse flow magnitude, transport of pyridine occurs at the same rate. When [Feed] > [Sink], the rate is possibly only slightly higher as the chemiosmotic contribution may be slightly stronger than the reverse fluid pressure.

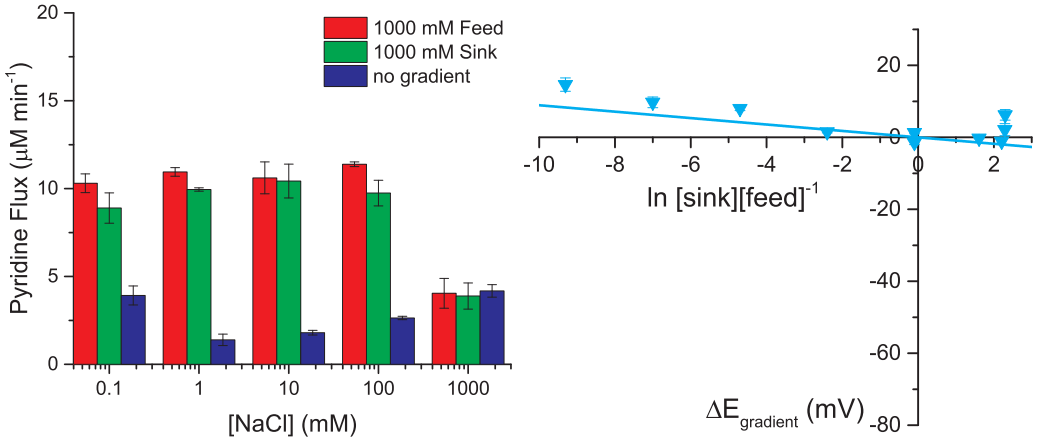

Figure 5.7: (a) Pyridine transport through NPG with NaCl background electrolyte as measured by UV absorption in sink reservoir over time. (b) Potential difference measured across NPG.

As shown in Figure 5.5, the presence of pyridine appeared to exhibit an opposite ΔE compared to the presence of BS^-. This may have been due to the small concentration of protonated pyridine at this pH. The transport number, calculated from the slope of Figure 5.7b, was -0.03 ± 0.01, which was much lower in magnitude than those calculated with BS^- as well as negative, suggesting a slightly anion semipermeable membrane. This was most likely an effect of pyridine adsorption to the NPG.[51] Regardless, introduction of a salt gradient across the NPG membrane promoted pyridine translocation, underscoring the utility of asymmetric electrolyte concentrations in the reservoirs.

5.2.6 Charged Tracer Transport with a Weakly Adsorbing Electrolyte

In order to separate the diffusioosmotic contribution to BS^- flux further, initial studies employing a weakly adsorbing anion rather than Cl^- were performed in an attempt to eliminate the NPG surface charge. Cl^-

anions strongly adsorb to Au, but ClO_4^- anions only weakly so. While the rate at which SBS translocated through the NPG was slightly decreased overall compared to the other electrolytes studied, there was still a sufficient difference between all gradient directions according to Figure 5.8a. This was not expected, but perhaps the weakly adsorbed ClO_4^-, as little as it may be, may be sufficient with such a large surface area as to induce diffusioosmosis. It was shown in Keh and Ma that even an extremely thin EDL or weakly charged membrane may exhibit diffusioosmotic flow.[50] Furthermore, the extremely high surface area and tortuous geometry may only serve to enhance even the smallest diffusioosmotic effects. Thus, future attempts to eliminate diffusioosmotic flow should incorporate a non-charged or hydrophobic surface. To meet such a goal, the use of F^- as a counterion was also explored (Figure 5.8b), but similar trends to ClO_4^- were observed possibly due to Cl^- contamination. This is apparent even in Figure 5.8c-d, where a slightly positive slope was observed in the ΔE vs $\ln {}^{[Sink]}/_{[Feed]}$ suggests a cation permselective membrane. Experiments without any tracer and only incorporating background electrolyte may be necessary to eliminate these issues. To a similar effect, experiments considering only the UV-Vis acquisition of BS^- transport without measuring potential may aid in reducing Cl^- contamination of the NPG.

5.3 Conclusions

NPG is easily fabricated through a free corrosion de-alloying technique to prepare free-standing membranes with average pore sizes of 50 ± 20 nm. At ionic strengths below 100 μM, the EDL is able to extend across the entire pore diameter, enabling control over transport through the NPG. The high surface pore density and extensive 3-dimensional pore network suggest that NPG is amenable towards molecular separations. It has been shown that a combination of diffusioosmosis and permselectivity of the EDL determine the rate at which molecules can translocate through NPG in the presence of a salt gradient. While the current analysis is quite qualitative in its approach, future work in applying transverse electric potentials as well as tuning the pore sizes of the NPG will aid in further elucidating the transport mechanisms that dominate molecular transport through NPG.

5.4 Experimental Details

5.4.1 Materials

Nitric acid, sulfuric acid, acetone, sodium benzenesulfonate (BS^-), methyl viologen (MV^{2+}), naphthalene disulfonic acid (NDS^{2-}), pyridine, potassium chloride, magnesium chloride, sodium chloride, sodium perchlorate, and sodium fluoride were purchased from Sigma-Aldrich and used without further purification.

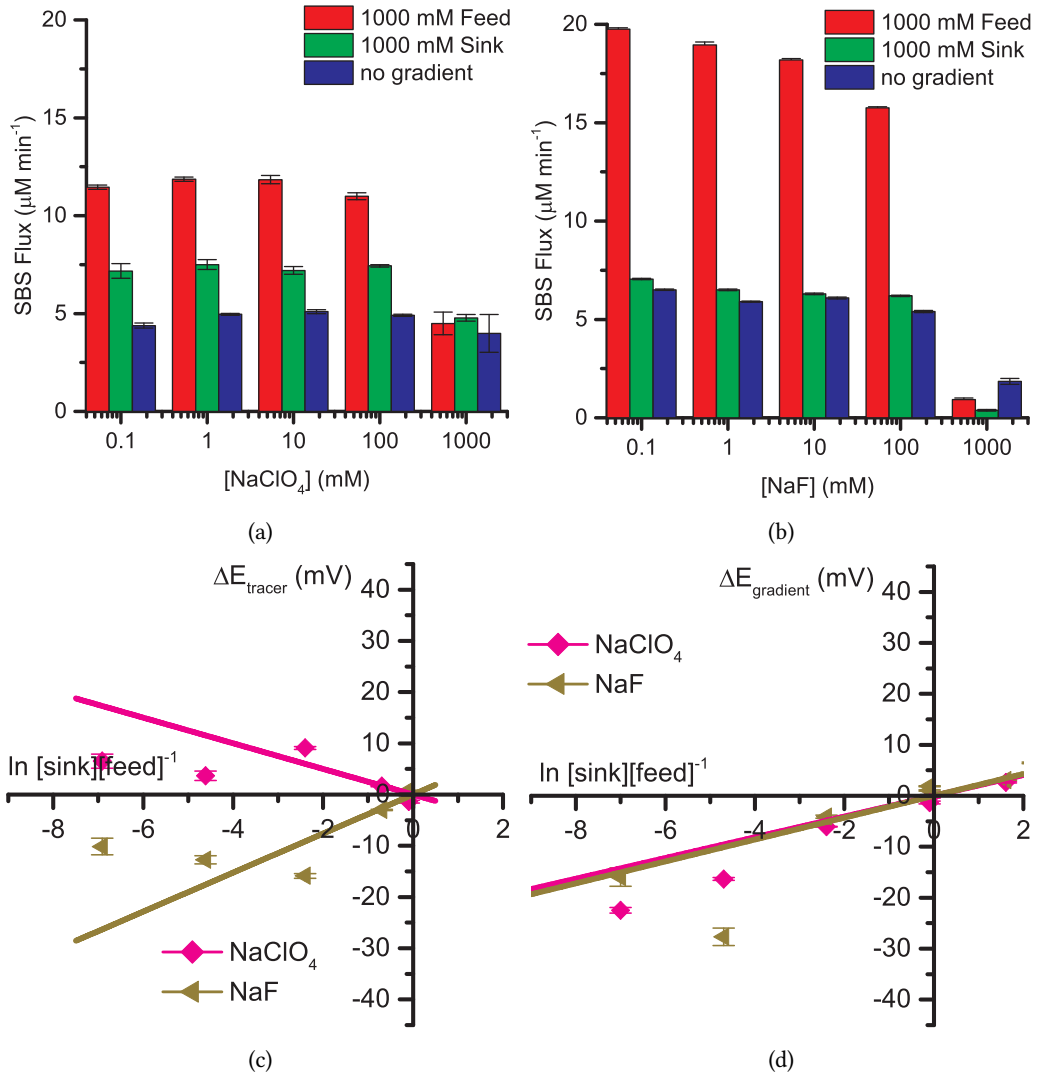

Figure 5.8: BS^- transport through NPG with (a) $NaClO_4$ and (b) NaF background electrolyte as measured by UV absorption in sink reservoir over time. (c) Potential difference measured across NPG with [Feed] = [Sink]. (d) Corrected potential difference across NPG as measured under the [Feed] > [Sink] and [Sink] > [Feed] gradient conditions.

250 μm thick 10 karat white Au alloy (Au, Cu, Ni, Zn) was purchased from Hoover and Strong and cut into 0.2 in. x 0.2 in. squares with a wire saw. All water was purified with an ELGA ultrapure water purification system to 18.2 MΩ cm and dispensed through a 0.22 μm filter cartridge.

5.4.2 Preparation and Characterization of NPG

The diced Au alloy pieces were rinsed in acetone and sonicated in ultrapure water for 10 minutes prior to individually immersing each piece in concentrated nitric acid dealloying bath for 48 hours, with replacement of the nitric acid after 24 hours. The resulting NPG was rinsed three times with water and then stored

in water until use.

Electrical contacts were prepared by electron beam deposition of a 10 nm Ti adhesion layer followed by 300 nm Au onto a Kapton polyimmide film (Dupont). Prior to electron beam deposition, 0.125 in. holes were punched through each film to allow for access to both sides of the NPG. Lacquer was applied around the edges of the NPG and allowed to dry, affixing the monoliths to the contacts.

Electrochemical polishing and surface area measurements were performed using cyclic voltammetry in 0.5 M sulfuric acid with a Pine AFCBP1 potentiostat. All potentials are versus a mercury-mercury sulfate (MSE) reference electrode. A Pt wire counter electrode was cleaned in 1:1 HNO_3:H_2O (%) heated to 50 °C and flame-annealed. Electrochemical polishing occurred between -0.6 and +1.1 V at a rate of $1\,V\,s^{-1}$ until a reproducible voltammogram was obtained. A slower scan cyclic voltammogram at $5\,mV\,s^{-1}$ was then performed to obtain an upper limit for oxidation (i.e., where the last surface oxide formation peak ended, generally +1 V). The surface area was then characterized by holding the potential at the upper limit until the measured current decayed to 0 A followed by subsequent stripping of the formed oxide by holding the potential at +0.2 V. Integration of the current passed during reduction provided the charge which was then converted to surface area using the ratio of $0.772\,mC\,cm^{-2}$.[42]

Scanning electron micrographs were taken with a Hitachi S-4700 SEM with an accelerating voltage of 30 kV in ultra-high resolution mode and a working distance of 6 mm.

5.4.3 UV-Visible Measurements

The NPG sealed on Kapton contact was sandwiched in a custom PTFE reservoir assembly that was fiber-optically coupled to a StellarNet (Tampa, Florida) deuterium lamp and either an EPP-2000 or a Black Comet spectrometer for UV-visible analysis with 400 µm solarization-resistant fiber optic patch cables (Thorlabs). Light was collimated through 5.55 mm sapphire ball lenses (Edmund Optics). Each reservoir contained 1 mL of solution during measurements to avoid pressure-driven flow through the NPG. Salt solutions on the feed side of the NPG membrane additionally contained 1 mM of either MV^{2+} or NDS^{2-}. For the detailed electrolyte species studies, 100 mM of either BS^- or pyridine was used as the tracer instead of MV^{2+} or NDS^{2-}. A higher concentration was used because the molar extinction coefficient is significantly lower for these species, and a higher concentration provides an increased flux. The tracers were monitored as they passively diffused into the sink reservoir by monitoring their UV absorbance for a maximum of 30 minutes. Data collected during the first 5 minutes were not included in transport rate calculations to allow for the tracer concentration within the NPG to equilibrate. The reservoirs were stirred with magnetic stir bars for the duration of the measurements to ensure good mixing and prevent possible ion concentration

polarization at the NPG faces.

MV^{2+} and NDS^{2-} measurements were performed by keeping the feed reservoir at a constant concentration and replacing the solution in the sink reservoir with the next higher concentration every 30 minutes. For measurements with either BS^- or pyridine, one reservoir was maintained at 1000 mM salt, while the other reservoir concentration was varied between 100 µM and 1000 mM salt. Hereafter, the gradients containing BS^- or pyridine are annotated as [Feed] > [Sink] or [Feed] < [Sink] if a concentration of 1000 mM electrolyte is maintained in the feed or sink reservoir, respectively. Additional BS^- and pyridine measurements where both reservoirs contained the same concentration of background electrolyte were also performed and are annotated as [Feed] = [Sink].

One Ag/AgCl reference electrode (1 M KCl, CH Instruments) was immersed in each reservoir for the duration of the UV-vis analysis. The potential between these electrodes was measured using a Kiethley 2100 multimeter (input resistance > 10 GΩ) every minute to observe the change in potential between the reservoirs and ensure that conductivity was maintained throughout the experiment.

5.5 References

1. Haywood, D. G.; Saha-Shah, A.; Baker, L. A.; Jacobson, S. C. Fundamental Studies of Nanofluidics: Nanopores, Nanochannels, and Nanopipets. *Analytical Chemistry* **2015**, *87*, 172–187, DOI: 10.1021/ac504180h.

2. Hyun, C.; Kaur, H.; Rollings, R.; Xiao, M.; Li, J. Threading Immobilized DNA Molecules through a Solid-State Nanopore at >100 µs per Base Rate. *ACS Nano* **2013**, *7*, 5892–5900, DOI: 10.1021/nn4012434.

3. Sun, S.; Wu, P. Easy Fabrication of Macroporous Gold Films Using Graphene Sheets as a Template. *ACS Applied Materials & Interfaces* **2013**, DOI: 10.1021/am400703v.

4. Buchsbaum, S. F.; Mitchell, N.; Martin, H.; Wiggin, M.; Marziali, A.; Coveney, P. V.; Siwy, Z.; Howorka, S. Disentangling Steric and Electrostatic Factors in Nanoscale Transport Through Confined Space. *Nano Letters* **2013**, *13*, 3890–3896, DOI: 10.1021/nl401968r.

5. Kovarik, M. L.; Zhou, K.; Jacobson, S. C. Effect of Conical Nanopore Diameter on Ion Current Rectification. *J. Phys. Chem. B* **2009**, *113*, 15960–15966, DOI: 10.1021/jp9076189.

6. Wanunu, M. Nanopores: A journey towards DNA sequencing. *Physics of Life Reviews* **2012**, *9*, 125–158, DOI: 10.1016/j.plrev.2012.05.010.

7. Kawano, R.; Schibel, A. E. P.; Cauley, C.; White, H. S. Controlling the Translocation of Single-Stranded DNA through α-Hemolysin Ion Channels Using Viscosity. *Langmuir* **2008**, *25*, 1233–1237, DOI: 10.1021/la803556p.

8. Li, W.; Bell, N. A. W.; Hernández-Ainsa, S.; Thacker, V. V.; Thackray, A. M.; Bujdoso, R.; Keyser, U. F. Single Protein Molecule Detection by Glass Nanopores. *ACS Nano* **2013**, *7*, 4129–4134, DOI: 10.1021/nn4004567.

9. Heng, J. B.; Aksimentiev, A.; Ho, C.; Marks, P.; Grinkova, Y. V.; Sligar, S.; Schulten, K.; Timp, G. The Electromechanics of DNA in a Synthetic Nanopore. *Biophysical Journal* **2006**, *90*, 1098–1106, DOI: 10.1529/biophysj.105.070672.

10. He, Z.; Zhou, J.; Lu, X.; Corry, B. Bioinspired Graphene Nanopores with Voltage-Tunable Ion Selectivity for Na+ and K+. *ACS Nano* **2013**, DOI: 10.1021/nn4043628.

11. Chun, K.-Y.; Stroeve, P. External Control of Ion Transport in Nanoporous Membranes with Surfaces Modified with Self-Assembled Monolayers. *Langmuir* **2001**, *17*, 5271–5275, DOI: 10.1021/la010066n.

12. Armstrong, J. A.; Bernal, E. E. L.; Yaroshchuk, A.; Bruening, M. L. Separation of Ions Using Polyelectrolyte-Modified Nanoporous Track-Etched Membranes. *Langmuir* **2013**, *29*, 10287–10296, DOI: 10.1021/la401934v.

13. Kaya, D.; Dinler, A.; San, N.; Kececi, K. Effect of Pore Geometry on Resistive-Pulse Sensing of DNA Using Track-Etched PET Nanopore Membrane. *Electrochimica Acta* **2016**, *202*, 157–165, DOI: 10.1016/j.electacta.2016.04.014.

14. Lan, W.-J.; Holden, D. A.; Zhang, B.; White, H. S. Nanoparticle Transport in Conical-Shaped Nanopores. *Analytical Chemistry* **2011**, *83*, 3840–3847, DOI: 10.1021/ac200312n.

15. Hulteen, J. C.; Jirage, K. B.; Martin, C. R. Introducing Chemical Transport Selectivity into Gold Nanotubule Membranes. *J. Am. Chem. Soc.* **1998**, *120*, 6603–6604, DOI: 10.1021/ja980045o.

16. Yu, S.; Lee, S. B.; Martin, C. R. Electrophoretic Protein Transport in Gold Nanotube Membranes. *Anal. Chem.* **2003**, *75*, 1239–1244, DOI: 10.1021/ac020711a.

17. Hou, Z.; Abbott, N. L.; Stroeve, P. Self-Assembled Monolayers on Electroless Gold Impart pH-Responsive Transport of Ions in Porous Membranes. *Langmuir* **2000**, *16*, 2401–2404, DOI: 10.1021/la991045k.

18. Martin, C. R.; Nishizawa, M.; Jirage, K.; Kang, M.; Lee, S. B. Controlling Ion-Transport Selectivity in Gold Nanotubule Membranes. *Advanced Materials* **2001**, *13*, 1351–1362, DOI: 10.1002/1521-4095(200109)13:18<1351::aid-adma1351>3.0.co;2-w.

19. Buyukserin, F.; Kohli, P.; Wirtz, M. O.; Martin, C. R. Electroactive Nanotube Membranes and Redox-Gating. *Small* **2007**, *3*, 266–270, DOI: 10.1002/smll.200600477.

20. Lee, S. B.; Martin, C. R. Electromodulated Molecular Transport in Gold-Nanotube Membranes. *Journal of the American Chemical Society* **2002**, *124*, 11850–11851, DOI: 10.1021/ja027494f.

21. Martin, C. R.; Nishizawa, M.; Jirage, K.; Kang, M. Investigations of the Transport Properties of Gold Nanotubule Membranes. *J. Phys. Chem. B* **2001**, *105*, 1925–1934, DOI: 10.1021/jp003486e.

22. Nishizawa, M.; Menon, V. P.; Martin, C. R. Metal Nanotubule Membranes with Electrochemically Switchable Ion-Transport Selectivity. *Science* **1995**, *268*, 700–702, DOI: 10.1126/science.268.5211.700.

23. Ramírez, P.; Mafé, S.; Alcaraz, A.; Cervera, J. Modeling of pH-Switchable Ion Transport and Selectivity in Nanopore Membranes with Fixed Charges. *The Journal of Physical Chemistry B* **2003**, *107*, 13178–13187, DOI: 10.1021/jp035778w.

24. Yu, S.; Lee, S. B.; Kang, M.; Martin, C. R. Size-Based Protein Separations in Poly(ethylene glycol)-Derivatized Gold Nanotubule Membranes. *Nano Lett.* **2001**, *1*, 495–498, DOI: 10.1021/nl0100441.

25. Amatore, C.; Oleinick, A. I.; Svir, I. Theory of Ion Transport in Electrochemically Switchable Nanoporous Metallized Membranes. *ChemPhysChem* **2009**, *10*, 211–221, DOI: 10.1002/cphc.200800481.

26. Erlebacher, J.; Aziz, M. J.; Karma, A.; Dimitrov, N.; Sieradzki, K. Evolution of nanoporosity in dealloying. *Nature* **2001**, *410*, 450–453, DOI: 10.1038/35068529.

27. Zhang, X.; Ding, Y. Unsupported nanoporous gold for heterogeneous catalysis. *Catalysis Science & Technology* **2013**, *3*, 2862–2868, DOI: 10.1039/c3cy00241a.

28. Wittstock, A.; Neumann, B.; Schaefer, A.; Dumbuya, K.; Kübel, C.; Biener, M. M.; Zielasek, V.; Steinrück, H.-P.; Gottfried, J. M.; Biener, J.; Hamza, A.; Bäumer, M. Nanoporous Au: An Unsupported Pure Gold Catalyst? *The Journal of Physical Chemistry C* **2009**, *113*, 5593–5600, DOI: 10.1021/jp808185v.

29. McCurry, D. A.; Kamundi, M.; Fayette, M.; Wafula, F.; Dimitrov, N. All Electrochemical Fabrication of a Platinized Nanoporous Au Thin-Film Catalyst. *ACS Appl. Mater. Interfaces* **2011**, *3*, 4459–4468, DOI: 10.1021/am2011433.

30. Zeis, R.; Mathur, A.; Fritz, G.; Lee, J.; Erlebacher, J. Platinum-plated nanoporous gold: An efficient, low Pt loading electrocatalyst for PEM fuel cells. *Journal of Power Sources* **2007**, *165*, 65–72, DOI: 10.1016/j.jpowsour.2006.12.007.

31. Pandey, B.; Demchenko, A.; Stine, K. Nanoporous gold as a solid support for protein immobilization and development of an electrochemical immunoassay for prostate specific antigen and carcinoembryonic antigen. *Microchimica Acta* **2012**, *179*, 71–81, DOI: 10.1007/s00604-012-0870-x.

32. Stine, K. J.; Jefferson, K.; Shulga, O. V., Nanoporous Gold for Enzyme Immobilization. In *Enzyme Stabilization and Immobilization: Methods and Protocols*, Minteer, S. D., Ed.; Methods in Molecular Biology; Humana Press: Totowa, NJ, 2011; Chapter Nanoporous Gold for Enzyme Immobilization, pp 67–83, DOI: 10.1007/978-1-60761-895-9_7.

33. Pandey, B.; Tan, Y. H.; Fujikawa, K.; Demchenko, A. V.; Stine, K. J. Comparative Study of the Binding of Concanavalin A to Self-Assembled Monolayers Containing a Thiolated α-Mannoside on Flat Gold and on Nanoporous Gold. *Journal of Carbohydrate Chemistry* **2012**, *31*, 466–503, DOI: 10.1080/07328303.2012.683909.

34. McCurry, D. A.; Bailey, R. C. Nanoporous Gold Membranes as Robust Constructs for Selectively Tunable Chemical Transport. *Journal of Physical Chemistry* **2016**, DOI: 10.1021/acs.jpcc.6b02759.

35. Tan, Y. H.; Davis, J. A.; Fujikawa, K.; Ganesh, N. V.; Demchenko, A. V.; Stine, K. J. Surface area and pore size characteristics of nanoporous gold subjected to thermal, mechanical, or surface modification studied using gas adsorption isotherms, cyclic voltammetry, thermogravimetric analysis, and scanning electron microscopy. *Journal of Materials Chemistry* **2012**, *22*, 6733–6745, DOI: 10.1039/c2jm16633j.

36. Seker, E.; Reed, M. L.; Begley, M. R. Nanoporous Gold: Fabrication, Characterization, and Applications. *Materials* **2009**, *2*, 2188–2215, DOI: 10.3390/ma2042188.

37. Briot, N. J.; Kennerknecht, T.; Eberl, C.; Balk, T. J. Mechanical properties of bulk single crystalline nanoporous gold investigated by millimetre-scale tension and compression testing. *Philosophical Magazine* **2014**, *94*, 847–866, DOI: 10.1080/14786435.2013.868944.

38. Battezzati, L.; Scaglione, F. De-alloying of rapidly solidified amorphous and crystalline alloys. *Journal of Alloys and Compounds* **2011**, *509, Supplement 1*, 8–12, DOI: 10.1016/j.jallcom.2010.12.209.

39. Scaglione, F.; Gebert, A.; Battezzati, L. Dealloying of an Au-based amorphous alloy. *Intermetallics* **2010**, *18*, 2338–2342, DOI: 10.1016/j.intermet.2010.08.005.

40. Lu, X.; Balk, T.; Spolenak, R.; Arzt, E. Dealloying of Au–Ag thin films with a composition gradient: Influence on morphology of nanoporous Au. *Thin Solid Films* **2007**, *515*, 7122–7126, DOI: 10.1016/j.tsf.2007.03.023.

41. Fischer, L. M.; Tenje, M.; Heiskanen, A. R.; Masuda, N.; Castillo, J.; Bentien, A.; Émneus, J.; Jakobsen, M. H.; Boisen, A. Gold cleaning methods for electrochemical detection applications. *Microelectronic Engineering* **2009**, *86*, 1282–1285, DOI: 10.1016/j.mee.2008.11.045.

42. Rouya, E.; Cattarin, S.; Reed, M. L.; Kelly, R. G.; Zangari, G. Electrochemical Characterization of the Surface Area of Nanoporous Gold Films. *Journal of the Electrochemical Society* **2012**, *159*, 97–102, DOI: 10.1149/2.097204jes.

43. Smeets, R. M. M.; Keyser, U. F.; Krapf, D.; Wu, M.-Y.; Dekker, N. H.; Dekker, C. Salt Dependence of Ion Transport and DNA Translocation through Solid-State Nanopores. *Nano Letters* **2006**, *6*, 89–95, DOI: 10.1021/nl052107w.

44. Dekker, C. Solid-state nanopores. *Nat Nano* **2007**, *2*, 209–215, DOI: 10.1038/nnano.2007.27.

45. Guo, W.; Tian, Y.; Jiang, L. Asymmetric Ion Transport through Ion-Channel-Mimetic Solid-State Nanopores. *Accounts of Chemical Research* **2013**, *46*, 2834–2846, DOI: 10.1021/ar400024p.

46. Wanunu, M.; Morrison, W.; Rabin, Y.; Grosberg, A. Y.; Meller, A. Electrostatic focusing of unlabelled DNA into nanoscale pores using a salt gradient. *Nature Nanotechnology* **2010**, *5*, 160–165, DOI: 10.1038/nnano.2009.379.

47. He, Y.; Tsutsui, M.; Scheicher, R.; Fan, C.; Taniguchi, M.; Kawai, T. Mechanism of How Salt-Gradient-Induced Charges Affect the Translocation of DNA Molecules through a Nanopore. *Biophysical journal* **2013**, *105*, 776–782, DOI: 10.1016/j.bpj.2013.05.065.

48. Dissociation Constants of Organic Acids and Bases. In, Haynes, W., Ed., 96th ed.; CRC Handbook of Chemistry and Physics; CRC Press: 2016; Chapter 5, pp 94–103.

49. Trefalt, G.; Behrens, S. H.; Borkovec, M. Charge Regulation in the Electrical Double Layer: Ion Adsorption and Surface Interactions. *Langmuir* **2016**, *32*, 380–400, DOI: 10.1021/acs.langmuir.5b03611.

50. Keh, H. J.; Ma, H. C. Diffusioosmosis of Electrolyte Solutions along a Charged Plane Wall. *Langmuir* **2005**, *21*, 5461–5467, DOI: 10.1021/la0504863.

51. Bilić, A.; Reimers, J. R.; Hush, N. S. Adsorption of Pyridine on the Gold(111) Surface: Implications for "Alligator Clips" for Molecular Wires. *The Journal of Physical Chemistry B* **2002**, *106*, 6740–6747, DOI: 10.1021/jp020590i.

Chapter 6

Towards Biomolecular Separations using Nanoporous Gold

6.1 Introduction

The analysis of biomolecules, including proteins and DNA, is rapidly moving towards lab-on-a-chip devices in an effort to minimize sample volume and sample loss while maintaining a low cost.[1,2] While some laboratories have focused on the analysis of biomolecules, including virus capsid sizing and DNA sequencing,[3–5] various other groups have explored methods of sample preconcentration and separations in microfluidic devices towards this goal.[2,6–9] One important application, currently receiving significant attention, is chromatin immunoprecipitation (ChIP), a technique used for determining specific DNA-protein binding interactions that regulate gene expression. Briefly, chromatin fragments bound to proteins are selectively precipitated by specific antibodies, purified, and finally analyzed using procedures such as polymerase chain reaction (PCR).[10] However, ChIP requires a large sample size, typically 10^6 to 10^7 cells, and introduces a number of steps that may lead to sample loss.[11,12] This prohibits the use of ChIP in applications where sample size is limited, such as for biopsies in a clinical setting, or where samples are highly heterogeneous, as is the case for many cancer tumors.[12,13]

Herein, nanoporous gold (NPG) was explored as a tunable separations device with the capability of being scaled down to a microfluidic device. NPG has been previously used for biomolecular capture and has shown promise in the field of drug delivery.[14–17] Modulation of an electric potential applied to nanoporous gold (NPG) membranes was used to direct a change in biomolecular transport through the pores with applications towards small volume separations. At length scales below 100 nm, interactions between solute and surfaces depend strongly on the electrical double layer. Charged surfaces introduce an exclusion region where only counterions may exist; co-ions are repelled by the similarly charged surface. The most commonly used method to alter the pore surface charge requires adjusting the pH of the solution, which

The efforts of John D. Orlet in obtaining some of the data presented in this chapter are gratefully acknowledged. Dr. Ivan L. Lenov is also acknowledged for his support in collecting the size exclusion chromatography data in the Sligar laboratory.

inhibits their use in biological applications.[18–21] By tuning the translocation through NPG electrochemically, however, this limitation is removed. For applications such as ChIP, this translates to the ability to selectively separate the desired fragments without the need for additional centrifugation and transfer steps that quite often increase the required sample size.

To that end, initial studies of potential-controlled gateable transport through NPG will be used to separate biomolecules. Proteins and fluorescently-labelled DNA of known size and charge will be used to characterize the system. Extension of this study to permit translocation of the larger DNA-protein complexes relevant to applications such as ChIP will also require tuning pore size during NPG fabrication. Additionally, a NPG-based separations membrane will be incorporated into a microfluidic device. This would provide a means of scaling ChIP down to a "lab-on-a-chip" setting, further decreasing the amount of sample required, and allowing for seamless integration with both upstream preparatory processes and downstream analysis.[22] The previously discussed fabrication techniques that require de-alloying of a large Au alloy monolith may not be amenable to translation to a smaller platform. Microfabrication of NPG with techniques such as electron beam deposition or co-sputtering Ag and Au alloys, will therefore be examined.[23]

6.2 Protein Transport through NPG

Three proteins, lysozyme (Lys), bovine hemoglobin (BHg), and bovine serum albumin (BSA) were selected for their different isoelectric points in order to study the effects of the NPG surface charge on protein translocation. $10\,\mathrm{mg\,mL^{-1}}$ protein was dissolved in various concentrations of either Tris/Borate/EDTA (TBE) buffer, phosphate buffer, or sodium chloride. In order to examine transport under low (pH=3) or high (pH=11) conditions, the pH was adjusted via dropwise addition of HCl or NaOH, respectively. The protein-containing solution was added to the feed reservoir and the corresponding protein-free solution was added to the sink reservoir. Transport of the protein was monitored in real time via the fiber-optically coupled StellarNet Black Comet UV-visible detector. Table 6.1 lists the pI and mass of each of the proteins studied.

Table 6.1: List of the proteins used for flux measurement along with pI and mass of each protein.

Protein	**pI**	**Mass (kDa)**
Lysozyme (Lys)	11.4	14.3
Bovine hemoglobin (BHg)	6.8	64.5
Bovine serum albumin (BSA)	4.7	66.4

Self-assembled monolayers (SAMs) were prepared on the NPG surface by immersing each sample in

thiol-containing solutions for at least 2 days. Proteins are often a significant source of biofouling in Au electrode-based sensing modalities and SAMs, especially those incorporating a polyethylene glycol (PEG) chain, have been shown to provide a biofouling-resistant surface coating.[24,25] The NPG samples were electrochemically polished in 0.5 M H_2SO_4 in order to remove any possible contaminants that may lead to poor monolayer formation.[26] The samples were rinsed well in ultrapure (18.2 MΩ cm) water prior to immersion in 200 proof ethanol. "The highly efficient" (t.h.e.) desiccant was added to the ethanol in order to ensure complete drying of the NPG samples, because the presence of water may cause the thiols to oxidize, leading to poor surface coverage. 10 mM *O*-(2-mercaptoethyl)-*O′*-methylhexa(ethylene glycol) (PEG), 6-mercaptohexanoic acid (-COOH), 6-mercapto-1-hexanol (-OH), or 1-hexanethiol (-CH_3) in 200 proof ethanol solutions were used to functionalize the NPG for at least 2 days. An excess of alkane-thiol was present to ensure sufficient surface coverage. During the functionalization, samples were kept in individual containers surrounded by desiccant and blanketed with dry ultra high purity Ar gas. After functionalization, the samples were rinsed well with 200 proof ethanol prior to rinsing with and immersion in ultrapure water to wet the NPG. In some cases, electrowetting of the NPG was required in order to draw water into the pores by applying a small (± 50 mV vs Ag/AgCl) potential to the NPG.[27]

As shown in Figure 6.1, protein flux through PEG-modified NPG was examined for each of the three proteins in both acidic (pH=3) and basic (pH=11) 100 mM phosphate buffer with multiple potentials applied. A transverse potential (ΔE, in orange) was applied between the reservoirs in order to drive the proteins across. In acidic conditions, all studied proteins should migrate towards the sink reservoir when $\Delta E = -1$ V as most are in the positively-charged state. Likewise, under basic conditions, the proteins should be negatively charged and migrate towards the sink reservoir when $\Delta E = -1$ V. An additional potential was applied directly to the NPG (E_{NPG}) in an attempt to gate translocation by imparting a different potential field within the NPG membrane, but this small potential window was likely too far above or below the potential of zero charge (pzc) of the NPG membrane to cause any significant changes. Figure 6.1 shows that appreciable flux was only observed for Lys; the BHg and BSA absorbance traces appeared flat for the duration of the runs. This was most likely due to the large size differences between the proteins (see Table 6.1). In fact, the use of NPG as a biofouling resistant electrode has been considered in the literature due to its ability to screen larger molecules from the pore interior.[28–30] Daggumati et al. has extensively examined the exclusion of biofouling proteins from the interior of NPG in an effort to perform electrochemical DNA assays in complex sample matrices. While quite successful, such results stand in stark contrast with the Stine group, which has focused on protein transport through NPG, rather than exclusion.[14,16,31] The NPG geometry is therefore a strong determining factor in protein permeability.

The effect of different SAMs on the NPG surface was also examined. As Lys provided the greatest

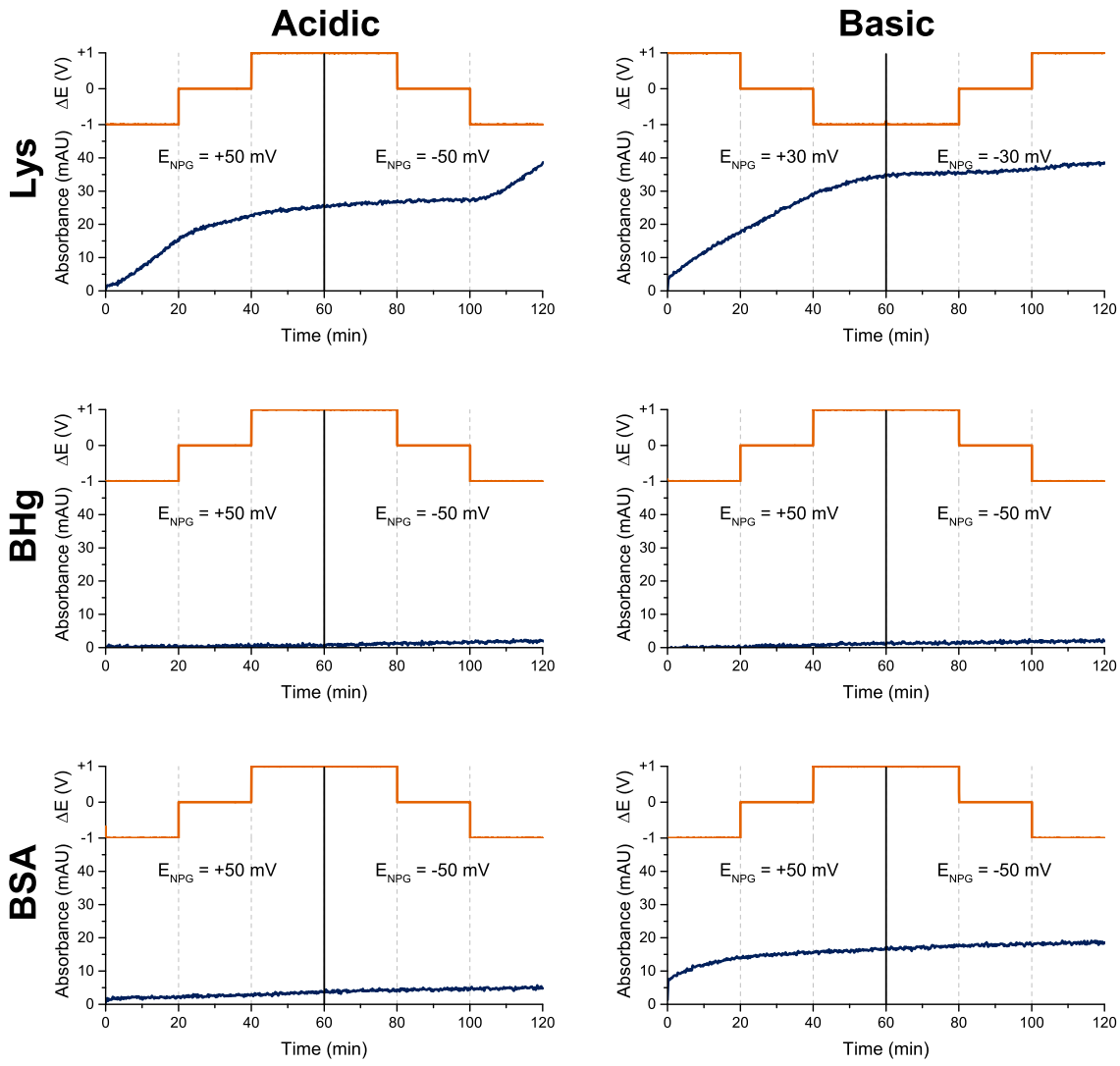

Figure 6.1: Lysozyme (Lys), bovine hemoglobin (BHg), and bovine serum albumin (BSA) flux through NPG under both acidic (pH=3) and basic (pH=11) conditions. The UV absorbance trace at 260 nm is shown in blue and the transverse potential, ΔE, applied across the reservoirs is shown in orange.

change in flux with PEG-modified NPG, flux through NPG coated with SAMs prepared with varying terminal moieties, carboxylic acid (-COOH), a hydroxyl group (-OH), and a methyl group (-CH_3), was examined, as shown in Figure 6.2. The -COOH group was pH dependent, becoming negatively charged in basic solution. The -OH group should be pH independent, but still hydrophilic. The -CH_3 group was hydrophobic and was expected to decrease the overall area available for protein flux within the pores. Surprisingly, the Lys flux showed the greatest fluctuations for the hydrophobic CH_3-modified NPG under basic conditions. At this pH, a significant amount (~30%) of the Lys is neutral, suggesting that a hydrophilic/hydrophobic gating effect may be much more efficient than charge alone. Clearly, the surface functionality plays an important role in protein translocation through NPG. While the remainder of this study focuses on the

PEG-modified NPG for its well-known biocompatibility, future efforts should examine the effects of the presented moiety in detail.

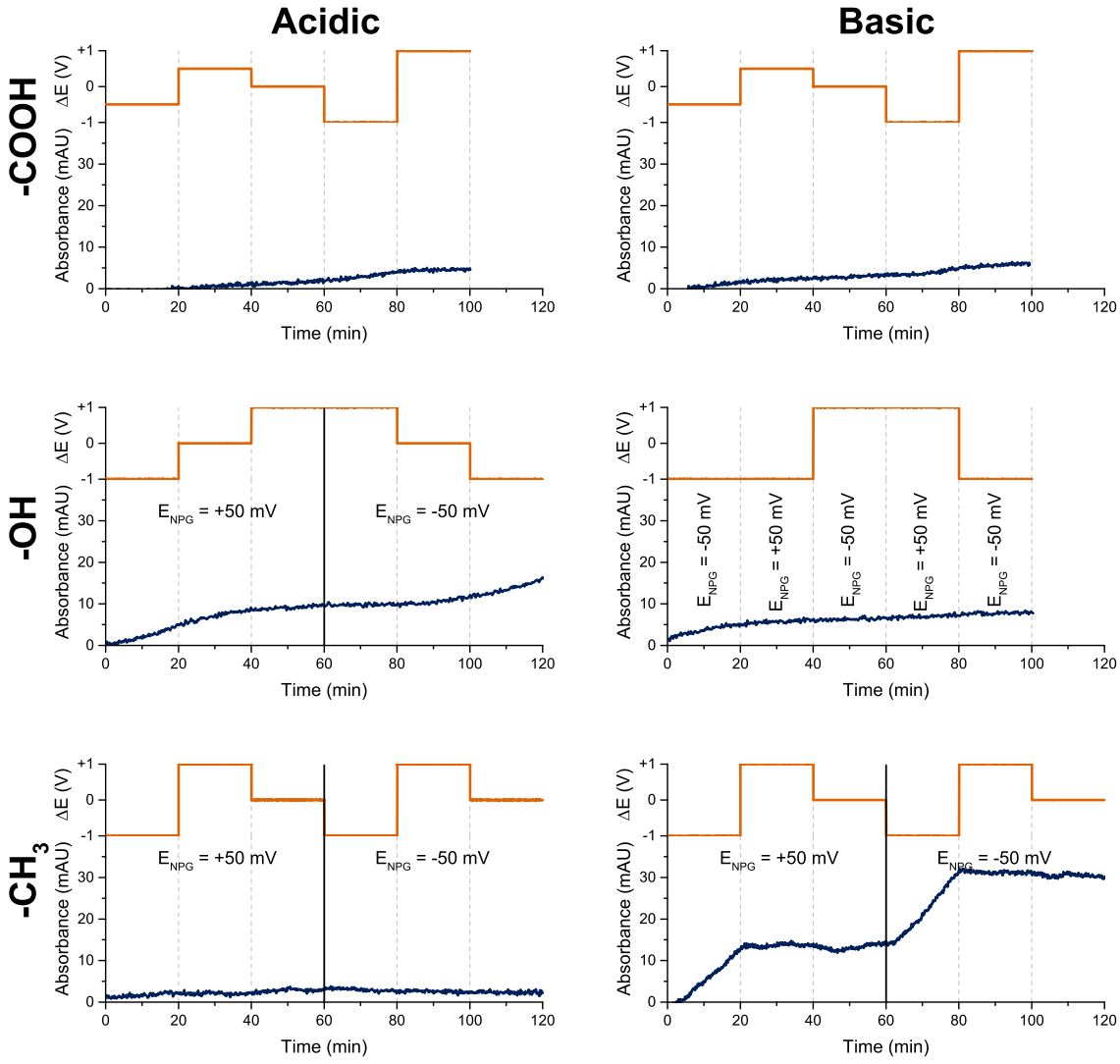

Figure 6.2: Lysozyme flux through NPG coated with different SAMs. The UV absorbance trace at 260 nm is shown in blue. Carboxylic acid (-COOH) presented a pH-dependent surface charge, the hydroxyl group (-OH) presented a hydrophilic surface that was ideally independent of pH, and the methyl group (-CH_3) presented a hydrophobic surface. The applied transverse potential is shown in orange.

6.2.1 Size-Selective Behavior of NPG

As mentioned in the previous section, Lys was the only protein that showed a significant flux magnitude with PEG-modified NPG (Figure 6.1). This was assumed to be due to the small pore diamater inhibiting pore translocation for the larger BHg and BSA proteins.[28,29] As a means of increasing throughput for the larger proteins, efforts in altering the pore diameter were explored. Aqua regia could be used to etch the

Au ligaments, but there was uncertainty in the homogeneity of the pore sizes through the NPG; aqua regia could potentially etch the exterior pores to a greater extent than the interior pores due to the rate of aqua regia permeation through the monolith. Rather, the NPG was annealed in a tube furnace to enlarge the average pore diameter. This method had been explored previously and it was discovered that annealing below the Au melting point causes surface Au to diffuse into the ligaments and subsequently widen the pore diameters.[32] Figure 6.3 shows a representative annealed NPG sample at 300 °C for 2 hr along with the BSA flux through as-prepared NPG (reproduced from Figure 6.1) compared to the BSA flux through the annealed NPG sample. There was a large increase in flux when a positive transverse potential was applied for the annealed sample as the steric hindrance for translocation has been decreased. For the larger proteins and in performing separations of a complex mixture, a large pore size distribution may aid in preventing complete inhibition of biomolecule translocation.

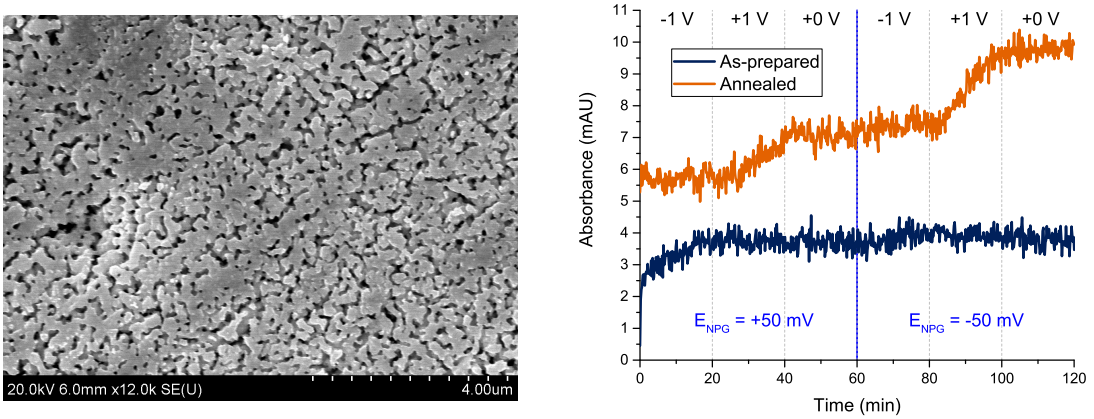

(a) (b)

Figure 6.3: (a) SEM image of a representative NPG sample after annealing at 300 °C in a tube furnace for 2 hr. Note the larger pore sizes compared to the as-prepared NPG, as shown in Figure 2.1. (b) Flux of BSA through an as-prepared NPG sample (blue) and after annealing NPG (orange) in response to an applied transverse potential (listed at top of graph).

The size-dependent behavior was further verified by size-exclusion chromatography (SEC). A 10 mg mL^{-1} commercial protein ladder sample was placed in the feed reservoir and allowed to translocate through the NPG to the sink reservoir over the course of 1 hr. Both the feed and sink reservoirs were then run through a SEC column and the chromatograms shown in Figure 6.4 were obtained. The chromatogram of the sink reservoir demonstrated a much larger ratio of the peak at 26.6 min, corresponding to the smaller proteins, to the peak at 17.3 min, corresponding to the larger proteins. The results suggest a molecular weight cutoff region for the NPG above which, protein transport was be greatly hindered.

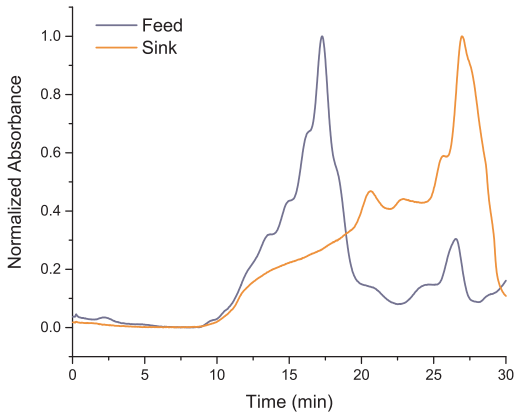

Figure 6.4: Normalized size exclusion chromatogram of the feed and sink solutions after a protein ladder was added to the feed reservoir and allowed to translocate for at least 1 hr. The ratio of the peaks at 26.6 min and 17.3 min, corresponding to the relative concentrations of the small and large mass proteins, respectively, was calculated for further comparison. Ratios of 0.302 and 3.15 were obtained for the feed and sink solutions, indicating a strong preference for small protein translocation.

6.3 DNA Transport through NPG

Compared to protein flux through NPG, it was surprisingly much more difficult to induce translocation of DNA through NPG. Although DNA is a popular analyte in much of the nanopore literature, especially considering the recent commercialization of nanopore-based sequencing instrumentation, DNA transport in previous studies is achieved only through very thin membranes, often below 100 nm in thickness.[3,33–36] Our NPG membrane is instead 250 µm thick and also presents an incredibly tortuous path from one face to the other. Attempts to translocate DNA in the presence of both AC and DC fields were performed using a fluorescence detection with a 5 mW HeNe laser excitation source. By attaching the fiber optics to the custom reservoir assembly at the 90° position, (see Figure C.7), an excitation maximum, λ_{ex}, of 632 nm and an emission maximum, λ_{em}, of 658 nm were obtained for a Cy5-labeled single-stranded DNA (ssDNA). As shown in Figure 6.5, however, there was no discernible translocation in either electric field.

Compared to single, cylindrical or conical pores, NPG more closely resembles the geometry examined by Cabodi and coworkers in their study of "entropic recoil".[37] Briefly, a series of pillars with nano-sized constrictions separated two reservoirs. An AC field was applied across the reservoirs, inducing DNA transport, as the negatively charged backbone encouraged DNA to migrate towards the cathode. In an AC field, however, the electric field polarity is rapidly alternating, so the DNA is pulled in both directions. The frequency of the applied AC field therefore dictated the distance the DNA traveled, with shorter strands demonstrating an increased mobility. DNA was able to move within the porous structure while the AC field was applied, but once the driving force was removed, any DNA remaining in the pores was fixed in a high energy, entropically unfavored state due to the diminished degrees of freedom within the struc-

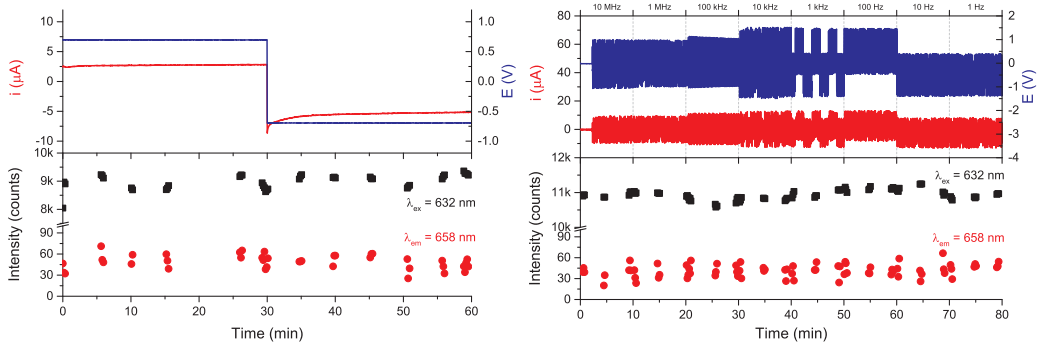

Figure 6.5: Cy5-labeled ssDNA translocation in a 1 mM NaCl solution through PEG-modified NPG with a (a) DC or (b) AC electric field applied across the reservoirs. Note that fluorescence data points were obtained only every 15 min in order to prevent photobleaching of the Cy5 label.

ture. The small DNA strands diffused much more quickly than the longer strands and therefore were able to completely thread through the porous structure at high frequencies. The longer strands, on the other hand, would only thread partially through the structure before the AC field was removed and would then be forcibly ejected from the structure. It is therefore likely that DNA translocation through NPG faces a very high energy barrier due to the decreased entropy within the NPG geometry, prohibiting transport.

Preliminary experiments employing a salt gradient rather than an applied electric field have shown some promise in DNA translocation. Figure 6.6 shows calf thymus DNA translocation through a PEG-modified NPG sample with 10 mM KCl in the feed reservoir and 100 mM KCl in the sink reservoir. For reference, an induced potential difference of +15 mV was recorded between the reservoirs for the duration of the experiment.

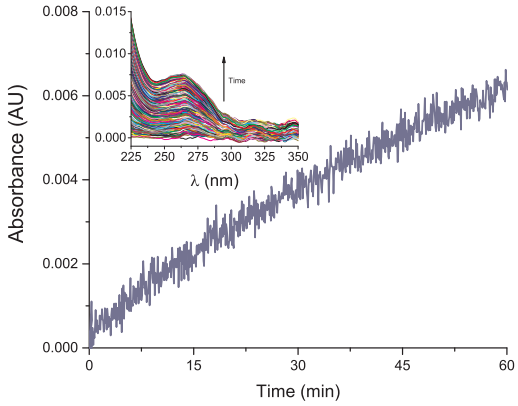

Figure 6.6: 0.1 mg mL^{-1} calf thymus DNA translocation through PEG-modified NPG with a 10:100 mM (feed:sink) KCl salt gradient. Inset shows the full UV-visible absorption spectrum.

6.4 Adaptation of Nanoporous Gold to Microfluidic Devices

6.4.1 Free-Standing NPG Leaf

Initial studies focused on modifying the membrane approach used by Bohn and Sweedler,[38] whereby a membrane was sandwiched between two slices of polydimethylsiloxane (PDMS) with microfluidic channels oriented perpendicular to each other above and below the membrane. The 250 µm thick monoliths were considered too thick to use in between the PDMS as they would lead to significant void spaces surrounding the membrane through which transport could also occur. Instead, nanoporous Au leaf was used as it was only 100 nm thick. Representative scanning electron micrographs are provided in Figure 6.7. The NPG leaf was de-alloyed from a 100 nm AgAu foil (12K, Sepp Leaf Products, Inc.) for at least 10 minutes in concentrated HNO_3.

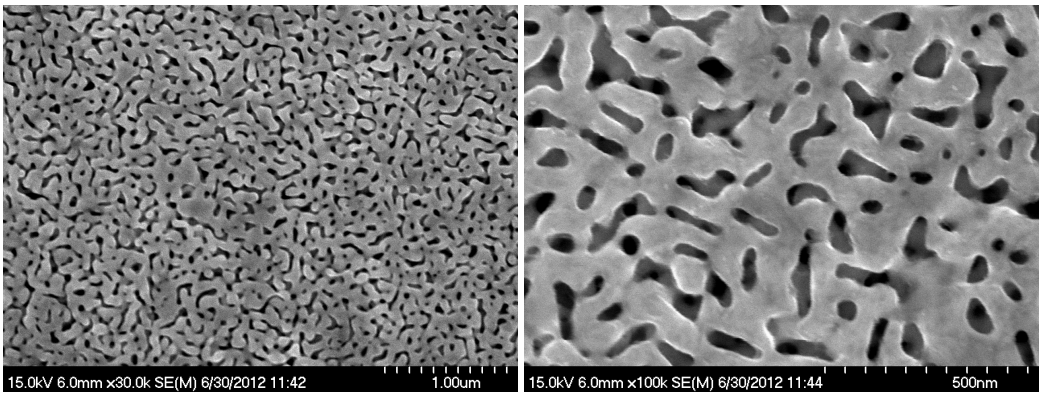

(a) (b)

Figure 6.7: Representative SEM image of NPG formed via free-corrosion de-alloying of 100 nm thick AuAg leaf at (a) high and (b) low magnifications.

Due to its thinness, NPG formed from the alloy leaf was extremely fragile and required much care in its preparation and subsequent use. The NPG was carefully scooped from the concentrated HNO_3 prior to floating in a water bath to thoroughly rinse the sample.[39] PDMS pieces were then submerged underneath the NPG and lifted up so that the leaf settled over the microfluidic channels. A representative NPG leaf over microfluidic channels prepared from a mask in Figure C.9 is presented in Figure 6.8. The serpentine geometry was used to maximize solution contact with the NPG face while maintaining structural support.[40] Despite the care taken, the leaf was decidedly too fragile and would often either disintegrate or collapse within the microfluidic channels.

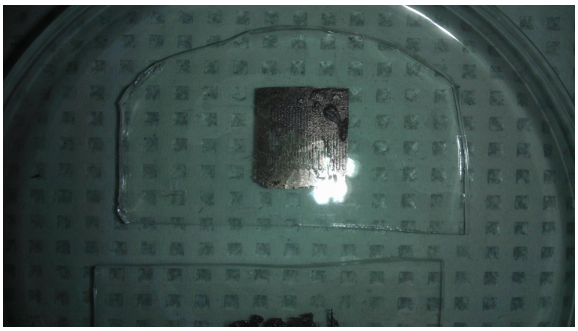

Figure 6.8: A representative NPG leaf over microfluidic channels sample. The NPG leaf was too fragile and would often collapse within the channels.

Microfluidic Master and PDMS Preparation

Masters were prepared on 3 in. silicon wafers via photolithographic patterning of SU-8 2050. SU-8 2050 (MicroChem Corp.) was spin coated on the wafer with the following steps, in order:

1. 500 RPM for 5 s with 100 $\mathrm{RPM\,s^{-1}}$ ramp
2. 1750 RPM for 30 s with 300 $\mathrm{RPM\,s^{-1}}$ ramp
3. 0 RPM with 200 $\mathrm{RPM\,s^{-1}}$ ramp

This program provided a height of approximately 90 µm according to the MicroChem Corp. datasheet. Heat treatment post spin-coating was performed at 65 °C for 5 min followed by 20 min at 95 °C on a bench-top hotplate. A photomask designed in AutoCAD (see Figure C.9 and Figure C.10) was taped to a quartz plate prior to placing directly on top of the SU-8 coated wafer. The wafer was exposed to UV light from a UV LED light source at 100% power for 30s. A postbake was performed at 65 °C for 5 min followed by 10 min at 95 °C. Excess uncured SU-8 was removed by immersing the wafer in propylene glycol monomethyl ether acetate (PGMEA) for 10 minutes, followed by further rinsing with PGMEA and isopropyl alcohol. The wafer was dried with N_2 gas and the master was inspected under a stereoscope for deformities.

PDMS was prepared by mixing 9 g PDMS and 1 g curing agent for a 9:1 ratio in a plastic weigh boat with a wooden tongue depressor. The mixture was then degassed in a vacuum desiccator for 10-20 min until the bubbles were gone. The SU-8 master was then placed, feature side up, at the bottom of a plastic (*plastic must be used as PDMS will irreversibly bond to glass*) evaporating dish. The PDMS mixture was slowly poured onto the center of the master. The PDMS was allowed to cure in a 70 °C oven for at least 1 hr. The cured PDMS was peeled from the master with the aid of a razor blade and blunt syringe tips were used to puncture the PDMS where inlet and outlet ports are desired. In order to bond PDMS to a glass substrate or to another PDMS sample, the PDMS was O_2 plasma-treated under low vacuum with O_2 gas leaked in to the chamber for at least 2 min.

6.4.2 Microfabrication of NPG

In order to increase durability of the NPG-integrated microfluidics, the NPG could be deposited on a rigid substrate with PDMS reservoirs on either end of the deposited NPG. The co-deposition of AgAu alloys for subsequent de-alloying has found use in electrochemical studies.[41,42] Figure 6.9 shows a schematic of the proposed fabricated device in the present study. A soda-lime glass microscope slide was masked with Kapton tape. A 10 nm adhesion layer of either Ti or Cr was deposited followed by deposition of an AgAu layer. Immersion of the fabricated device in concentrated HNO_3 for 10 min created a red structure. Finally, a PDMS device could be placed over the resulting film in order to create a reservoir assembly similar to those discussed in prior chapters.

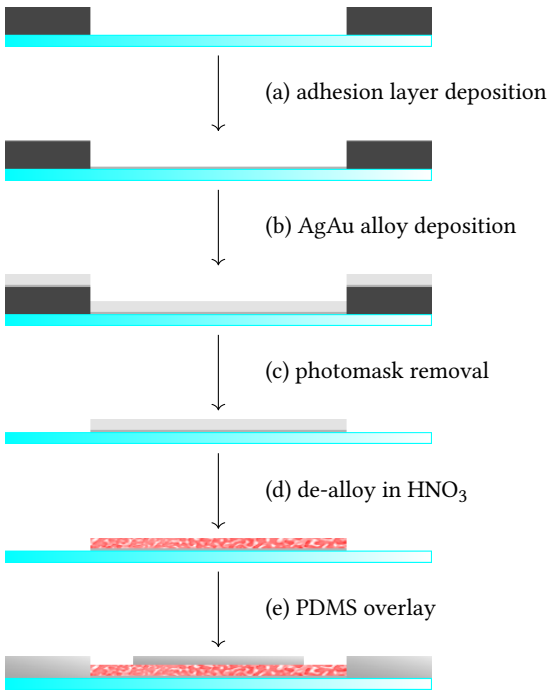

Figure 6.9: Schematic representation of desired microfluidic device fabrication. (a) An adhesion layer of either Cr or Ti is deposited on the substrate. (b) The AgAu alloy is deposited either through co-deposition or layered followed by a subsequent annealing step. (c) The photomask is removed. (d) Immersion in concentrated HNO_3 de-alloys in AgAu. (e) PDMS is prepared and sealed over the surface of the deposit, forming two reservoirs on either end.

Layer-by-Layer Electron Beam Deposition

Au and Ag layers were grown sequentially on the glass substrate using electron bead deposition, as the local facilities at the Frederick Seitz Materials Research Laboratory did not currently support dual electron beam deposition. A 10 nm Ti adhesion layer was evaporated onto the glass substrates. 50 nm Au was then evaporated in order to form the first layer of Au as well as provide a barrier between the alloy and the

adhesion layer. Evaporation of Ag and Au was then alternated to provide two 42 nm Ag layers with an 18 nm Au layer in between. The growth of more layers would provide a thicker substrate, but the alternating process was very time-intensive, as the sources need time to cool prior to switching. In order to sufficiently mix the deposited layers for de-alloying, the samples were annealed in a Rapid Thermal Anneal (RTA) tube furnace. The furnace was stepped up to 500 °C, as any higher would cause the soda-lime glass microscope slides to melt (melting temperature of 550 °C). N_2 process gas was used for the duration of the 10 min anneal to prevent surface oxides from forming. Cooling occurred under N_2 gas. Figure 6.10 shows SEM images of the resulting deposit after de-alloying both an as-deposited sample and an annealed sample.

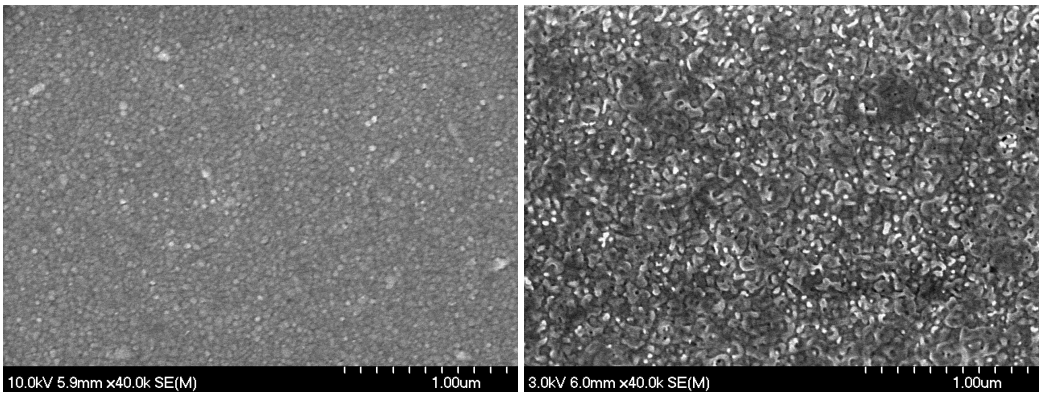

(a) (b)

Figure 6.10: SEM images of de-alloyed (a) as-deposited and (b) annealed electron beam evaporated AgAu on glass with a Ti adhesion layer.

There did appear to be some porosity, or at the very least pitting, of the sample in Figure 6.10b compared to the sample in Figure 6.10a. Although this indicated that the annealing step is necessary, as otherwise the Ag layers simply delaminated from the Au underlayers, the sample did not develop the desired nanoporosity exhibited in the 250 µm thick monoliths. Energy dispersive x-ray (EDX) spectroscopy was performed on the resulting samples, as shown in Figure 6.11. The samples prior to de-alloying (Figure 6.11a,b) appear to be compositionally similar, as expected. De-alloying of the annealed sample in Figure 6.11d still shows a Ag peak, however, compared to the EDX spectrum of the non-annealed sample in Figure 6.11c.

The elemental composition of the samples in Figure 6.11 are summarized in Table 6.2. Both the as-prepared and annealed samples are nearly 70% Au and 30% Ag, which is close to the parting limit of AgAu alloys.[43] As such, the annealed sample may have passivated before fully de-alloying, as evidenced by the 54% Ag remaining after HNO_3 immersion.

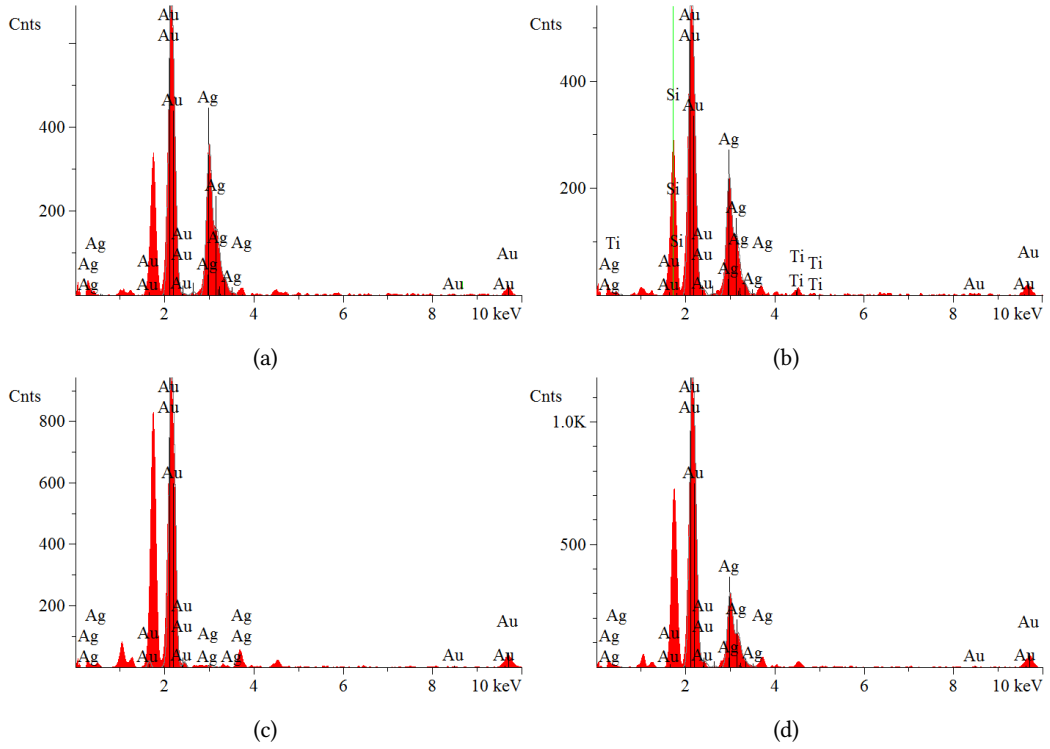

Figure 6.11: EDX spectra of (a) as-prepared and (b) annealed at 500 °C AgAu alloys on glass, along with (c,d) corresponding EDX spectra of the respective samples post-HNO_3 immersion for at least 15 min.

Bulk Electron Beam Deposition

In order to better control the AgAu ratio of the resulting deposit, 50 nm Au followed by 200 nm Ag was deposited on top of a 15 nm Ti adhesion layer, rather than alternating the Ag and Au deposition steps. Initial thought assumed that the alternating layers would improve the mixing during the annealing step, but, as Figure 6.12 shows, there appeared to be significant ligament growth with just a thick Ag layer on top of the Au. Furthermore, the Ag peak seemed to be fully removed after de-alloying (Figure 6.13). Table 6.3 lists the exact ratios obtained prior to and after de-alloying the bulk electron beam deposited sample. Initially, the sample appeared to be 90% Ag. The presence of a Si peak in Figure 6.13b and lack of a Si peak in Figure 6.13a, however, suggests that the sample is much thinner after de-alloying. In this fabrication scheme, it is therefore most likely that mixing did indeed occur at the AgAu interface, but the bulk of the sample above the glass was not mixed. The electron beam did not penetrate deep enough into the sample and was instead only measuring the surface composition, providing the $Ag_{0.90}Au_{0.10}$ ratio in Table 6.3.

An image of the resulting deposits is provided in Figure 6.14. The deposits were "T"-shaped as a larger section external to the channel was desired for electrical contact within the microfluidic device. The edges of each sample were very rough and a faded region was present where the NPG had delaminated. A much more durable adhesion layer was therefore required.

Table 6.2: EDX elemental composition of the samples analyzed in Figure 6.11.

Element	Line	Intensity (c/s)	Atomic %	wt. %
As-prepared				
Ag	La	91.43	69.434	55.437
Au	Ma	145.15	30.566	44.563
As-prepared post-dealloy				
Ag	La	2.32	4.920	2.756
Au	Ma	210.62	95.080	97.244
Annealed				
Ag	La	69.29	64.366	49.729
Au	Ma	142.80	35.634	50.271
Annealed post-dealloy				
Ag	La	77.92	54.875	39.975
Au	Ma	251.33	45.125	60.025

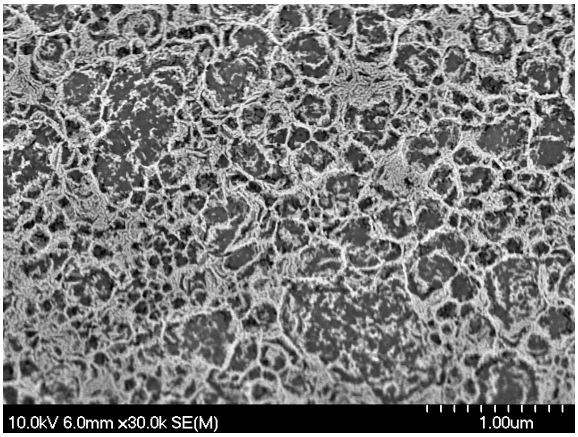

Figure 6.12: Bulk electron beam evaporated AgAu alloy on glass substrate following thermal anneal and subsequent de-alloying in concentrated HNO_3.

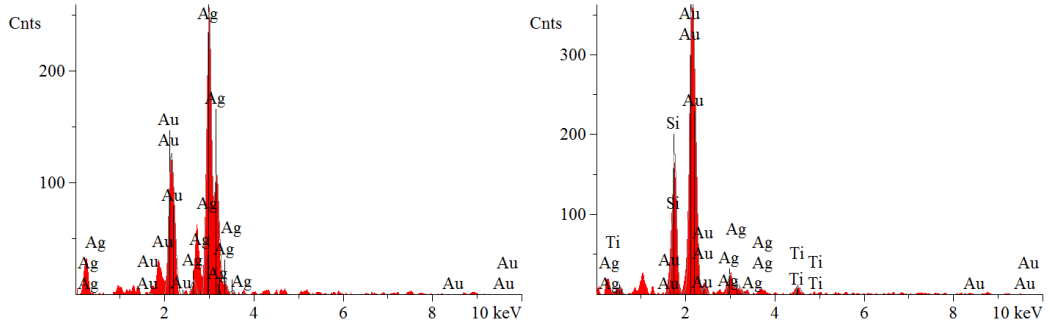

(a) (b)

Figure 6.13: EDX spectra of (a) as-prepared and (b) de-alloyed AgAu alloys on glass.

Co-sputtered AgAu Alloy

To alleviate the issue of insufficient mixing, Ag and Au can be co-deposited so that an additional annealing step is rendered unnecessary. While a prepared AgAu source would be ideal, the use of two independent

Table 6.3: EDX elemental composition of the samples analyzed in Figure 6.13.

Element	Line	Intensity (c/s)	Atomic %	wt. %
As-prepared				
Ag	La	55.46	89.614	82.534
Au	Ma	23.96	10.386	17.466
De-alloyed				
Ag	La	5.92	26.572	16.540
Au	Ma	69.25	73.428	83.460

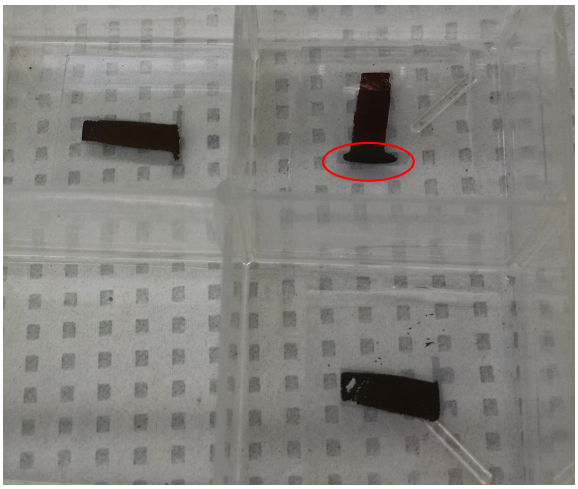

Figure 6.14: De-alloyed NPG on glass prepared via bulk electron beam deposition. The red circle denotes an example of delamination.

targets set to the appropriate power ratios for an alloy below the parting limit is also acceptable.

The base chamber pressure of the AJA Sputter Coater was maintained at 3 µtorr. Ar process gas was used at a rate of 5.9 SCCM ($cm^3\ min^{-1}$). Cr was deposited at a DC power of 120 W for a rate of ~1 $Å\,s^{-1}$. A thickness of 29 Å was obtained. Instrumental limitations for co-deposition required the use of DC power for one target and AC for the other. The Au gun was powered first at a DC power of 15 W to begin the plasma followed by stepping back to 3 W. Deposition occurred at a rate of 0.8 $Å\,s^{-1}$. A thin layer of Au was desired so that a protection layer between the Cr and alloy was present. The Ag gun was powered with AC power at 40 W for a rate of 1.2 $Å\,s^{-1}$. The rate of Ag was maintained higher than Au so that the alloy was sufficiently Au deficient as to permit complete de-alloying.[43] As the crystal used for estimating deposition thickness was only calibrated for Au, an exact thickness could not be determined during the deposition process. The sputtering was allowed to proceed for 50 min. At a total combined rate of roughly 2 $Å\,min^{-1}$, the final thickness was estimated to be 150 nm.

EDX spectra and the corresponding compositional analysis are provided in Figure 6.15 and Table 6.4, respectively. Unfortunately, with the parameters described above, the AgAu ratio was well above the part-

ing limit. Although an attempt at de-alloying was performed, it is clear from Table 6.4 that the composition did not change significantly after immersion in concentrated HNO_3. A different deposition ratio could be attempted, but the Au plasma was too difficult to maintain at the low power (3 W) used and the Ag power would therefore need to be increased.

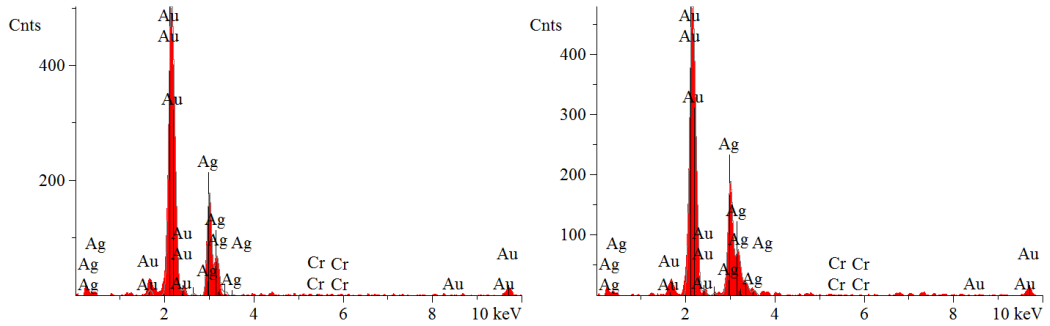

Figure 6.15: EDX spectra of (a) as-prepared and (b) dealloyed co-sputtered AgAu alloy on glass with a Cr adhesion layer.

Table 6.4: EDX elemental composition of the as-prepared and de-alloyed sputter- coated NPG samples.

Element	Line	Intensity (c/s)	Atomic %	wt. %
As-prepared				
Ag	La	75.30	58.493	43.559
Au	Ma	205.65	41.507	56.441
De-alloyed				
Ag	La	88.55	62.585	47.810
Au	Ma	199.13	37.415	52.190

6.5 Future Outlook

This chapter provided only recent work regarding NPG for biomolecular transport modulation and the scaling down of NPG membranes in a microfluidic device. As such it should serve as a useful starting point for the continuation of the project. Protein flux through NPG seems to be a viable path in the near future for further development of the NPG as a membrane material, as comprehensive studies of surface functionalization combined with tunable pore sizes have shown the most promising results. Transport of DNA, on the other hand, presents quite a challenge and other, more fundamental studies are required in order to truly understand the difficulties encountered. As mentioned in Section 6.3, the entropically unfavorable conditions within the tortuous geometry are most likely the major contributing factor towards DNA flux inhibition. Studies considering the transport of simple linear and branched polymers may therefore

provide significant insight as to how the flexibility of the analyte influences transport.

In terms of microfluidic advances, AgAu alloys have previously been microfabricated successfully. In the present study, instrumental capabilities seemed to be the major factors limiting our fabrication. Using a single, prefabricated Ag_xAu_{1-x} target should allow for much better control over the alloy composition on the substrate. Another alternative not considered in the present study involves the electrochemical deposition of AgAu alloys. Electrochemical reduction of Ag and Au from a sodium thiosulfate/thiosulfite solution has been shown to provide adequate control over the resulting composition of the alloy and subsequent de-alloying has demonstrated the desired nanoporosity.[44] In order to develop our microfluidic device, the evaporation or sputtering of an Au underlayer could provide a conductive substrate on which to electrochemically grow such an alloy.

6.6 References

1. Yi, C.; Li, C.-W.; Ji, S.; Yang, M. Microfluidics technology for manipulation and analysis of biological cells. *Analytica Chimica Acta* **2006**, *560*, 1–23, DOI: 10.1016/j.aca.2005.12.037.

2. Zhang, C.; Xu, J.; Ma, W.; Zheng, W. PCR microfluidic devices for DNA amplification. *Biotechnology Advances* **2006**, *24*, 243–284, DOI: 10.1016/j.biotechadv.2005.10.002.

3. Wanunu, M. Nanopores: A journey towards DNA sequencing. *Physics of Life Reviews* **2012**, *9*, 125–158, DOI: 10.1016/j.plrev.2012.05.010.

4. Harms, Z. D.; Selzer, L.; Zlotnick, A.; Jacobson, S. C. Monitoring Assembly of Virus Capsids with Nanofluidic Devices. *ACS Nano* **2015**, *9*, 9087–9096, DOI: 10.1021/acsnano.5b03231.

5. Harms, Z. D.; Haywood, D. G.; Kneller, A. R.; Selzer, L.; Zlotnick, A.; Jacobson, S. C. Single-Particle Electrophoresis in Nanochannels. *Analytical Chemistry* **2015**, *87*, 699–705, DOI: 10.1021/ac503527d.

6. Li, F.; Guijt, R. M.; Breadmore, M. C. Nanoporous Membranes for Microfluidic Concentration Prior to Electrophoretic Separation of Proteins in Urine. *Analytical Chemistry* **2016**, DOI: 10.1021/acs.analchem.6b02096.

7. Yu, C.; Davey, M. H.; Svec, F.; Fréchet, J. M. J. Monolithic Porous Polymer for On-Chip Solid-Phase Extraction and Preconcentration Prepared by Photoinitiated in Situ Polymerization within a Microfluidic Device. *Analytical Chemistry* **2001**, *73*, 5088–5096, DOI: 10.1021/ac0106288.

8. Foote, R. S.; Khandurina, J.; Jacobson, S. C.; Ramsey, J. M. Preconcentration of Proteins on Microfluidic Devices Using Porous Silica Membranes. *Analytical Chemistry* **2005**, *77*, 57–63, DOI: 10.1021/ac049136w.

9. Kim, S. M.; Burns, M. A.; Hasselbrink, E. F. Electrokinetic Protein Preconcentration Using a Simple Glass/Poly(dimethylsiloxane) Microfluidic Chip. *Analytical Chemistry* **2006**, *78*, 4779–4785, DOI: 10.1021/ac060031y.

10. Collas, P. The Current State of Chromatin Immunoprecipitation. *Molecular Biotechnology* **2010**, *45*, 87–100, DOI: 10.1007/s12033-009-9239-8.

11. Massie, C. E.; Mills, I. G. ChIPping away at gene regulation. *EMBO Rep* **Apr. 2008**, *9*, 337–343, DOI: 10.1038/embor.2008.44.

12. Dahl, J. A.; Collas, P. A rapid micro chromatin immunoprecipitation assay (ChIP). *Nature Protocols* **2008**, *3*, 1032–1045, DOI: 10.1038/nprot.2008.68.

13. Gerlinger, M. et al. Intratumor Heterogeneity and Branched Evolution Revealed by Multiregion Sequencing. *N Engl J Med* **2012**, *366*, 883–892, DOI: 10.1056/NEJMoa1113205.

14. Stine, K. J.; Jefferson, K.; Shulga, O. V., Nanoporous Gold for Enzyme Immobilization. In *Enzyme Stabilization and Immobilization: Methods and Protocols*, Minteer, S. D., Ed.; Methods in Molecular Biology; Humana Press: Totowa, NJ, 2011; Chapter Nanoporous Gold for Enzyme Immobilization, pp 67–83, DOI: 10.1007/978-1-60761-895-9_7.

15. Tan, Y. H.; Schallom, J. R.; Ganesh, N. V.; Fujikawa, K.; Demchenko, A. V.; Stine, K. J. Characterization of protein immobilization on nanoporous gold using atomic force microscopy and scanning electron microscopy. *Nanoscale* **2011**, *3*, 3395–3407, DOI: 10.1039/C1NR10427F.

16. Pandey, B.; Tan, Y. H.; Fujikawa, K.; Demchenko, A. V.; Stine, K. J. Comparative Study of the Binding of Concanavalin A to Self-Assembled Monolayers Containing a Thiolated α-Mannoside on Flat Gold and on Nanoporous Gold. *Journal of Carbohydrate Chemistry* **2012**, *31*, 466–503, DOI: 10.1080/07328303.2012.683909.

17. Gittard, S. D.; Pierson, B. E.; Ha, C. M.; Wu, C.-A. M.; Narayan, R. J.; Robinson, D. B. Supercapacitive transport of pharmacologic agents using nanoporous gold electrodes. *Biotechnology Journal* **2010**, *5*, 192–200, DOI: 10.1002/biot.200900250.

18. Ramírez, P.; Mafé, S.; Alcaraz, A.; Cervera, J. Modeling of pH-Switchable Ion Transport and Selectivity in Nanopore Membranes with Fixed Charges. *The Journal of Physical Chemistry B* **2003**, *107*, 13178–13187, DOI: 10.1021/jp035778w.

19. Chun, K.-Y.; Stroeve, P. Protein Transport in Nanoporous Membranes Modified with Self-Assembled Monolayers of Functionalized Thiols. *Langmuir* **2002**, *18*, 4653–4658, DOI: 10.1021/la011250b.

20. Yeh, L.-H.; Zhang, M.; Qian, S. Ion Transport in a pH-Regulated Nanopore. *Analytical Chemistry* **2013**, *85*, 7527–7534, DOI: 10.1021/ac401536g.

21. White, H. S.; Bund, A. Ion Current Rectification at Nanopores in Glass Membranes. *Langmuir* **2008**, *24*, 2212–2218, DOI: 10.1021/la702955k.

22. Wu, A. R.; Hiatt, J. B.; Lu, R.; Attema, J. L.; Lobo, N. A.; Weissman, I. L.; Clarke, M. F.; Quake, S. R. Automated microfluidic chromatin immunoprecipitation from 2,000 cells. *Lab Chip* **2009**, *9*, 1365–1370, DOI: 10.1039/B819648F.

23. Seker, E.; Reed, M. L.; Begley, M. R. Nanoporous Gold: Fabrication, Characterization, and Applications. *Materials* **2009**, *2*, 2188–2215, DOI: 10.3390/ma2042188.

24. Kingshott, P.; Griesser, H. J. Surfaces that resist bioadhesion. *Current Opinion in Solid State and Materials Science* **1999**, *4*, 403–412, DOI: 10.1016/s1359-0286(99)00018-2.

25. Flynn, N. T.; Tran, T. N. T.; Cima, M. J.; Langer, R. Long-Term Stability of Self-Assembled Monolayers in Biological Media. *Langmuir* **2003**, *19*, 10909–10915, DOI: 10.1021/la035331e.

26. Fischer, L. M.; Tenje, M.; Heiskanen, A. R.; Masuda, N.; Castillo, J.; Bentien, A.; Émneus, J.; Jakobsen, M. H.; Boisen, A. Gold cleaning methods for electrochemical detection applications. *Microelectronic Engineering* **2009**, *86*, 1282–1285, DOI: 10.1016/j.mee.2008.11.045.

27. Powell, M. R.; Cleary, L.; Davenport, M.; Shea, K. J.; Siwy, Z. S. Electric-field-induced wetting and dewetting in single hydrophobic nanopores. *Nature Nanotechnology* **2011**, *6*, 798–802, DOI: 10.1038/nnano.2011.189.

28. Daggumati, P.; Appelt, S.; Matharu, Z.; Marco, M. L.; Seker, E. Sequence-Specific Electrical Purification of Nucleic Acids with Nanoporous Gold Electrodes. *J. Am. Chem. Soc.* **2016**, *138*, 7711–7717, DOI: 10.1021/jacs.6b03563.

29. Daggumati, P.; Matharu, Z.; Wang, L.; Seker, E. Biofouling-Resilient Nanoporous Gold Electrodes for DNA Sensing. *Anal Chem* **2015**, *87*, 8618–22, DOI: 10.1021/acs.analchem.5b02969.

30. Daggumati, P.; Matharu, Z.; Seker, E. Effect of Nanoporous Gold Thin Film Morphology on Electrochemical DNA Sensing. *Analytical Chemistry* **2015**, DOI: 10.1021/acs.analchem.5b00846.

31. Pandey, B.; Demchenko, A.; Stine, K. Nanoporous gold as a solid support for protein immobilization and development of an electrochemical immunoassay for prostate specific antigen and carcinoembryonic antigen. *Microchimica Acta* **2012**, *179*, 71–81, DOI: 10.1007/s00604-012-0870-x.

32. Tan, Y. H.; Davis, J. A.; Fujikawa, K.; Ganesh, N. V.; Demchenko, A. V.; Stine, K. J. Surface area and pore size characteristics of nanoporous gold subjected to thermal, mechanical, or surface modification studied using gas adsorption isotherms, cyclic voltammetry, thermogravimetric analysis, and scanning electron microscopy. *Journal of Materials Chemistry* **2012**, *22*, 6733–6745, DOI: 10.1039/c2jm16633j.

33. Wanunu, M. Nanopores: Past, present and future. *Physics of Life Reviews* **2012**, *9*, 174–176, DOI: 10.1016/j.plrev.2012.05.017.

34. Lindsay, S. The promises and challenges of solid-state sequencing. *Nat Nano* **2016**, *11*, 109–111, DOI: 10.1038/nnano.2016.9.

35. Ip, C. L. et al. MinION Analysis and Reference Consortium: Phase 1 data release and analysis. *F1000Research* **2015**, DOI: 10.12688/f1000research.7201.1.

36. Dekker, C. Solid-state nanopores. *Nat Nano* **2007**, *2*, 209–215, DOI: 10.1038/nnano.2007.27.

37. Cabodi, M.; Turner, S. W.; Craighead, H. G. Entropic recoil separation of long DNA molecules. *Anal Chem* **2002**, *74*, 5169–74, DOI: 10.1021/ac025879a.

38. Kuo, T.-C.; Cannon, D. M.; Chen, Y.; Tulock, J. J.; Shannon, M. A.; Sweedler, J. V.; Bohn, P. W. Gateable Nanofluidic Interconnects for Multilayered Microfluidic Separation Systems. *Analytical Chemistry* **2003**, *75*, 1861–1867, DOI: 10.1021/ac025958m.

39. Ding, Y.; Kim, Y.-J.; Erlebacher, J. Nanoporous Gold Leaf: "Ancient Technology"/Advanced Material. *Advanced Materials* **2004**, *16*, 1897–1900, DOI: 10.1002/adma.200400792.

40. Sheng, Y.; Bowser, M. T. Size selective DNA transport through a nanoporous membrane in a PDMS microfluidic device. *The Analyst* **2012**, *137*, 1144, DOI: 10.1039/c2an15966j.

41. Quan, X.; Fischer, L. M.; Boisen, A.; Tenje, M. Development of nanoporous gold electrodes for electrochemical applications. *Microelectronic Engineering* **2011**, *88*, 2379–2382, DOI: 10.1016/j.mee.2010.12.121.

42. Kurtulus, O.; Daggumati, P.; Seker, E. Molecular release from patterned nanoporous gold thin films. *Nanoscale* **2014**, *6*, 7062–7071, DOI: 10.1039/C4NR01288G.

43. Erlebacher, J. An Atomistic Description of Dealloying: Porosity Evolution, the Critical Potential, and Rate-Limiting Behavior. *Journal of The Electrochemical Society* **2004**, *151*, C614–C626, DOI: 10.1149/1.1784820.

44. McCurry, D. A.; Kamundi, M.; Fayette, M.; Wafula, F.; Dimitrov, N. All Electrochemical Fabrication of a Platinized Nanoporous Au Thin-Film Catalyst. *ACS Appl. Mater. Interfaces* **2011**, *3*, 4459–4468, DOI: 10.1021/am2011433.

Chapter 7

Conclusions

Nanopores have transformed current practices in DNA sequencing. From their humble beginnings as bacterial secretions, they have grown to become finely tunable, microfabricated machines.

To that history, we append free-standing, electrically accessible nanoporous gold monoliths. A material known for its high surface area, NPG has proven to be a fantastic catalyst substrate as well as a biomolecular capture agent. The present study capitalized on these features in order to examine dynamic, in situ control over membrane transport. Fabrication of NPG membranes is incredibly simple, requiring only a few days time to achieve a highly porous substrate. Well-known Au surface modification via thiol self-assembled monolayer chemistry permitted modulation of molecular translocation rates either electrochemically or by altering solution pH.

The background electrolyte was also found to dictate ion advection. When a salt gradient was imposed across the NPG membrane, molecular translocation rates changed dramatically. In addition to the induced potential arising from the Gibbs-Donnan effect, the osmostic pressure and fluid motion were able to either enhance or diminish molecular flux in a process known as diffusioosmosis. While not touched upon in the present work, this suggests that NPG may have potential future applications in desalination.

While still in its infancy, initial studies attempting biomolecular separations have shown the true versatility of NPG. The pore sizes of the prepared NPG demonstrated a molecular weight cutoff region for proteins while the tortuous geometry significantly limited DNA translocation. Altering the surface functional groups tethered to the NPG surface has shown to have a strong effect on biomolecule transport and should be studied in futher detail.

The facile transition to microfluidic devices will only serve to improve personalized medicine. The proposed route in this thesis faced numerous challenges, but most, if not all, were caused by instrumental limitations. Numerous examples of NPG microfabrication are present in the literature and further development will only aid in reaching our ultimate goal: performing dynamic small volume separations in a microfluidic device.

Appendix A

COMSOL Reports

A.1 NPG Interior Diffusion

1 Global Definitions

Date	Jun 27, 2015 1:06:20 PM

Global settings

Name	NPG with imported geometry with laminar flow.mph
Path	/home/dmccurr2/windows-share/Documents/COMSOL/15.07.20/NPG with imported geometry with laminar flow.mph
COMSOL version	COMSOL 5.2 (Build: 220)

Used products

COMSOL Multiphysics
Batteries & Fuel Cells Module
Microfluidics Module

1.1 Parameters 1

Parameters

Name	Expression	Value	Description
surfq	-0.0001[C/m^2]	−1E−4 C/m²	surface charge density
bulk	100[mol/m^3]	100 mol/m³	bulk concentration
debye	(0.304e-9/sqrt(bulk/1000[mol/m^3]))[m]	9.6133E−10 m	debye length
zeta	surfq*debye/(ewater*e0)	−1.3555E−4 V	zeta potential
e0	8.854187817e-12[F/m]	8.8542E−12 F/m	vacuum permittivity
ewater	80.1	80.1	relative permittivity of water
avo	6.022e23[1/mol]	6.022E23 1/mol	Avagadro's number
e	1.60217657e-19[C]	1.6022E−19 C	elementary charge
Esink	1[V]	1 V	Potential in sink

2 Component 1

2.1 Definitions

2.1.1 Selections

cln1x

Selection type
Explicit

Selection
No boundaries

2.1.2 Coordinate Systems

Boundary System 1

Coordinate system type	Boundary system
Tag	sys1

2.2 Geometry 1

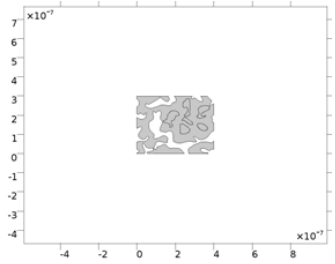

Geometry 1

Units

Length unit	m
Angular unit	deg

2.3 Materials

2.3.1 Water

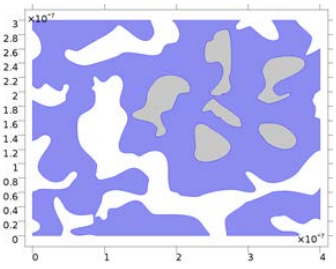

Water

Selection

Geometric entity level	Domain
Selection	Domains 1, 8

2.3.2 Au - Gold

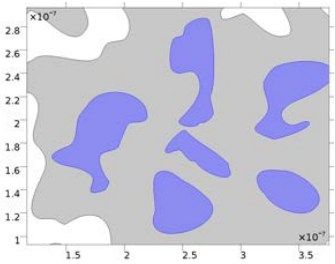

Au - Gold

Selection

Geometric entity level	Domain
Selection	Domains 2–7

2.4 Transport of Diluted Species

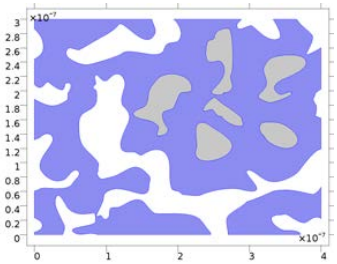

Transport of Diluted Species

Equations

$$\nabla \cdot (-D_i \nabla c_i - z_i u_{m,i} F c_i \nabla V) + \mathbf{u} \cdot \nabla c_i = R_i$$
$$\mathbf{N}_i = -D_i \nabla c_i - z_i u_{m,i} F c_i \nabla V + \mathbf{u} c_i$$

Features

Transport Properties 1
No Flux 1
Initial Values 1
Concentration 1
Concentration 2
Open Boundary 1

2.4.1 Transport Properties 1

Equations

$$\nabla \cdot (-D_i \nabla c_i - z_i u_{m,i} F c_i \nabla V) + \mathbf{u} \cdot \nabla c_i = R_i$$

$$\mathbf{N}_i = -D_i \nabla c_i - z_i u_{m,i} F c_i \nabla V + \mathbf{u} c_i$$

2.4.2 No Flux 1

Equations

$$-\mathbf{n} \cdot \mathbf{N}_i = 0$$

2.4.3 Concentration 1

Equations

$$c_i = c_{0,i}$$

2.4.4 Concentration 2

Equations

$$c_i = c_{0,i}$$

2.4.5 Open Boundary 1

Equations

$$-\mathbf{n} \cdot D_i \nabla c_i = 0 \quad \text{if } \mathbf{n} \cdot \mathbf{u} \geq 0$$
$$c_i = c_{0,i} \quad \text{if } \mathbf{n} \cdot \mathbf{u} < 0$$

2.5 Electrostatics

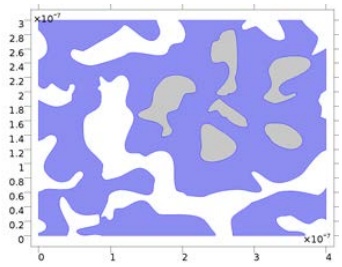

Electrostatics

Equations

$$\nabla \cdot \mathbf{D} = \rho_v$$
$$\mathbf{E} = -\nabla V$$

Features

Charge Conservation 1
Zero Charge 1
Initial Values 1
Surface Charge Density 1
Electric Potential 1
Electric Potential 2
Space Charge Density 1

2.5.1 Charge Conservation 1

Equations

$$\mathbf{E} = -\nabla V$$
$$\nabla \cdot (\epsilon_0 \epsilon_r \mathbf{E}) = \rho_v$$

2.5.2 Zero Charge 1

Equations

$$\mathbf{n} \cdot \mathbf{D} = 0$$

2.5.3 Surface Charge Density 1

Equations

$$\mathbf{n} \cdot (\mathbf{D}_1 - \mathbf{D}_2) = \rho_s$$

2.5.4 Electric Potential 1

Equations

$$V = V_0$$

2.5.5 Electric Potential 2

Equations

$$V = V_0$$

2.5.6 Space Charge Density 1

Equations

$$\nabla \cdot \mathbf{D} = \rho_v$$

2.6 Laminar Flow

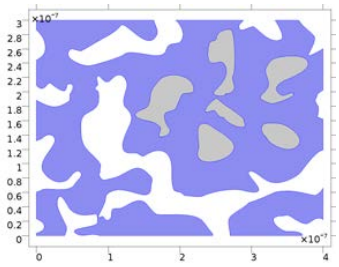

Laminar Flow

Equations

$$\rho(\mathbf{u} \cdot \nabla)\mathbf{u} =$$
$$\nabla \cdot \left[-p\mathbf{I} + \mu\left(\nabla \mathbf{u} + (\nabla \mathbf{u})^T\right)\right] + \mathbf{F}$$
$$\rho \nabla \cdot (\mathbf{u}) = 0$$

Features

Fluid Properties 1
Wall 1
Initial Values 1
Open Boundary 1

2.6.1 Fluid Properties 1

Equations

$$\rho\frac{\partial \mathbf{u}}{\partial t} + \rho(\mathbf{u}\cdot\nabla)\mathbf{u} =$$
$$\nabla\cdot\left[-p\mathbf{I} + \mu\left(\nabla\mathbf{u} + (\nabla\mathbf{u})^{T}\right)\right] + \mathbf{F}$$
$$\rho\nabla\cdot(\mathbf{u}) = 0$$

2.6.2 Wall 1

Equations

$$\mathbf{u} = \mu_{eo}\mathbf{E}_t\ ,\ \mu_{eo} = -\frac{\epsilon_r\epsilon_0\zeta}{\mu}\ ,\ \mathbf{E}_t = \mathbf{E} - (\mathbf{E}\cdot\mathbf{n})\mathbf{n}$$

2.6.3 Open Boundary 1

Equations

$$\left[-p\mathbf{I} + \mu\left(\nabla\mathbf{u} + (\nabla\mathbf{u})^{T}\right)\right]\mathbf{n} = -f_0\mathbf{n}$$

2.7 Mesh 1

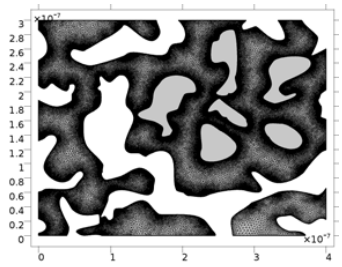

Mesh 1

3 Study 2

Computation information

Computation time	
CPU	Intel(R) Xeon(R) CPU E5-4650 0 @ 2.70GHz, 32 cores
Operating system	Linux

3.1 Parametric Sweep

Parameter name	Parameter value list
surfq	range(-0.005,0.0025,0.005)
bulk	10^{range(-1,1,3)}
Esink	range(2,-1,-2)

3.2 Stationary

Study settings

Description	Value
Include geometric nonlinearity	Off

Physics and variables selection

Physics interface	Discretization
Transport of Diluted Species (tds)	physics
Electrostatics (es)	physics
Laminar Flow (spf)	physics

Mesh selection

Geometry	Mesh
Geometry 1 (geom1)	mesh1

4 Results

4.1 Data Sets

4.1.1 Study 2/Solution 1

Solution

Description	Value
Solution	Solution 1
Component	Save Point Geometry 1

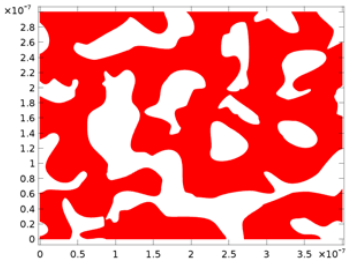

Data set: Study 2/Solution 1

4.1.2 Cut Line 2D 1

Data

Description	Value
Data set	Study 2/Solution 1

Line data

Description	Value
Line entry method	Two points
Points	{{0, 1.5e-7}, {4e-7, 1.5e-7}}
Bounded by points	Off

Advanced

Description	Value
Space variable	cln1x

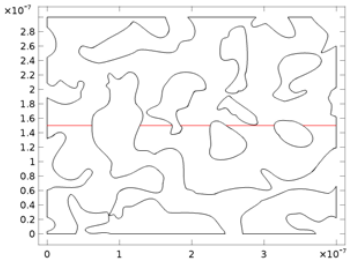

Data set: Cut Line 2D 1

4.1.3 Parametric Extrusion 2D 1

Data

Description	Value
Data set	Study 2/Solution 1

Settings

Description	Value
Level scale factor	2.000000000000001E-8

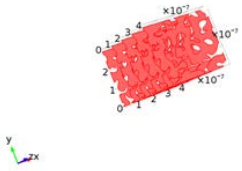

Data set: Parametric Extrusion 2D 1

4.1.4 Cut Plane 1

Data

Description	Value
Data set	Parametric Extrusion 2D 1

Plane data

Description	Value
Plane type	General
Plane entry method	Three points
Points	{{2.0E-7, 1.5E-7, 2.0E-7}, {0.7989200000000002, 1.5E-7, 0.601435}, {-0.03837600000000001, 0.9979620000000001, 0.05097730000000001}}

Advanced

Description	Value
Space variables	{cpl1x, cpl1y}

4.1.5 -5 mC Q

Data

Description	Value
Data set	Study 2/Solution 1

Settings

Description	Value
Level scale factor	1.0000000000000005E-7

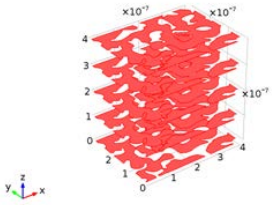

Data set: -5 mC Q

5 Plot Groups

5.1.1 Concentration (tds)

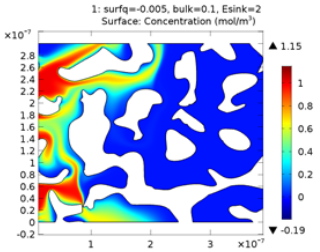

1: surfq=-0.005, bulk=0.1, Esink=2 Surface: Concentration (mol/m³)

5.1.2 Electric Potential (es)

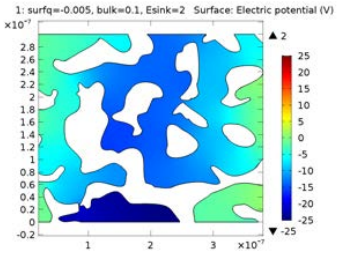

1: surfq=-0.005, bulk=0.1, Esink=2 Surface: Electric potential (V)

5.1.3 Laminar Flow

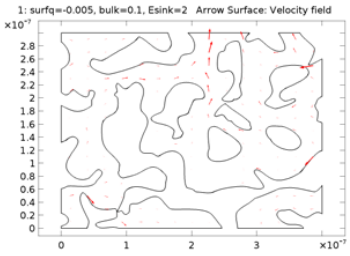

1: surfq=-0.005, bulk=0.1, Esink=2 Arrow Surface: Velocity field

5.1.4 1D Plot Group 5

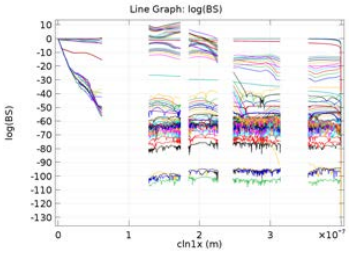

Line Graph: log(BS)

5.1.5 3D Plot Group 6

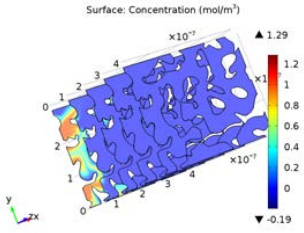

Surface: Concentration (mol/m³)

5.1.6 2D Plot Group 7

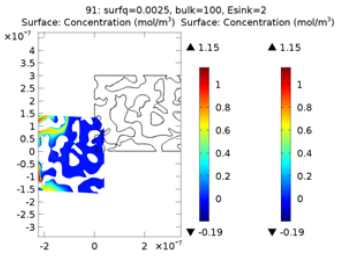

91: surfq=0.0025, bulk=100, Esink=2 Surface: Concentration (mol/m³) Surface: Concentration (mol/m³)

5.1.7 logBS

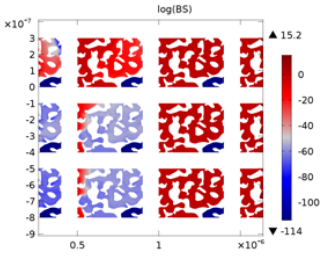

log(BS)

5.1.8 E

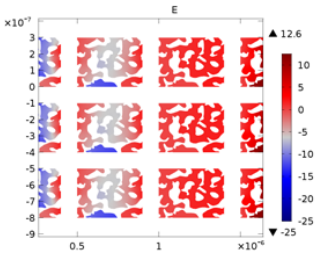

E

5.1.9 LAMINAR

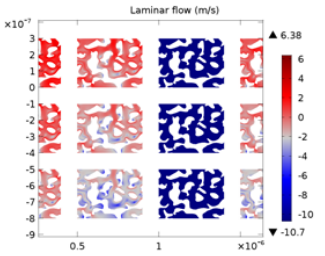

Laminar flow (m/s)

5.1.10 2D Plot Group 12

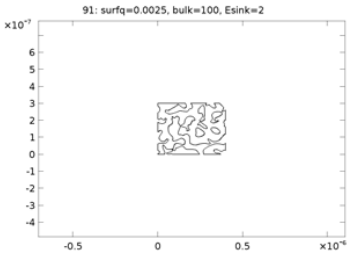

91: surfq=0.0025, bulk=100, Esink=2

A.2 Single Pore Approximation

1 Global Definitions

Date	Apr 21, 2016 10:22:08 PM

Global settings

Name	NPG porous media with EOF using transport module single porous pore approx, conductivity.mph
Path	/home/dmccurr2/windows-share/Documents/COMSOL/16.04.21/NPG porous media with EOF using transport module single porous pore approx, conductivity.mph
COMSOL version	COMSOL 5.2 (Build: 220)

Used products

COMSOL Multiphysics
AC/DC Module
Batteries & Fuel Cells Module
CFD Module

1.1 Parameters 1

Parameters

Name	Expression	Value	Description
T	298.15[K]	298.15 K	temperature
D_cat	1.957e-9[m^2/s]	1.957E−9 m²/s	cation diffusion coef
D_an	2.032e-9[m^2/s]	2.032E−9 m²/s	anion diffusion coef
D_trace	6.56e-10[m^2/s]	6.56E−10 m²/s	tracer diffusion coef
dE	-0.0225[V]	−0.0225 V	induced potential
c_feed	999[mol/m^3]	999 mol/m³	feed conc
c_sink	10[mol/m^3]	10 mol/m³	sink conc
c_trace	0.333[mol/m^3]	0.333 mol/m³	tracer conc
eps_p	0.5	0.5	Porosity
a	25[nm]	2.5E−8 m	Average pore radius
eps_w	80.2*epsilon0_const	7.1011E−10 F/m	Electric permittivity
eta	1e-3[Pa*s]	0.001 Pa·s	Dynamic viscosity
k_p	eps_p*a^2/(8*eta)	3.9063E−14 m³·s/kg	Prefactor, flow-velocity pressure term

Name	Expression	Value	Description
k_V	eps_p*eps_w*E_NPG/eta	3.0179E−8 m²/(V·s)	Prefactor, flow-velocity electroosmotic term
perm	(2*a)^2	2.5E−15 m²	permeability
zn	1	1	tracer charge
E_NPG	0.085[V]	0.085 V	NPG surface potential
Rt	25e-9[m]	2.5E−8 m	pore radius
Lcat	73.48e-4[m^2*S*mol^ - 1]	0.007348 s³·A²/(kg·mol)	conductivity from cation
Lan	76.31e-4[m^2*S*mol^ - 1]	0.007631 s³·A²/(kg·mol)	conductivity from anion
I_sink	c_sink	10 mol/m³	Sink ionic strength
I_feed	(c_feed*2 + c_trace*4 + c_trace*2)/2	1000 mol/m³	Feed ionic strength
t	dE/dE_exp	−0.19016	transport coefficient
dE_exp	-R_const*T/F_const*log(I_sink/I_feed)	0.11832 V	expeced dE
p_feed	I_feed*R_const*T	2.479E6 J/m³	
p_sink	I_sink*R_const*T	24790 J/m³	
surfq	-1e-9[C/m^2]	−1E−9 C/m²	

2 Component 1

2.1 Definitions

2.1.1 Variables

Variables 1

Selection

Geometric entity level	Entire model

Name	Expression	Unit	Description
k	1/sqrt((eps_w*k_B_const*T)/(2*N_A_const*(e_const^2)*I))	1/m	debye length
I	0.5*(cat + an + tracer*zn^2)	mol/m^3	ionic strength
sigma	-sqrt(8*(abs(cat)/1000)*eps_w*R_const*T)*sinh((1*e_const*E_NPG)/(2*k_B_const*T))	C/m^2	surface charge density
r_eo	k_V*Vr	m/s	electro-osmotic term,

Name	Expression	Unit	Description
			r
z_eo	k_V*Vz	m/s	electro-osmotic term, z
rho	cat*F_const + an*F_const* - 1 + tracer*F_const*2	C/m^3	space charge density
lambda	(2*(0.5*abs(cat + an)/1000*1[1/mol]*e_const^2)/(eps_w*k_B_const*T))^(-1/2)	m	debye length
ai	Rt/lambda		Length scale vs Debye Length
zeta	surfq*lambda/eps_w	V	

2.1.2 Component Couplings

Integration 1

Coupling type	Integration
Operator name	intop1

Integration 2

Coupling type	Integration
Operator name	intop2

2.1.3 Coordinate Systems

Boundary System 1

Coordinate system type	Boundary system
Tag	sys1

2.2 Geometry 1

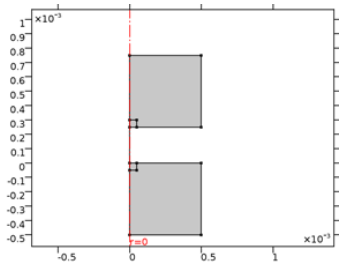

Geometry 1

Units

Length unit	m
Angular unit	deg

2.3 Materials

2.3.1 Water, liquid 1

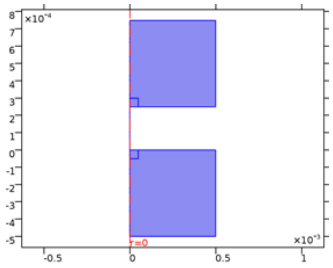

Water, liquid 1

Selection

Geometric entity level	Domain
Selection	Domains 1–7

2.4 Creeping Flow

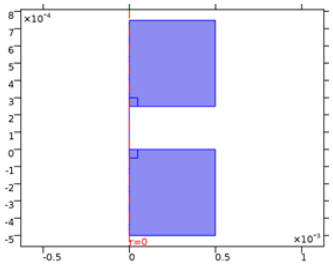

Creeping Flow

Equations

$$\rho\frac{\partial \mathbf{u}}{\partial t} =$$
$$\nabla \cdot \left[-p\mathbf{I} + \mu\left(\nabla \mathbf{u} + (\nabla \mathbf{u})^T\right)\right] + \mathbf{F}$$
$$\rho\nabla \cdot (\mathbf{u}) = 0$$

Features

Fluid Properties 1
Initial Values 1
Axial Symmetry 1
Wall 1
Open Boundary 1

2.4.1 Fluid Properties 1

Equations

$$\rho\frac{\partial \mathbf{u}}{\partial t} =$$
$$\nabla \cdot \left[-p\mathbf{I} + \mu\left(\nabla \mathbf{u} + (\nabla \mathbf{u})^T\right)\right] + \mathbf{F}$$
$$\rho\nabla \cdot (\mathbf{u}) = 0$$

2.4.2 Wall 1

Equations

$$\mathbf{u} = \mathbf{0}$$

2.4.3 Open Boundary 1

Equations

$$\left[\mu\left(\nabla \mathbf{u} + (\nabla \mathbf{u})^T\right)\right]\mathbf{n} = 0$$

2.5 Transport of Diluted Species

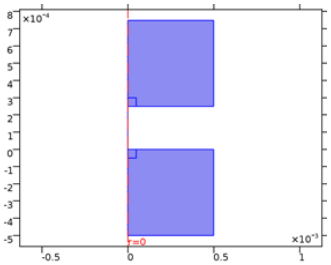

Transport of Diluted Species

Equations

$$\frac{\partial c_i}{\partial t} + \nabla \cdot (-D_i\nabla c_i - z_i u_{m,i} F c_i \nabla V) + \mathbf{u} \cdot \nabla c_i = R_i$$
$$\mathbf{N}_i = -D_i\nabla c_i - z_i u_{m,i} F c_i \nabla V + \mathbf{u} c_i$$

Features

Transport Properties 1
Axial Symmetry 1
No Flux 1
Initial Values 1
Initial Values 2
Concentration 1
Concentration 2
Transport Properties 2

2.5.1 Transport Properties 1

Equations

$$\frac{\partial c_i}{\partial t} + \nabla \cdot (-D_i\nabla c_i - z_i u_{m,i} F c_i \nabla V) + \mathbf{u} \cdot \nabla c_i = R_i$$
$$\mathbf{N}_i = -D_i\nabla c_i - z_i u_{m,i} F c_i \nabla V + \mathbf{u} c_i$$

2.5.2 No Flux 1

Equations

$$-\mathbf{n} \cdot \mathbf{N}_i = 0$$

2.5.3 Concentration 1

Equations

$$c_i = c_{0i}$$

2.5.4 Concentration 2

Equations

$$c_i = c_{0i}$$

2.5.5 Transport Properties 2

Equations

$$\frac{\partial c_i}{\partial t} + \nabla \cdot (-D_i \nabla c_i - z_i u_{m,i} F c_i \nabla V) + \mathbf{u} \cdot \nabla c_i = R_i$$

$$\mathbf{N}_i = -D_i \nabla c_i - z_i u_{m,i} F c_i \nabla V + \mathbf{u} c_i$$

2.6 Electrostatics

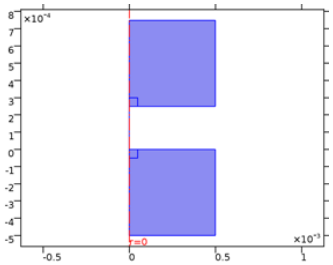

Electrostatics

Equations

$$\nabla \cdot \mathbf{D} = \rho_v$$

$$\mathbf{E} = -\nabla V$$

Features

Charge Conservation 1
Axial Symmetry 1
Zero Charge 1
Initial Values 1
Surface Charge Density 1
Ground 1
Terminal 1

2.6.1 Charge Conservation 1

Equations

$$\mathbf{E} = -\nabla V$$

$$\nabla \cdot (\epsilon_0 \epsilon_r \mathbf{E}) = \rho_v$$

2.6.2 Zero Charge 1

Equations

$$\mathbf{n} \cdot \mathbf{D} = 0$$

2.6.3 Surface Charge Density 1

Equations

$$\mathbf{n} \cdot (\mathbf{D}_1 - \mathbf{D}_2) = \rho_s$$

2.6.4 Ground 1

Equations

$$V = 0$$

2.6.5 Terminal 1

Equations

$$\int_{\partial\Omega} \mathbf{D} \cdot \mathbf{n} \, dS = Q_0$$

2.7 Meshes

2.7.1 Mesh 1

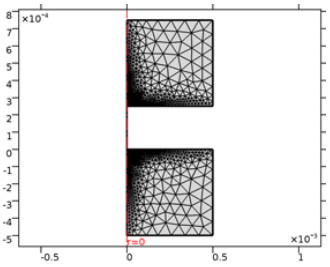

Mesh 1

2.7.2 Mesh 2

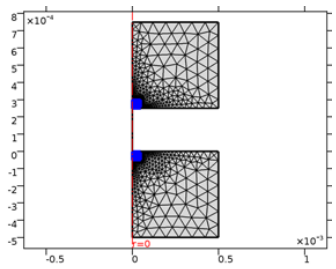

Mesh 2

3 Study 1

Computation information

Computation time	2 min 36 s
CPU	Intel(R) Xeon(R) CPU E5-4650 0 @ 2.70GHz, 32 cores
Operating system	Linux

4 Study 2

Computation information

Computation time	15 min 18 s
CPU	Intel(R) Xeon(R) CPU E5-4650 0 @ 2.70GHz, 32 cores
Operating system	Linux

4.1 Time Dependent

Study settings

Description	Value
Include geometric nonlinearity	Off

Times	Unit
0,10^{range(-3,0)}	s

Physics and variables selection

Physics interface	Discretization
Creeping Flow (spf)	physics
Transport of Diluted Species (tds)	physics
Electrostatics (es)	physics

Mesh selection

Geometry	Mesh
Geometry 1 (geom1)	mesh2

5 Results

5.1 Data Sets

5.1.1 Study 1/Solution 1

Solution

Description	Value
Solution	Solution 1
Component	Save Point Geometry 1

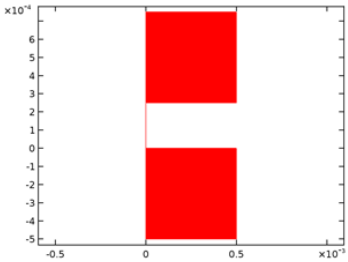

Data set: Study 1/Solution 1

5.1.2 Revolution 2D 1

Data

Description	Value
Data set	Study 1/Solution 1

Axis data

Description	Value
Axis entry method	Two points
Points	{{0, 0}, {0, 1}}

Revolution layers

Description	Value
Start angle	-90
Revolution angle	225

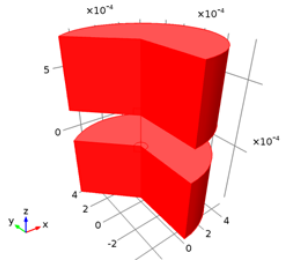

Data set: Revolution 2D 1

5.1.3 Revolution 2D 2

Data

Description	Value
Data set	Study 1/Solution 1

Axis data

Description	Value
Axis entry method	Two points
Points	{{0, 0}, {0, 1}}

Data set: Revolution 2D 2

5.1.4 No Solution (2)

Solution

Description	Value
Component	Geometry 1

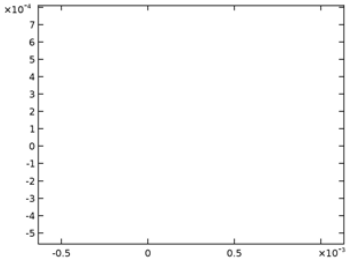

Data set: No Solution (2)

5.1.5 Revolution 2D 3

Data

Description	Value
Data set	No Solution (2)

Axis data

Description	Value
Axis entry method	Two points
Points	{{0, 0}, {0, 1}}

Revolution layers

Description	Value
Start angle	-90
Revolution angle	225

Data set: Revolution 2D 3

5.1.6 Revolution 2D 4

Data

Description	Value
Data set	No Solution (2)

Axis data

Description	Value
Axis entry method	Two points
Points	{{0, 0}, {0, 1}}

Data set: Revolution 2D 4

5.1.7 No Solution (3)

Solution

Description	Value
Component	Geometry 1

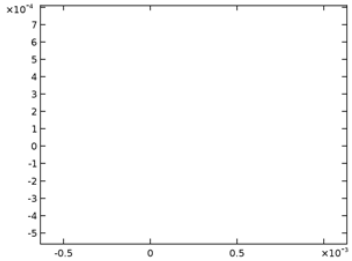

Data set: No Solution (3)

5.1.8 Revolution 2D 5

Data

Description	Value
Data set	No Solution (3)

Axis data

Description	Value
Axis entry method	Two points
Points	{{0, 0}, {0, 1}}

Revolution layers

Description	Value
Start angle	-90
Revolution angle	225

Data set: Revolution 2D 5

5.1.9 Revolution 2D 6

Data

Description	Value
Data set	No Solution (3)

Axis data

Description	Value
Axis entry method	Two points
Points	{{0, 0}, {0, 1}}

Data set: Revolution 2D 6

5.1.10 Study 2/Solution 2

Solution

Description	Value
Solution	Solution 2
Component	Save Point Geometry 1
Frame	Material (r, phi, z)

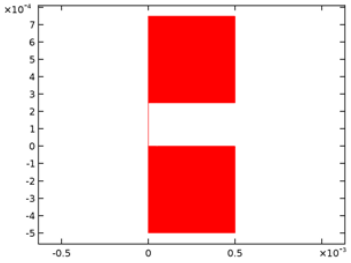

Data set: Study 2/Solution 2

5.1.11 Revolution 2D 7

Data

Description	Value
Data set	Study 2/Solution 2

Axis data

Description	Value
Axis entry method	Two points
Points	{{0, 0}, {0, 1}}

Revolution layers

Description	Value
Start angle	-90
Revolution angle	225

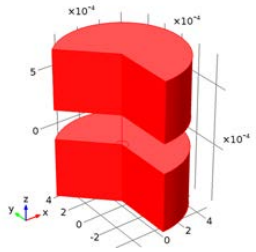

Data set: Revolution 2D 7

5.2 Plot Groups

5.2.1 Electric Potential (es)

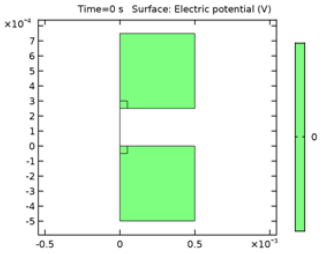

Time=0 s Surface: Electric potential (V)

5.2.2 Electric Potential, Revolved Geometry (es)

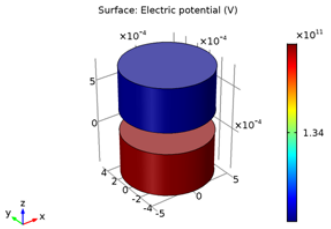

Surface: Electric potential (V)

5.2.3 1D Plot Group 5

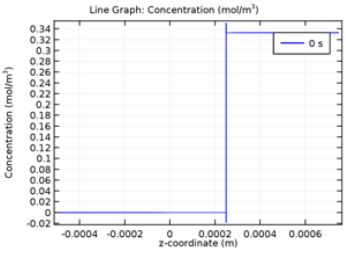

Line Graph: Concentration (mol/m^3)

5.2.4 1D Plot Group 6

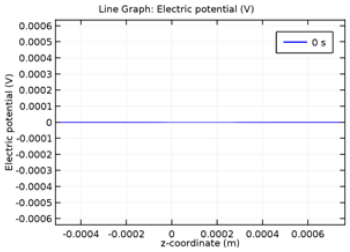

Line Graph: Electric potential (V)

5.2.5 Concentration (tds) 2

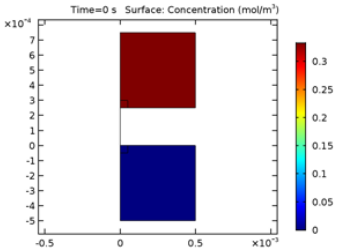

Time=0 s Surface: Concentration (mol/m^3)

5.2.6 Concentration (tds) 3

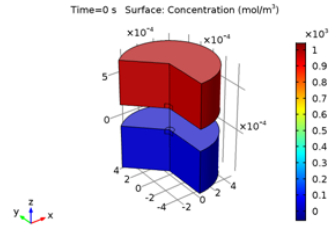

Time=0 s Surface: Concentration (mol/m^3)

5.2.7 2D Plot Group 9

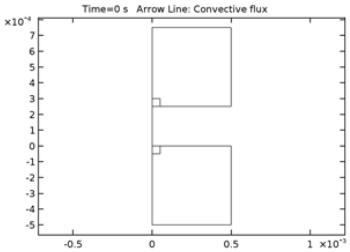

Time=0 s Arrow Line: Convective flux

5.2.8 1D Plot Group 10

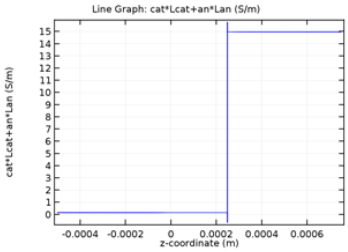

*Line Graph: cat*Lcat+an*Lan (S/m)*

5.2.9 2D Plot Group 11

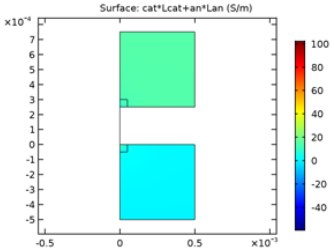

*Surface: cat*Lcat+an*Lan (S/m)*

Appendix B

LabVIEW Diagrams

B.1 Pine AFCBP1 Bipotentiostat Control

The Pine AFCBP1 bipotentiostat was connected to a PCI-6040E (PCI-MIO-16E-4) interface board. Control of the potentiostat could then be determined by the 8 digital output ports with potential offsets of each working electrode set by 2 analog output ports. Potential and current data could then be retrieved through analog input ports. Digital control of the potentiostat was performed by sending a 64 byte message packet to the potentiostat along the 8 digital I/O lines. Further information regarding the packet content and timing can be found on the Pine website, `http://www.voltammetry.net`. The source code, written in C and provided by Pine with the potentiostat, was adapted to LabVIEW as shown in the following images:

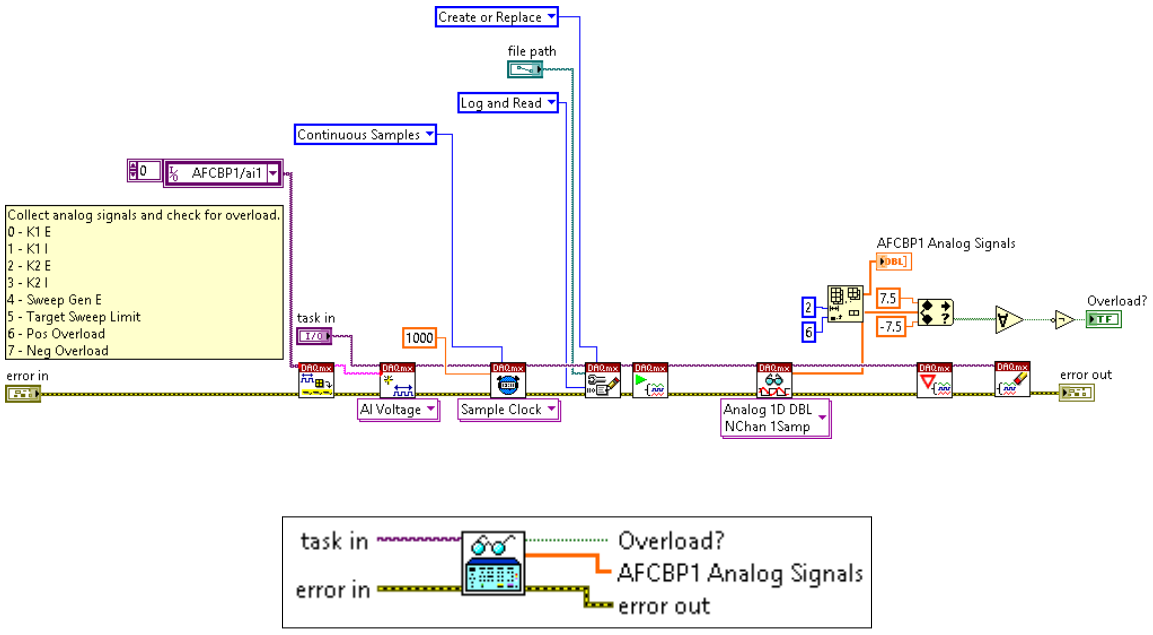

Figure B.1: SubVI to read analog data from AFCBP1 bipotentiostat.

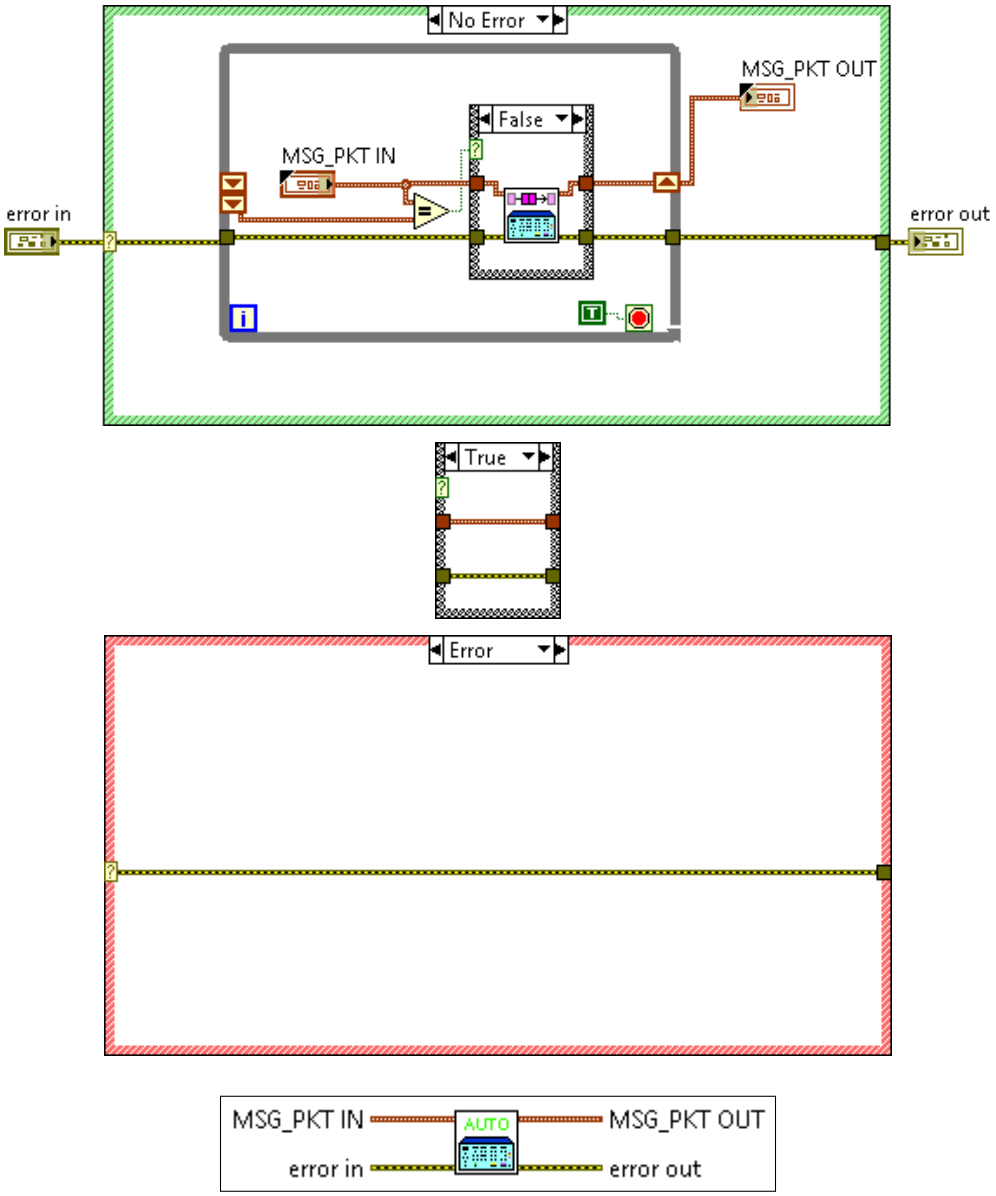

Figure B.2: SubVI to automatically send AFCBP1 potentiostat commands if they changed since last call.

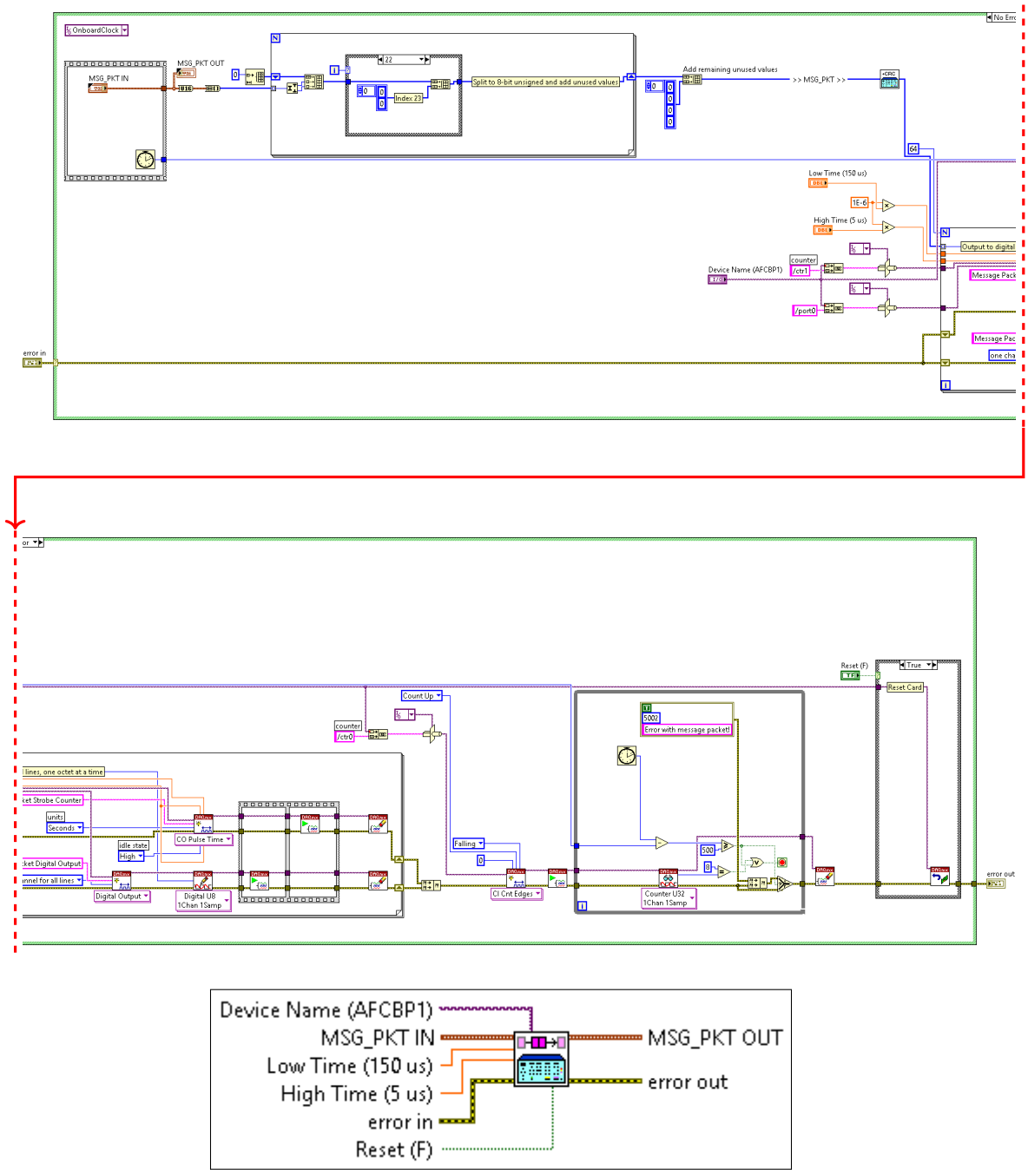

Figure B.3: SubVI for digital communications with Pine AFCBP1 potentiostat. Adapted from instrument software source code.

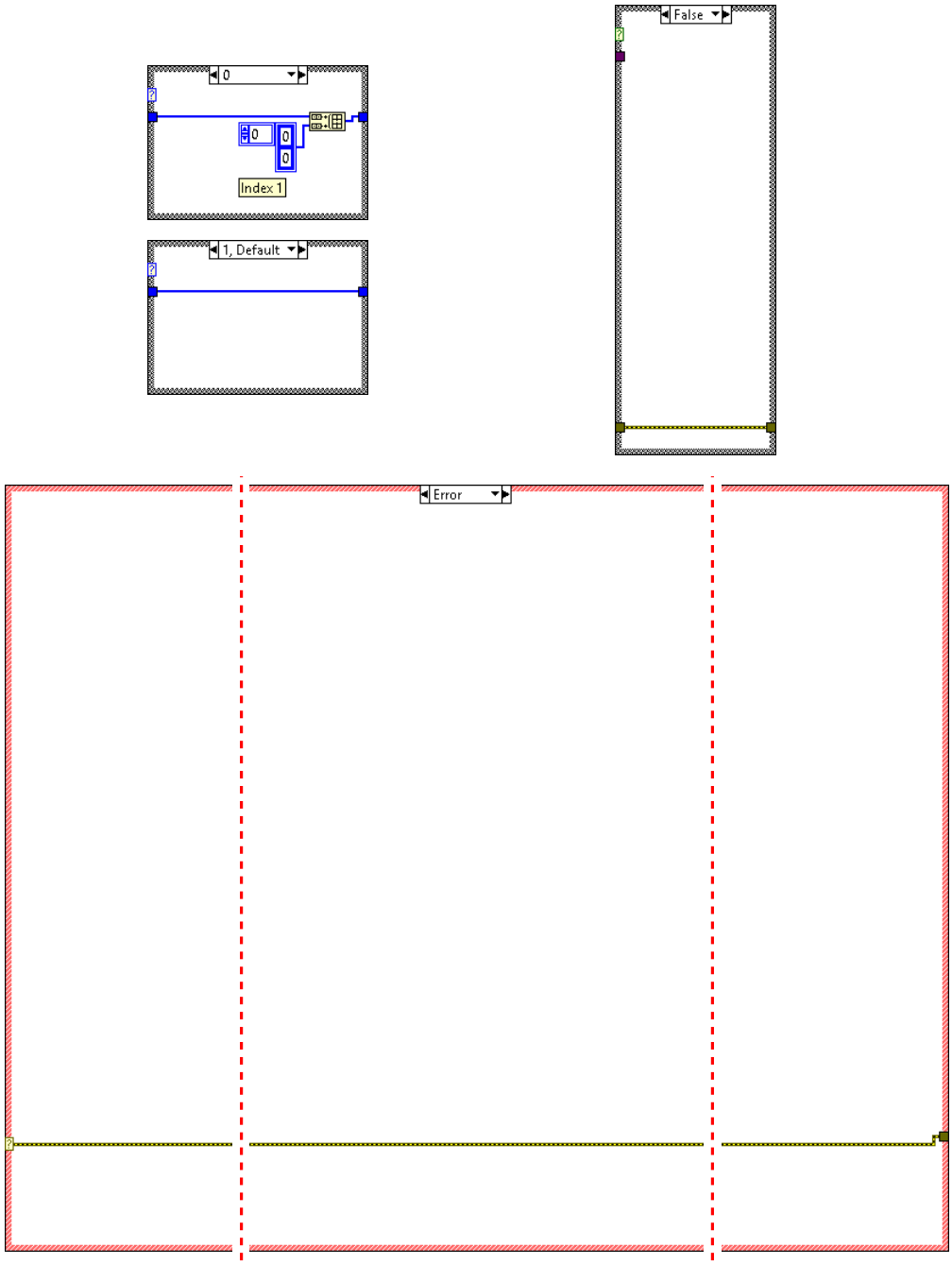

Figure B.3: *(continued)* SubVI components for digital communcations with the Pine AFCBP1 bipotentiostat.

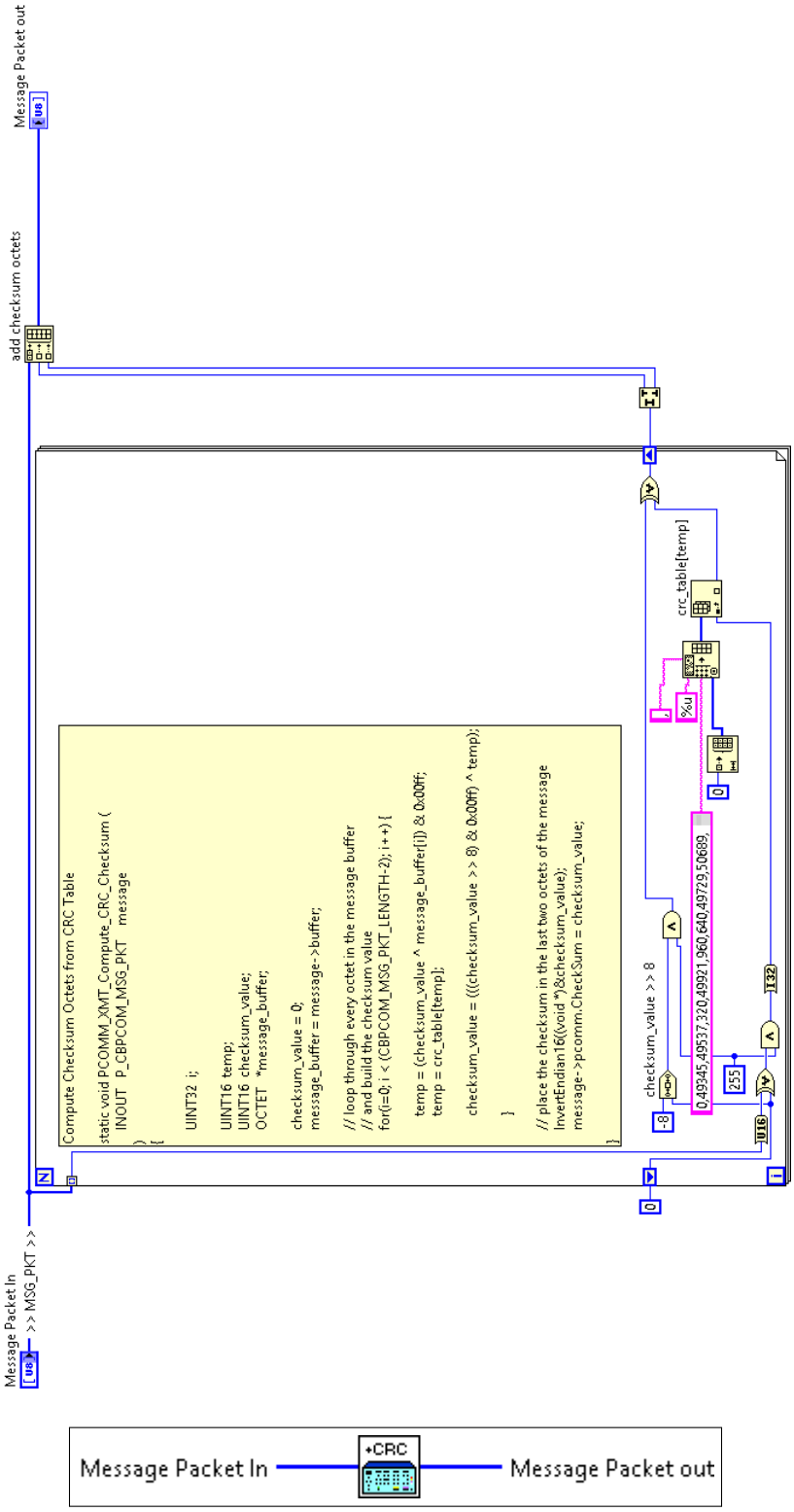

Figure B.4: SubVI included in AFCBP1 digital communications SubVI (Figure B.3) to compute the checksum of the message packet being sent to the potentiostat. Adapted from Pine AFCBP1 software source code.

B.2 Transverse and NPG Electric Potential Control

The potential to the cell was controlled using custom software that applied an array of potentials for provided amounts of time. The program would record both the applied potential and the measured current.

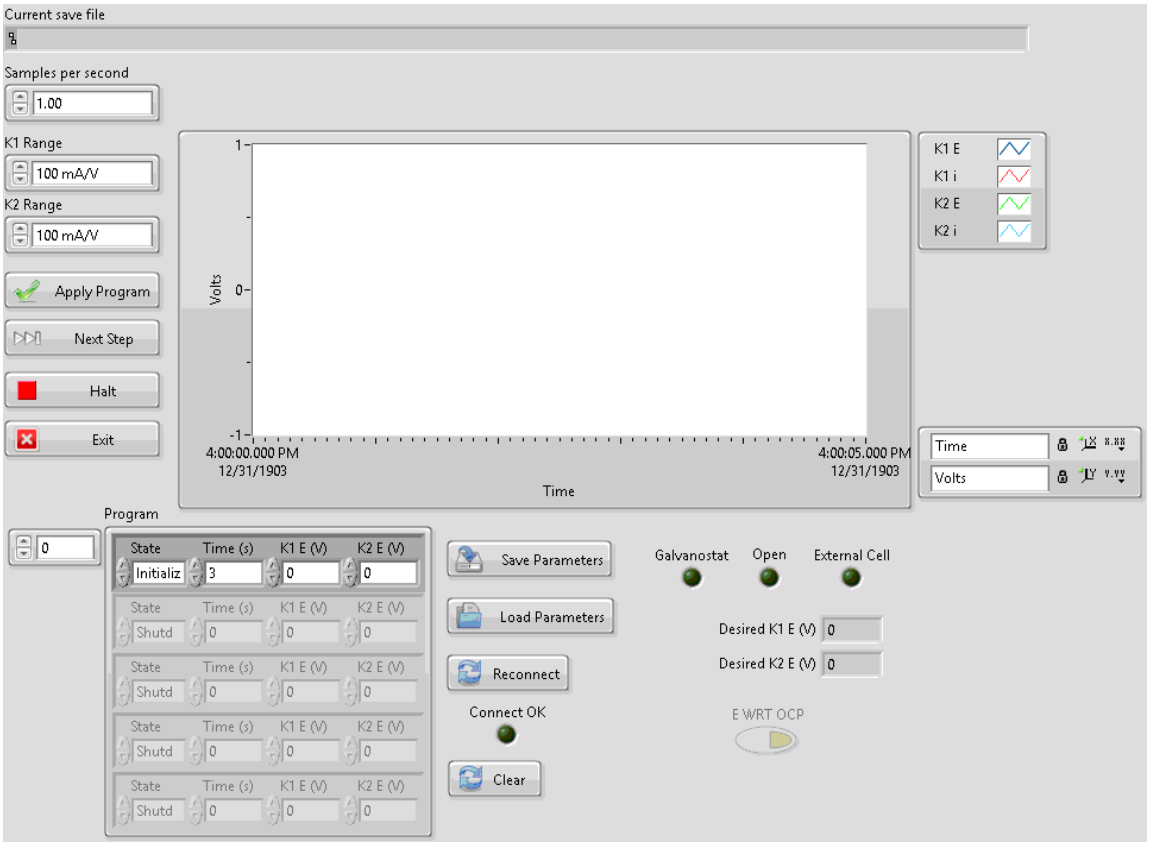

Figure B.5: Front panel display of custom Pine AFCBP1 software. Potentials can be either applied or measured for a set amount of time, depending if mode is set to "Apply E" or "OCP", respectively.

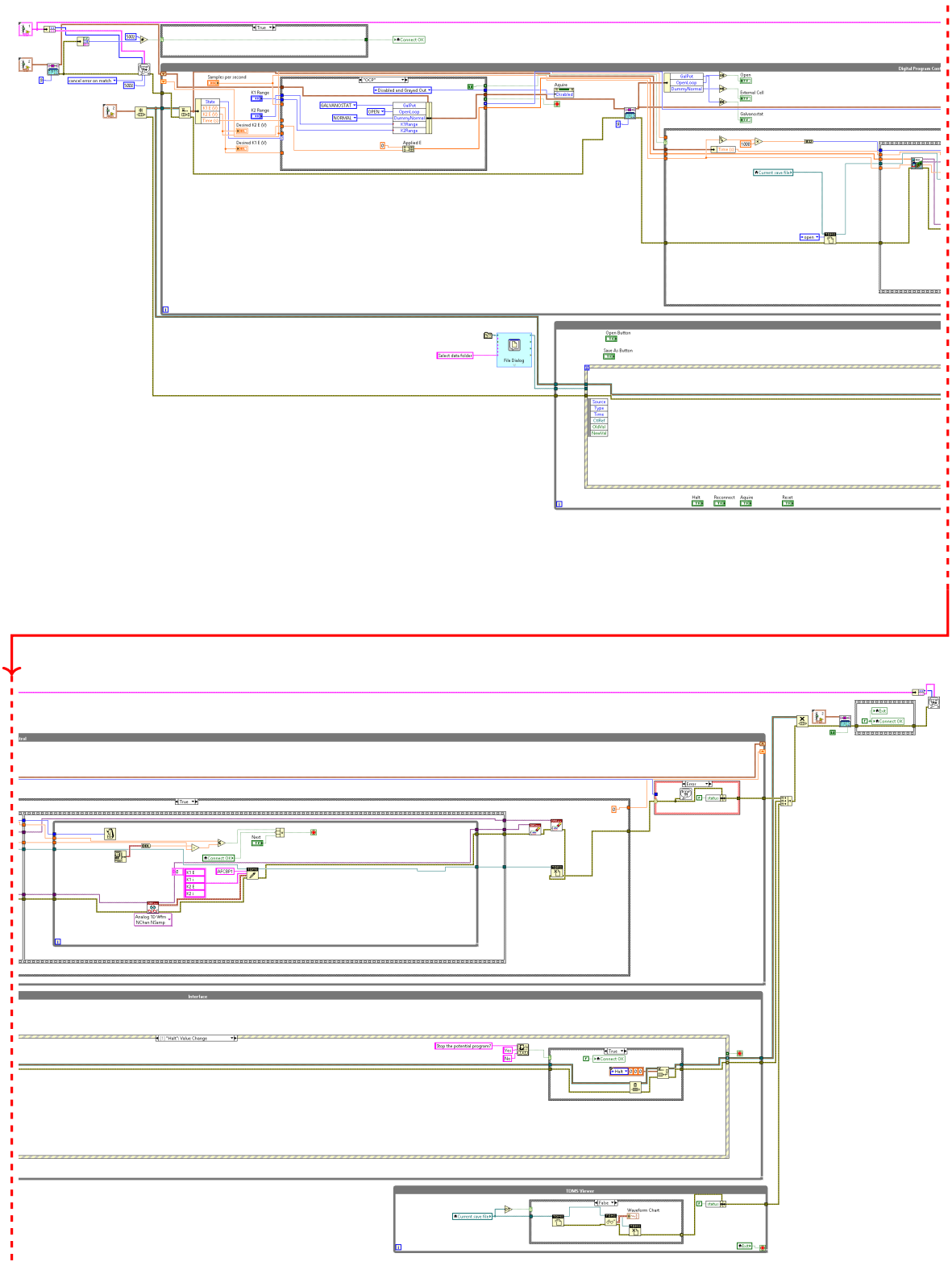

Figure B.6: Block diagram for the custom Pine AFCBP1 software.

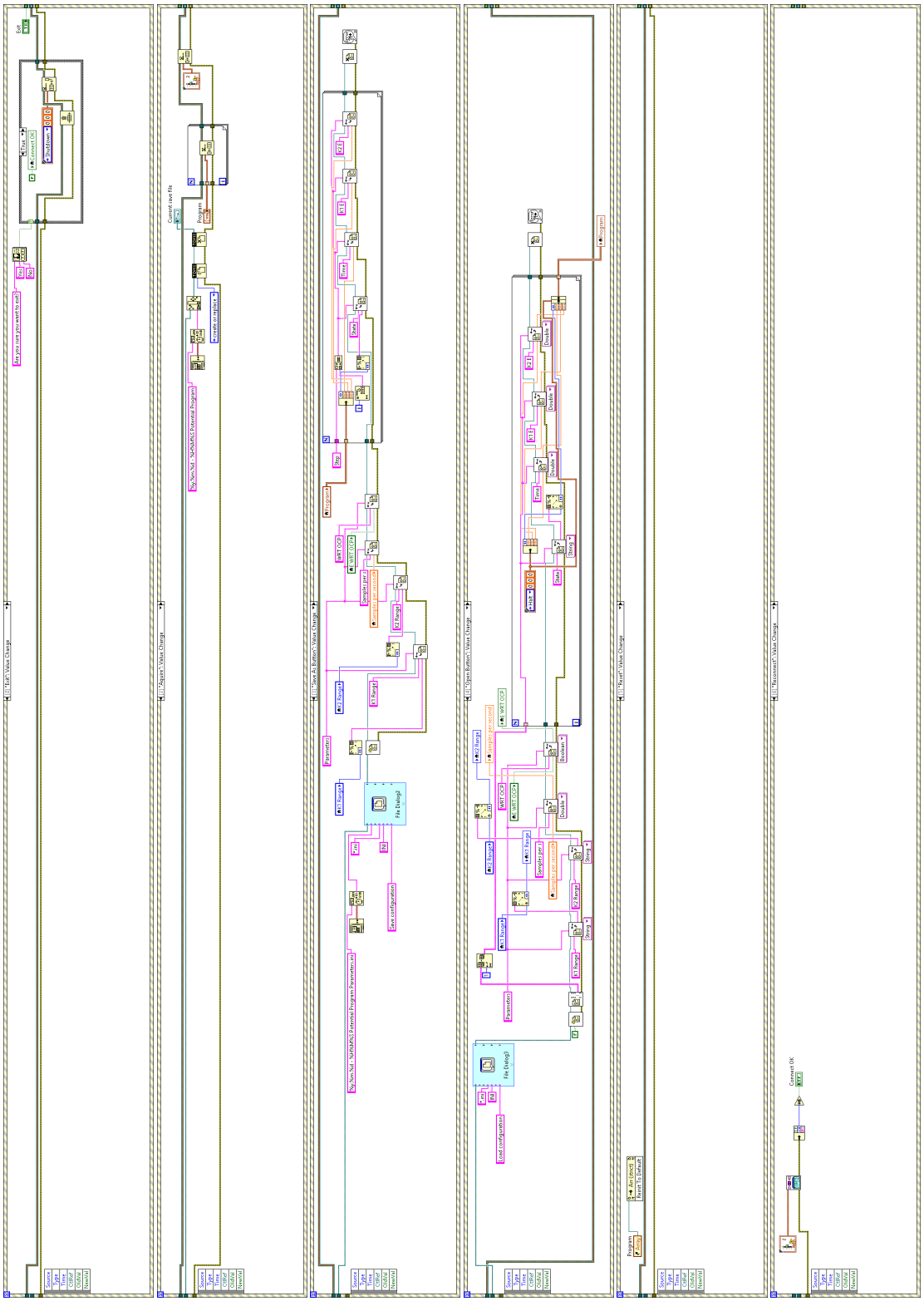

Figure B.6: *(continued)* Block diagram components for the custom Pine AFCBP1 software.

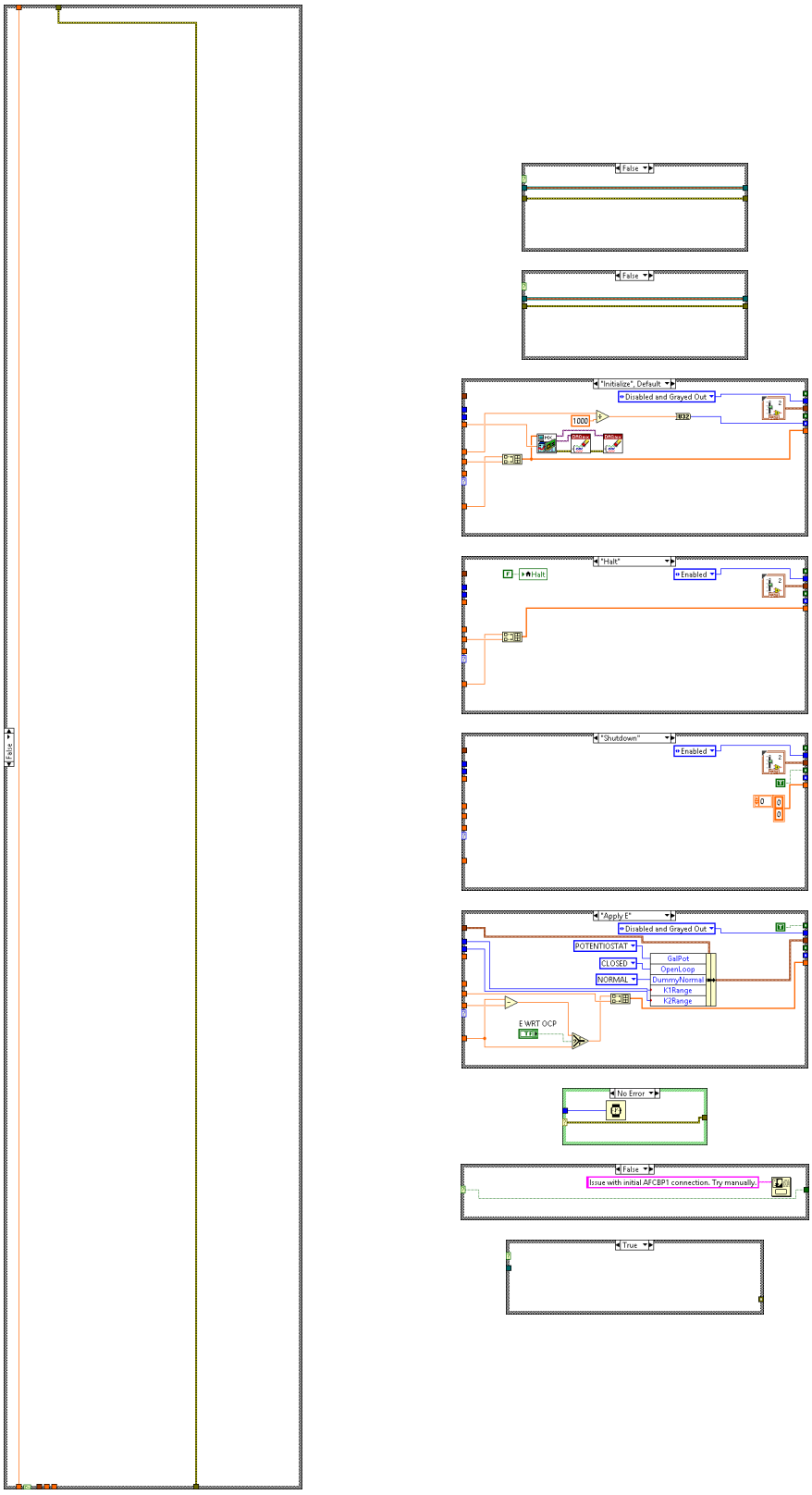

Figure B.6: *(continued)* Block diagram components for the custom Pine AFCBP1 software.

B.3 UV-Vis and Potential Difference Measurement

Salt gradient measurements required synchronized data collection of both the potential difference across the reservoirs and the UV-visible absorbance spectrum. This VI did not use the Pine AFCBP1 subVI as it was only for passive measurement. Instead, this program was interfaced with the StellarNet Black Comet spectrometer and Kiethley 2100 multimeter.

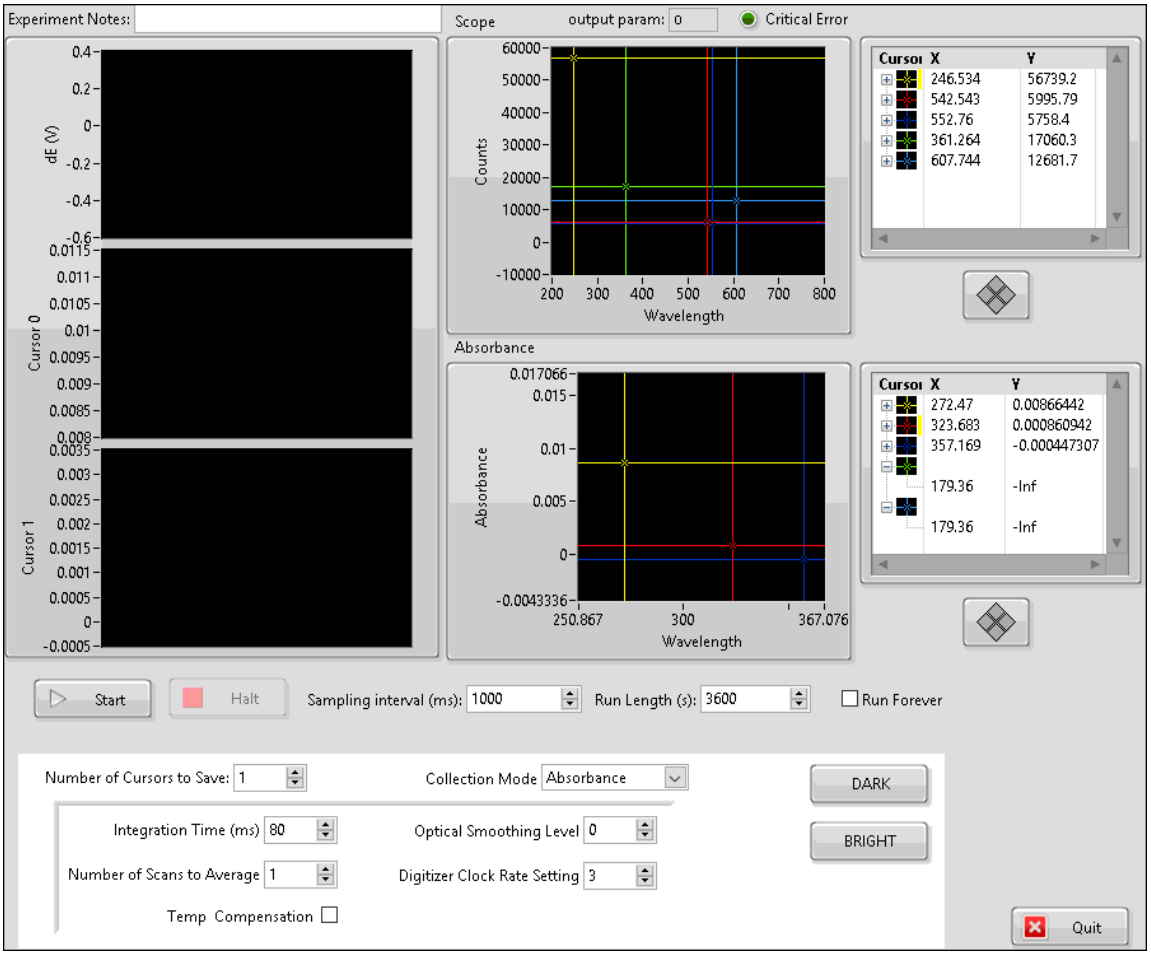

Figure B.7: Front panel for synchronized UV-visible and potentiometric measurements using the StellarNet Black Coment spectrometer and Kiethley 2100 multimeter.

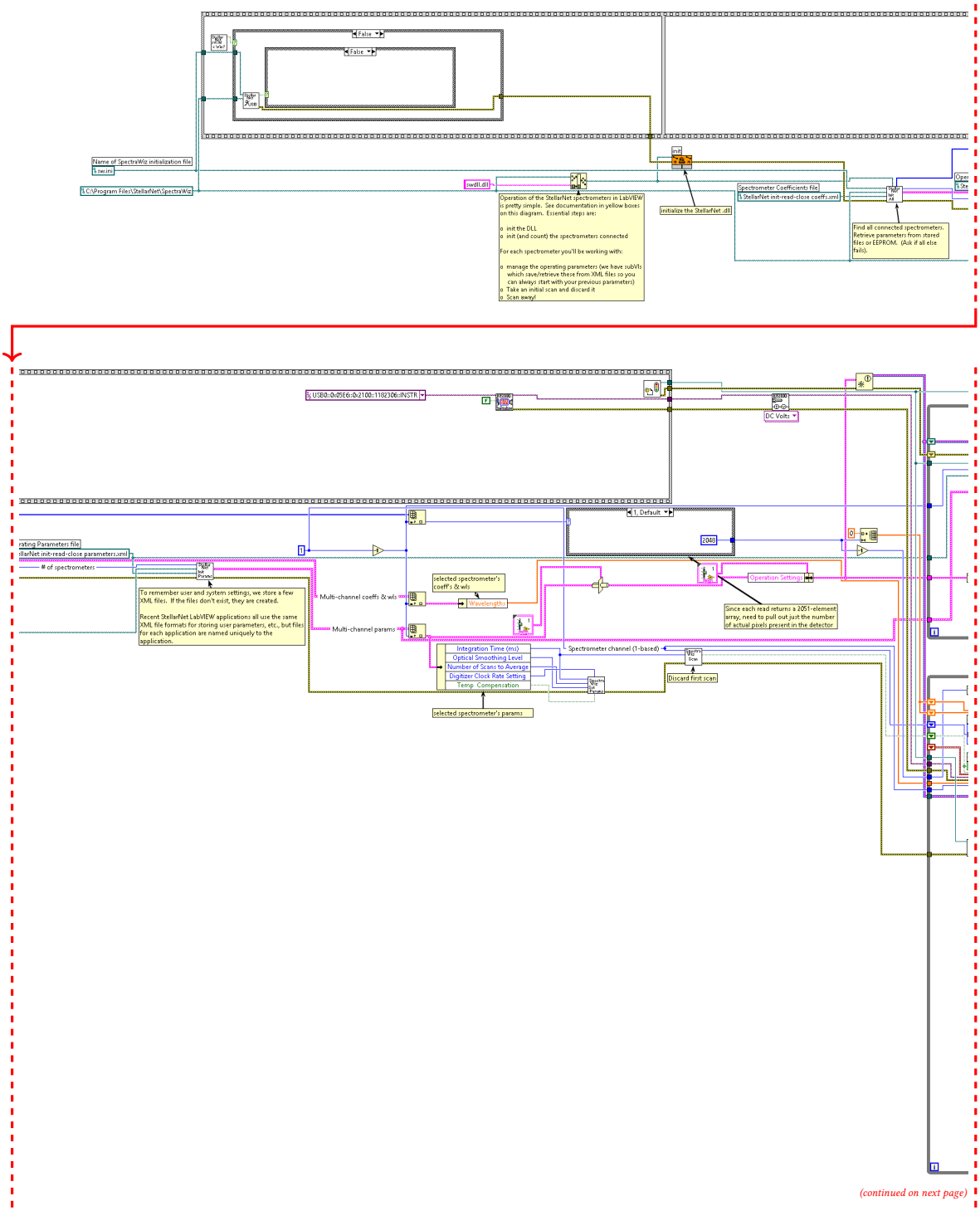

Figure B.8: Block diagram for synchronized UV-visible and potentiometric measurements.

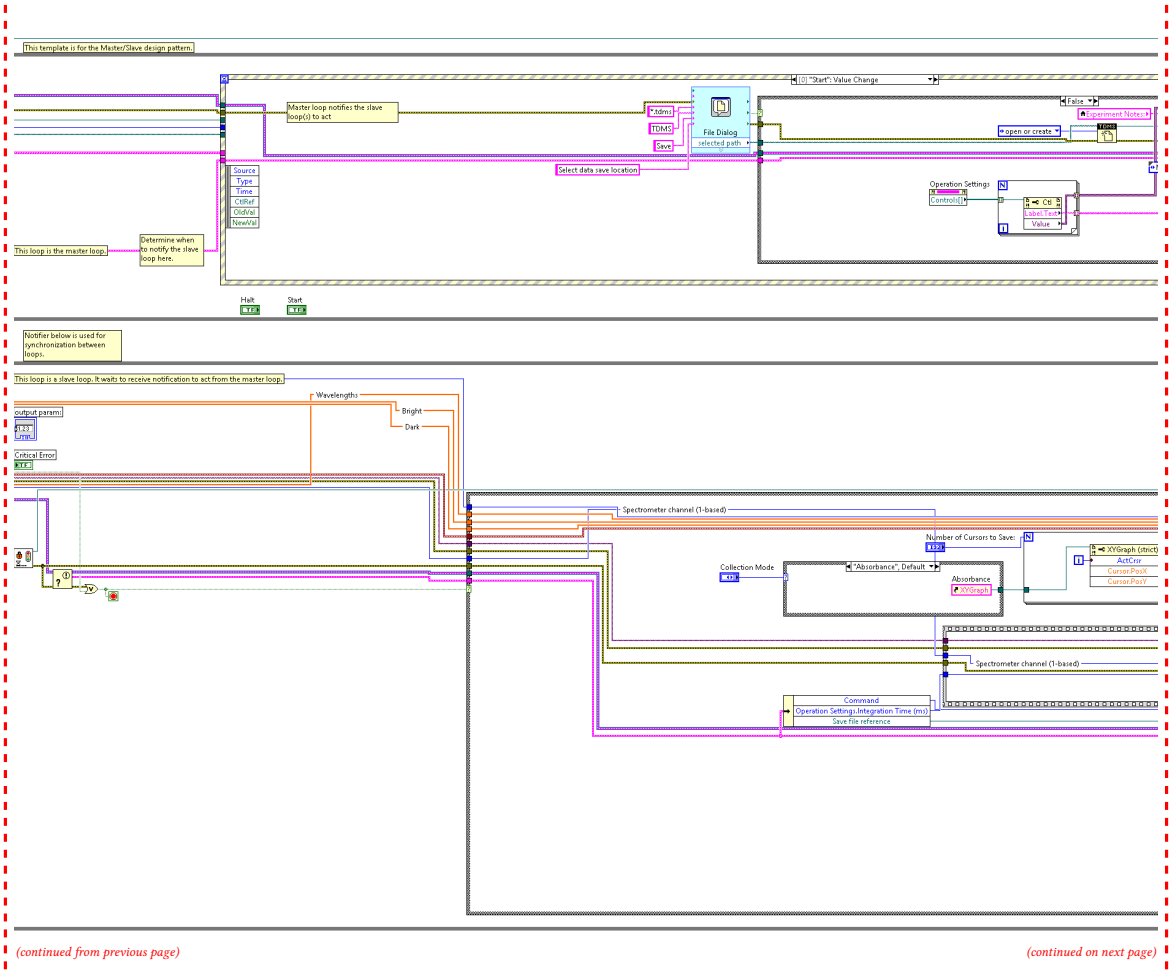

Figure B.8: *(continued)* Block diagram for synchronized UV-visible and potentiometric measurements.

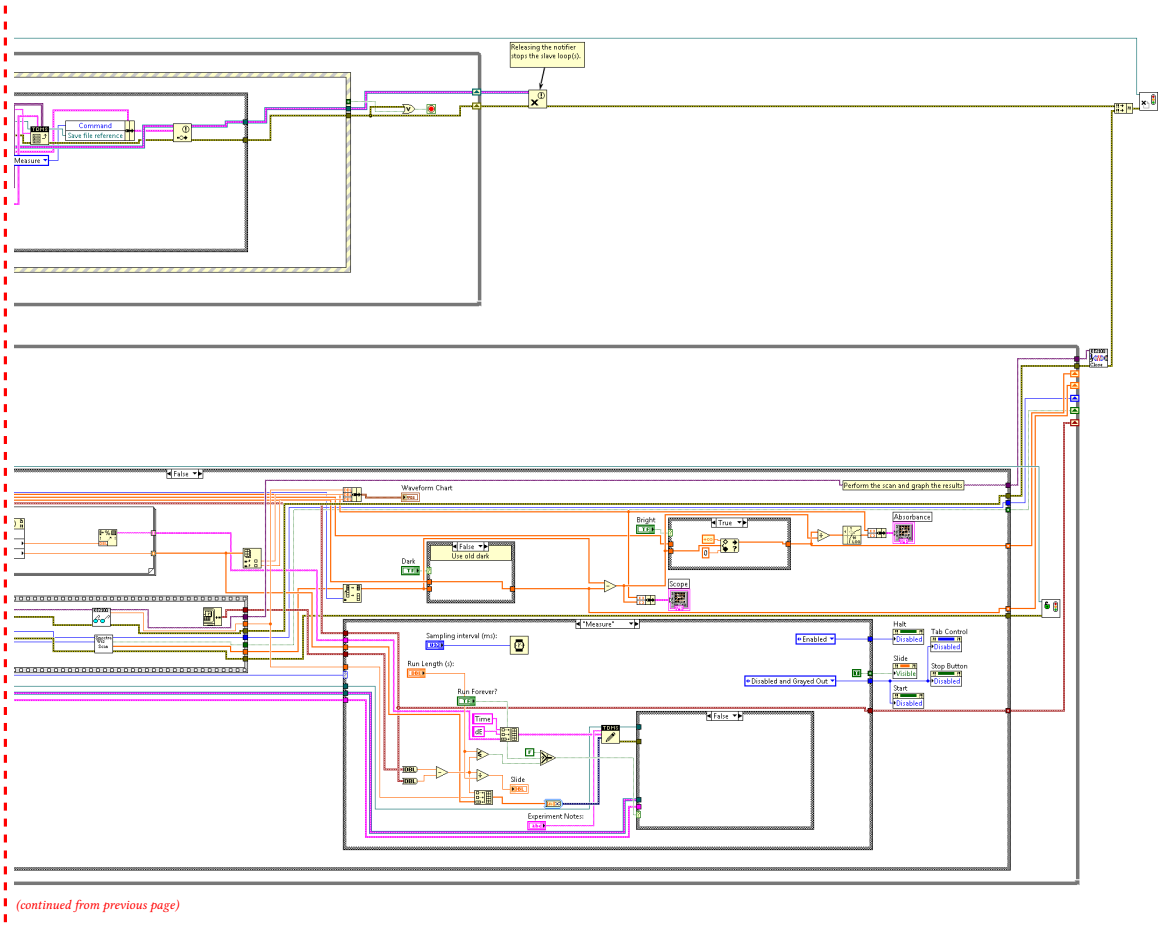

(continued from previous page)

Figure B.8: *(continued)* Block diagram for synchronized UV-visible and potentiometric measurements.

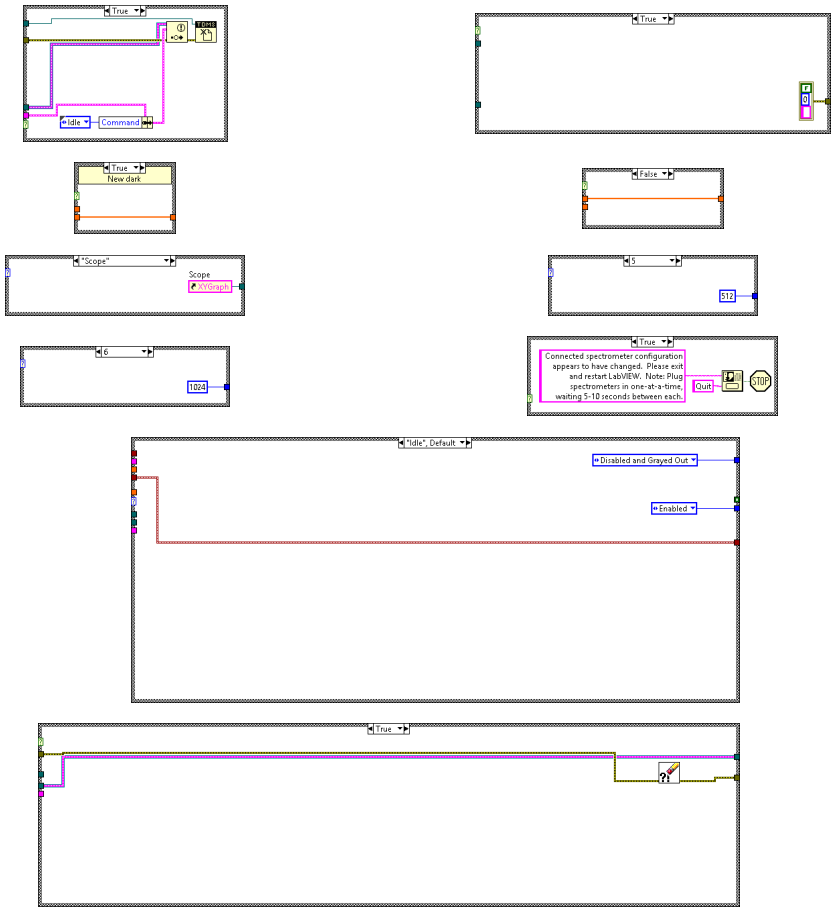

Figure B.8: *(continued)* Block diagram components for synchronized UV-visible and potentiometric measurements.

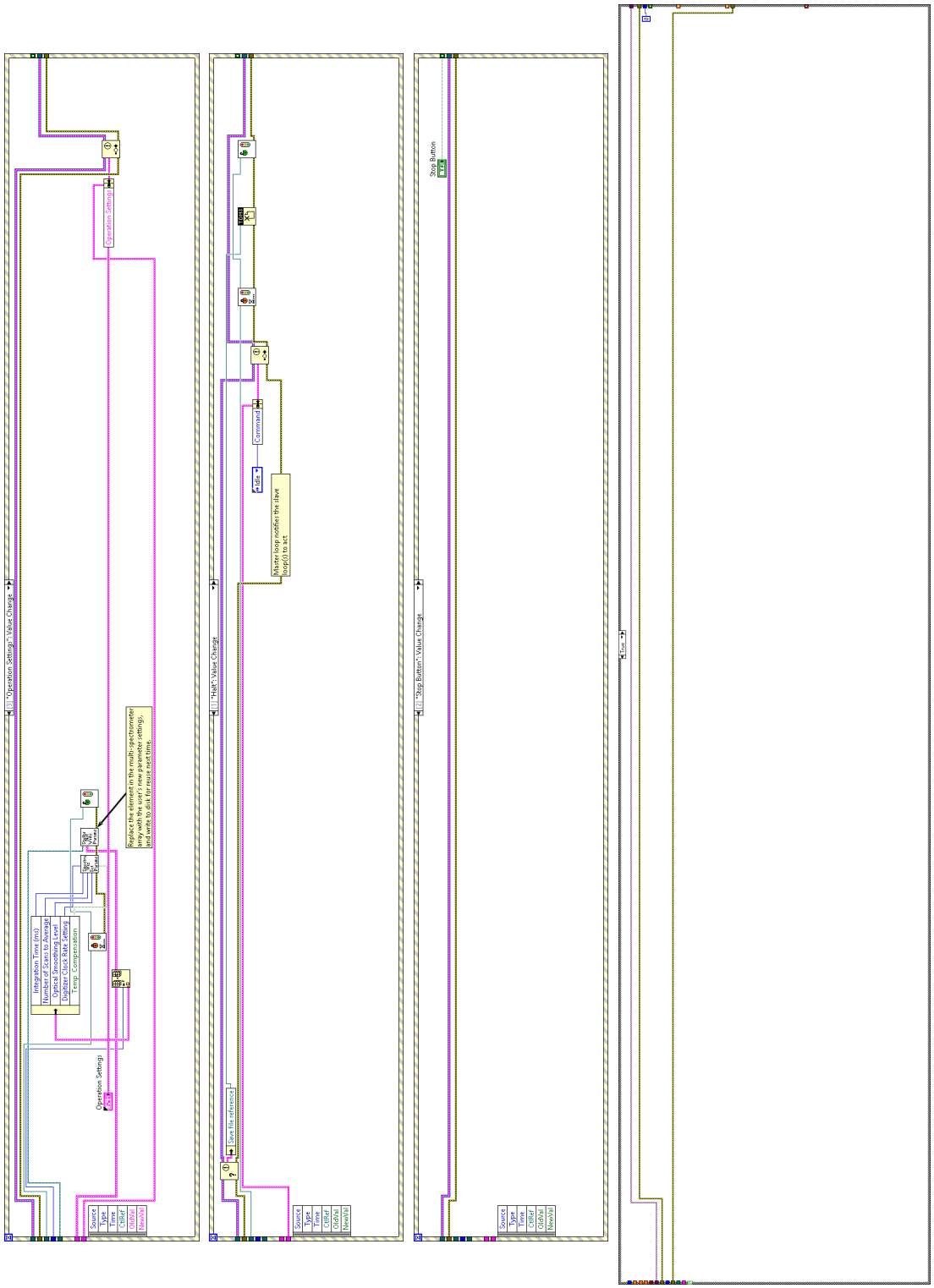

Figure B.8: *(continued)* Block diagram components for synchronized UV-visible and potentiometric measurements.

Appendix C

CAD Diagrams

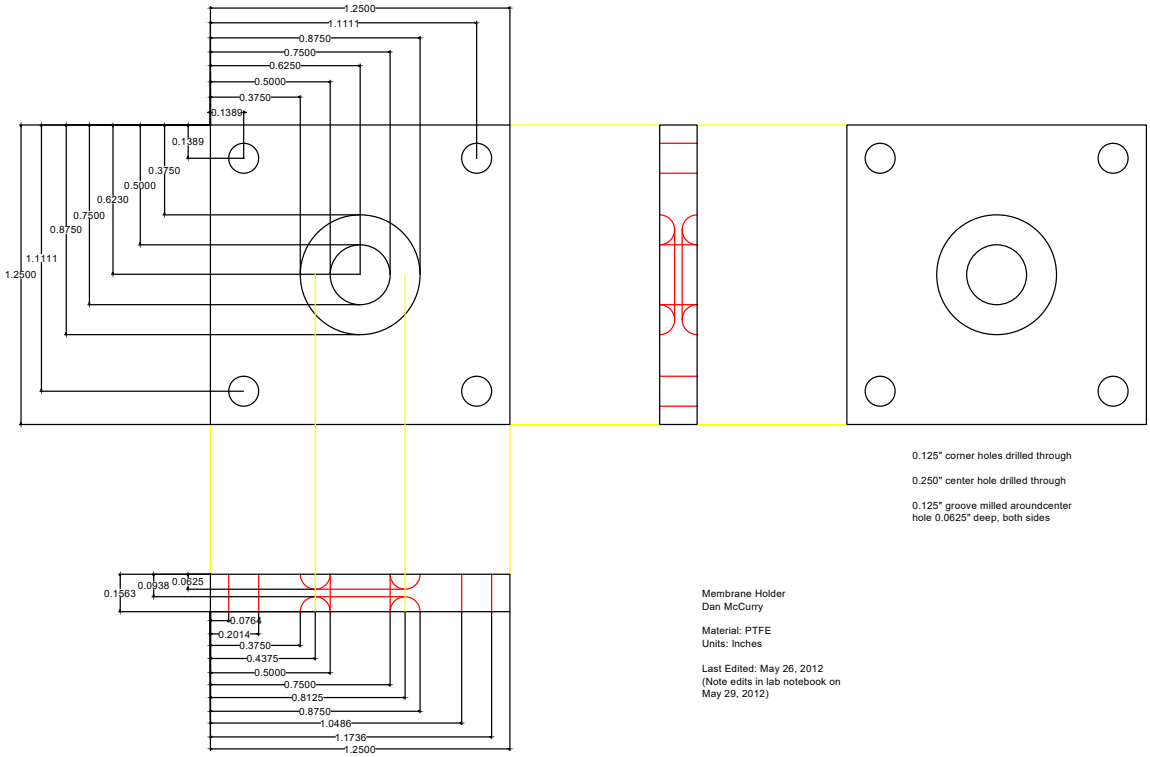

Figure C.1: An early NPG holder that was used to keep the NPG from cracking between the two glass cuvettes with sidearms.

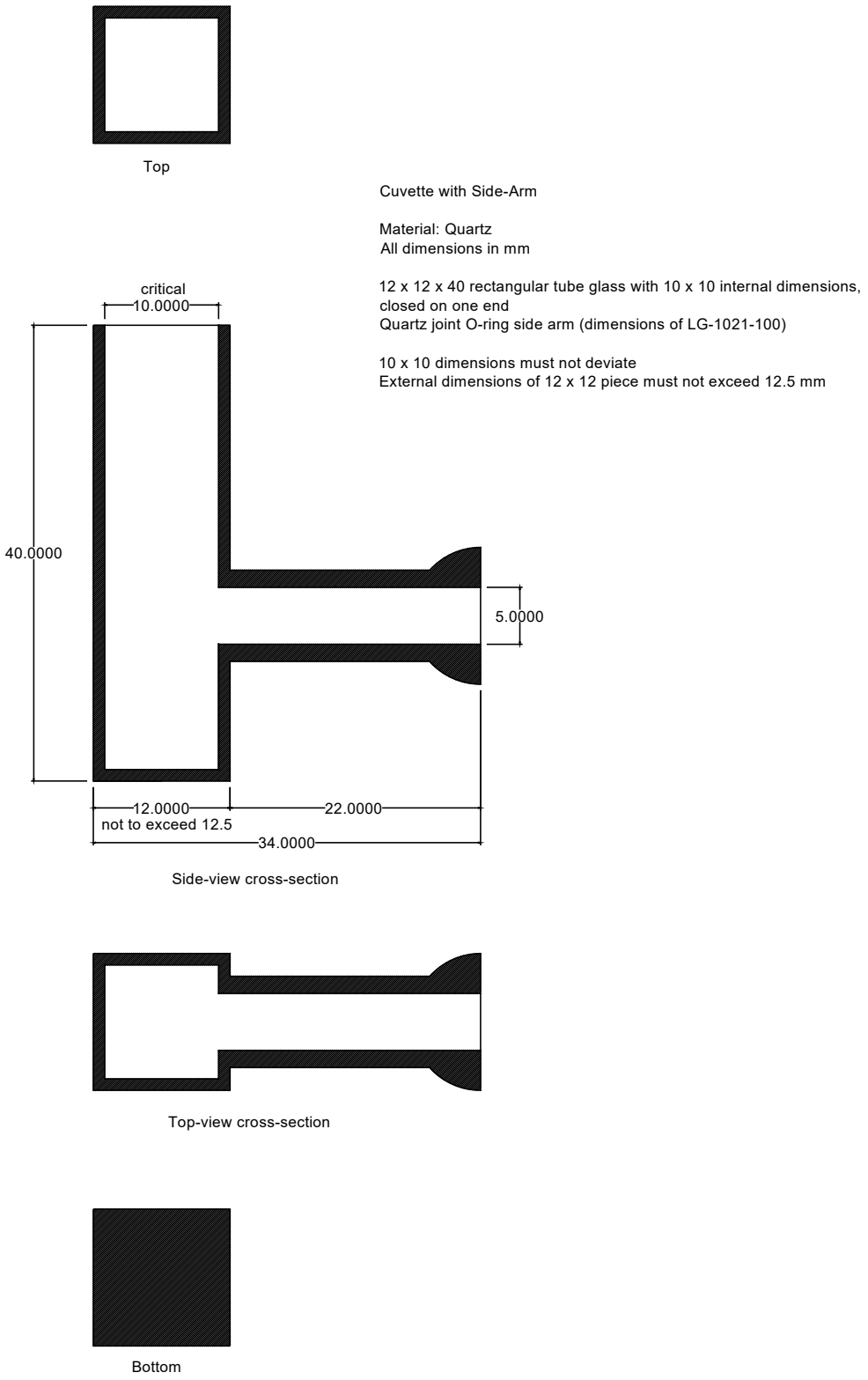

Figure C.2: Glass cuvettes were used prior to the custom PTFE or PTCFE cuvettes. These required external coupling to the fiber optics.

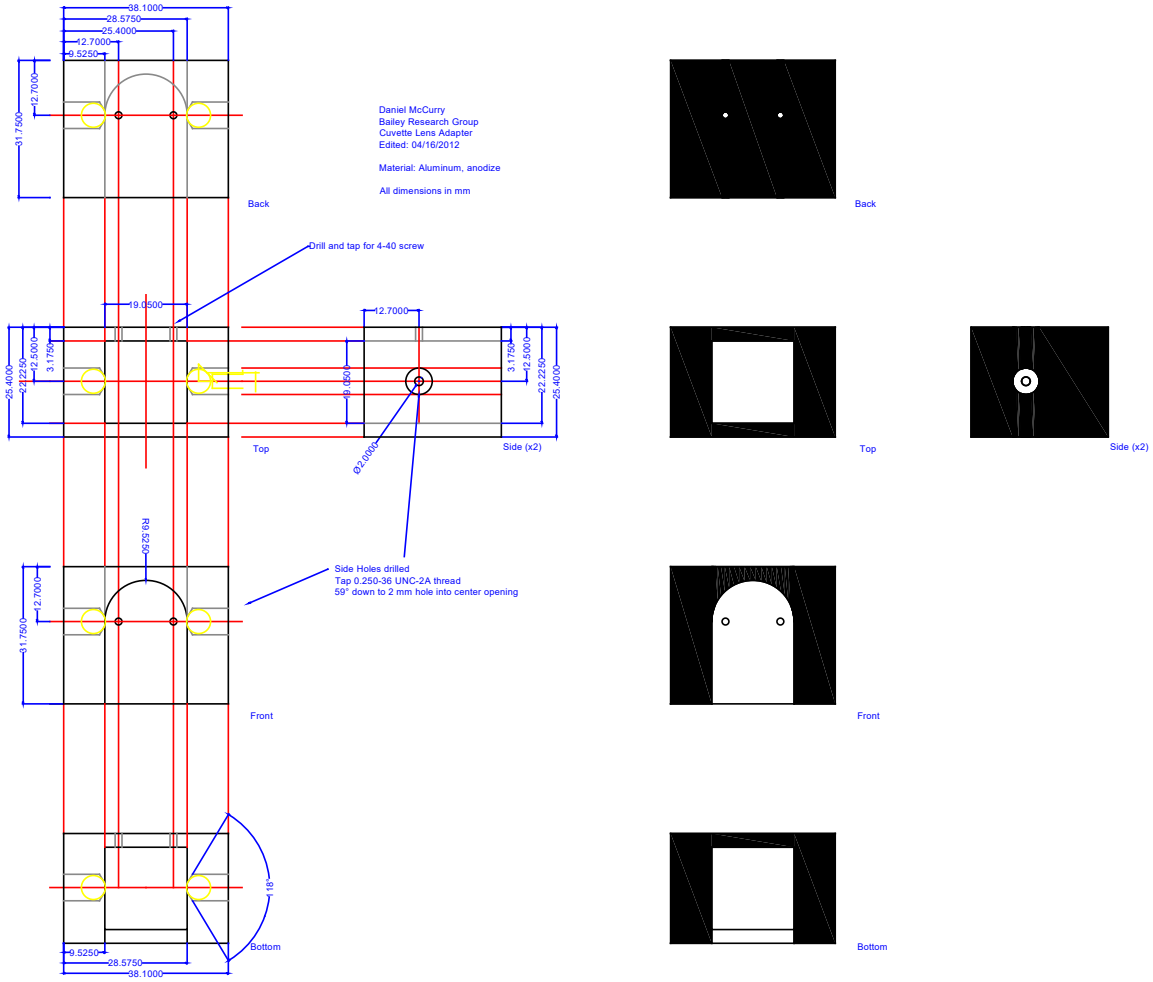

Figure C.3: This was used to align the fiber optics when using the glass cuvette assembly.

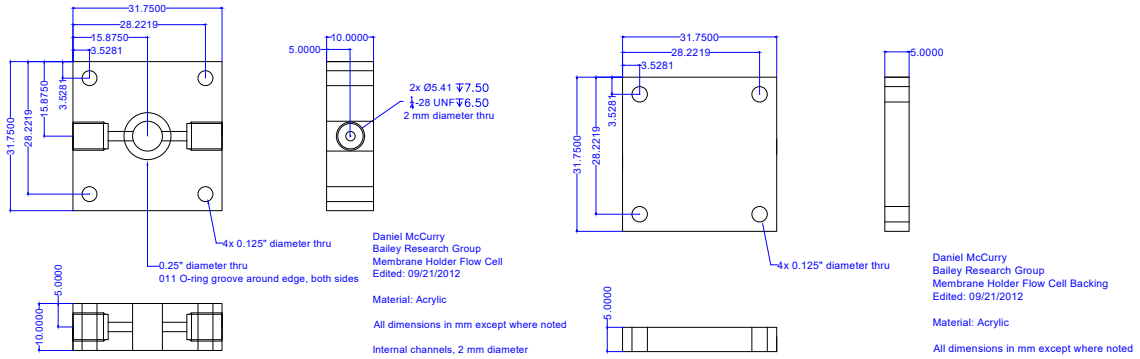

Figure C.4: The membrane holder could instead be fixed to a flow chamber to circulate and collect translocating analyte.

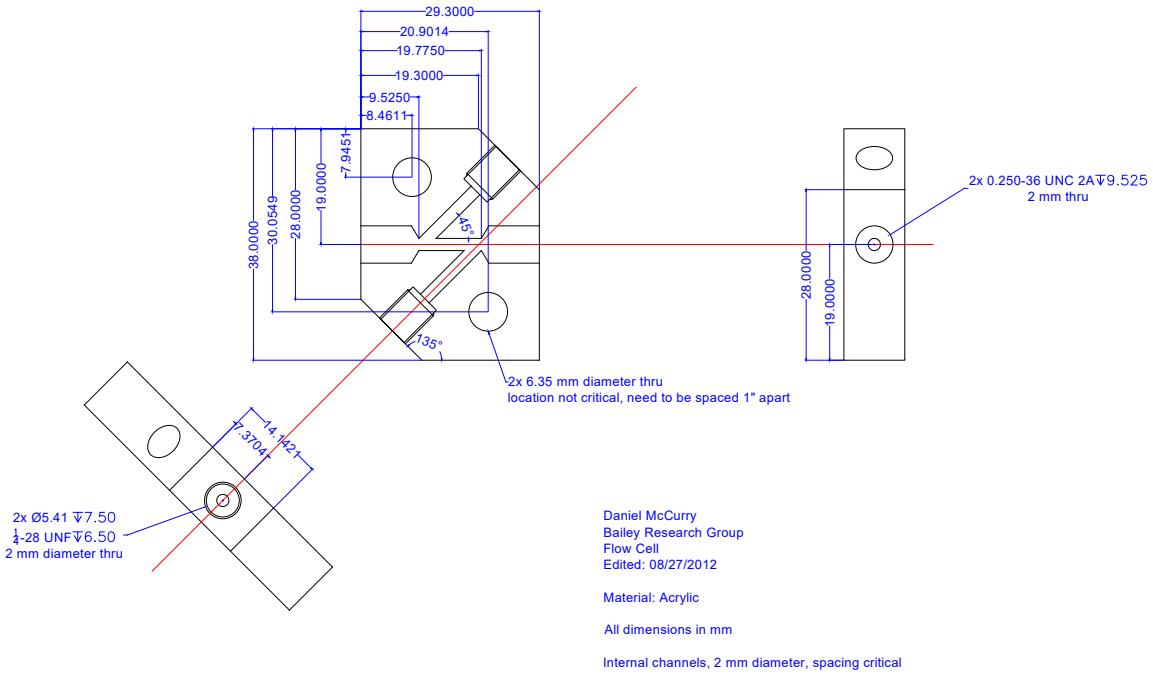

Figure C.5: When attached to a peristaltic pump, this would circulate solution through a channel for real-time UV-visible analysis.

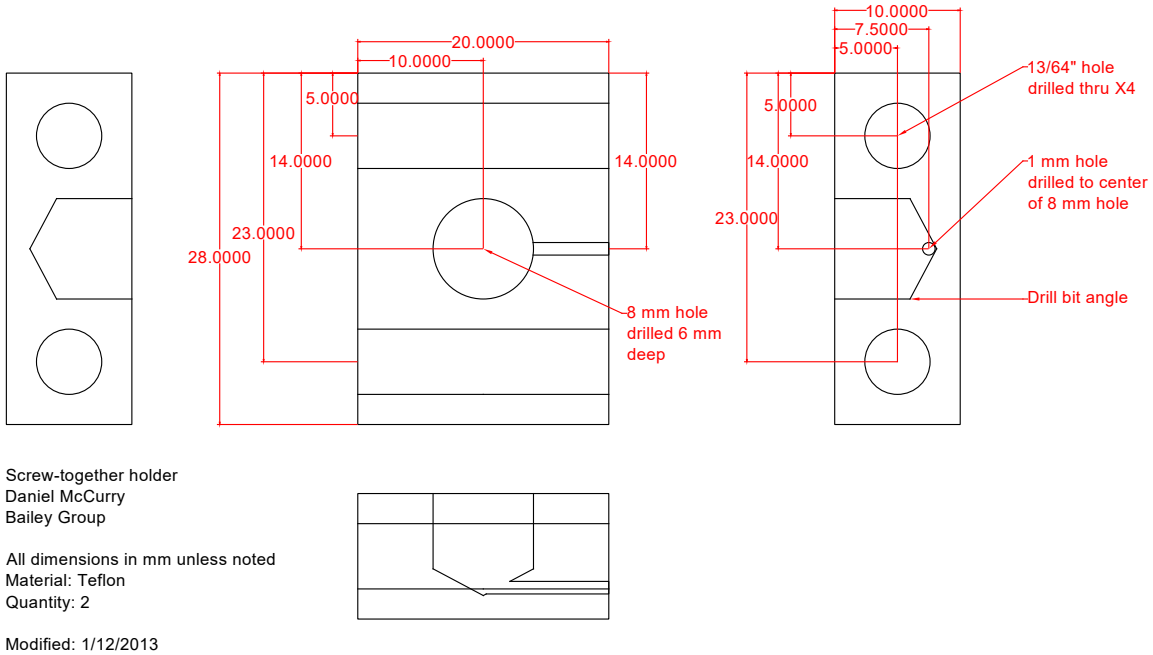

Figure C.6: Conductivity measurements were performed with the NPG sandwiched between two PTFE reservoirs.

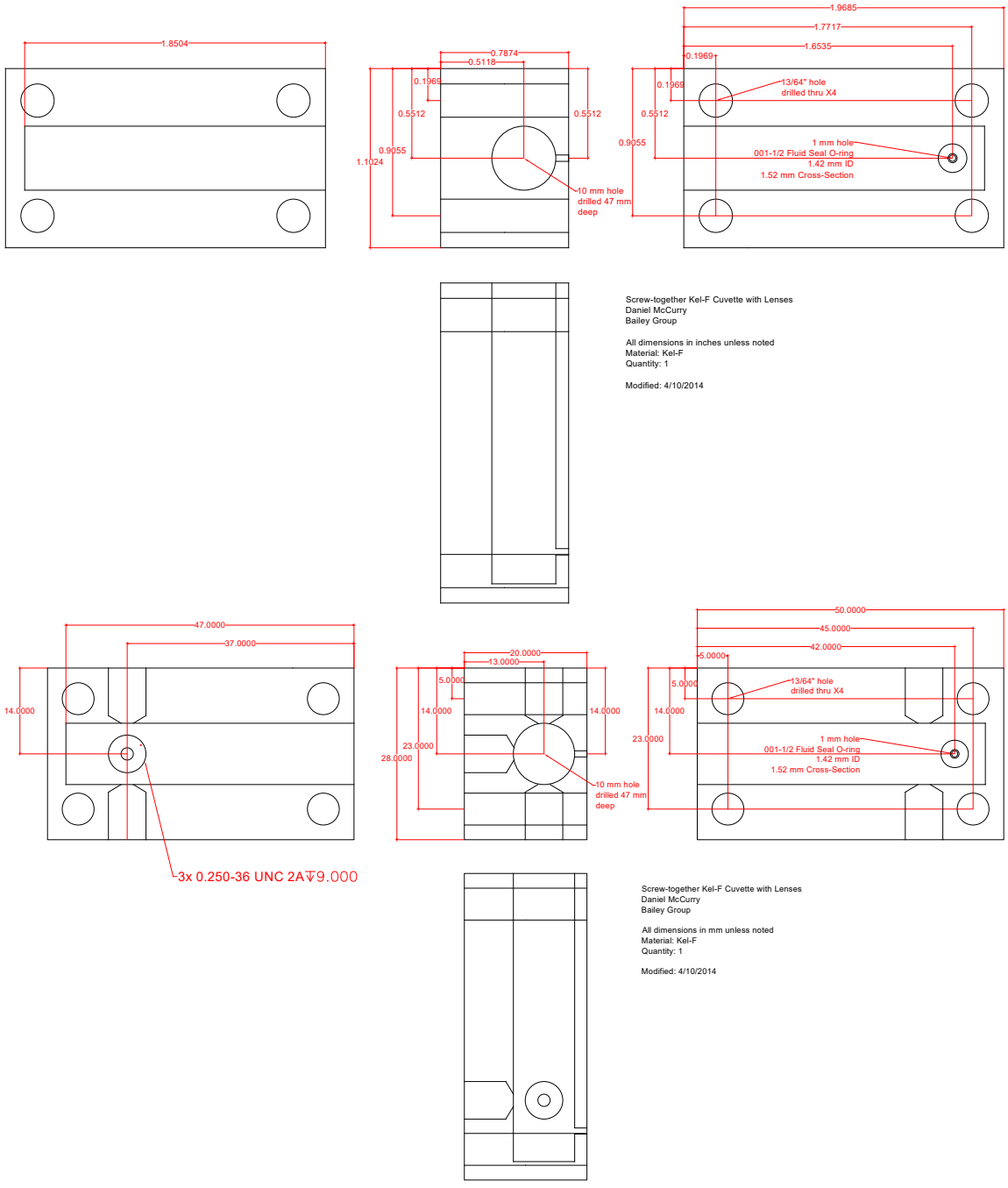

Figure C.7: Real-time absorbance measurements were taken via a fiber-optically coupled, custom reservoir assembly.

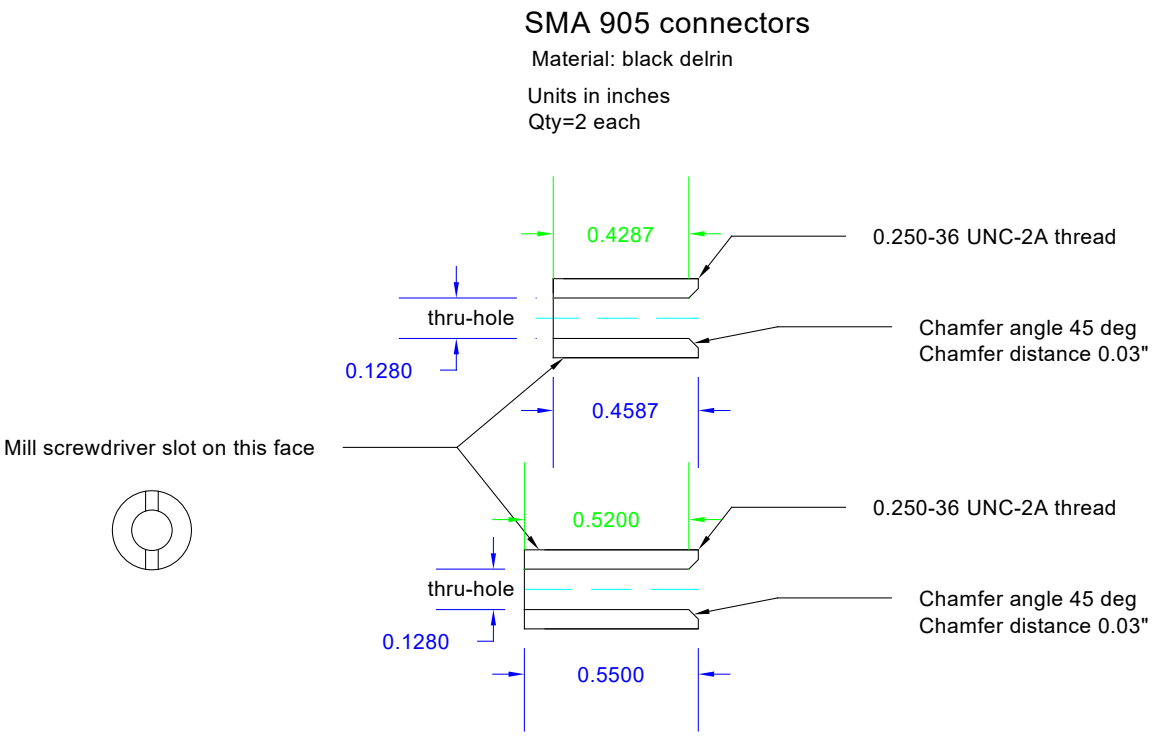

Figure C.8: SMA 905 connectors used to couple fiber optics to custom cuvettes. The chamfer on one end sealed against a glass ball lens used to collimate the light.

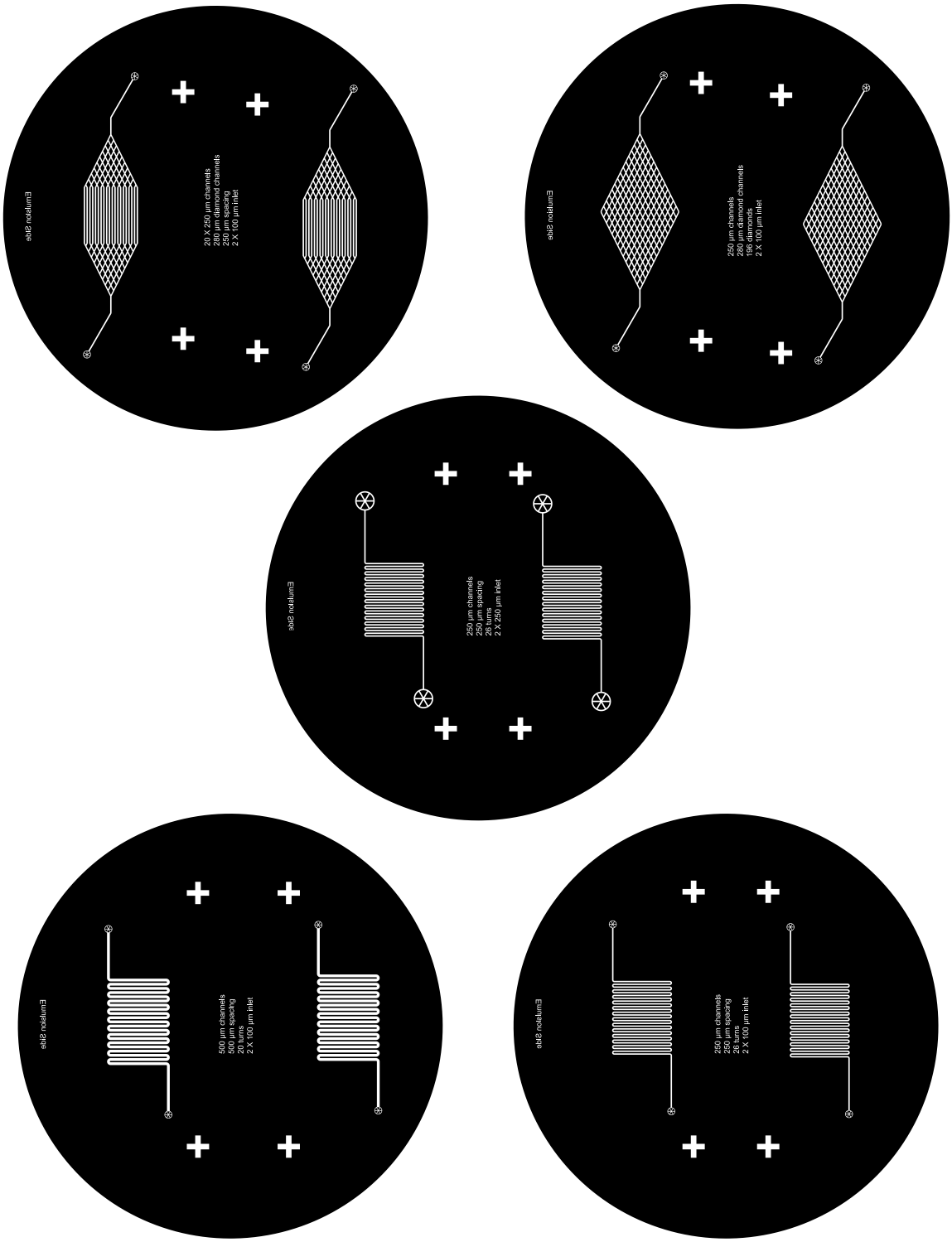

Figure C.9: Photomasks designed for microfluidic devices containing NPG. The NPG would sit within the large channel areas and the two PDMS halves would be aligned using the + alignment marks.

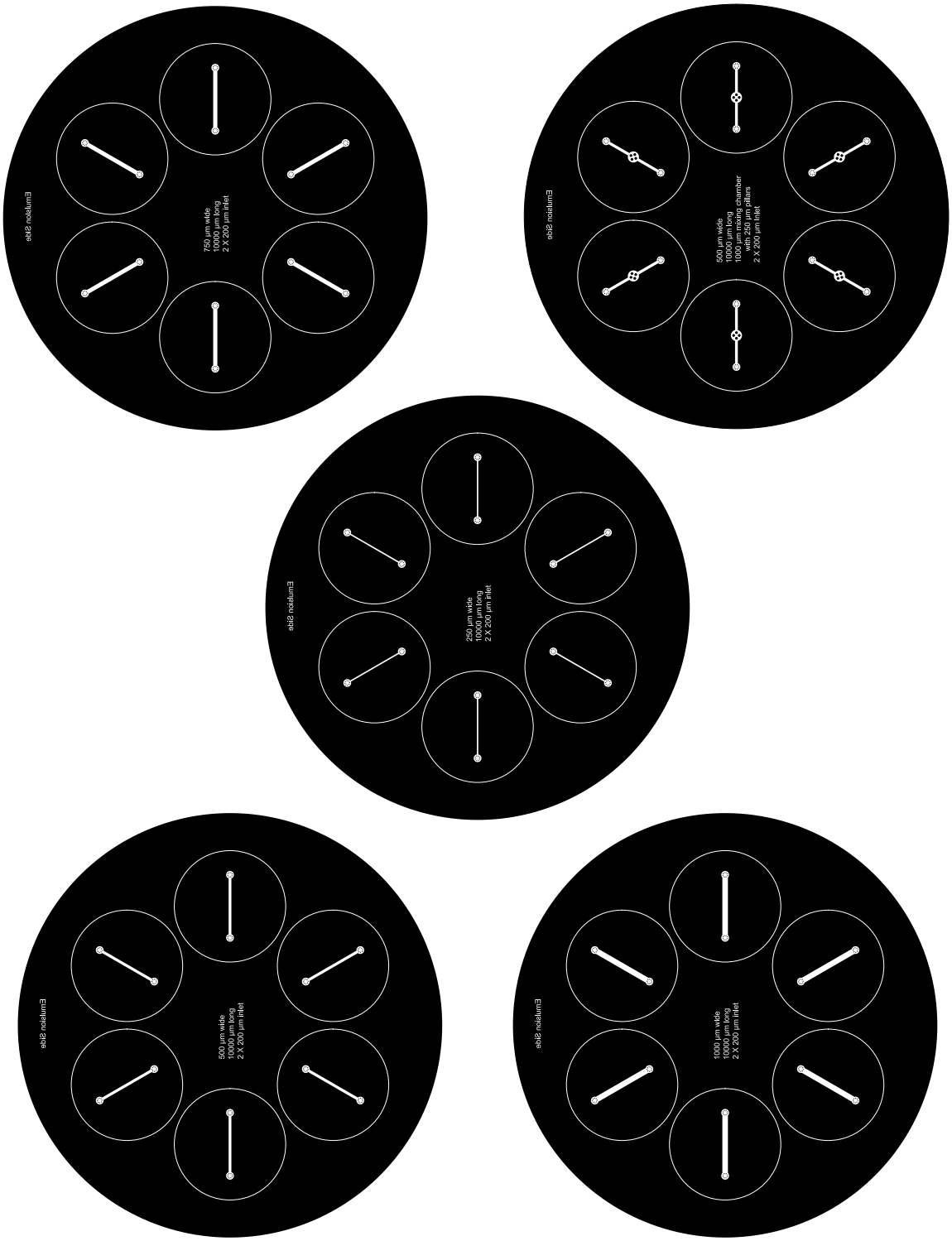

Figure C.10: Photomasks designed for single channel microfluidic devices containing NPG. The NPG would sit in between two PDMS halves and the single channels would be aligned perpendicular to each other.